Technical Physics, Vol. 48, No. 5, 2003, pp. 523–526. Translated from Zhurnal Tekhnicheskoĭ Fiziki, Vol. 73, No. 5, 2003, pp. 1–4.

ATOMS, SPECTRA, RADIATION

Gasdynamic Parameters of a Supersonic Molecular Beam Seeded by Fullerene Molecules

M. A. Khodorkovskiĭ, S. V. Murashov, T. O. Artamonova, Yu. A. Golod, A. L. Shakhmin, V. L. Varentsov, and L. P. Rakcheeva

Prikladnaya Khimiya Russian Scientific Center, St. Petersburg, 197198 Russia

e-mail: khodorkovskii@mail.ru

Received September 17, 2002

Abstract—Gasdynamic parameters of a molecular beam formed by passing a pulsed beam of a neutral gas through a Knudsen cell filled with a fullerene vapor are studied experimentally. It is shown that this method can be used to advantage in generating supersonic molecular beams of virtually any substances, which is of special importance for depositing epitaxial films and films of low-volatility materials. *© 2003 MAIK "Nauka/Interperiodica".*

Supersonic molecular beams seeded by atoms or molecules of low-volatility materials are usually generated by the flow of gas mixtures through a sub- or supersonic free-jet nozzle. In this case, binary mixtures are commonly used where the ratio between the partial pressures of heavy and light (carrier) gases does not exceed several fractions of a percent. Under such conditions, the axial portion of the beam generated is considerably seeded by the heavy component of the mixture, while the transient velocity of the beam, as well as its temperature and velocity distribution, is governed by the nozzle flow of the light component. This method allows the generation of monokinetic beams of heavy gases with a kinetic energy as high as several hundreds of electron volts [1].

The conventional method for generating seeded beams uses, as a rule, mixtures of inert or atmospheric gases [2]. Studies in which the vapors of high-volatility compounds are used as a heavy component [3] are uncommon, and those where the beams are seeded by atoms of low-volatility compounds [4] are virtually absent. The reason is that in experiment it is difficult to create nozzles (especially pulsed nozzles) that can be heated to a temperature sufficient to reach a reasonable concentration of low-volatility compounds.

In [5], a pulsed gasdynamic molecular beam of fullerene (the temperature of vaporization exceeds 250°C) was generated by passing a supersonic molecular helium beam through a Knudsen cell filled with the fullerene vapor. This beam was used to deposit thin fullerene films whose structure and properties depended considerably on the kinetic energy of adsorbate molecules [6–9].

The strong correlation between the properties of the thin films and the parameters of the beam has dictated the need for determining a set of gasdynamic parameters of fullerene beams obtained with this method. Associated experimental data have subsequently been used to elaborate a qualitative beam formation model.

The source of a molecular fullerene beam consists of a subsonic pulsed nozzle with an outlet diameter of 0.13 mm that was filled with helium to a pressure of 2 to 5 atm and of a Knudsen cell filled with the fullerene vapor at temperatures of 600 to 650 K (Fig. 1). At these temperatures, the vapor pressure of fullerene varies between 10^{-5}–10^{-4} Torr. The length and inner diameter of the cell are 28 and 6 mm, respectively. A pulsed helium flow passes through the cell whose axis is aligned with the nozzle axis. The cell edge nearest to the nozzle is 3 to 5 mm away from its end face. Down-

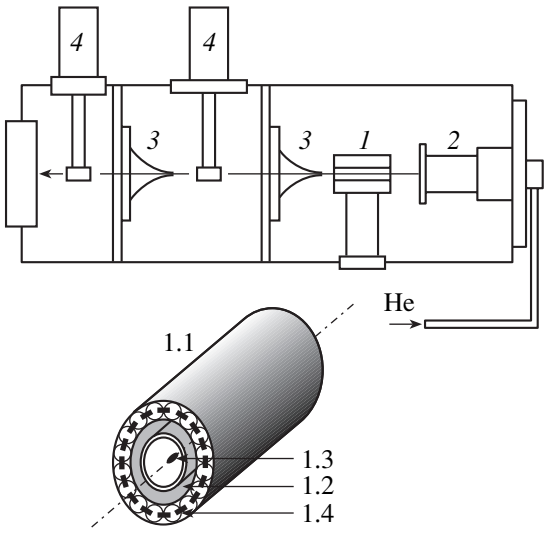

Fig. 1. Design of the experimental setup. (*1*) Knudsen cell: (1.1) Knudsen cell on an enlarged scale, (1.2) fullerene-filled interior, (1.3) hole for fullerene vapor, and (1.4) heating coil; (*2*) pulsed nozzle, (*3*) skimmer, and (*4*) mass spectrometer.

1063-7842/03/4805-0523$24.00 © 2003 MAIK "Nauka/Interperiodica"

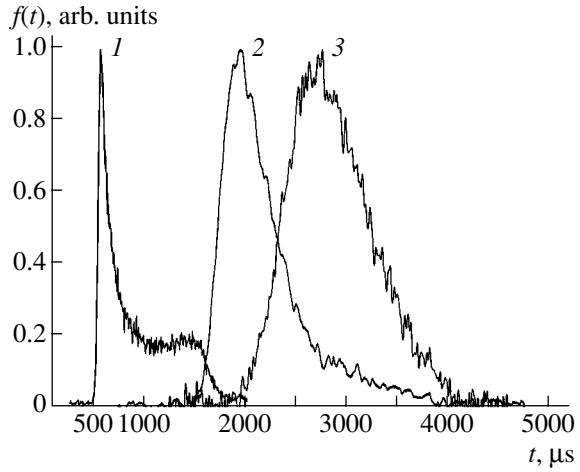

Fig. 2. TOF spectra of the pulsed molecular fullerene (C_{60}) beam recorded by (*1*) TOF mass spectrometer and (*2*, *3*) two quadruple mass spectrometers placed at distances of 90, 450, and 750 mm from the Knudsen cell.

stream of the opposite edge of the cell (at a distance of 10 mm), the first skimmer with an outlet diameter of 1 mm is placed. The other skimmer (with an outlet diameter of 2 mm) is placed at a distance of 600 mm. All the chambers separated by the skimmers are independently evacuated with high-vacuum pumps (a residual pressure of no more than 10^{-9} Torr) and are equipped with quadruple mass spectrometers with their ionization heads located at the axis of the beam. The distances between the Knudsen cell and centers of the mass spectrometers are 450 and 750 mm. An electron gun placed at a distance of 90 mm from the nozzle provides the diagnostics of the beam by means of a time-of-flight mass spectrometer, which is also located at the axis of the beam. In the experiment, the operating parameters of the pulsed subsonic nozzle were as follows: the pulse width t_p = 100–800 μs, and the frequency of nozzle opening is 1–30 Hz. The gasdynamic parameters of the beam were determined from the waveforms of signals for the helium and fullerene (C_{60}) masses that come from the quadruple and time-of-flight mass spectrometers. The operation of the spectrometers was synchronized with nozzle opening. The measurements were made in a wide range of external parameters, such as the pressure in the nozzle chamber, the frequency and duration of nozzle opening, the temperature of the fullerene-filled cell, and the nozzle–cell spacing.

Figure 2 shows typical time-of-flight (TOF) fullerene spectra recorded by the quadruple mass spectrometers. If the exact spacing between the spectrometers is known, the transient velocity is easy to calculate. At the same time, to find the thermal velocity, Mach number, and velocity ratio is a challenge, since one must have an idea of how the instrumental function of the beam source and detectors affect the width of the TOF spectra. The instrumental function was determined by taking the signal waveforms for the residual gases when they undergo pulsed ionization in the ionization head of the mass spectrometer. It turned out that the instrumental function, which is defined by the traveling time of ions in the quadruple trap, can be neglected, since this time is no larger than several microseconds (depending on the ion mass). The width of the fullerene beam source was estimated by taking TOF spectra in the TOF mass spectrometer, in which, as was mentioned above, the ionization area is at a small distance (90 mm) from the nozzle.

As follows from Fig. 2, this TOF spectrum is considerably narrower than those taken at distances of 450 and 750 mm. Assuming that the beam velocity distribution in the region adjacent to the Knudsen cell is close to that obtained in the mass spectrometers, one can easily find the beam width $\Delta\tau$ at the exit from the Knudsen cell.

Our estimates show that this width is a maximum of 50 μs, which is more than one order of magnitude less than the width Δt of the TOF spectrum recorded by the mass spectrometers. With $\Delta t/\Delta\tau = 5$, the error in measuring the width of the TOF spectrum is no higher than 2.5% [10]. In our case (Fig. 1), the widths of the TOF spectra taken by the quadruple mass spectrometers at distances of 450 and 750 mm from the Knudsen cell are, respectively, 577 and 947 μm, that is, more than one order of magnitude larger than the width of the TOF spectrum at the cell. Hence, the condition $\Delta t/\Delta\tau = 5$ is fulfilled *a fortiori* and the TOF distribution is close to the true distribution. This result allows us to ignore the effect of the instrumental function on the shape of the TOF spectra shown in Fig. 2.

Figure 2 shows that the TOF spectrum obtained with the TOF mass spectrometer has, along the narrow distribution of fast fullerene molecules, an extended plateau, which is formed by molecules with a wide velocity distribution. Such a shape of the spectrum is due to the fact that the drift chamber of the TOF mass spectrometer receives fullerene molecules that leave the Knudsen cell over a wide range of angles and not only those traveling along the nozzle's axis, which is aligned with the beam axis. Therefore, the flow under study contains not only fast particles with a narrow velocity distribution but also an appreciable (in the integral sense) amount of particles that have not formed into a directed molecular beam.

On calculating the gasdynamic parameters in the axial portion of the fullerene beam, the influence of the scattered gas on the velocity distribution function was not taken into account, since the residual pressure in the measuring chamber was below 10^{-7} Torr during the measurements. The low residual pressure allowed the velocity distribution function $f(v)$ to be approximated by the Maxwell function with a transient velocity v_{tr} [11, 12].

The function $f(v)$ (Fig. 3) can be found from the TOF distributions $f(t)$ (Fig. 2). Figure 3 demonstrates

that, in the velocity space, the TOF distributions obtained by both mass spectrometers are nearly coincident, which is another indication that the beam particles do not interact when traveling between the detectors.

Using the expression for the beam intensity [13], the molecule velocity distribution can be written as

$$\frac{dN}{dv} = A_0\frac{n_0}{\pi z^2}(v_t)^{-3}v^2\exp\left[-\frac{v-v_{tr}}{v_t}\right]^2 2\Delta\tau = Af(v),$$

where dN is the amount of fullerene molecules in a velocity interval dv, A_0 is the cross-sectional area of the skimmer inlet, n_0 is the molecule concentration at the skimmer inlet, z is the distance downstream of the skimmer, $v_t = \sqrt{2kT/m}$ is the thermal velocity of the molecule, and T is the gas temperature at the skimmer inlet.

The function $f(t)$ found in the experiment can then be represented as

$$f(t)dt = Af(v)\frac{v^2}{l}dv,$$

where l is the path length.

Thus, the theoretical velocity distribution is given by

$$f(v) = av^2v_t^{-3}\exp\left[-\frac{v-v_{tr}}{v_t}\right]^2, \qquad (1)$$

where a is the normalizing factor.

Varying the parameters v_t and v_{tr} in (1), one can determine the temperature and mass-averaged velocity of the flow that are fitted by the experimental distribution most accurately (Fig. 3).

Calculations show that, under our experimental conditions, the transient velocity of fullerene molecules is v_{tr} = 371 m/s; thermal velocity, v_t = 112 m/s; temperature, T = 560 K; and Mach number, M = 4. The kinetic energy of the molecules that is calculated from v_{tr} was found to be 0.526 eV.

The parameters of the forming fullerene beam can be estimated based on the shock tube model where the pulsed nozzle acts as a high-pressure chamber (P_h) and the Knudsen cell replaces a low-pressure chamber (P_l) [14]. If the ratio P_h/P_l tends to infinity, the Mach number in a shock tube can be calculated by the formula [15]

$$M_{p_h/p_l} = \frac{k_{l+1}}{k_h - 1}\frac{a_h}{a_l}, \qquad (2)$$

where k_h = 1.33 and k_l = 1.66 are the adiabatic exponents for helium and fullerene, respectively, and a_h and a_l are the velocities of sound in the high- and low-pressure chambers, respectively.

Formula (2) may certainly be used to calculate the Mach number in our case, since the fullerene pressure in the Knudsen cell does not exceed 10^{-4} Torr and the pressure in the helium flow at the cell inlet exceeds 10 Torr, as follows from the numerical calculation of the gasdynamic parameters of the pulse nozzle. This formula requires knowing the velocities of sound in the high- and low-pressure chambers to calculate the Mach number. These velocities obtained elsewhere [15, 16] are 131.345 and 96 m/s, respectively. The Mach number calculated for our conditions was found to be 4.7, which is in good agreement with the experimental value mentioned above.

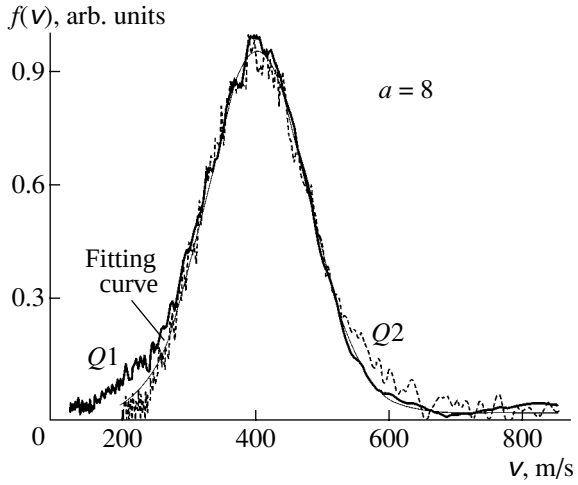

Fig. 3. Spectra of the pulsed molecular fullerene (C_{60}) beam in the velocity space recorded by the two quadruple mass spectrometers and the velocity distribution (fine approximating curve) obtained from expression (1).

ACKNOWLEDGMENTS

This work was supported by the Russian Foundation for Basic Research (grant no. 01-03-33162) and by the All-Russia Research Program "Fullerenes and Atomic Clusters."

REFERENCES

1. E. Kolodney, A. Budrevich, and B. Tsipinyuk, J. Phys. Chem. **100**, 1475 (1996).
2. M. A. Khodorkovsky, A. N. Zavilopulo, and A. I. Dolgin, Phys. Scr. **50**, 696 (1994).
3. A. Giardini-Guidoni, D. Toja, and S. Piccirillo, in *Book of Abstracts of the 17th International Symposium on Molecular Beams, Paris XI University, Orsay, France, 1997*.
4. M. Ehbrecht, M. Färber, F. Rohmund, *et al.*, Chem. Phys. Lett. **214**, 34 (1993).
5. M. A. Khodorkovskiĭ, A. L. Shakhmin, S. V. Murashov, *et al.*, Pis'ma Zh. Tekh. Fiz. **24** (10), 20 (1998) [Tech. Phys. Lett. **24**, 379 (1998)].
6. Ch. Girard, Ph. Lambin, A. Dereux, *et al.*, Phys. Rev. B **49**, 11425 (1994).

7. E. J. Snyder, M. S. Anderson, W. M. Tong, *et al.*, Science **253**, 171 (1991).
8. J. L. Wragg, J. E. Chamderlain, H. W. White, *et al.*, Nature **348**, 623 (1990).
9. V. Paillard, P. Melinon, V. Dupuis, *et al.*, Phys. Rev. B **49**, 11433 (1994).
10. O. F. Hagena and A. K. Warma, Rev. Sci. Instrum. **39**, 42 (1968).
11. A. Deursen, A. Luming, and I. Reuss, Int. J. Mass Spectrom. Ion Phys. **18**, 129 (1975).
12. M. A. Khodorkovskiĭ, A. A. Markov, and A. I. Dolgin, Zh. Tekh. Fiz. **59** (8), 89 (1989) [Sov. Phys. Tech. Phys. **34**, 898 (1989)].
13. J. B. Anderson and J. B. Fenn, Phys. Fluids **8**, 780 (1965).
14. S. A. Losev, Itogi Nauki Tekh., Ser.: Mekh. Zhidk. Gaza **18**, 270 (1984).
15. L. G. Loĭtsyanskiĭ, *Fluid Mechanics* (Nauka, Moscow, 1973).
16. B. Sundqvist, Adv. Phys. **48** (1), 1 (1999).

Translated by V. Isaakyan

Technical Physics, Vol. 48, No. 5, 2003, pp. 527–534. Translated from Zhurnal Tekhnicheskoĭ Fiziki, Vol. 73, No. 5, 2003, pp. 5–12.

GASES AND LIQUIDS

On the Stability of a Nonaxisymmetric Charged Jet of a Viscous Conducting Liquid

S. O. Shiryaeva, A. I. Grigor'ev, T. V. Levchuk, and M. V. Rybakova

Demidov State University, Sovetskaya ul. 14, Yaroslavl, 150000 Russia

e-mail: shir@uniyar.ac.ru

Received July 10, 2002; in final form, October 28, 2002

Abstract—A dispersion equation is derived for axisymmetric and nonaxisymmetric capillary oscillations in a jet of viscous conducting liquid subjected to a constant potential. It is shown that conditions arising when the surface charge density in the jet is high cause the instability of nonaxisymmetric, rather than axisymmetric, modes with the resulting disintegration of the jet into drops of various sizes. This theoretical finding allows one to correctly interpret of experimental data for the spontaneous disintegration of charged jets. © *2003 MAIK "Nauka/Interperiodica".*

(1) The capillary disintegration of charged liquid jets is of interest for applications in various areas of technology and applied chemistry (see, for example, [1] and references therein) and, therefore, has been the subject of much experimental [2, 3] and theoretical [4–10] investigation. Nevertheless, some issues, in particular, the disintegration of nonaxisymmetric jets, remain unclear. The nonaxisymmetric disintegration of charged jets was carefully studied in experiments [2, 3]. It was ascertained that the nonaxisymmetric disintegration is enhanced with an increase in an electric potential applied to the jet. In addition, this phenomenon is of interest for the geophysically oriented investigations of the disintegration of free-falling charged drops in an external electrostatic field. In [11], the ejection of liquid jets from the opposite ends of a drop in the direction of an external electrostatic field with the subsequent nonaxisymmetric disintegration of the jets into daughter droplets was observed. When studying the electrostatic atomization of a liquid from the end of a capillary (the phenomenon that has vast applications [12]) through which the liquid is fed into a discharge system, Cloupeau and Prunet-Foch [13] also observed the ejection of fine liquid jets from the top of the meniscus at the capillary end that nonaxisymmetrically disintegrate into tiny droplets. These features of the nonaxisymmetric disintegration of liquid jets give rise to a great variety of electrostatic liquid atomization conditions observed experimentally [14, 15]. In what follows, emphasis will be on studying the instability of nonaxisymmetric charged jets of a conducting liquid.

(2) Let an infinite cylindrical jet of a viscous incompressible liquid with a mass density ρ, kinematic viscosity ν, and surface tension σ move at a constant velocity $\mathbf{U}_0$ along the symmetry axis and be under a constant electric potential Φ_*. The radius of the jet is R. We assume that the liquid is perfectly conducting and the electric charge is uniformly distributed over the unperturbed cylindrical jet surface with a surface charge density κ_0. Since the jet is infinite, we simplify the problem by passing to the inertial coordinate system moving together with the jet at the same velocity $\mathbf{U}_0$. Then, the flow velocity field $\mathbf{U}(\mathbf{r}, t)$ in the jet is completely defined by capillary (for example, thermal) oscillations of the jet surface and is of the same order of smallness as the oscillation amplitude. We will study instability conditions for the capillary oscillations of the jet surface.

Calculations will be performed in the cylindrical coordinate system r, ϕ, z with the unit vector $\mathbf{n}_z$ aligned with the symmetry axis of the jet. The equation of the jet surface disturbed by capillary wave motion can be written in the form

$$r = R + \xi(z, \phi, t), \quad |\xi| \ll R.$$

The mathematical formulation of the problem of capillary oscillations in the jet includes the equations of fluid dynamics and electrostatics (under the assumption that the flow velocity is much lower than the relativistic one)

$$\frac{d\mathbf{U}}{rt} = -\frac{1}{\rho}\nabla P + \nu\Delta\mathbf{U},$$

$$\nabla\mathbf{U} = 0, \quad \Delta\Phi = 0$$

with the boundedness conditions

$$r \longrightarrow 0: \quad |\mathbf{U}| < \infty,$$

$$r \longrightarrow \infty: \quad |\nabla\Phi| \longrightarrow 0;$$

the kinematic hydrodynamic boundary condition at the free surface of the jet

$$r = R + \xi: -\frac{\partial\xi}{\partial t} + \mathbf{U}\cdot\nabla[r - (R + \xi(z, \phi, t))] = 0;$$

and the dynamic boundary conditions for the tangential components,

$$r = R + \xi: \frac{\partial U_\phi}{\partial r} + \frac{1}{r}\frac{\partial U_r}{\partial \phi} - \frac{1}{r}U_\phi = 0,$$

$$\frac{\partial U_z}{\partial r} + \frac{\partial U_r}{\partial z} = 0,$$

and for the normal component

$$r = R + \xi: -P(\mathbf{r}, t) - P_0 + 2\nu\frac{\partial U_r}{\partial r} - P_\kappa + P_0 = 0,$$

of the velocity field. We also assume that the jet surface is equipotential:

$$\Phi = \Phi_*.$$

Here U_r, U_ϕ, U_z are the components of the velocity field in the cylindrical coordinate system; $P(\mathbf{r}, t)$ is the hydrodynamic pressure; P_0 is the atmospheric pressure; P_κ is the electric field pressure; P_σ is the pressure of surface tension forces; Φ is the electrostatic potential; and $|\xi|/R$ is Laplacian.

A solution to the problem will be sought as the expansion in the small parameter $|\xi|/R$. In the zeroth approximation, we will obtain a stationary cylindrical liquid column and also the well-known expressions for bubble pressure under a free cylindrical liquid surface and for the pressure of an electric field on the surface of a uniformly charged infinite cylinder of fixed radius.

(3) In the linear approximation in $|\xi|/R$ (with the same notation of physical quantities), the problem stated in dimensionless variables such that $R = 1$, $\rho = 1$, and $\sigma = 1$ takes the form

$$r = 1 + \xi(\phi, z, t), \quad |\xi| \ll 1, \tag{1}$$

$$\frac{\partial \mathbf{U}}{\partial t} = -\nabla p + \nu\Delta\mathbf{U}, \tag{2}$$

$$\nabla\mathbf{U} = 0, \tag{3}$$

$$\Delta\varphi = 0, \tag{4}$$

$$r \longrightarrow 0: |\mathbf{U}| < \infty, \tag{5}$$

$$r \longrightarrow \infty: |\nabla\varphi| \longrightarrow 0, \tag{6}$$

$$r = 1: -\frac{\partial \xi}{\partial t} + U_r = 0, \tag{7}$$

$$\frac{\partial U_\phi}{\partial r} + \frac{\partial U_r}{\partial \phi} - U_\phi = 0, \tag{8}$$

$$\frac{\partial U_z}{\partial r} + \frac{\partial U_r}{\partial z} = 0, \tag{9}$$

$$-p + 2\nu\frac{\partial U_r}{\partial r} - p_\kappa + p_\sigma = 0, \tag{10}$$

$$\varphi - 4\pi\kappa_0\xi = 0. \tag{11}$$

In Eqs. (1)–(11), φ, p, p_κ, and p_σ are the capillary-oscillation-induced corrections (of first order of smallness in $|\xi|$) to the electric potential, hydrodynamic pressure, electric force pressure, and surface tension force pressure, respectively.

Expanding the standard analytical expressions for bubble pressure, $P_\sigma = \mathrm{div}\,\mathbf{n}$ (where $\mathbf{n}$ is the unit normal to surface (1)), and for electric field pressure, $P_\kappa = 2\pi\kappa_0^2$ (see the Appendix), in the small parameter ξ, one easily obtains the following relationships for the first-order parameters p_κ and p_σ entering into (10):

$$p_\sigma = -\left(\xi + \frac{\partial^2\xi}{\partial\phi^2} + \frac{\partial^2\xi}{\partial z^2}\right), \tag{12}$$

$$p_\kappa = -4\pi\kappa_0^2\xi - \kappa_0\frac{\partial\varphi}{\partial r}. \tag{13}$$

(4) We solve the set of Eqs. (2) and (3) by the method of operator scalarization (for details, see [16]), representing the velocity field $\mathbf{U}(\mathbf{r}, t)$ as the sum of three orthogonal vector fields with the help of differential vector operators $\hat{\mathbf{N}}_i$:

$$\mathbf{U}(\mathbf{r}, t) = \sum_{i=1}^{3}\hat{\mathbf{N}}_i\psi_i(\mathbf{r}, t) \quad (i = 1, 2, 3). \tag{14}$$

The operators $\hat{\mathbf{N}}_i$ satisfy the orthogonality conditions

$$\hat{\mathbf{N}}_j^+\mathbf{N}_i = 0 \ (\text{at } i \neq j;\ i, j = 1, 2, 3) \tag{15}$$

and the conditions of commutativity with the Laplacian operator

$$\Delta\hat{\mathbf{N}}_i = \hat{\mathbf{N}}_i\Delta. \tag{16}$$

In expressions (14) and (15), $\psi_i(\mathbf{r}, t)$ are unknown scalar functions and $\hat{\mathbf{N}}_j^+$ are operators Hermitean conjugate to the operators $\hat{\mathbf{N}}_j$.

Since the equilibrium shape of the jet has axial symmetry, the operators $\hat{\mathbf{N}}_i$ can be taken in the form

$$\hat{\mathbf{N}}_1 = \nabla, \quad \hat{\mathbf{N}}_2 = \nabla\times\mathbf{e}_z, \quad \hat{\mathbf{N}}_3 = \nabla\times(\nabla\times\mathbf{e}_z).$$

The velocity field $\mathbf{U}(\mathbf{r}, t)$ in the cylindrical coordinate system has the following components expressed through the scalar functions $\psi_i(\mathbf{r}, t)$:

$$U_r = \frac{\partial\psi_1}{\partial r} + \frac{1}{r}\frac{\partial\psi_2}{\partial\phi} + \frac{\partial^2\psi_3}{\partial z\partial r},$$

$$U_\phi = \frac{1}{r}\frac{\partial\psi_1}{\partial\phi} - \frac{\partial\psi_2}{\partial r} + \frac{1}{r}\frac{\partial^2\psi_3}{\partial z\partial\phi}, \tag{17}$$

$$U_z = \frac{\partial \psi_1}{\partial z} - \left[\frac{1}{r}\frac{\partial}{\partial r}\left(r\frac{\partial \psi_3}{\partial r}\right) + \frac{1}{r^2}\frac{\partial^2 \psi_3}{\partial \phi^2}\right].$$

Substituting expansion (14) into the set of Eqs. (2) and (3) and using the properties of operators (15) and (16) yields the set of scalar equations

$$\Delta\psi_1 = 0, \quad \Delta\psi_i - \frac{1}{\nu}\frac{\partial \psi_i}{\partial t} = 0 \ (i = 2, 3), \tag{18}$$

$$p = -\frac{\partial \psi_1}{\partial t}. \tag{19}$$

Using (12), (13), (17), and (19), we transform boundary conditions (7)–(10) into those for the unknown functions ψ_i and ξ:

$$r = 1: \frac{\partial \xi}{\partial t} - \left[\frac{\partial \psi_1}{\partial t} + \frac{1}{r}\frac{\partial \psi_2}{\partial \phi} + \frac{\partial^2 \psi_3}{\partial z \partial r}\right] = 0,$$

$$2\frac{\partial}{\partial \phi}\left\{\frac{\partial \psi_1}{\partial r} - \psi_1\right\} - \left\{\frac{\partial^2 \psi_2}{\partial r^2} - \frac{\partial \psi_2}{\partial r} - \frac{\partial^2 \psi_2}{\partial \phi^2}\right\}$$

$$+ 2\frac{\partial^2}{\partial z \partial \phi}\left\{\frac{\partial \psi_3}{\partial r} - \psi_3\right\} = 0,$$

$$\frac{\partial}{\partial r}\left\{\frac{\partial \psi_1}{\partial z} - \left[\frac{1}{r}\frac{\partial}{\partial r}\left(r\frac{\partial \psi_3}{\partial r}\right) + \frac{1}{r^2}\frac{\partial^2 \psi_3}{\partial \phi^2}\right]\right\} \tag{20}$$

$$+ \frac{\partial}{\partial z}\left\{\frac{\partial \psi_1}{\partial r} + \frac{1}{r}\frac{\partial \psi_2}{\partial \phi} + \frac{\partial^2 \psi_3}{\partial z \partial r}\right\} = 0,$$

$$\frac{\partial \psi_1}{\partial t} + 2\nu\frac{\partial}{\partial r}\left\{\frac{\partial \psi_1}{\partial r} + \frac{1}{r}\frac{\partial \psi_2}{\partial \phi} + \frac{\partial^2 \psi_3}{\partial z \partial r}\right\}$$

$$+ 4\pi\kappa_0^2\xi + \kappa_0\frac{\partial \varphi}{\partial r} - \left(\xi + \frac{\partial^2 \xi}{\partial \phi^2} + \frac{\partial^2 \xi}{\partial z^2}\right) = 0.$$

The functions ξ, φ, and ψ_i describe small deviations from the equilibrium state; therefore, in order to follow the evolution of these deviations with time, we assume that they vary with time exponentially:

$$\xi, \varphi, \psi_i \sim \exp(st),$$

where s is the complex frequency.

With this in mind, we will seek solutions to Eqs. (18) and (4) that satisfy boundedness conditions (5) and (6) in the cylindrical coordinate system in the form of expansions in waves traveling along the z axis:

$$\psi_1 = \int_0^\infty \sum_{m=0}^{\infty} C_1 I_m(kr)\exp(im\phi)\exp(ikz)\exp(st)dk,$$

$$\psi_i = \int_0^\infty \sum_{m=0}^{\infty} C_i I_m(lr)\exp(im\phi)\exp(ikz)\exp(st)dk \tag{21}$$

$$(i = 2, 3),$$

$$\varphi = \int_0^\infty \sum_{m=0}^{\infty} C_4 K_m(kr)\exp(im\phi)\exp(ikz)\exp(st)dk. \tag{22}$$

The function $\xi(z, \phi, t)$ is represented in a similar way:

$$\xi(z, \phi, t) = \int_0^\infty \sum_{m=0}^{\infty} D\exp(im\phi)\exp(ikz)\exp(st)dk. \tag{23}$$

In (21)–(23), k is the wave number, $l^2 \equiv k^2 + s/\nu$, m are azimuthal numbers (integers characterizing the deviation of the solutions from axial symmetry), $I_m(x)$ and $K_m(x)$ are the modified Bessel functions of the first and second kind, and C_i and D are the m- and k-dependent expansion coefficients (i = 1–4).

From equipotentiality condition (11) for the jet surface, solutions (22) and (23), and the orthonormality properties of the functions $\exp(im\phi)$ and $\exp(ikz)$];

$$\int_0^{2\pi} \exp[i(m_1 - m_2)\phi]d\phi = \delta_{m_1, m_2},$$

$$\int_{-\infty}^{\infty} \exp[i(k_1 - k_2)z]dz = \delta(k_1 - k_2), \tag{24}$$

where δ_{m_1, m_2} is the Kronecker symbol and $\delta(k_1 - k_2)$ is the Dirac function, one easily finds a relation between the coefficients D and C_4:

$$C_4 = \frac{4\pi\kappa_0 D}{K_m(k)}. \tag{25}$$

Substituting (21)–(23) into boundary conditions (20) subject to (25) and relationships (24), we obtain a set of equations for the unknown coefficients D and C_i (i = 1–3):

$$Ds - C_1 kI_m'(k) - C_2 imI_m(l) - C_3 iklI_m'(l) = 0,$$

$$C_1 2im(kI_m'(k) - I_m(k)) + C_2(lI_m'(l) - m^2 I_m(l) - l^2 I_m''(l))$$

$$+ C_3 2mk(I_m(l) - lI_m'(l)) = 0,$$

$$C_1 2ik^2 I_m'(k) - C_2 mkI_m(l) - C_3(l^3 I_m'''(l) + l^2 I_m''(l) \tag{26}$$

$$+ l(k^2 - m^2 - 1)I_m'(l) + 2m^2 I_m(l)) = 0,$$

$$D\left\{4\pi\kappa_0^2\left(1+\frac{kK_m'(k)}{K_m(k)}\right)+k^2+m^2-1\right\}$$

$$+C_1(sI_m(k)+2\nu k^2 I_m''(k))+C_2 2\nu im(lI_m'(l)-I_m(l))$$

$$+C_3 2\nu ikl^2 I_m''(l)=0.$$

Primes in (26) denote the derivatives of the *m*th-order Bessel functions with respect to their arguments. These derivatives can be expressed through *m*th- and $(m+1)$th-order Bessel functions with the recurrence relationships

$$I_m'(x)=I_{m+1}(x)+\frac{m}{x}I_m(x)=I_{m-1}(x)-\frac{m}{x}I_m(x),$$

$$I_m''(x)=-\frac{1}{x}I_{m+1}(x)+\left(1+\frac{m(m-1)}{x^2}\right)I_m(x),$$

$$I_m'''(x)=\left(1+\frac{m^2+2}{x^2}\right)I_{m+1}(x)$$

$$+\frac{m-1}{x}\left(1+\frac{m(m-2)}{x^2}\right)I_m(x),$$

$$K_m'(x)=\frac{m}{x}K_m(x)-K_{m+1}(x).$$

Recall that the set of homogeneous linear equations (26) has a nontrivial solution only if its determinant is equal to zero; that is, $\det[a_{ij}]=0$, where the elements a_{ij} are given by

$$a_{11}=s,\quad a_{21}=a_{31}=0,$$

$$a_{41}=k^2+m^2-1+4\pi\kappa_0^2\left\{1+m-k\frac{K_{m+1}(k)}{K_m(k)}\right\},$$

$$a_{12}=-(kI_{m+1}(k)+mI_m(k)),$$

$$a_{22}=2im(kI_{m+1}(k)+(m-1)I_m(k)),$$

$$a_{32}=2ik(kI_{m+1}(k)+mI_m(k)),$$

$$a_{42}=[s+2\nu(k^2+m(m-1))]I_m(k)-2\nu kI_{m+1}(k),$$

$$a_{13}=-imI_m(l),\ a_{23}=2lI_{m+1}(l)-(l^2+2m(m-1))I_m(l),\quad (27)$$

$$a_{33}=-mkI_m(l),\ a_{43}=2\nu im(kI_{m+1}(l)+(m-1)I_m(l)),$$

$$a_{14}=-ik(lI_{m+1}(l)+mI_m(l)),$$

$$a_{24}=-2mk(lI_{m+1}(l)+(m-1)I_m(l)),$$

$$a_{34}=-(l^2+k^2)(lI_{m+1}(l)+mI_m(l)),$$

$$a_{44}=2\nu ik([l^2+m(m-1)]I_m(l)-lI_{m+1}(l)).$$

(5) Expanding the fourth-order determinant with elements (27), we obtain a dispersion relation for the frequencies *s* of the nonaxisymmetric oscillations of the jet surface as functions of the wave number *k*:

$$s^2\{m[l^2(l^2+k^2)+2m(m-1)l^2]$$

$$+F_m(l)l[(l^2+k^2)(l^2-4m)+2l^2m^2]-2l^2(l^2+k^2)F_m^2(l)\}$$

$$+2s\nu\{-ml^2(l^2-k^2)(k^2-m(m-1))$$

$$+F_m(l)l[l^2k^2(l^2+k^2)+l^2m(m-1)(l^2-2m(m+1))$$

$$+l^2k^2m(3m+1)-4k^2m(k^2-m(m^2-1))]$$

$$-2l^2[k^2(l^2+k^2)+m(m^2-1)(l^2-k^2)]F_m^2(l)$$

$$-F_m(k)k(2l^2(l^2k^2+m^2(m^2-1))+l^2m(l^2+k^2(4m-5))$$

$$+F_m(l)l[l^4-5l^2k^2+4m(m^2-1)(l^2-k^2)] \quad (28)$$

$$+2l^2(m^2-1)(l^2-k^2)F_m^2(l))\}=f(m,w,k)$$

$$\times\{m(l^2m(l^2-k^2)+F_m(l)l[l^2(l^2-k^2)-2m(l^2-2k^2)]$$

$$-2l^2(l^2-k^2)F_m^2(l))+F_m(k)k(m[l^2(l^2-k^2)-2ml^2]$$

$$+l(l^2-k^2)(l^2-4m)F_m(l)-2l^2(l^2-k^2)F_m^2(l))\},$$

$$f(m,w,k)\equiv\left[1-m^2-k^2-w\left(1+m-\frac{kK_{m+1}(k)}{K_m(k)}\right)\right],$$

$$w\equiv 4\pi\kappa_0^2,\quad F_m(x)\equiv\frac{I_{m+1}(x)}{I_m(x)}.$$

In general, Eq. (28) can be analyzed by only numerical techniques.

A dispersion relation for the axisymmetric oscillations of a charged jet with simplifications discussed in [4–10] is easy to obtain from (28) with $m=0$:

$$s^2+2\nu k^2 s\left[1-F_0(k)\left(\frac{2kl}{(l^2+k^2)F_0(l)}+\frac{l^2-k^2}{k(l^2+k^2)}\right)\right]$$

$$=k\frac{l^2-k^2}{l^2+k^2}F_0(k)f(0,w,k).$$

At $w=0$, this expression coincides with the dispersion relation for an uncharged jet of a viscous liquid [17].

For a jet of a low-viscosity liquid, when condition $l\gg k$ is fulfilled, Eq. (28) simplifies to

$$s^2+2s\nu(k^2+m(m-1)-kF_m(k))$$

$$=f(m,w,k)(m+kF_m(k)). \quad (29)$$

At a low viscosity, the term linear in *s* in (29) can also be omitted [17]:

$$s^2=f(m,w,k)(m+kF_m(k)). \quad (30)$$

At $f > 0$, relationship (30) defines the instability increment for a cylindrical wave $s = \sqrt{f}\,(m + kF_m(k))^{1/2}$. Equating the first derivative of the increment with respect to the wave number to zero, one finds the wave number of a capillary wave with a maximum increment; then, substituting it into (30) yields the increment itself. Figure 1 shows the results of such calculations (performed with the Matematika program for analytical calculations) presented in the form of the functions $s = s(w)$ and $k = k(w)$ for the first five values of the azimuthal number m.

From Fig. 1a, it is seen that the increments of the axisymmetric mode ($m = 0$) and nonaxisymmetric modes ($m = 1$–4), noticeably differing at small values of w, approach each other when the surface charge density κ_0 is sufficiently high (at large values of w). According to Fig. 1b, in such a situation, the wave numbers of nonaxisymmetric waves exceed markedly that of the axisymmetric wave. This means that, at the same value of the electric potential of the jet, instability conditions are established simultaneously for the axisymmetric mode and several nonaxisymmetric modes of surface oscillations. Thus, the jet disintegrates into drops of different sizes and becomes unstable against twisting about its axis (whipping in terms of [2]), which was also observed in experiments [3, 11, 13].

In the general case, when it is impossible to neglect the term linear in s in (29), the positive root of Eq. (29) corresponding to the instability increment takes the form

$$s = -\nu G(m, k) + (\nu^2 G^2(m, k) + f(m, w, k)(m + kF_m(k)))^{1/2},$$
$$G(m, k) = (k^2 + m(m-1) - kF_m(k)). \quad (31)$$

It easy to see that the critical conditions for jet instability development in the approximation used do not depend on the viscosity. Indeed, the critical conditions for instability development in an inviscid liquid jet are defined, according to (30), by the condition $f > 0$; otherwise, s becomes imaginary, which corresponds to the periodic variation of the wave amplitudes with time. From (31), it follows that positive solutions to Eq. (29), which define instability increments, also appear at $f > 0$. The effect of viscosity, in this case, causes the increments to decrease and the wave numbers corresponding to the most unstable waves to decline. However, this effect depends on the range of wave numbers and on m.

In the ranges of dimensionless wave numbers $k = 4$–6 and dimensionless increments $\sqrt{f} = 5$–10 (which are of interest for the development of unstable waves at large values of the surface charge; see Figs. 1a, 1b), the effect of viscosity (at $\nu \ll 1$) on the instability will be weak, showing up as a decrease in the increments and wave numbers of the most unstable waves by roughly 20%. This is illustrated in Fig. 2, where the calculated results for $\nu = 0.1$ are presented as the functions $s = s(w)$ and $k = k(w)$ for the first five values of the azimuthal

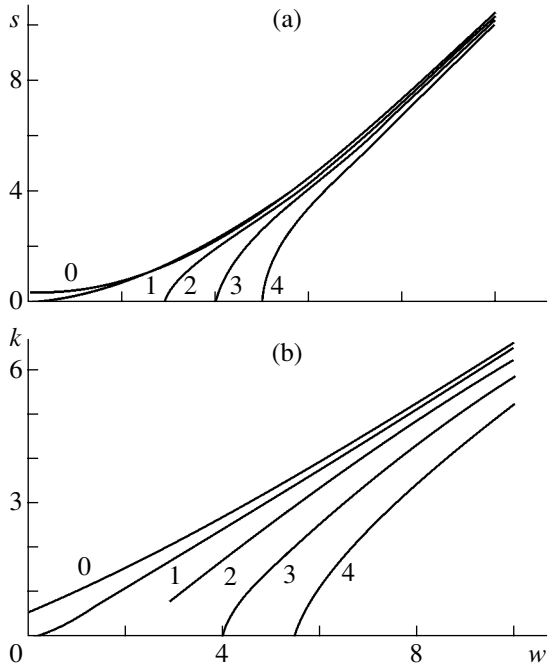

Fig. 1. (a) Dimensionless increment and (b) dimensionless wave number (b) of the most unstable wave as functions of the dimensionless parameter w characterizing the surface charge. The curves are plotted in the absence of viscosity. The numbers by the curves are the values of the azimuthal parameter m.

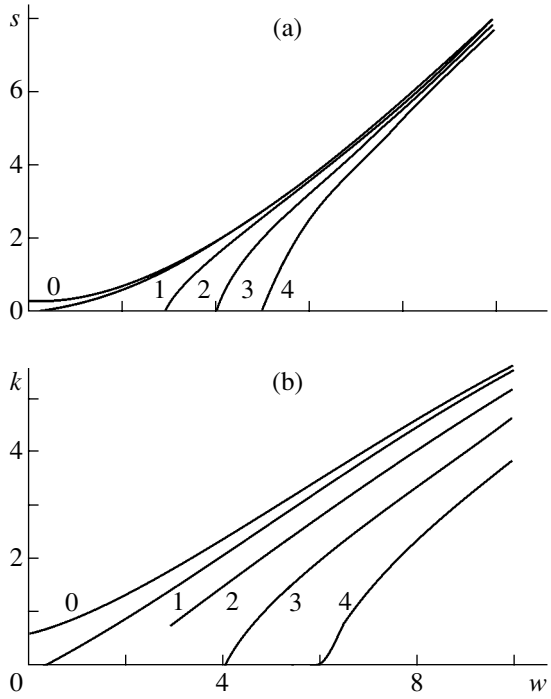

Fig. 2. The same as in Fig. 1 for $\nu = 0.1$.

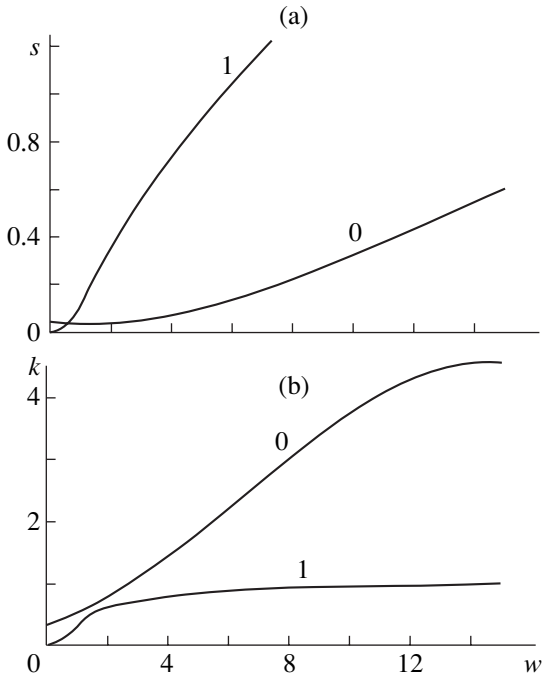

Fig. 3. The same as in Fig. 1 for ν = 3.

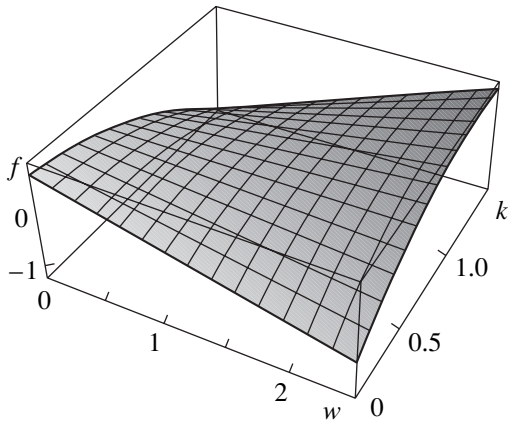

Fig. 4. Factor $f(m, w, k)$ as a function of the parameter w and dimensionless wave number k with $m = 0$.

number m. The data in Fig. 2 evidence that making allowance for viscosity, even if low, favors the instability development of nonaxisymmetric waves.

To study the effect of viscosity on the instability of jets at $\nu \approx 1$, we will analyze the asymptotics of dispersion relation (28) when $l \approx k$ or $k^2 \gg s/\nu$. In this approximation, expanding l and $F_m(x)$ in s/ν and retaining terms linear in s/ν, we obtain

$$s^2\{-6F_0^2k^2 + 2H(m,k)k^3[k^2 + m(m-4)] + m[3k^2 + 2m(m-1)] + F_0[4k^3 - 8H(m,k)k^4 + km(3m-8)]\} + 2ks\nu\{-2F_0^3k^2(m^2-1) + F_0[k^4 - 4H(m,k)k^5 + 4k^2m(m-1) - 3m^2(m-1)^2] - 3F_0^2k[k^2 + 2m(m^2-1)] + 2k[m^2(m-1) + H(m,k)k(k^4 + 2k^2m(m-1) + m^2(m-1)(3+m))]\} + f(m,w,k)k[F_0^2k^2(2F_0 - k) - 2F_0km(k - 3F_0) - m^2(2H(m,k)k^2 + k - 3F_0)] + 8F_0\nu^2k^3m^2(m-1) = 0, \quad (32)$$

$$H(m,k) \equiv 1 - F_m^2(k) - \frac{2m+1}{k}F_m(k).$$

The results of numerical calculation (by Eq. (32)) of the increment and wave number of the most unstable mode vs. parameter w for $m = 0$ and $m = 1$ with $\nu = 3$ are presented in Fig. 3. When the viscosity is high, the increment of the nonsymmetric wave with $m = 1$ exceeds considerably that of the axisymmetric wave; however, the absolute values of the increments in both cases are lower than those for low-viscosity jets.

It is interesting that, at $m = 0$ and low wave numbers ($k \le 0.7$), the increment lowers slightly with w increasing from zero to $w \approx 1.6$. This effect is associated with the nonmonotonicity of the function $f = f(k, w)$ in Eqs. (29)–(31) for $0 < w \le 1.6$ (Fig. 4).

(6) It is appropriate to apply the results obtained to considering the dropwise disintegration of a jet of a conducting liquid kept at a constant electric potential. It should be noted that, under natural conditions, jets forming when the charged liquid surface is unstable [11, 13] take a conical shape. Such jets disintegrate both by the separation of droplets from their thin end, experiencing whipping, and by the breakup of their continuous part away from the end [2, 13]. Such a disintegration causes a wide daughter droplet size distribution and a variety of conditions for electrical liquid dispersion [13–15].

Our investigation showed that a conical jet kept at a constant electrostatic potential is characterized by different values of the surface charge density in various cross sections: the density is inversely proportional to the jet radius, increasing toward the thin end. This means that, in the same jet, various waves with different values of the azimuthal parameter m may be unstable, depending on the z coordinate. For example, the disintegration of the thin end into drops is influenced by nonaxisymmetric waves, whereas in a cross section with a large radius, where the surface charge density is low, the disintegration will occur because of the instability of the axisymmetric mode. The effect of viscosity will also be radius dependent: the dimensionless viscosity $\nu = \nu_0(\rho/\sigma R)^{1/2}$ will be higher at the thin end and lower at the wide one.

CONCLUSIONS

In the spontaneous capillary disintegration of charged jets (kept at a constant electrostatic potential), the droplet size distribution is greatly affected by the instability of nonaxisymmetric waves. The instability increments of nonaxisymmetric waves in low-density jets become comparable to the instability increment of the axisymmetric wave when the surface charge density is high, whereas in high-viscosity jets, they considerably exceed the latter.

APPENDIX

Derivation of an Expression for the Electric Field Pressure on the Jet Surface

Let us calculate the electric field pressure on the charged surface of a cylindrical jet of a perfectly conducting inviscid incompressible liquid. We assume that the electric current in the jet is absent, the electric field strength inside the conductor is equal to zero and has only the normal component at the jet surface, and the jet charge due to electrification is uniformly distributed over the jet surface with a density κ_0. It is also taken into account that, in the approximation of perfectly conducting liquid, the capillary-oscillation-induced charge redistribution over the jet surface occurs at an infinitely high rate, instantly following surface vibrations and providing surface equipotentiality at any instant of time. Under these conditions, the time variation of the electric field potential Φ of the jet is entirely defined by the time variations of the jet shape, and the dependence of the potential Φ on the spatial variables can be found from the Laplace equation (since hydrodynamic velocities are much less than the velocity of light).

The electric field pressure P_κ on the surface of a charged jet is given by the well-known expression

$$P_\kappa = \frac{(\nabla\Phi)^2}{8\pi},$$

where the potential Φ of the electric field outside the jet is a solution to the boundary problem

$$\Delta\Phi = 0,$$

$$r = 1 + \xi: \Phi = \Phi_*,$$

$$r \longrightarrow \infty: \nabla\Phi \longrightarrow 0.$$

Let us represent the potential Φ in the form of the expansion

$$\Phi = \Phi^0 + \varphi,$$

where Φ^0 is the electric field potential near the unperturbed jet surface and φ is the correction of first order of smallness in $|\xi|$, where $\xi(z, \phi, t)$ is a surface perturbation.

Splitting the problem in orders of smallness, we obtain

$$\Delta\Phi^0 = 0,$$

$$r = 1: \Phi^0 = \Phi_*,$$

$$r \longrightarrow \infty: \nabla\Phi^0 \longrightarrow 0$$

in the zeroth approximation in $|\xi|$ and

$$\Delta\varphi = 0,$$

$$r = 1: \varphi = -\frac{\partial\Phi^0}{\partial r}\xi,$$

$$r \longrightarrow \infty: \nabla\varphi \longrightarrow 0$$

in the first-order approximation.

We also take into account that the electric field at the jet surface has only the normal component:

$$r = 1: \mathbf{E}_0 \cdot \mathbf{n} = 4\pi\kappa_0, \quad \mathbf{E}_0 \cdot \boldsymbol{\tau} = 0,$$

where $\mathbf{n}$ and $\boldsymbol{\tau}$ are the unit vectors that are normal and tangential to the jet surface.

In the zeroth order of smallness, the electric field near the unperturbed cylindrical surface of the jet has the form

$$\mathbf{E}_0 = -\nabla\Phi^0 = \frac{4\pi\kappa_0\mathbf{r}}{r^2}.$$

In the cylindrical coordinate system, an expression for the potential φ that satisfies the boundedness condition at $r \longrightarrow \infty$ and an expression for the distortion $\xi(z, \phi, t)$ of the cylindrical jet shape will be written in the form of expansion in waves traveling along the z axis (along the axis of jet symmetry)

$$\varphi = \int_0^\infty \sum_{m=0}^{\infty} C_4 K_m(kr)\exp(im\varphi)\exp(ikz)\exp(st)dr,$$

$$\xi(z, \phi, t) = \int_0^\infty \sum_{m=0}^{\infty} D\exp(im\phi)\exp(ikz)\exp(st)dk,$$

where m are integers, k is the wave number, $K_m(kr)$ is the modified Bessel function of the second kind, and C_4 and D are the expansion coefficients depending on k and m.

At the jet surface,

$$r = 1: \varphi = 4\pi\kappa_0\xi.$$

The relation between the coefficients D and C_4 is straightforward:

$$C_4 = \frac{4\pi\kappa_0}{K_m(k)}D.$$

When deriving this relationship, we took into account the linear independence of the functions

$\exp(im\phi)$ at various m and of the functions $\exp(ikz)$ at various wave numbers k.

A perturbation $\xi(z, \phi, t)$ of the cylindrical jet surface caused by wave motion changes the pressure P_κ. Since the perturbation ξ is small, the pressure P_κ can be expanded in ξ in the form

$$P_\kappa\big|_{r=1+\xi} \approx \frac{1}{8\pi}(\nabla\Phi^0 + \nabla\varphi)^2\big|_{r=1+\xi}$$

$$\approx \frac{1}{8\pi}((\nabla\Phi^0)^2 + 2(\nabla\varphi)\cdot(\nabla\Phi^0))\big|_{r=1+\xi}$$

$$\approx \frac{1}{8\pi}((\nabla\Phi^0)^2 + 2\nabla\Phi^0\cdot\frac{\partial}{\partial r}(\nabla\Phi^0)\xi + 2(\nabla\varphi)\cdot(\nabla\Phi^0))\big|_{r=1}.$$

Using the expression for the electric field strength near the unperturbed surface of a cylindrical jet, for the pressure component linear in $|\xi|$, $p_\kappa(\xi)$, we obtain the expression

$$r = 1\colon\ p_\kappa(\xi) = -4\pi\kappa_0^2\xi - \kappa_0\frac{\partial\varphi}{\partial r}.$$

Replacing the functions ξ and φ by their integral representations, we arrive at the final expression for the electric field pressure related to the perturbation of the jet surface shape:

$$p_\kappa(\xi) = -4\pi\kappa_0^2 D\left(1 + k\frac{K_m'(k)}{K_m(k)}\right)\exp i(kz + m\varphi)\exp(st).$$

ACKNOWLEDGMENTS

This work was supported by a grant from the President of the Russian Federation (grant no. 00-15-9925).

REFERENCES

1. E. V. Ametistov, V. V. Blazhenkov, A. K. Gorodov, *et al.*, *Monodispersion of Materials: Principles and Applications* (Énergoatomizdat, Moscow, 1991).
2. R. H. Magarvey and L. E. Outhouse, J. Fluid Mech. **13**, 151 (1962).
3. A. L. Huebner, J. Fluid Mech. **38**, 679 (1969).
4. J. Schneider, C. Lindbland, and Hendrics, Jr., J. Appl. Phys. **38**, 2599 (1967).
5. D. H. Michael and M. E. O Neill, Can. J. Phys. **47**, 1215 (1969).
6. S. Grossmann and A. Muller, Z. Phys. B **57**, 161 (1984).
7. S. S. Nazin, A. N. Izotov, and V. B. Shikin, Dokl. Akad. Nauk SSSR **283**, 121 (1985) [Sov. Phys. Dokl. **30**, 606 (1985)].
8. A. F. Ginevskiĭ, in *Collection of Scientific Works* (Mosk. Énerg. Inst., Moscow, 1986), No. 119, pp. 18–27.
9. A. F. Ginevskiĭ and A. I. Motin, Inzh.-Fiz. Zh. **60**, 576 (1991).
10. V. N. Gorshkov and M. G. Chaban, Zh. Tekh. Fiz. **69** (1), 1 (1999) [Tech. Phys. **44**, 1259 (1999)].
11. W. A. Macky, Proc. R. Soc. London **133**, 565 (1931).
12. A. I. Grigor'ev and S. O. Shiryaeva, Izv. Akad. Nauk, Mekh. Zhidk. Gaza, No. 3, 3 (1994).
13. M. Cloupeau and B. Prunet-Foch, J. Electrost. **25**, 165 (1990).
14. S. O. Shiryaeva and A. I. Grigor'ev, Zh. Tekh. Fiz. **64** (3), 13 (1994) [Tech. Phys. **39**, 229 (1994)].
15. S. O. Shiryaeva and A. I. Grigor'ev, J. Electrost. **34**, 51 (1995).
16. S. O. Shiryaeva, A. É. Lazaryants, A. I. Grigor'ev, *et al.*, Preprint No. 27, IM RAN (Institute of Microelectronics, Russian Academy of Sciences, Yaroslavl, 1994).
17. V. G. Levich, *Physicochemical Fluid Dynamics* (Fizmatgiz, Moscow, 1959).

Translated by N. Mende

Technical Physics, Vol. 48, No. 5, 2003, pp. 535–540. Translated from Zhurnal Tekhnicheskoĭ Fiziki, Vol. 73, No. 5, 2003, pp. 13–18.

GASES AND LIQUIDS

Effect of Diffusion on the Separation of Components in a Biological Fluid upon Wedge-Shaped Dehydration

Yu. Yu. Tarasevich and A. K. Ayupova

Astrakhan State Pedagogical University, Astrakhan, 414056 Russia

e-mail: tarasevich@astranet.ru

Received August 20, 2002

Abstract—Experiments with model fluids imitating human blood serum are performed. A model explaining the spatial distribution of biological fluid components in the course of wedge-shaped dehydration, a process that has found application in medical diagnosis, is suggested. Calculations within this model are carried out. © *2003 MAIK "Nauka/Interperiodica".*

WEDGE-SHAPED DEHYDRATION METHOD

The process termed wedge-shaped dehydration of biological fluids [1] has found wide applications in diagnostic tests used in medical practice [1]. The tests are conducted as follows [1]. Using a pipette, a 10- to 20-μl drop of a biological fluid (blood serum, saliva, tissue or spinal fluid, etc.) is placed onto a chemically cleaned (decreased) glass slide lying on a strictly horizontal surface. The diameter of such a drop on the slide is 5–7 mm, its average thickness is about 1 mm, and the angle of contact is 25°–30° [2]. The sample is allowed to dry at 20–25°C and a relative air humidity of 65–70% for 18–24 h. The dried drop is referred to as a facies and has a complex structure. Its exterior appearance is used for diagnosing many diseases.

Unfortunately, today, there is no model adequately describing the processes occurring in the course of wedge-shaped dehydration. Moreover physical, chemical, and biological processes that accompany the formation of the structures observed in the facies have not yet been understood. For example, the authors of this method attribute the occurrence of these structures to "the conflict between osmotic and oncotic forces."

EXPERIMENTS WITH MODEL FLUIDS

Because of the complex composition of blood serum and the diversity of physicochemical processes occurring in the body, it is difficult to separate out factors responsible for the formation of the aforementioned structures. In this situation, experiments with simple model fluids appear to be promising. This approach makes it possible to minimize the number of factors affecting the formation of the structures and to controllably modify the parameters of test fluids.

Blood serum is a complex colloidal system consisting of water (90%) and dissolved substances (10%). The latter include proteins (70%), inorganic salts (approximately 10%), and low-molecular organic compounds (≈20%). For the purposes of clinical diagnosis by laboratory methods, specialists have developed the concept of the norm (normal content) with respect to blood protein; i.e., they have determined the range of the total protein concentration for healthy people. This range is 65–85 g/l [3]. The total blood protein concentration exceeding this range (hyperproteinemia) or falling below its lower limit (hypoproteinemia) are evidence for the development of a pathological process.

In this study, model fluids were used to reveal basic effects taking place upon wedge-shaped dehydration. Its purpose was to find out whether specific structures form in the model fluids that are similar to blood plasma in composition and, if so, to estimate their similarity to the structures observed in natural fluids and find a correlation between the composition of the model fluids and the forming structures.

The model fluids were as follows: (1) bovine serum albumin dissolved in water and (2) bovine serum albumin dissolved in a 0.9% sodium chloride solution (below referred to as water and saline solutions, respectively). In both cases, the concentration of albumin ranged from 80 to 120 g/l.

The wedge-shaped dehydration of either concentration was performed twice, and the results were highly reproducible. In the case of the water solutions, the radial cracking of the sample prevailed at a protein concentration of 80 g/l; at higher concentrations, no regular cracking pattern was observed. Any specific structures in the samples were absent (Fig. 1).

In the samples of the saline solutions, radial cracking was observed at all protein concentrations. At 120 g/l, the cracks radial the center of the facies. The facies consisted of three distinct zones: the circumferential zone of protein structures, the transition zone of protein–salt structures, and the central zone of crystalline (saline) structures (Fig. 1). The crystalline structures significantly varied with the protein concentration in the solution. At 80 g/l, they had the shape of den-

1063-7842/03/4805-0535$24.00

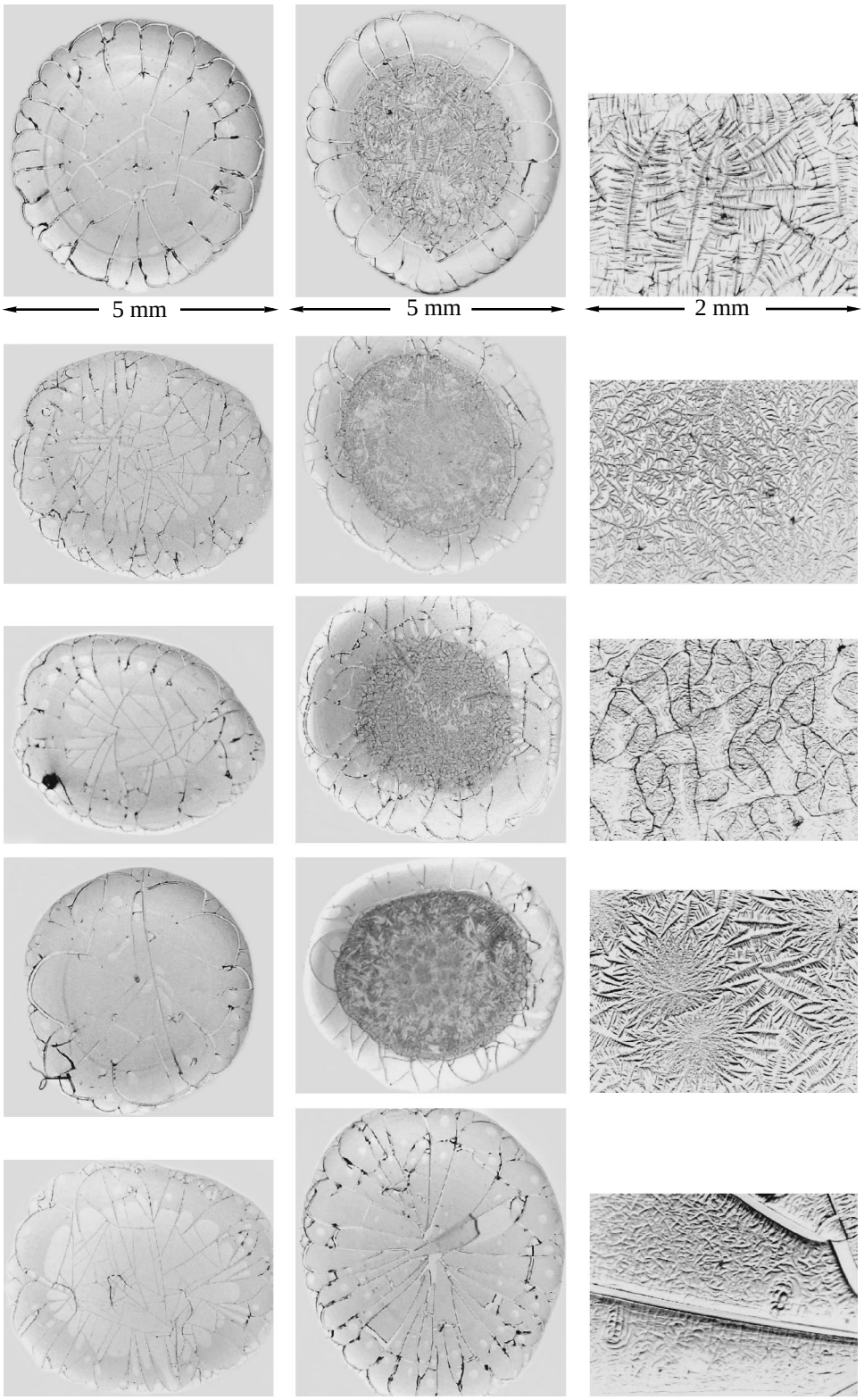

Fig. 1. Facies of albumin solutions with concentrations ranging from 80 g/l (top row) to 120 g/l (bottom row) in 10 g/l steps. Left column, water solutions; middle column, saline solutions; and right column, fragments of the facies shown in the middle column. The photographs were made in a Leica MZ12.5 stereomicroscope.

drites with long straight branches of first and second orders. Third-order branches were underdeveloped. The density of the dendrites was relatively low. At 90 g/l, the dendrites were short and thick with curved branches. At 100 g/l, dendritic structure was changed to chains of fine crystallites against the background of secondary cracking of the protein matrix. At 110 g/l, the dendrites appeared again. Some of them were dense and had central symmetry ("flowers"). The structure formed at 120 g/l consisted of fine and dense crystallites (Fig. 1).

CONCLUSIONS

(1) The model fluid consisting of the albumin solution in water does not show the properties of blood serum upon drying (wedge-shaped dehydration), as the structures observed in the dried drops of this fluid bear no resemblance to the structures appearing in normal blood serum.

(2) The model fluid consisting of albumin dissolved in the sodium chloride solution reproduces the structures found in the dried (dehydrated) drops of normal blood serum.

(3) The structures formed in the model fluids vary with protein concentration, indicating that the method of wedge-shaped dehydration may be used in the diagnosis of hypo- and hyperproteinemia [4].

(4) The facies of the model fluids are virtually indistinguishable from the facies of normal blood serum (Fig. 1). Fine features regarded as indicators of pathological processes were not detected in them.

QUALITATIVE MODEL

The redistribution of salt and protein is one of the main processes occurring in a drying drop: protein accumulates at the periphery of the facies, while salt accumulates in its central part. Eventually, the protein component of the facies cracks and salt crystallizes (Fig. 1). In the norm, cracks produce a regular radial pattern. Let us consider these processes on a qualitative basis.

The rate of water evaporation from the drop surface is nonuniform and depends on its curvature. As the volume of water decreases, the concentrations of protein and salt increase. The rate of change of the protein concentration is higher at sites where the relative thinning of the drop is greater, i.e., at the periphery (Fig. 2). The resulting concentration gradient gives rise to a centripetal flow.

As the diffusion coefficient of salt is two orders of magnitude higher than that of protein, the relative concentration of salt increases at the center of the drop. This effect, in turn, may cause the displacement of protein toward the periphery (cross diffusion). A decrease in the volume due to evaporation changes the shape of the drop surface and, hence, the rate of change of the

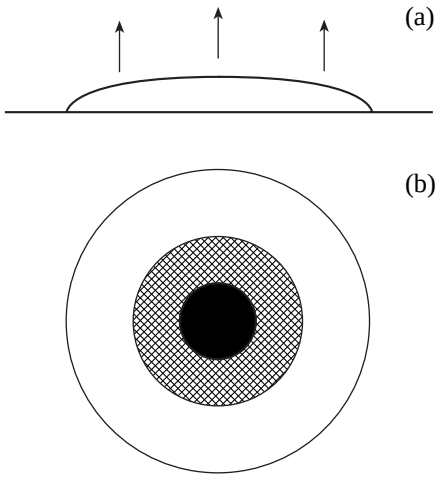

Fig. 2. Drop of biological fluid on the plane surface: (a) cross section and (b) top view. Upon drying, protein accumulates mainly at the periphery of the drop (open zone) and salt accumulates at the center (closed zone). The transition zone is hatched.

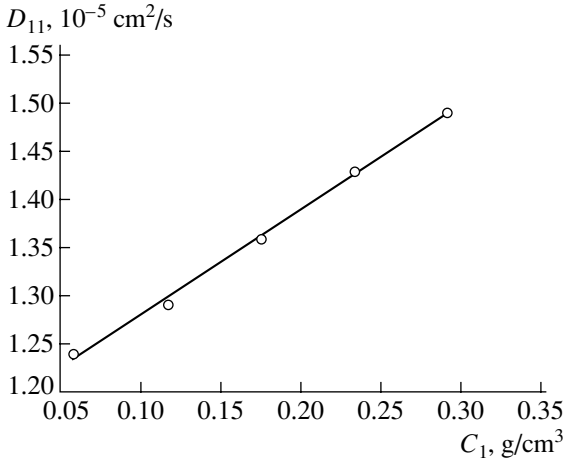

Fig. 3. Diffusion coefficient of sodium chloride as a function of its concentration in water solution (approximation by the least-squares method).

dissolved component concentrations. When a major part of water is lost by evaporation, the concentrations of salt and protein increase to the extent that their diffusion coefficients markedly change. This is especially the case with protein, which undergoes the sol–gel transition; as a result, its diffusion coefficient approaches zero. The diffusion coefficient of salt also decreases as the protein concentration in the solution grows [5]. On the other hand, this coefficient increases proportionally to the salt concentration [6]. This dependence is well approximated by the linear function (Fig. 3):

$$D_{11} = 1.094C_1 + 1.17.$$

When the salt concentration saturates, the solution starts crystallizing. The presence of salt extends the gelation period compared with that in a pure protein

solution, and protein begins to precipitate at high salt concentrations (salting).

Thus, wedge-shaped dehydration is accompanied by various and, more importantly, interrelated processes. wedge-shaped dehydration is a nonequilibrium and essentially nonlinear process.

MATHEMATICAL MODEL

In the three-component system in question, only two flows are independent. Let these be the salt and protein flows. In a solution, they are described by the Gibbs–Duhem equation

$$J_i = -\sum_{k=1}^{n-1} D_{ik}\nabla C_k,$$

where J is the diffusion flow, D_{ik} is the tensor diffusion coefficient ($D_{ik} = D_{ki}$), C_k is the concentration of a kth component in a solution, and n is the number of components.

Since

$$\frac{\partial C}{\partial t} = -\nabla J,$$

we have

$$\frac{\partial C_i}{\partial t} = \nabla\sum_{k=1}^{n-1} D_{ik}\nabla C_k.$$

To the first approximation, effects related to the variation of the concentration along the vertical axis may be ignored, because the thickness of the drop is smaller than its diameter. In this case, the system is centrosymmetric and it is appropriate to use the polar coordinates:

$$\begin{aligned}\frac{\partial C_i}{\partial t} &= \sum_{k=1}^{n-1}\left(D_{ik}\frac{\partial^2 C_k}{\partial r^2} + \frac{D_{ik}}{r}\frac{\partial C_k}{\partial r} + \frac{\partial D_{ik}}{\partial r}\frac{\partial C_k}{\partial r}\right)\\ &= \sum_{k=1}^{n-1}\left(D_{ik}\frac{\partial^2 C_k}{\partial r^2} + \frac{D_{ik}}{r}\frac{\partial C_k}{\partial r} + \frac{\partial D_{ik}}{\partial C_k}\left(\frac{\partial C_k}{\partial r}\right)^2\right).\end{aligned} \quad (1)$$

Equation (1) describes the variation of the concentration due to diffusion. In addition, it is necessary to take into account the variation caused by water evaporation:

$$\frac{\partial C_i}{\partial t} = f(r, t). \quad (2)$$

The form of the function $f(r, t)$ depends on many factors, such as the curvature of the drop surface at a given point, the surface tension coefficient, etc. For simplicity we assume that this function depends only on the distance to the center of the drop and on time and ignore the concentration dependence of the diffusion coefficients.

Such assumptions mean that we consider the initial stages of water evaporation, when the concentrations of the components in the solution are far from saturation. At the stage of gelation, the diffusion coefficient of protein approaches zero and the evaporation pattern changes. Still later, salt crystallizes and the system loses axial symmetry.

With the above approximations, we obtain

$$\begin{aligned}\frac{\partial C_1}{\partial t} &= D_{11}\frac{\partial^2 C_1}{\partial r^2} + \frac{D_{11}}{r}\frac{\partial C_1}{\partial r}\\ &+ D_{12}\frac{\partial^2 C_2}{\partial r^2} + \frac{D_{12}}{r}\frac{\partial C_2}{\partial r} + f_1(r, t),\\ \frac{\partial C_2}{\partial t} &= D_{11}\frac{\partial^2 C_2}{\partial r^2} + \frac{D_{22}}{r}\frac{\partial C_2}{\partial r}\\ &+ D_{12}\frac{\partial^2 C_1}{\partial r^2} + \frac{D_{12}}{r}\frac{\partial C_1}{\partial r} + f_2(r, t).\end{aligned} \quad (3)$$

It is of interest to consider relations between the phenomenological coefficients D_{ii} and D_{ij} ($i, j = 1, 2$). According to [7], these relations, with regard to the Onsager principle of reciprocity ($D_{12} = D_{21}$), are as follows:

$$D_{12}^2 < D_{11}D_{22}, \quad D_{11} > 0, \quad D_{22} > 0.$$

At $D_{11} = 1.5 \times 10^{-5}$ cm^2/s for sodium chloride and $D_{22} = 7.7 \times 10^{-7}$ cm^2/s for albumin [8], $|D_{12}| < 3.4 \times 10^{-6}$ cm^2/s (with a plus or minus sign).

COMPUTING EXPERIMENT

Let us consider a simple model in order to estimate the possibility of the distribution of components in a solution drop becoming nonuniform in the course of wedge-shaped dehydration. It is assumed that $D_{i,j} = 0$ for $i \neq j$ (i.e., the components have no effect on each other) and the drop is wedge-shaped in the cross section (Fig. 4). The maximum thickness of the drop is h_0, the angle of contact is α ($\tan\alpha = k$), and the radius of the drop is R.

Assuming that the water evaporates at a constant rate v only from the upper surface of the wedge, we obtain the following equation for this surface:

$$y = h_0 - kr - vt.$$

The lateral surfaces are considered to be impermeable:

$$\left.\frac{\partial C(r, t)}{\partial r}\right|_{r=R} = 0.$$

According to the law of conservation of matter,

$$C(r, t + dt)y(r, t + dt) = C(r, t)y(r, t).$$

Therefore, if diffusion is ignored, it follows from this law that

$$\frac{\partial C(r,t)}{\partial t} = -\frac{\partial y(r,t)}{\partial t}\frac{C(r,t)}{y(r,t)} = v\frac{C(r,t)}{h_0 - kr - vt}.$$

When diffusion is taken into account, we obtain

$$\frac{\partial C}{\partial t} = D\left(\frac{\partial^2 C}{\partial r^2} + \frac{1}{r}\frac{\partial C}{\partial r}\right) + \frac{vC}{h_0 - kr - vt}. \quad (4)$$

Hereafter, the arguments of the functions are omitted. To simplify further analysis, it is expedient to make Eq. (4) dimensionless by changing the variables:

$$\tau = \frac{vt}{h_0}, \quad \xi = 1 - \frac{kr}{h_0}, \quad x = \frac{C}{C_0}.$$

Thus,

$$\frac{\partial c}{\partial \tau} = d\left(\frac{\partial^2 c}{\partial \xi^2} - \frac{1}{\xi - 1}\frac{\partial c}{\partial \xi}\right) + \frac{c}{\xi - \tau} \quad (5)$$

with

$$d = \frac{Dk^2}{vh_0}.$$

Naturally, this equation holds only if

$$vt \ll h_0 (\tau \ll \xi),$$

because the concentration dependence of the diffusion coefficient can be ignored only under this condition. Then, $(\xi - \tau)^{-1} \approx (\xi + \tau)/\xi^2$ and the equation can be recast as

$$\frac{\partial c}{\partial \tau} = d\left(\frac{\partial^2 c}{\partial \xi^2} + \frac{1}{\xi - 1}\frac{\partial c}{\partial \xi}\right) + c\frac{\xi - \tau}{\xi^2}.$$

The dimensionless coefficient d acquires a clear physical meaning when written in the form

$$d = k^2\frac{D}{h_0^2}\frac{h_0}{v} = k^2\frac{\tau_{\text{shift}}}{\tau_{\text{diff}}}.$$

Here, τ_{shift} is the characteristic time of shift of the wedge upper surface, and τ_{diff} is the relaxation time (the time it takes for the solute concentration to change by a factor of e due to diffusion). Thus, the coefficient d shows what process, diffusion or water evaporation, is responsible for the variation of the solute concentration.

According to our estimates, d for protein and salt is on the order of 0.01 and 1, respectively. Therefore, diffusion has an insignificant effect on the protein concentration variation.

In the absence of diffusion, the solute concentration is governed only by evaporation. As follows from Eq. (5),

$$c = 1 + \ln\frac{\xi}{\xi - \tau} \approx 1 + \frac{\tau}{\xi}.$$

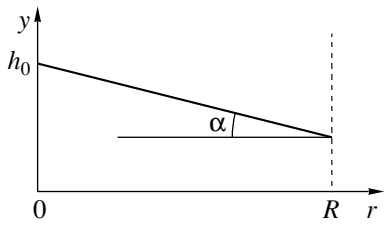

Fig. 4. Shape of the drop surface adopted in the model.

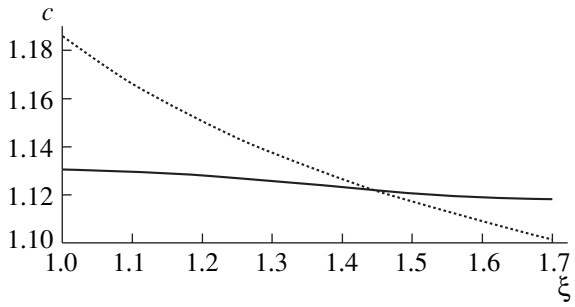

Fig. 5. Spatial distribution of the salt concentration at the initial stages of wedge-shaped dehydration ($\tau = 0.1568$) calculated with (solid line) and without (broken line) considering the effect of diffusion.

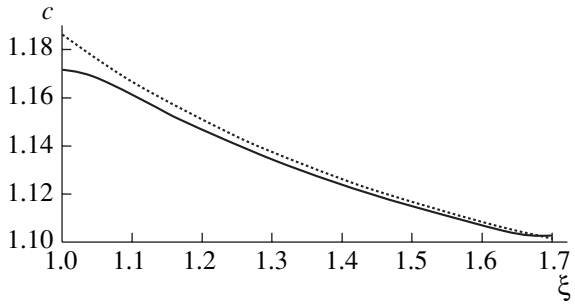

Fig. 6. The same as in Fig. 5 for protein.

Figures 5 and 6 show the results of calculation for salt and protein with and without taking into account the effect of diffusion. The accuracy of calculation was estimated by checking the fulfillment of the law of conservation of matter

$$\int_0^R C(r,t)y(r,t)rdr = \text{const}.$$

These results confirm that diffusion is not a key factor in the behavior of the protein concentration in the drying drop. At the same time, it markedly smooths out the effect of salt concentration at its periphery.

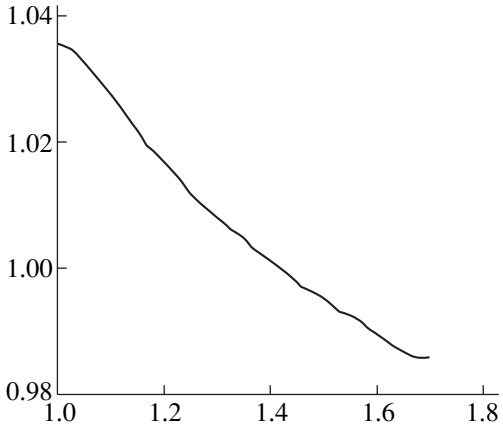

Fig. 7. Variation of the salt and protein concentrations in the solution compared with their initial distribution (τ = 0.1568).

CONCLUSIONS

The model proposed makes it possible to explain the solute spatial redistribution during the wedge-shaped dehydration of biological fluids (Fig. 7). In the absence of diffusion, the local relative concentrations of salt and protein in the drop would remain constant, with their absolute concentrations increasing toward the periphery. The effects of cross diffusion and of the concentration dependence of the diffusion coefficients remained unaccounted for because of the lack of experimental data. However, these effects can be estimated qualitatively. As the concentration of protein increases, its diffusion coefficient decreases. Therefore, the equalizing effect of diffusion on the concentration becomes weaker and the distribution of the protein concentration becomes still closer to that estimated by taking into account water evaporation alone. In the case of salt, the diffusion coefficient increases with concentration, which leads to a faster equalization of the salt concentration within the drop. Thus, the effect estimated by the calculation is further enhanced when the concentration dependence of the diffusion coefficients is taken into consideration.

To check the results of initiation quantitatively, experimental data on the spatial distribution of the salt and protein concentrations in the course of wedge-shaped dehydration are needed.

ACKNOWLEDGMENTS

The authors are grateful to V.Yu. Gershanov for the fruitful discussion.

This work was supported by the Astrakhan Regional Project “Investigation into Processes of Self-Organization in Biological Crystalline Structures as Indicators of Progression of Mycobacterioses.”

REFERENCES

1. V. N. Shabalin and S. N. Shatokhina, *Morphology of Body Fluids* (Khrizostom, Moscow, 2001).
2. V. N. Shabalin and S. N. Shatokhina, Vestn. Akad. Med. Nauk, No. 3, 45 (2000).
3. M. P. Belyaev, M. I. Gneushev, *et al.*, *Handbook of Laboratory and Functional Indices of Healthy Human Organism* (Moscow, 1992).
4. N. G. Morozova, S. N. Shatokhina, and V. N. Shabalin, in *Crystallographic Methods for Medical Applications: Collection of Scientific Works of the 1st All-Russia Scientific and Practical Conference* (Moscow, 1997), pp. 129–131.
5. L. Masaro and X. X. Zhu, Prog. Polym. Sci. **24**, 731 (1999).
6. *Tables of Physical Quantities: A Handbook*, Ed. by I. K. Kikoin (Atomizdat, Moscow, 1976).
7. R. Haase, *Thermodynamik der irreversiblen Prozesse* (Steinkopff, Darmstadt, 1963; Mir, Moscow, 1967).
8. V. A. Rabinovich and Z. Ya. Khavin, *Concise Handbook on Chemistry*, Ed. by A. A. Potekhin and A. E. Efimov (Khimiya, Leningrad, 1991, 3rd ed.).

Translated by N. Gorgolyuk

Technical Physics, Vol. 48, No. 5, 2003, pp. 541–545. Translated from Zhurnal Tekhnicheskoĭ Fiziki, Vol. 73, No. 5, 2003, pp. 19–23.

GASES AND LIQUIDS

Use of the Two-Moment Boundary Condition in the Problem of Rarefied Gas Slip over a Solid Cylindrical Surface

V. N. Popov

Lomonosov Pomor State University, Arkhangel'sk, 163006 Russia

e-mail: popov.vasily@pomorsu.ru

Received October 3, 2002

Abstract—The slip velocity of a rarefied gas nonuniform in temperature and mass velocity is calculated for gas slip over the surface of a right circular cylinder. The calculation uses the two-moment boundary condition in an approximation linear in Knudsen number. Corrections to the slip velocity that are due to the interface curvature, volume temperature stresses, and nonuniform temperature distribution in the Knudsen layer are studied as functions of the accommodation coefficients in the first two moments of the distribution function. The Bhatnagar–Gross–Krook model of the Boltzmann kinetic equation is employed as the basic equation for the gas state. © *2003 MAIK "Nauka/Interperiodica".*

INTRODUCTION

A variety of works have recently been published that concern the construction of exact analytical solutions to inhomogeneous model kinetic equations in boundary-value problems of the kinetic theory of rarefied gases. In these problems, a gas that is nonuniform in temperature and mass velocity flows around the surface of a sphere or a right circular cylinder [1–8]. Here, the diffuse reflection model is used as the boundary condition for the surfaces flowed around by the gas. In a number of cases, however, such a boundary condition is inadequate [9]. The Maxwell mirror–diffuse [10] and Cercignani boundary conditions [11] seem to be more realistic.

The use of the Maxwell mirror–diffuse boundary condition in gas slip problems makes it possible to take into account the effect of the accommodation coefficient of the tangential momentum on the slip velocity of the gas flowing around the surface. At the same time, such an approach causes stubborn mathematical difficulties when applied to the construction of solutions to boundary-value problems in the kinetic theory of rarefied gases by using rigorous analytical techniques. Today, exact analytical solutions to boundary-value problems of slip that are obtained with the Maxwell mirror–diffuse boundary condition are lacking.

The Cercignani boundary condition is an alternative to the mirror–diffuse condition and allows reflected molecules to partially conserve information about the incident molecule distribution.

In linearized problems of gas slip around a solid planar surface, the distribution function is written in the form $f = f^0[1 + \varphi(\mathbf{r}, \mathbf{C})]$ and the boundary condition at the surface that is imposed on the function $\varphi(\mathbf{r}, \mathbf{C})$ has the form

$$\varphi(0, \mathbf{C}) = 2d_1 C_y, \quad C_x > 0.$$

Here, the x axis is directed into the gas and the y axis is aligned with the vector of the gas mass velocity. The value of d_1 is found from the condition that the accommodation coefficient q_1 of the tangential momentum ($0 < q_1 < 1$) can be determined by the expression

$$(1 - q_1) \int_{C_x < 0} f(\mathbf{r}, \mathbf{C}) C_x C_y d\mathbf{C} = - \int_{C_x > 0} f(\mathbf{r}, \mathbf{C}) C_x C_y d\mathbf{C}. \quad (1)$$

The case $d_1 = 0$ corresponds to the diffuse reflection of the molecules by the surface. The disadvantage of the Cercignani condition is that it sometimes fails when describing the interaction of gas molecules with the surface. For example, when it is applied to the problem of thermal slip (creep), the thermal slip velocity is totally independent of the accommodation coefficient of the tangential momentum.

With this in mind, Latyshev and Yushkanov [12] made an attempt to generalize the Cercignani boundary condition. Their generalization takes into account not only the accommodation coefficient q_1 of the tangential momentum (which is, in essence, the accommodation coefficient of the first moment of the distribution function) but also the accommodation coefficient of the second moment q_2 of the distribution function ($0 < q_2 < 1$). In this case, the boundary condition at the surface flowed around by the gas is written as

$$\varphi(0, \mathbf{C}) = 2d_1 C_y + 2d_2 C_x C_y, \quad C_x > 0, \quad (2)$$

where the parameter d_2 is found from the condition

$$(1 - q_2) \int_{C_x < 0} f(\mathbf{r}, \mathbf{C}) C_x^2 C_y d\mathbf{C} = \int_{C_x > 0} f(\mathbf{r}, \mathbf{C}) C_x^2 C_y d\mathbf{C}. \quad (3)$$

In this work, two-moment boundary condition (2) is used to calculate the slip velocity of a gas that is nonuniform in temperature and mass velocity that slips

1063-7842/03/4805-0541$24.00

around a solid cylindrical surface of radius R. This boundary condition takes into account the effect of the surface curvature on the thermal slip coefficient, as well as the presence of volume temperature stresses and nonuniform temperature distribution in the Knudsen layer. In the approximation linear in Knudsen number, the desired slip velocity is written in the form [13]

$$U_\tau|_S = K_{TS}\nu\frac{\partial \ln T}{\partial \tau} - K_{TS}^{(0)}\nu\beta'_\tau \mathrm{Kn}\frac{\partial \ln T}{\partial \tau} + C_m\lambda\frac{\partial U_\tau}{\partial \rho} - K_{TS}^{(0)}\beta_B\nu\lambda\frac{T_{\rho\varphi}}{2T} + K_{TS}^{(0)}\beta_R\nu\mathrm{Kn}\frac{\partial^2 \ln T}{\partial\rho\partial\varphi}. \quad (4)$$

Here, C_m, K_{TS}, and β_B are the coefficients of isothermal, thermal, and Barnett slips, respectively; β_R is the coefficient responsible for the temperature distribution nonuniformity in the Knudsen layer; β'_τ is the factor taking into account the effect of the surface curvature on the thermal slip coefficient; $K_{TS}^{(0)} = 1.14995$ is the value of the thermal slip coefficient for the totally diffuse reflection of gas molecules from the surface; ν is the kinematic viscosity of the gas; λ is the mean free path of gas molecules; $U_\tau|_S$ is the mass velocity component tangent to the surface; and $T_{\rho\varphi}$ is the nonzero component of the volume temperature stress tensor. For the gas flowing around the surface in the longitudinal direction, the nonzero mass velocity component is $U_z|_S$; for the flow in the transverse direction, $U_\varphi|_S$ [2, 5, 8].

The relationship between C_m, K_{TS}, and accommodation coefficients q_1 and q_2 was found in [12]:

$$C_m = -C_m^{(0)}(2-q_2) \times \frac{(q_1^{-1}-1)(\sqrt{\pi}+\pi Q_1/2)-(1-\pi/4)}{1-\pi/4+(1-q_2)(1+\pi/4+\sqrt{\pi}Q_1)}, \quad (5)$$

$$K_{TS} = K_{TS}^{(0)} \times \frac{(2-q_2)(1-\pi/4)+(1-q_2)(\sqrt{\pi}Q_1/2+\pi/4)K^{-1}}{1-\pi/4+(1-q_2)(1+\pi/4+\sqrt{\pi}Q_1)}. \quad (6)$$

Here, $C_m^{(0)} = 1.14665$ is the value of the thermal slip coefficient for the totally diffuse reflection of gas molecules by the surface and Q_n denotes Loyalka integrals [14]:

$$Q_n = \frac{1}{\sqrt{\pi}}\int_0^\infty \frac{X^-(\eta)}{\lambda^-(\eta)}\eta^{n+1}\exp(-\eta^2)d\eta, \quad Q_1 = -1.01619,$$

$$\lambda^\pm(\eta) = \lambda(\eta) \pm \sqrt{\pi}i\eta\exp(-\eta^2),$$

$$\lambda(z) = 1 + \frac{1}{\sqrt{\pi}}z\int_{-\infty}^\infty \frac{\exp(-\mu^2)}{\mu - z}d\mu,$$

$$X(z) = \frac{1}{z}\exp\left\{\frac{1}{\pi}\int_0^\infty \frac{\Theta(\tau)-\pi}{\tau - z}d\tau\right\},$$

$$X^\pm(\eta) = -\frac{\lambda^\pm(\eta)}{|\lambda^+(\eta)|}X(\eta),$$

$$\Theta(\tau) - \pi = -\pi/2 - \arctan\frac{\lambda(\tau)}{\sqrt{\pi}\tau\exp(-\tau^2)}.$$

Thus, the problem posed is reduced to finding the q_1 and q_2 dependences of β'_τ, β_B, and β_R.

THERMAL SLIP

When a rarefied gas flows around the surface of a circular right cylinder in the transverse direction, to find the q_1 and q_2 dependences of β'_φ means to solve the equation [5, 8, 12]

$$\mu\frac{\partial Y_a^{(2)}}{\partial x} + Y_a^{(2)}(x,\mu) = \frac{1}{\sqrt{\pi}}\int_{-\infty}^\infty Y_a^{(2)}(x,\tau)\exp(-\tau^2)d\tau + \mu Y_a^{(1)}(x,\mu) - \frac{3}{2}\frac{\partial Y_a^{(1)}}{\partial \mu} + 3\mu Y_b^{(1)}(x,\mu) - \frac{3}{2}\frac{\partial Y_b^{(1)}}{\partial \mu}, \quad (7)$$

where

$$x = r - R,$$

$$Y_a^{(1)}(x,\mu) = \int_0^\infty a(\eta)F(\eta,\mu)\exp(-x/\eta)d\eta,$$

$$Y_b^{(1)}(x,\mu) = k_T\exp(-x/\mu)\Theta_+(\mu),$$

$$F(\eta,\mu) = \frac{1}{\sqrt{\pi}}\eta P\frac{1}{\eta-\mu} + \exp(\eta^2)\lambda(\eta)\delta(\eta-\mu),$$

$$a(\eta) = \frac{k_T\exp(-\eta^2)(\eta - Q)X(-\eta)}{2|\lambda^+(\eta)|^2}, \quad k_T = \frac{\partial \ln T}{\partial \varphi}.$$

Here, $\lambda(z)$ is the Cercignani dispersion function, Px^{-1} is the distribution in the sense of the principal value upon integrating x^{-1}, $\delta(x)$ is the Dirac function, and $\Theta_+(\mu) = 0$ (or 1) if $\mu \le 0$ (or >0). The boundary conditions are as follows:

$$Y_a^{(2)}(0,\mu) = 2d_1^{(2)} + 2\mu d_2^{(2)}, \quad \mu > 0, \quad (8)$$

$$Y_a^{(2)}(\infty,\mu) = 2U_\varphi^{(2)}|_S. \quad (9)$$

To find $d_1^{(2)}$ and $d_2^{(2)}$, we come to the set of integral

equations for the moments

$$(1-q_1)\int_{-\infty}^{\infty}\exp(-\mu^2)\mu Y_a^{(2)}(0,\mu)d\mu = -q_1\int_0^{\infty}\exp(-\mu^2)\mu Y_a^{(2)}(0,\mu)d\mu, \quad (10)$$

$$(1-q_2)\int_{-\infty}^{\infty}\exp(-\mu^2)\mu Y_a^{(2)}(0,\mu)d\mu = (2-q_2)\int_0^{\infty}\exp(-\mu^2)\mu^2 Y_a^{(2)}(0,\mu)d\mu, \quad (11)$$

from which it follows [12] that

$$d_1^{(2)} = -\frac{(1-q_2)\pi}{2(2-q_2)(1-\pi/4)}U_\varphi^{(2)}\big|_S, \quad (12)$$

$$d_2^{(2)} = \frac{(1-q_2)\sqrt{\pi}}{(2-q_2)(1-\pi/4)}U_\varphi^{(2)}\big|_S. \quad (13)$$

In view of results obtained in [3], the parameter $U_\varphi^{(2)}\big|_S$ is given by the condition

$$\int_0^{\infty}\frac{X^-(\mu)}{\lambda^-(\mu)}f(\mu)\exp(-\mu^2)d\mu = 0. \quad (14)$$

Unlike [3], in our case,

$$f(\mu) = -2\psi(\mu) - Q_2\mu + \frac{1}{2}a(\mu)\exp(\mu^2), \quad (15)$$

where

$$\psi(\mu) = U_\varphi^{(2)}\big|_S - d_1^{(2)} - \mu d_2^{(2)} = \left[1+\frac{\sqrt{\pi}}{2}\frac{(1-q_2)(\sqrt{\pi}-2\mu)}{(2-q_2)(1-\pi/4)}\right]U_\varphi^{(2)}\big|_S. \quad (16)$$

Substituting (15) and (16) into (14) and taking into account the results obtained in [3] yields

$$U_\varphi^{(2)}\big|_S = \frac{3}{4}\left[1+\frac{\sqrt{\pi}}{2}\frac{(1-q_2)(\sqrt{\pi}+2Q_1)}{(2-q_2)(1-\pi/4)}\right]^{-1}\times[Q_3+Q_1Q_2]k_T. \quad (17)$$

Here, $Q_3 = -1.8207$ and $Q_2 = -1.2663$. Passing in (17) to dimensional quantities and writing the expression for $U_\varphi^{(2)}\big|_S$ in the form adopted in the kinetic theory of rarefied gases, we find that

$$U_\varphi^{(2)}\big|_S = -K_{TS}^{(0)}\beta'_{0\varphi}\beta_T\mathrm{Kn}\nu k_T.$$

Thus,

$$\beta'_\varphi = \beta'_{0\varphi}\left[1+\frac{\sqrt{\pi}}{2}\frac{(1-q_2)(\sqrt{\pi}+2Q_1)}{(2-q_2)(1-\pi/4)}\right]^{-1}. \quad (18)$$

Here, $\beta'_{0\varphi} = 1.7684$ is the factor that takes into account the dependence of the thermal slip coefficient on the surface curvature when a rarefied gas flows around the surface in the transverse direction and gas molecules diffusely reflect from the surface.

Bearing in mind that a correction for curvature in the case of longitudinal flow around a cylindrical surface is three times as small as in the case of transverse flow [2, 5, 8], we arrive at

$$\beta'_z = \beta'_{0z}\left[1+\frac{\sqrt{\pi}}{2}\frac{(1-q_2)(\sqrt{\pi}+2Q_1)}{(2-q_2)(1-\pi/4)}\right]^{-1}. \quad (19)$$

Here, $\beta'_{0z} = \beta'_{0\varphi}/3 = 0.589495$ is the factor that takes into account the dependence of the thermal slip coefficient on the surface curvature when a rarefied gas flows around the surface in the longitudinal direction and gas molecules diffusely reflect from the surface.

BARNETT SLIP

The calculation of the Barnett slip velocity as a function of the accommodation coefficients of the distribution function moments is reduced to the solution of the equation [15]

$$\mu\frac{\partial Y_a^{(2)}}{\partial x} + Y_a^{(2)}(x,\mu) = \frac{1}{\sqrt{\pi}}\int_{-\infty}^{\infty}Y_a^{(2)}(x,\tau)\exp(-\tau^2)d\tau$$

with the boundary conditions

$$Y_a^{(2)}(0,\mu) = 2d_1^{(2)} + 2\mu d_2^{(2)}, \quad \mu > 0, \quad (20)$$

$$Y_a^{(2)}(\infty,\mu) = 2U_B^{(2)}\big|_S + 2\mu\left(\mu^2-\frac{1}{2}\right)k_B, \quad k_B = \frac{T_{\rho\varphi}}{2T}. \quad (21)$$

As in the previous case, the parameters $d_1^{(2)}$ and $d_2^{(2)}$ are found from the set of equations (1) and (11) for the moments, from which we find, in view of (2) and (21), that

$$d_1^{(2)} = -\frac{\sqrt{\pi}}{1-\pi/4}\left[\frac{1-q_1}{q_1}k_B + \frac{1-q_2}{2-q_2}\frac{\sqrt{\pi}}{2}U_B^{(2)}\big|_S\right], \quad (22)$$

$$d_2^{(2)} = \frac{\sqrt{\pi}}{1-\pi/4}\left[\frac{1-q_1}{q_1}\frac{\sqrt{\pi}}{2}k_B + \frac{1-q_2}{2-q_2}U_B^{(2)}\big|_S\right]. \quad (23)$$

Here, the parameter $U_B^{(2)}\big|_S$ is determined from condition (14), where, according to [15],

$$f(\mu) = U_B^{(2)}\big|_S + \mu\left(\mu^2-\frac{1}{2}\right)k_B - d_1^{(2)} - \mu d_2^{(2)}. \quad (24)$$

Substituting (24) into (14), carrying out necessary rearrangements, and taking into account (22) and (23), we find

$$U_{\mathrm{B}}^{(2)}\big|_S = \left[Q_3 - \frac{1}{2}Q_1 - \frac{\sqrt{\pi}}{1-\pi/4}\frac{1-q_1}{q_1}\left[1+\frac{\sqrt{\pi}}{2}Q_1\right]\right] \times \left[1+\frac{\sqrt{\pi}}{1-\pi/4}\frac{1-q_2}{2-q_2}\left[\frac{\sqrt{\pi}}{2}+Q_1\right]\right]^{-1} k_{\mathrm{B}}. \quad (25)$$

Passing in (25) to dimensional quantities and writing the expression for $U_{\mathrm{B}}^{(2)}\big|_S$ in the form adopted in the kinetic theory of rarefied gases, we obtain

$$U_{\mathrm{B}}^{(2)}\big|_S = -K_{\mathrm{TS}}^{(0)}\beta_{\mathrm{B}}\nu\lambda\frac{T_{\rho\varphi}}{2T}.$$

Thus,

$$\beta_{\mathrm{B}} = \beta_{\mathrm{B}0}\left[1-\frac{1}{Q_3-Q_1/2}\frac{\sqrt{\pi}}{1-\pi/4}\frac{1-q_1}{q_1}\left[1+\frac{\sqrt{\pi}}{2}Q_1\right]\right] \times \left[1+\frac{\sqrt{\pi}}{1-\pi/4}\frac{1-q_2}{2-q_2}\left[\frac{\sqrt{\pi}}{2}+Q_1\right]\right]. \quad (26)$$

Here, $\beta_{\mathrm{B}0} = 5.80$ is the Barnett slip coefficient for the diffuse reflection of gas molecules from the surface [15].

SECOND-ORDER THERMAL SLIP

For second-order thermal slip, the problem is reduced to the solution of the equation [7]

$$\mu\frac{\partial Y_a^{(2)}}{\partial x} + Y_a^{(2)}(x,\mu) = \frac{1}{\sqrt{\pi}}\int_{-\infty}^{\infty}\exp(-\tau^2)Y_a^{(2)}(x,\tau)d\tau - k_R[Z_1(x,\mu)+\gamma(\mu^2+1/2)Z_2(x,\mu)]$$

with the boundary conditions

$$Y_a^{(2)}(0,\mu) = 2d_1^{(2)} + 2\mu d_2^{(2)}\ (\mu>0),$$

$$Y_a^{(2)}(\infty,\mu) = 2U_R^{(2)}\big|_S.$$

Here, $Z_1(x, \mu)$ and $Z_2(x, \nu)$ are the functions that were constructed by Latyshev [16] in solving the problem of temperature jump, $\gamma^2 = 2/3$, and $k_R = \partial^2\ln T/\partial\rho\partial\varphi$. The parameters $d_1^{(2)}$ and $d_2^{(2)}$ are given by (12) and (13), respectively, and $U_R^{(2)}\big|_S$ is found from condition (14), where, in our case, [7]

$$f(\mu) = [-2\psi(\mu) - (2\mu-\varepsilon_{\mathrm{T}})(\mu^2-1/2) - \varepsilon_n]k_R, \quad (27)$$

$$\psi(\mu) = U_R^{(2)}\big|_S - d_1^{(2)} - \mu d_2^{(2)} = \left[1+\frac{\sqrt{\pi}}{2}\frac{(1-q_2)(\sqrt{\pi}-2\mu)}{(2-q_2)(1-\pi/4)}\right]U_R^{(2)}\big|_S. \quad (28)$$

Here, $\varepsilon_{\mathrm{T}} = 1.3013$ and $\varepsilon_n = -0.5633$ [7]. Substituting (27) and (28) into (14) and taking into account the results obtained in [7], we find

$$U_R^{(2)}\big|_S = \frac{1}{2}[Q_1 - 2Q_3 + \varepsilon_{\mathrm{T}}(Q_2+1/2) + \varepsilon_n] \times \left[1+\frac{\sqrt{\pi}}{2}\frac{(1-q_2)(\sqrt{\pi}+2Q_1)}{(2-q_2)(1-\pi/4)}\right]^{-1}. \quad (29)$$

The value of the first bracketed factor in (29), $0.5323k_R$, coincides with that of the similar expression [7] obtained upon considering the diffuse reflection of gas molecules from the surface.

Passing in (29) to dimensional quantities and writing the expression for $U_R^{(2)}\big|_S$ in the form adopted in the kinetic theory of rarefied gases, we find that

$$U_R^{(2)}\big|_S = K_{\mathrm{TS}}^{(0)}\beta_R\nu\mathrm{Kn}\frac{\partial^2\ln T}{\partial\rho\partial\varphi}.$$

Thus,

$$\beta_R = \beta_{R0}\left[1+\frac{\sqrt{\pi}}{2}\frac{(1-q_2)(\sqrt{\pi}+2Q_1)}{(2-q_2)(1-\pi/4)}\right]^{-1}. \quad (30)$$

Here, $\beta_{R0} = 2.3524$ is the coefficient of second-order thermal slip for the diffuse reflection of gas molecules from the surface [7].

CONCLUSIONS

Thus, the slip velocity of a rarefied gas flowing around the surface of a circular right cylinder is calculated in the approximation linear in Knudsen number. The calculation includes the accommodation coefficients for the first two moments of the distribution function. The expression for the slip velocity takes into consideration the dependence of the thermal slip coefficient on the surface curvature, the presence of volume temperature stresses, and the temperature nonuniformity of the Knudsen layer.

Figures 1–3 show that the coefficients C_m, K_{TS}, β_{B}, β_R, and β_τ' depend substantially on the coefficient q_2. At the same time, K_{TS}, β_R, and β_τ' do not depend on q_1. For $q_1 = q_2 = 1$, these coefficients take values (see (5), (6), (18), (19), (26), and (30)) obtained for the diffuse reflection of gas molecules from the surface.

As follows from measured data [9] for the accommodation coefficient q_1 of the tangential momentum, for surfaces that underwent no special treatment (technical surfaces such as aerosol surfaces), q_1 lies within the interval 0.95–1.00. At the same time, experimental data for q_2 are apparently lacking. However, from the measured values of the thermophoresis velocity of coarse aerosol particles [17], one can assume that the values of K_{TS} fall into the interval 1.1–1.2. This interval

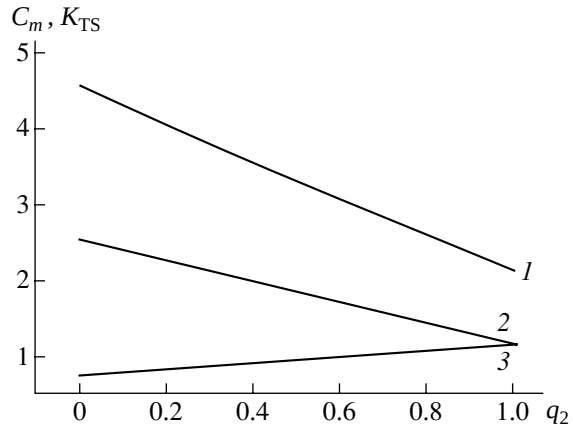

Fig. 1. Isothermal slip coefficient C_m (q_1 = (*1*) 0.5 and (*2*) 1.0) and (*3*) thermal slip coefficient K_{TS} vs. accommodation coefficient q_2.

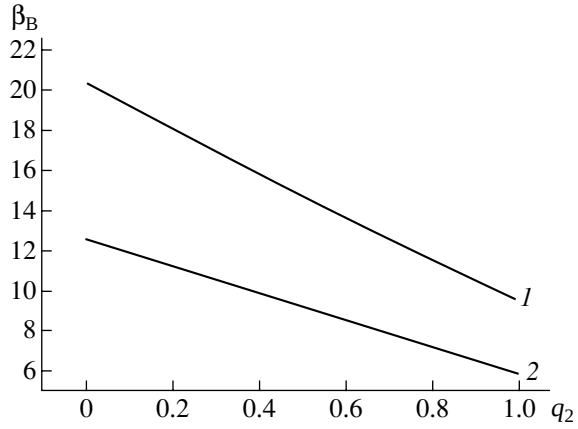

Fig. 2. Barnett slip coefficient β_B vs. accommodation coefficient q_2 for q_1 = (*1*) 0.5 and (*2*) 1.0.

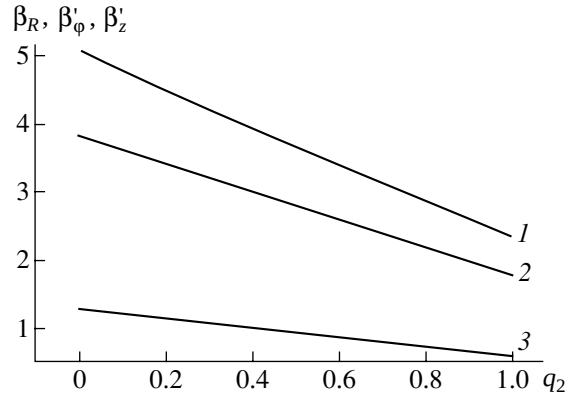

Fig. 3. (*1*) Coefficient β_R of second-order thermal slip and the coefficients β'_φ and β'_z taking into account the K_{TS} vs. surface curvature dependence for (*2*) transverse and (*3*) longitudinal gas flow around the cylindrical surface as functions of q_2.

results from (6) if q_2 = 0.87–1.00. From (5), (18), and (19), it follows that, with q_1 = 1, the isothermal slip coefficient and the curvature corrections to the thermal slip coefficient for the transverse and longitudinal flows around a cylindrical surface are 1.14665–1.329377, 1.768485–2.0176403, and 0.589495–0.6725468, varying, respectively within 15.94, 14.09, and 14.09%. For q_1 = 1, the Barnett slip coefficient (see (26)) and the coefficient of second-order thermal slip (see (30)) lie in the intervals 5.80000–6.617141 and 2.376842–2.711707, respectively, both varying within 14.09%.

The results obtained can be used for calculating the thermophoresis velocity of aerosol particles taking account of the accommodation coefficients [18].

REFERENCES

1. M. N. Gaĭdukov and V. N. Popov, Izv. Akad. Nauk, Mekh. Zhidk. Gaza, No. 2, 165 (1998).
2. A. V. Latyshev, V. N. Popov, and A. A. Yushkanov, Pis'ma Zh. Tekh. Fiz. **28** (5), 70 (2002) [Tech. Phys. Lett. **28**, 204 (2002)].
3. A. V. Latyshev, V. N. Popov, and A. A. Yushkanov, Sib. Zh. Indust. Mat. **3** (11), 103 (2002).
4. A. V. Latyshev, V. N. Popov, and A. A. Yushkanov, Inzh.-Fiz. Zh. **75** (3), 104 (2002).
5. V. N. Popov, Zh. Tekh. Fiz. **72** (10), 15 (2002) [Tech. Phys. **47**, 1219 (2002)].
6. V. N. Popov, Inzh.-Fiz. Zh. **75** (3), 107 (2002).
7. V. N. Popov, Pis'ma Zh. Tekh. Fiz. **28** (19), 10 (2002) [Tech. Phys. Lett. **28**, 800 (2002)].
8. V. N. Popov, Prikl. Mekh. Tekh. Fiz. No. 5, 105 (2002).
9. O. A. Kolenchits, *Thermal Accommodation of Gas–Solid Systems* (Nauka i Tekhnika, Minsk, 1977).
10. M. N. Kogan, *Dynamics of a Rarefied Gas: A Kinetic Theory* (Nauka, Moscow, 1967).
11. C. Cercignani, *Mathematical Methods in Kinetic Theory* (Plenum, New York, 1969; Mir, Moscow, 1973).
12. A. V. Latyshev and A. A. Yushkanov, Inzh.-Fiz. Zh. **73** (3), 63 (2001).
13. E. G. Mayasov, A. A. Yushkanov, and Yu. I. Yalamov, Pis'ma Zh. Tekh. Fiz. **14**, 498 (1988) [Sov. Tech. Phys. Lett. **14**, 220 (1988)].
14. S. K. Loyalka, Transp. Theory Stat. Phys. **4**, 55 (1975).
15. V. N. Popov and M. N. Gaĭdukov, in *Interuniversity Collection of Scientific Works of Mathematical Departments* (Lomonosov Pomor Gos. Univ., Arkhangel'sk, 1997), No. 1, pp. 26–31.
16. A. V. Latyshev, Prikl. Mat. Mekh. **54**, 581 (1990).
17. B. V. Deriaguin and Yu. I. Yalamov, in *International Review on Aerosol Physics and Chemistry* (Pergamon, Oxford, 1972), Vol. 3, Part 2, pp. 1–200.
18. Yu. I. Yalamov and R. A. Safiullin, Teplofiz. Vys. Temp. **32**, 271 (1994).

Translated by V. Isaakyan

Technical Physics, Vol. 48, No. 5, 2003, pp. 546–551. Translated from Zhurnal Tekhnicheskoĭ Fiziki, Vol. 73, No. 5, 2003, pp. 24–29.

GASES AND LIQUIDS

Van der Waals Waves in Free-Surface Liquids

Yu. V. Sanochkin

Bauman State Technical University, Vtoraya Baumanskaya ul. 5, Moscow, 107005 Russia
e-mail: bauman@bmstu.ru

Received December 11, 2001; in final form, June 13, 2002

Abstract—It is shown that, along with gravity waves, surface and internal waves caused by van der Waals forces may exist in a liquid with a horizontal free surface. A dispersion relation is found by using the stepwise approximation for the coefficients of a wave equation derived for these waves. The surface waves are similar to surface gravity waves in dispersion and amplitude distribution but differ in frequency by several orders of magnitude. Another sequence of roots in the spectrum corresponds to internal van der Waals waves that have an upper frequency bound and the dispersion law typical of a multimode waveguide. © *2003 MAIK "Nauka/Interperiodica".*

(1) A liquid in mechanical and thermal equilibrium with a gas is nonuniformly strained near the gas–liquid interface due to van der Waals forces [1]. Its density decreases toward the interface. The density variation is caused by a pressure gradient arising in the surface liquid layer to compensate for the volume van der Waals force. The uniformity breaks at macroscopic distances that are many times larger than the molecule size. Asymptotics both for local quantities and for one- and two-particle distribution functions at large distances from the free surface were first calculated by Rusanov and Kuni (see, e.g., [2, 3]). Strictly speaking, the method used in [2, 3] is valid in the case of gases. However, the calculations [5–7] based on the macroscopic theory of van der Waals forces [4], which is applicable to media in any aggregative state, substantiated the asymptotics in [2, 3]. Refined expansion coefficients whose numerical values may be noticeably different from those in [2, 3] are expressed in [5–7] through the permittivities of media. In a surface layer extending to a depth of 3–4 nm, relative deviations of the liquid density from the volumetric value ρ_∞ may reach 10–15% [6, 7]. The density profile is found with the one-particle distribution function.

The study of waves caused by van der Waals forces in liquids is of certain interest. For these waves, the inclusion of the temperature effect and the specific thermal motion of particles requires a kinetic approach. In this paper, a hydrodynamic approximation is employed. The validity of the hydrodynamic description of the liquid flow in layers of thickness mentioned above has been established in many papers devoted to the numerical simulations of molecular dynamics. For instance, the motion of 1536 argon atoms along 10×10-nm walls spaced by 4 nm from each other (this corresponds to the density of liquid argon) in the uniform field of external forces was studied in [8].

Interaction of each pair of particles (including the interaction with molecules in the lattice sites of a solid) is described by the modified 6–12 potential. The motion of a single atom is Brownian with a drift along the force direction and temporal localization in the vicinity of walls. Although the density distribution has not been studied, molecular ordering near the walls has been reported. The averaging procedure results in a hydrodynamic velocity that differs from the velocity due to thermal fluctuations. The resulting velocity profile is in agreement with the solution to the hydrodynamic equations for the Poiseuille flow. Simultaneously, the macroscopic no-slip boundary condition is confirmed based on microscopic physical considerations. The viscosity calculated by fitting the Stokes parabola to the flow velocity distribution is expressed via the parameters of the intermolecular potential and has an observable value. In [8], the flow of a liquid with a thickness substantially smaller than 4 nm is considered within the problem of a moving boundary between three phases. In addition to the papers concerned with numerical simulations, there are those devoted to generalized hydrodynamics [9]. The latter are aimed at extending the equations of conventional macroscopic hydrodynamics to the microscale. In generalized hydrodynamics, generalized transport coefficients, which differ from the conventional one on small scales, are introduced. According to [9], conventional hydrodynamics is applicable to scales larger than three molecular diameters and to time intervals exceeding the kinetic time scale by one order of magnitude ($\sim 10^{-13}$ s).

The study of van der Waals surface waves using the model of a layer of homogeneous liquid on solid substrate was conducted in [10]. It turned out that, in the case of thin ($l < 400$ nm) layers, the waves strongly decay. If a layer of a low-viscous liquid is sufficiently thick, the existence and, hence, observation of weakly damped van der Waals waves seem to be possible

1063-7842/03/4805-0546$24.00

because of a decrease in the bottom friction, which makes a major contribution to the damping. The approach used in [10] turns out to be inapplicable in this case. It is appropriate to introduce the volume van der Waals force into the hydrodynamic equations and reject the uniform density approximation.

The aim of this paper is to determine the spectrum of the eigenfrequencies of free waves caused by van der Waals forces in a free-surface liquid.

(2) Let the horizontal plane $z = 0$ be the equilibrium interface between a liquid and environment (occupying the domain $z > 0$). The interface displacement in a wave is denoted by $z = \zeta(x, y, t)$. The problem is considered in the incompressible nonviscous liquid approximation. In this case, the initial hydrodynamic equations have the form [11]

$$\rho\frac{d\mathbf{v}}{dt} = -\nabla\rho + \rho\mathbf{g} + \rho\mathbf{f}, \quad \frac{d\rho}{dt} = 0, \quad \mathrm{div}\mathbf{v} = 0. \quad (1)$$

Here, $\mathbf{v} = v(\mathbf{u}, w)$; $\mathbf{u}$ and w are the horizontal and vertical velocity components, respectively; $\mathbf{q}$ is the acceleration due to gravity; and $\mathbf{f}$ is the specific van der Waals force. In equilibrium, the force $\mathbf{f}_0(z)$ and the force of gravity are directed downward. The additive approximation [1] can be used to determine this force. Let the intermolecular potential in the liquid have the form $U = -\beta r^{-6}$, where r is the intermolecular spacing and β is the interaction constant. Determining the energy of interaction between a probing molecule and other particles [12, 13] yields for the specific force

$$f_0(z) = A/(2\pi\rho_\infty z^4), \quad (2)$$

where $A = \pi^2 n^2 \beta$ is the Hamaker constant and $n = n_\infty$ is the concentration of molecules of the liquid.

Expression (2) is singular at the interface and represents the principal term of the force asymptotics away from the interface. It is conventionally assumed that such expansions are applicable starting from distances of greater than three or four monolayers from the interface. According to (1), in the equilibrium state, the pressure and density are related by

$$\frac{dp_0}{dz} = -(g + f_0)\rho_0(z). \quad (3)$$

The condition $f_0(b) = g$ defines the range of macroscopic van der Waals forces, $b = (A/2\pi\rho_\infty g)^{1/4}$. For typical values $A = 6.28 \times 10^{-20}$ J and $\rho_\infty = 10^3$ kg/m^3, we have $b = 10^{-6}$ m. The mean and especially maximum values of the force f_0 are many orders of magnitude higher than g. The equilibrium density gradient is given by the thermodynamic relationship

$$\frac{d\rho_0}{dz} = \chi\rho_0\frac{dp_0}{dz} = -\chi(g + f_0)\rho_0^2, \quad (4)$$

where χ is the isothermal compressibility.

The coordinate dependence of the density is basically determined by the nonuniformity of the force $f_0(z)$. According to (2) and (4), within the range of van der Waals forces, the principle term of the density asymptotics has the form $\rho_\infty - \rho_0 \sim z^{-3}$. This is in agreement with [5–7] and lends further support to the validity of the hydrodynamic approach and expression (2) for the force. The quantity $h = \varepsilon/\chi\rho_\infty f_s$ is taken as the thickness of a layer where the density gradient varies most considerably. Here, $\varepsilon = (\rho_\infty - \rho_0(0))/\rho_\infty$ is the maximum relative density difference and f_s is a certain characteristic force. This thickness may be as large as several hundreds of nanometers.

(3) Hereafter, we will consider harmonic waves. In this case, the free surface profile is sinusoidal. The instantaneous value of the specific force $\mathbf{f}$ for such a profile is difficult to calculate in the additive approximation. An approximate expression for the force perturbation $\mathbf{f}' = \mathbf{f} - \mathbf{f}_0$ due to the interface distortion can be found from physical considerations. The force $\mathbf{f}'$ has to be a harmonic function of x, y, and t and vanish for $\zeta \longrightarrow 0$ and also away from the free surface. The dynamic force $\mathbf{f}$ is directed normally to the interface only in vertical sections of symmetry A and B that pass through crests ($\zeta > 0$) and troughs ($\zeta < 0$) of the waves. For simplicity's sake, the amplitude of the free interface displacement $\zeta_m = \max|\zeta|$ is assumed to be smaller than the layer thickness h. A liquid particle with a coordinate z in the equilibrium state has a coordinate $\zeta - z$ in the dynamic case. In view of the condition $\zeta_m \ll \lambda$ (λ is the wavelength), which is adopted in the linear theory, the forces $f(z)$ in sections A and B are assumed to differ weakly from $f_0(\zeta - z)$. Then, the vertical component f'_z at $z < 0$ is given by $(df_A/dz)\zeta$ and $(df_B/dz)\zeta$ in sections A and B, respectively. Here, f_A and f_B are power functions similar to (2). In section A, $f_A > f_0(\zeta - z)$ because of a weak additional downward attraction of molecules compared to the attraction at the interface; in section B, the situation is reverse $f_B < f_0(\zeta - z)$. In intermediate sections, f'_z gradually changes its behavior according to the relationship

$$f'_z = \left(\frac{df_q}{dz}\right)\zeta,$$

where f_q is a slowly varying function of the coordinate q reckoned along the wave propagation direction. This function can be replaced by the q-averaged function $f_n(z)$. Then, f'_z is written as

$$f'_z = \frac{df_n}{dz}\zeta. \quad (5)$$

In a similar way, one can find that the horizontal component of the force perturbation is proportional to the gradient of ζ:

$$\mathbf{f}' = -f_\tau(z)\nabla\zeta, \quad (6)$$

where f_τ is a power function similar to (2).

Linearizing (1) in the vicinity of the stationary state given by (3) and (4) in view of (5) and (6) yields the set of equations for perturbations

$$\rho_0\frac{\partial \mathbf{v}}{\partial t} = -\nabla p - (g + f_0)\rho\nabla z + \rho_0 f_n'\zeta\nabla z - \rho_0 f_\tau\nabla\zeta,$$
$$\frac{\partial \rho}{\partial t} + \frac{d\rho_0}{dz}w = 0, \quad \mathrm{div}\mathbf{v} = 0. \tag{7}$$

In (7), the primes by the perturbations of pressure p and density ρ are omitted. The procedure of sequential elimination of unknowns [11] reduces (7) to the equation in w

$$\frac{\partial^2}{\partial t^2}\left(\Delta w + \frac{1}{\rho_0}\frac{d\rho_0}{dz}\frac{\partial w}{\partial z}\right) + N^2(z)\Delta_2 w = M(z)\Delta_2 w(x, y, 0, t). \tag{8}$$

Here, Δ and Δ_2 denote three-dimensional and horizontal Laplacians, respectively, and the Väisälä frequency $N^2(z)$ and the $M(z)$ function are given by

$$N^2 = -(g + f_0)\frac{1}{f_0}\frac{d\rho_0}{dz}, \quad M = \frac{1}{\rho_0}\frac{d\rho_0}{dz}f_\tau + f_n' + f_\tau',$$

where the primed functions are the derivatives with respect to z.

If $M = 0$, Eq. (8) coincides in form with the well-known equation for gravity waves [11]. In view of (4), the Väisälä frequency is nonnegative. This is evidence of the stability of the equilibrium density distribution and indicates that the nonmonotonic time evolution of the perturbations is a possibility. In (8), the gravity force appears in explicit form in N^2 and implicitly through density gradient (4). The thickness l of the liquid is assumed to be relatively thin; so one can neglect the density variation across the thickness due to pressure variation in the volume, where $f = 0$. In this case, g in N^2 can be omitted. The surface pressure is taken into account on the free surface to preserve generality:

$$(p_0 + p)_{z=\zeta} - p_a = -\gamma\Delta_2\zeta. \tag{9}$$

Here, p_a is the constant atmospheric pressure and γ is the surface tension coefficient. Linearizing (9) involves the Lagrange finite-increment formula

$$p_0(\zeta) - p_0(0) = p_0'(z_s)\zeta = -f_s\rho_s\zeta, \quad 0 < z_x < \zeta,$$

where $f_s = f_0(z_s)$ and $\rho_s = \rho_0(z_s)$. It is taken into account that $f_s \gg g$.

The coordinate z_s increases with increasing amplitude ζ_m. The standard formula for the increment of a function with a rapidly varying derivative (see (3)) is inapplicable at the point $z = 0$, where it is undefined. It is acceptable to substitute ρ_∞ for both ρ_s and $\rho_0(0)$ in subsequent formulas. The linearization of (9) yields the following condition on the unperturbed surface:

$$p|_{z=0} = \rho_\infty f_s\zeta - \gamma\Delta_2\zeta.$$

Having eliminated p by using (7) and ζ by using the kinematic condition, one arrives at the dynamic boundary condition for w

$$\left[(f_s + f_\tau)\Delta_2 w - \frac{\gamma}{\rho_0}\Delta_2\Delta_2 w - \frac{\partial^3 w}{\partial t^2\partial z}\right]_{z=0} = 0. \tag{10}$$

In the case of perturbations with $\lambda < 2l$, one can put $w(-\infty) = 0$ as the second boundary condition for (8). Then, the gravity force is no longer involved in the statement of the problem. Hence, it has no influence on van der Waals waves. On the contrary, by eliminating the van der Waals force ($\mathbf{f} = 0$) from (7) and (8) and restoring the eliminated gravity force in (10), one comes to the problem of gravity capillary waves in deep water.

(4) We use the Boussinesq approximation, implying that the density gradient is retained only in the expression for the Väisälä frequency. The solution is looked for in the form of a harmonic wave,

$$w \sim \Phi(z)\exp[i(k_x x + k_y y) - i\omega t], \quad k = (k_x^2 + k_y^2)^{1/2}.$$

In view of (10), the velocity amplitude is determined from the eigenvalue problem

$$\Phi'' + k^2\left(\frac{N^2(z)}{\omega^2} - 1\right)\Phi = \frac{k^2}{\omega^2}M(z)\Phi(0),$$
$$\Phi(-\infty) = 0, \quad \omega^2\Phi'(0) = k\Omega^2\Phi(0), \tag{11}$$
$$\Omega^2 = [(f_s + f_\tau)k + \gamma k^3/\rho_0]_{z=0}.$$

There is another essential difficulty to be overcome in rigorously (including numerically) determining the characteristics of the free-wave spectrum with set (11). All the coefficients of the function in (11) are not defined in the entire domain $z \le 0$, where the solution exists. The asymptotics of ρ_0, f_0, and other functions, as well as their maxima and minima, are unknown at $z \longrightarrow 0$. The initial qualitative solution can be found under the assumption that these functions are single-valued continuous functions taking finite values for $z \le 0$. In view of (4), the function $N^2(z)$ in (11) is proportional to $(d\rho_0/dz)^2$, and its absolute value is small outside the layer, i.e., at $|z| < h$. This function increases as $N^2 \sim z^{-8}$ when approaching the free surface. The function M is similar to N^2. The specific behavior of the coefficients of Eq. (11) makes it possible to study the basic properties of the waves in the framework of the simplified model of a surface waveguide, in which the coefficients are approximated by stepwise (piecewise constant) expressions. In the vicinity of the free surface (inside the layer) $-h < z < 0$ (domain *1*), the functions $N^2(z)$ and $M(z)$ are replaced by the constants N_m^2 =

$\chi\rho_\infty f_s^2$ and M. Outside the layer, i.e., for $z < -h$ (domain *2*), one may put $N^2 = M = 0$. This frequently used expedient allows one to derive the dispersion relation in explicit form and determine the type of motion. The values of both constants and the characteristic force f_s remain undetermined. Inside the liquid, the solution to (11) has the form

$$\Phi_2 = a_2 \exp(kz). \tag{12}$$

If $\lambda < 2l$, the bottom friction is of no significance. This confirms the validity of using the nonviscous liquid model. If the frequency satisfies the inequality $\omega < N_m$, the solution to (11) in domain *1* is

$$\Phi_1 = a_1 \sin\alpha kz + b_1 \cos\alpha kz + b_1\left(\frac{\alpha^2\omega_2}{M} - 1\right)^{-1},$$
$$\alpha = \left[\frac{N_m^2}{\omega^2 - 1}\right]^{1/2}. \tag{13}$$

Since $f_0(z)$ is continuous, solutions (12) and (13), as well as their first derivatives, have to be joined together at the boundary between domains *1* and *2* [1]. This results in a set of homogeneous equations for the coefficients. This set has a solution if the following dispersion relation is satisfied:

$$\Omega^2\alpha(\sin\alpha kh + \alpha\cos\alpha kh) = M + (\alpha^2\omega^2 - M)(\cos\alpha kh - \alpha\sin\alpha kh). \tag{14}$$

(5) First, we will find the roots of (14) at $M = 0$; then, the dependence of the solution on M will be studied by the method of successive approximations. Equation (14) at $M = 0$ is reduced to

$$\tan\alpha kh = \frac{\alpha(\omega^2 - \Omega^2)}{\alpha^2\omega^2 + \Omega^2}. \tag{15}$$

If $\omega > N_m$, α becomes a purely imaginary number $i|\alpha|$ and dispersion relation (15) turns into

$$\tan|\alpha|kh = \frac{|\alpha|(\omega^2 - \Omega^2)}{\Omega^2 - |\alpha|^2\omega^2}. \tag{16}$$

Since $f_s \gg g$, purely capillary perturbations correspond to values of λ that are much smaller than those in the case of gravity capillary waves. For instance, for water, assuming that $A = 1.65 \times 10^{-19}$ J, $f_s = f_0(a)$, $a = 5\sigma$, $\sigma = 2.64 \times 10^{-10}$ m, and $\gamma = 0.072$ J/m^2, we find that $\lambda < 10^{-8}$ m ($kh \gg 1$). The study of these perturbations seems to be of little interest; therefore,

$$\Omega^2 = \kappa f_s k \quad (\kappa = 1 + f_\tau(0)/f_s) \tag{17}$$

will be used below as the characteristic frequency.

5.1. In terms of the variable $\tau = \alpha kh$, Eq. (15) in view of (17) can be written as

$$\tan\tau = F(\tau), \quad F = \frac{\alpha^2(\omega/N_m)^2\varepsilon - \alpha\kappa\tau}{\alpha^3(\omega/N_m)^2\varepsilon + \kappa\tau}. \tag{18}$$

At a fixed frequency ω, the coefficients of the fractional linear function F are constant. Over the entire range of variation of the argument, F is a monotonically decreasing function varying from $F(0) = \alpha^{-1}$ to $F(\infty) = -\alpha$. Hence, Eq. (18) has a countable set of roots τ_0, τ_1, τ_2, …, that corresponds to the sequence of points where $F(\tau)$ crosses the branches of $\tan\tau$. The eigenvalues of problem (11),

$$k_n(\omega) = \tau_n(\omega)/h\alpha(\omega); \quad n = 0, 1, 2, \ldots,$$

completely define the eigenwaves w_n.

At higher frequencies, $\omega > N_m$, dispersion relation (16) is transformed in a similar way ($\tau = |\alpha|kh$):

$$\tan\tau = F_1(\tau), \quad F_1 = \frac{|\alpha|^2(\omega/N_m)^2\varepsilon - |\alpha|\kappa\tau}{\kappa\tau - |\alpha|^3(\omega/N_m)^2\varepsilon}. \tag{19}$$

The function F_1 has an infinite discontinuity at $\kappa\tau_\infty = |\alpha|^3(\omega/N_m)^2\varepsilon$ and equals zero at $\kappa\tau_m = |\alpha|(\omega/N_m)^2\varepsilon$. It is positive and monotonically decreases from ∞ to 0 only for $\tau_\infty < \tau < \tau_m$. Consequently, dispersion relation (19) has a unique solution for any frequency $\omega > N_m$.

The least root τ_0 of (18) is small. The estimation of the first term in the numerator of $F(\tau)$ yields $\alpha(\omega/N_m)^2\varepsilon < \varepsilon\omega/N_m < \varepsilon$. As a result, $\tau_0 = \alpha(\omega/N_m)^2(\varepsilon/\kappa)$ is the solution to (18) in the first approximation in ε. Substituting $\tau_0 = \alpha k_0 h$ yields the dispersion relation

$$\omega^2 = \kappa f_s k, \tag{20}$$

which is similar to that in the case of surface gravity waves [11]. As the van der Waals acceleration, instead of g, appears in (20), these waves are naturally referred to as surface van der Waals waves. These waves can be considered as high-frequency ones in comparison with gravity waves. The solution to Eq. (19) shows that its roots, while not small, also describe surface van der Waals waves. Curve *1* in Fig. 1 is drawn through the eigenvalues $k_0(\omega)$ calculated from the exact roots $\tau_0(\omega)$ and $\tau(\omega)$ of Eqs. (18) and (19) for $(\varepsilon/\kappa) = 0$ and 1, respectively. The equation of curve *1*,

$$k_0 h = (\varepsilon/\kappa)(\omega/N_m)^2$$

expresses relationship (20) in dimensionless form. Curves *2–4* in Fig. 1 show the solutions of complete dispersion relation (14) as functions of M. The curves corresponding to $M = (1 - 2)N_m^2$ merge with curve *1* in Fig. 1. Parallel lines *1–4* extend dependence (20) to the case of finite M. The increase in the relative difference

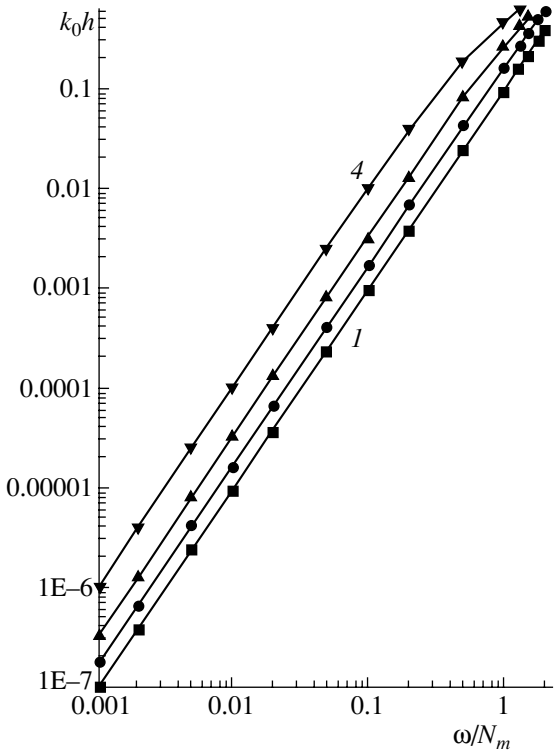

Fig. 1. Dispersion relations for surface van der Waals waves at M/N_m^2 = (*1*) 0, (*2*) 5, (*3*) 8, and (*4*) 10.

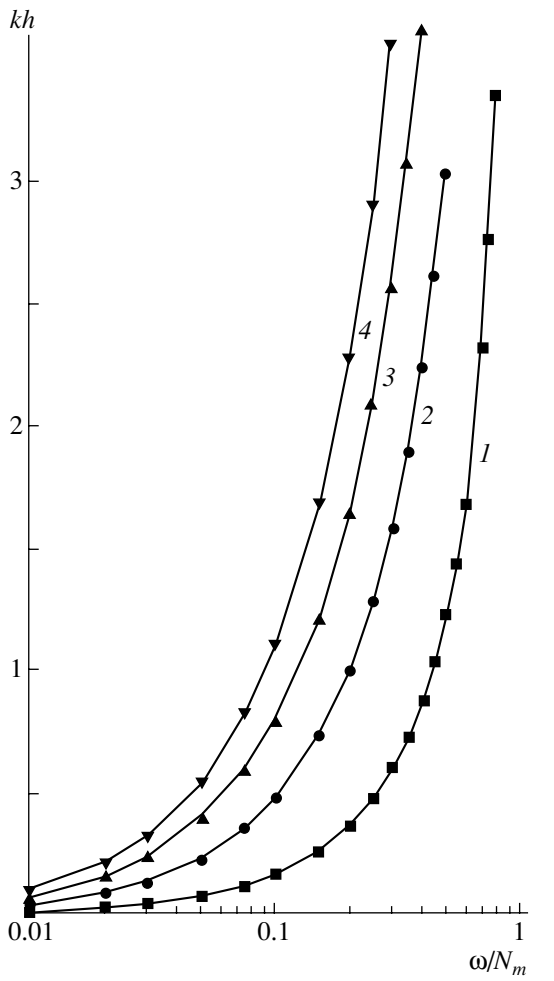

Fig. 2. Dispersion law for internal van der Waals waves ($\varepsilon/\kappa = 0.1$ and $M = 0$).

in the density ε also causes the parallel upward shift of the dispersion curve. This shift is small at small ε. Eigenfunctions (12) and (13), which correspond to surface waves, peak on the free surface and, decreasing monotonically with depth, turn to zero only at the bottom.

Perturbations obeying dispersion law (20) were observed in thin layers ($l \simeq 20$ nm) in superfluid helium [14], which has a very low surface tension coefficient. These waves were called third sound. The data presented here indicate that surface van der Waals waves can also be excited in ordinary classical fluids. In deep low-viscous liquids, the wave attenuation must be low.

5.2. Along with surface waves, the set of eigenwaves at $\omega < N_m$ involves covers corresponding to the subsequent roots τ_1, τ_2, … of dispersion relation (18). These are internal van der Waals waves. The first four eigenvalues $k_n(\omega)$ are shown in Fig. 2 (curves *1–4*). The dispersion law found is typical of a multimode waveguide, which validates the term "surface waveguide." The wavelength diminishes with growing harmonic number. At the same wavelengths, van der Waals frequencies may exceed those of gravity waves by several orders of magnitude. For internal waves in the ocean, vertical displacements of particles are maximal at a depth where the density gradient is the highest. In our case, the regions of maximal gradient are located in a shallow layer of thickness *h* at the surface. According to (12), internal waves, like surface waves, propagate in a layer of depth ~λ. The necessary conditions for the existence of van der Waals waves are identical to those for internal gravity waves in the dead zone, where freshwater overlies salt (heavier) water [11]. In both cases, hydrostatic equilibrium is stable, convection does not appear, and the gradients of density and force are parallel to each other. Therefore, the branch corresponding to internal van der Waals waves in the excitation spectrum is not unexpected.

5.3. It is of interest to consider surface van der Waals waves in the limiting case when the amplitude ζ_m of the free surface displacement surface is much higher than *h*. Under the assumptions made above for the depth *l* of the liquid, its density can be considered constant outside the surface layer. For waves with vertical particle displacements ~*l*, the consideration can be restricted to the flow in the bulk of the liquid outside the surface layer with a nonuniform density. In terms of the hydrodynamic approach applied to this layer, one can take into account the action of the van der Waals force by appropriately modifying boundary condition (9) to fit

the equation in the volume. In determining the increment $p_0(\zeta) - p_0(0)$, one should bear in mind that the values of $p_0(\zeta)$ and $p_0(r\zeta)$ differ from each other insignificantly when r and b/ζ_m are of the same order of magnitude. Substituting $p_0(r\zeta)$ with constant r for $p_0(\zeta)$ virtually means that the boundary of the layer with a nonuniform density has the same shape as the free surface. By virtue of the condition $\zeta_m \ll \lambda$, such an approximation seems to be admissible. Then, after the linearization of (9), the dynamic boundary condition on the unperturbed free surface can be written in the form

$$p|_{z=0} = f_{\lim}\rho_\infty\zeta - \gamma\Delta_2\zeta, \qquad (21)$$

where $f_{\lim}$ is the limiting value of f_s when $\zeta_m \gtrsim b$.

The boundary condition for w on the free surface, which results from (21) after eliminating p and ζ, differs from (10) only by the substitution of $f_{\lim}$ for f_s. The equations of motion in the bulk result from (7) if $\mathbf{f} = d\rho_0/dz = 0$. From these equations it follows that density perturbations are absent and the influence of buoyancy forces can be neglected. Set (7) is reduced to the equation for w that is well known in the theory of capillary gravity waves [11]. If the no-percolation condition at $z = -l$ is met, this equation has the solution

$$w = \sinh k(z + l)\exp[i(k_x x + k_y y - \omega t)].$$

Substituting this expression into the dynamic boundary condition yields the dispersion relation

$$\omega^2 = (\kappa f_{\lim} k + \gamma k^3/\rho_0(0))\tanh kl. \qquad (22)$$

At $k^2 \ll \kappa\rho_\infty f_{\lim}/\gamma$, expression (22) takes the form

$$\omega^2 = \kappa f_{\lim} k. \qquad (23)$$

Thus, the dispersion law for surface van der Waals waves in deep liquid, which implies proportionality between ω^2 and k, is valid for any perturbation amplitudes admissible in the linear theory. The proportionality coefficient depends on the value of the volume van der Waals force.

(6) Physical analysis of the field of van der Waals forces in a liquid gives an expression for the specific mass force that is in agreement with the density profile resulting from the rigorous theory. Therefore, it can be included in the hydrodynamic equations, specifically, in the equations for perturbations. The boundary condition allowing for van der Waals forces at the interface is derived. The physical model of a surface waveguide using a reasonable approximation of the coefficients in the wave equation is considered. A dispersion relation approximating the spectra of both surface and internal waves is derived.

REFERENCES

1. Yu. S. Barash, *Van der Waals Forces* (Nauka, Moscow, 1988).
2. A. I. Rusanov and F. M. Kuni, Zh. Fiz. Khim. **42**, 1189 (1968).
3. F. M. Kuni and A. I. Rusanov, Zh. Fiz. Khim. **42**, 2569 (1968).
4. I. E. Dzyaloshinskiĭ, E. M. Lifshits, and L. P. Pitaevskiĭ, Zh. Éksp. Teor. Fiz. **37**, 222 (1959).
5. V. M. Nabutovskiĭ, V. R. Belosludov, and A. M. Korotkikh, Kolloidn. Zh. **41**, 876 (1979).
6. P. V. Pikhitsa and G. I. Salistra, Ukr. Phys. J. **25**, 974 (1980).
7. V. M. Nabutovskiĭ and V. R. Belosludov, Koloidn. Zh. **45**, 263 (1983).
8. J. Koplik, J. R. Banavar, and J. F. Willemsen, Phys. Rev. Lett. **60**, 1282 (1988); Phys. Fluids A **1**, 781 (1989).
9. B. J. Alder and W. E. Alley, Phys. Today, No. 1, 56 (1984).
10. Yu. V. Sanochkin, Izv. Akad. Nauk, Mekh. Zhidk. Gaza, No. 4, 156 (2000).
11. L. M. Brekhovskiĭ and V. V. Goncharov, *Introduction to Mechanics of Continua* (Nauka, Moscow, 1982).
12. H. C. Hamaker, Physica **4**, 1058 (1937).
13. Ya. I. Frenkel, *Kinetic Theory of Liquids* (Nauka, Leningrad, 1945; Clarendon, Oxford, 1946).
14. S. J. Putterman, *Superfluid Hydrodynamics* (North-Holland, Amsterdam, 1974, 2nd ed.; Mir, Moscow, 1978).

Translated by M. Fofanov

Technical Physics, Vol. 48, No. 5, 2003, pp. 552–556. Translated from Zhurnal Tekhnicheskoĭ Fiziki, Vol. 73, No. 5, 2003, pp. 30–34.

GAS DISCHARGES, PLASMA

Interior Ballistics of a Single-Stage Plasmatron and the General Features of Radiative Heat Exchange

D. B. Volov

Samara Engineering Institute of Railway Transport, Pervyĭ Bezymyannyĭ per. 18, Samara, 443066 Russia

Received July 3, 2002

Abstract—A mathematical model of a single-stage ballistic plasmatron for producing radiating gas is proposed. Various operating conditions are analyzed and compared with experimental data. The general features of radiative heat exchange in the device are outlined. © *2003 MAIK "Nauka/Interperiodica".*

INTRODUCTION

Ballistic plasmatrons are widely used in various fields of thermal physics. High-temperature gases produced in these devices by compression liberate the stored energy in the form of optical radiation, which can be used to pump solid-state lasers [1, 2]. This radiation can also be used in plasmochemistry and photochemistry [3]. High-temperature gases are employed in studying the effect of shock waves on various objects, etc. To find optimal operating conditions, it is necessary to develop a mathematical model that could describe the dynamics of the device operation and could give practical recommendations on the choice of the compression regime.

EXPERIMENTAL SETUP

A BP-3 ballistic plasmatron (Fig. 1) consists of barrel *1* and piston *2* initially fixed at the end with the help of fixing wire *3*. The pushing gas (air) is contained in balloon *4*. The irradiated object is placed in chamber *5*. This may be the rod of a solid-state laser, a specimen for studying the effect of shock waves at high temperatures, medical instruments to be sterilized, etc. The chamber is usually separated from the barrel by breaking membrane *6*.

After evacuation, the barrel is filled up with a working gas at a given pressure. The pushing gas is fed into balloon *4*. After pressing the start button, the pushing gas enters the plasmatron through an electromagnetic valve, thereby moving the piston. In a time of about 10 ms, the working gas is compressed to a pressure of 1000 atm and heated to a temperature of about 8000 K. At such a temperature, a fraction of the energy accumulated in the gas during its compression is radiated. After the membrane is broken, the radiating gas is ejected into the chamber.

MATHEMATICAL MODEL OF A PLASMATRON

Let us derive equations that will allow us to determine the parameters of the working gas in the plasmatron.

First, we derive the equation of motion of the plasmatron piston. The force exerted by the pushing gas on the piston is $F_1 = p_1 S_\sigma$, and the force exerted by the working gas is $F_2 = p_2 S_\sigma$, where p is pressure and S_σ is the piston area. Here and below, index 1 refers to the parameters of the pushing gas and index 2 refers to the parameters of the working gas. The friction force F_f acts against the piston motion.

It was shown in [4] that, under the given conditions, the pushing and working gases can be described by the equation of state for an ideal gas.

In the first approximation, the friction force can be written as

$$F_f = -\beta \frac{dx/dt}{|dx/dt|},$$

where x is the running coordinate of the piston center of mass, the factor β is determined experimentally, and t is time.

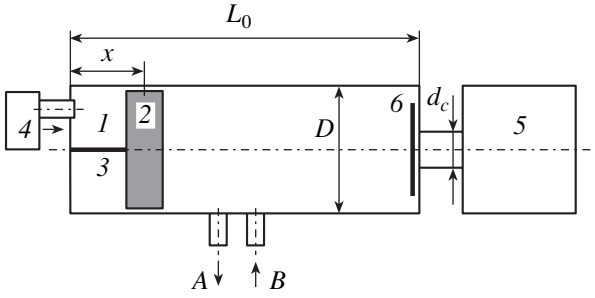

Fig. 1. Schematic of a single-stage ballistic plasmatron: (*1*) plasmatron barrel, (*2*) piston, (*3*) fixing wire, (*4*) balloon with the pushing gas, (5) optical chamber, (*6*) membrane, (*A*) evacuation, (*B*) working gas supply.

1063-7842/03/4805-0552$24.00 © 2003 MAIK "Nauka/Interperiodica"

Taking into account the equations of state for the working and pushing gases, the equation of motion of the piston,

$$m_p \frac{d^2\mathbf{x}}{dt^2} = \sum_i \mathbf{F}_i,$$

can be rewritten in the form

$$m_p \frac{d^2x}{dt^2} = \frac{m_1 R_0 T_1}{\mu_1 (x - l_p/2)} - \frac{m_2 R_0 T_2}{\mu_2 (L_0 - (x + l_p/2))} - \beta \frac{dx/dt}{|dx/dt|}, \quad (1)$$

where m_p is the piston mass, m_1 and m_2 are the gas masses, μ_1 and μ_2 are the molar masses, R_0 is the universal gas constant, L_0 is the barrel length, l_p is the piston length, and the temperatures T_1 and T_2 are determined from the energy balance equation.

As the gas flows out of balloon *4* (Fig. 1), the mass of the pushing gas in the barrel varies. Since the pressure difference across the valve is supercritical, we can write

$$\frac{dm_b}{dt} = -\frac{m_b}{V_b} a_b \frac{\pi d^2}{4}, \quad (2)$$

where m_b is the gas mass in the balloon, V_b is the balloon volume, a_b is the speed of sound in the balloon, and d is the diameter of the electric valve nozzle.

The mass of the gas in the plasmatron barrel is equal to

$$m_1 = m_{01} + (m_{0b} - m_b), \quad (3)$$

where m_{01} and m_{0b} are the initial gas masses in the barrel and balloon, respectively.

When the gas pressure in the balloon decreases below a certain value p_v, the valve is closed and a fraction of the pushing gas with the mass m_v remains in the balloon. Therefore, after integrating Eq. (2), formula (3) takes the form

$$m_1 = \begin{cases} m_{01} + m_{0b}\left(1 - \exp\left(-\dfrac{\pi d^2}{4V_b} a_b t\right)\right), & m_b > m_v \\ m_{01} + (m_{0b} - m_v), & m_b = m_v, \end{cases} \quad (4)$$

where

$$m_v = p_v \frac{\mu_1 V_b}{R_0 T_0}.$$

In order to utilize the compression energy most efficiently, the piston is provided with fixing wire *3* (Fig. 1). The wire attaches the piston to the barrel end and is broken when the applied force exceeds a certain value F_{st}. The fixing wire allows one to increase the pressure of the pushing gas in the barrel before the piston starts moving. Hence, equation of motion (1) takes the form

$$m_p \frac{d^2x}{dt^2} = \begin{cases} 0, & \sum_i F_i \le F_{st} \\ \dfrac{m_1 R_0 T_1}{\mu_1 (x - l_p/2)} - \dfrac{m_2 R_0 T_2}{\mu_2 (L_0 - (x + l_p/2))} - \beta \dfrac{dx/dt}{|dx/dt|} & \\ & \sum_i F_i > F_{st}, \end{cases}$$

where m_1 is defined by formula (4).

The temperatures T_1 and T_2 can be determined from the energy balance equation

$$\frac{dU}{dt} = \sum_i W_i + \sum_j H_j G_j, \quad (5)$$

in which, for simplicity, indexes 1 and 2 are omitted. Here, $U = mc_v T$ is the internal gas energy; W_i is the energy source power; $H = c_p T$ is the enthalpy; G is the gas flow rate; and c_p and c_v are the specific heats at constant pressure and constant volume, respectively. For a single outlet, we have $j = 1$.

For the working gas (index 2), without allowance for convective and diffusive losses, the total source power is the sum of the radiative losses e_{rad} and the work done on gas compression $dA_2 = -p_2 dV_2$ per unit time:

$$\sum_i W_i = -e_{rad} - \frac{p_2 dV_2}{dt}.$$

After the membrane is broken, the pressure difference across the valve is supercritical; hence, the gas flow rate through the nozzle with the area S can be calculated by the formula

$$\frac{dm_2}{dt} = -\frac{m_2}{V_2} a_2 S, \quad (6)$$

where

$$a_2 = \sqrt{\gamma_2 \frac{R_0}{\mu_2} T_2}$$

is the speed of sound.

Equation (6) can also be used in the case of a discharge without membrane *6* (Fig. 1), because the pressure difference between the barrel and the chamber quickly passes through the critical level. Then, for the working gas, equation (5) can be written in the form

$$\frac{dU_2}{dt} = -e_{rad} - p_2 \frac{dV_2}{dt} - c_{p2} T_2 \rho_2 a_2 S,$$

where ρ_2 is the gas density. After some algebraic manipulations, this equation takes the form

$$\frac{dT_2}{dt} = (\gamma_2 - 1)\frac{T_2}{V_2}\left(-\frac{dV_2}{dt} - a_2 S\right) - \frac{e_{\text{rad}}}{c_{v2}\rho_2 V_2}. \quad (7)$$

When the working gas is compressed in a closed volume ($S = 0$) in the absence of radiative losses, equation (7) describes an adiabatic process; the case in which the gas issues into a chamber with a constant volume ($V_2 = \text{const}$) was considered in detail in [5].

To determine T_1, we can also use energy equation (5). However, the problem can be simplified taking into account the fact that, by the time when the fixing wire is broken, most of the pushing gas has already flowed into the plasmatron barrel and, then, its mass changes only slightly. Since the radiative losses are negligibly small, the expansion of the pushing gas can be considered adiabatic:

$$\frac{T_1}{T_0} = \left(\frac{V_0}{V_1}\right)^{\gamma_1 - 1} = \left(\frac{x_0 - l_p/2}{x - l_p/2}\right)^{\gamma_1 - 1}.$$

In this paper, as in [6, 7], the radiative loss power is sought in the form

$$e_V = \frac{4\sigma T_2^4 V_2}{a'}\left[1 - \exp\left(-\frac{a'G'\rho_2 T_2 \exp(-I/T_2)}{4\sigma T_2^4}\right)\right], \quad (8)$$

$$a' = \frac{D}{1 + D/(2(L_0 - (x - l_p/2)))},$$

where σ is the Stephan–Boltzmann constant, a' is the reduced linear dimension, D is the inner diameter of the plasmatron, and G' and I are constants that depend on the sort of gas used [5].

After some algebraic transformations, the set of equations describing the gas parameters in a single-stage ballistic plasmatron can be rewritten in a form

$$\frac{d^2x}{dt^2} = \frac{1}{m_p} \times \begin{cases} 0, & \sum_i F_i \le F_{\text{st}} \\ \dfrac{m_1 R_0 T_0 (x_0 - l_p/2)^{\gamma_1 - 1}}{\mu_1 (x - l_p/2)^{\gamma_1}} - \dfrac{m_2 R_0 T_2}{\mu_2 (L_0 (x + l_p/2))} & \\ -\beta \dfrac{dx/dt}{|dx/dt|}, & \sum_i F_i > F_{\text{st}}, \end{cases} \quad (9)$$

$$\frac{dT_2}{dt} = (\gamma_2 - 1)\frac{T_2}{V_2}\left(-\frac{dV_2}{dt} - a_2 S\right) - \frac{e_{\text{rad}}}{c_{v2} m_2},$$

$$\frac{dm_2}{dt} = -\frac{m_2}{V_2} a_2 S,$$

where m_1 is determined by formula (4), e_{rad} is described by expression (8), and $V_2 = (\pi D^2/4)(L_0 - (x + l_p/2))$. The initial conditions of the problem are the following: $x = x_0$, $dx/dt = 0$, $T_1 = T_2 = T_0$, $m_1 = m_{01}$, and $m_2 = m_{02}$.

As the gas flows out through the nozzle, at a certain instant, the mass of the working gas becomes zero, $m_2 = 0$. Then, the set of Eqs. (9) should be replaced with other equations describing a collision of the piston with the end of the plasmatron barrel. We do not present these equations here, because this problem is beyond the scope of this study.

NUMERICAL CALCULATIONS OF THE GAS PARAMETERS IN THE PLASMATRON

The set of Eqs. (9) was integrated by the Runge–Kutta fourth-order method with a constant integration step up to $N = 50000$. The results of calculations show that, within the given temperature and pressure ranges, the computed parameter values are established at $N > 35000$ and the integration error at $N = 50000$ does not exceed 1%.

The experiments were carried out at the Institute of Chemical Physics of the Russian Academy of Sciences in the device with the following parameters: $L_0 = 1.26$ m, $l_p = 50$ mm, $D = 58$ mm, the diameter of the electric valve nozzle was $d = 8$ mm, the piston mass was $m_p = 0.357$ kg, $\beta = 4N$, and the pressure at which the valve was closed was $p_v = 4.125$ atm. The initial conditions of the problem were the following: $x_0 = 175$ mm, $dx/dt = 0$, $T_0 = 300$ K, $m_{01} = 5.112 \times 10^{-4}$ kg, and m_{02} varied depending on the degree of evacuation.

Let us first consider the case in which the gas is compressed in a finite volume ($d_n = 0$) without using a fixing wire. The working gas is air ($\gamma_2 = 1.4$, $\mu_2 = 0.029$ kg/mol, and $p_2 = 1.013 \times 10^5$ Pa), and the initial pressure of the pushing gas is 6.0 atm. The calculations show that, in this case, the compression efficiency is low: the fraction of the compression energy in the first pulse is only 22% of the total energy stored in the pushing gas ($p_{\max} = 3.37$ atm, $T_{\max} = 423$ K). This is explained, first of all, by the finite time during which the gas flows out of the balloon into the plasmatron barrel.

The compression efficiency can be substantially increased by preliminary fixing the piston position. Thus, for a fixing force of $F_{\text{st}} = 2500$ N, the pressure in the first pulse increases up to $p_{\max} = 11.1$ atm at $T_{\max} = 595$ K.

As F_{st} increases further, the values of $p_{\max}$ and $T_{\max}$ increase monotonically (Fig. 2). Under certain conditions, the maxima of the pressure and temperature are observed in the second (rather than the first) pulse. The minimum distance to the barrel end wall Δ decreases monotonically as F_{st} increases (Fig. 2, curve *3*). If the

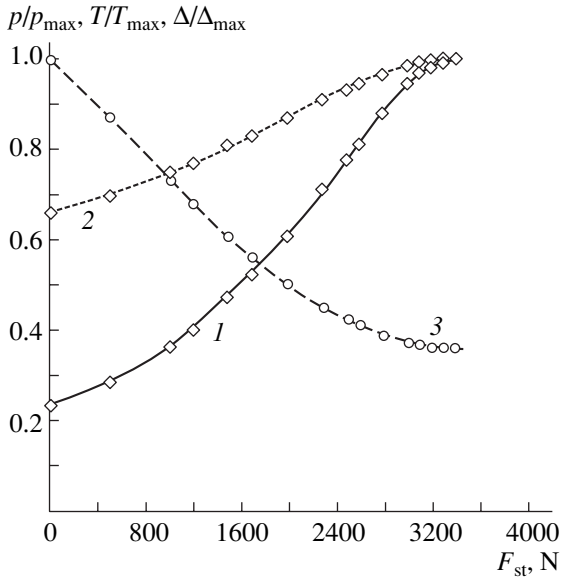

Fig. 2. (*1*) Maximum pressure and (*2*) maximum temperature in a pulse and (*3*) the minimum distance of the piston from the barrel end wall as functions of the fixing force F_{st} for d_n = 0 mm, p_{max} = 14.3 atm, T_{max} = 639 K, and Δ_{max} = 0.449 m.

force F_{st} exceeds the sum of other forces, then the fixing wire is not broken.

The available energy of the pushing gas can be deposited in a smaller mass of the working gas; this will increase the maximum temperature achieved during compression. In other words, a rarefied working gas is more appropriate for compression. For this purpose, provision is made for the evacuation of the device. For evacuation down to $p_2 = 1.094 \times 10^4$ Pa, the calculated time behaviors of the working gas pressure and temperature are shown in Figs. 3a and 3c, respectively. The calculated parameters in the first pulse are the following: p_{max} = 354 atm and T_{max} = 3021 K. The calculated results agree well with the experimental data on the amplitude and repetition rate of the pulses (Fig. 3b).

The parameters of the nozzle substantially affects the compression process. The appropriate choice of the nozzle diameter guarantees, in many respects, the high compression efficiency. Thus, with d_n = 1 mm, a large portion of the working gas has no time to flow into the chamber during the first pulse; hence, the compression energy cannot be efficiently utilized. In this case, the time dependence $m_2(t)$ is a step curve (Fig. 4), which corroborates the assumptions [8] that the gas flows into the chamber only when the piston approaches the position corresponding to Δ_{min}. For this regime, we have p_{max} = 361 atm and T_{max} = 3036 K. At larger nozzle diameters, the working gas has time to flow into the chamber during 3–4 pulses. The time dependences of the coordinate and velocity of the piston for d_n = 3.5 mm are shown in Fig. 5.

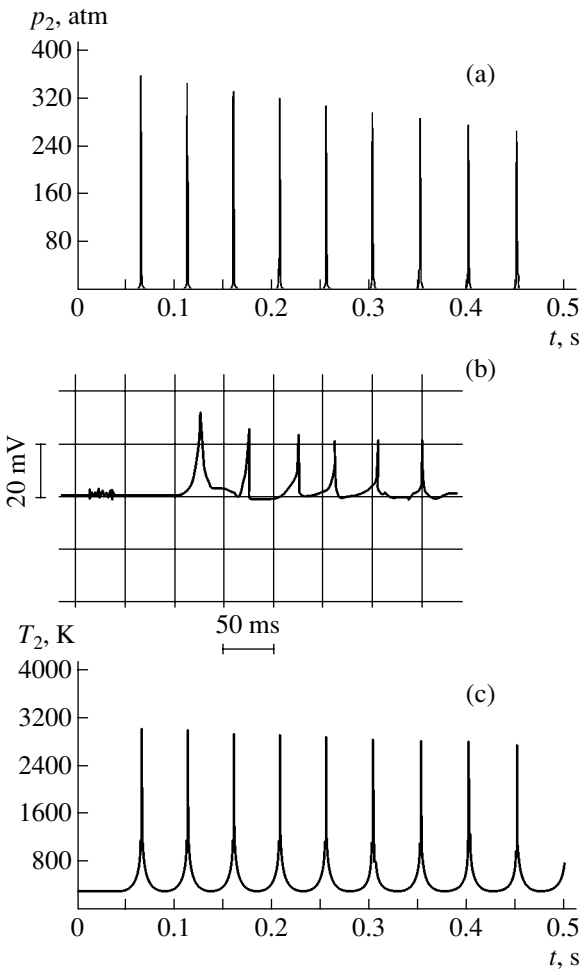

Fig. 3. Waveforms of the gas pressure (a) and temperature (c) calculated for d_n = 0 and evacuation down to $p_2 = 1.094 \times 10^4$ Pa and (b) the experimental pressure waveform measured under the same conditions (1 mV = 11.6 atm).

Let us choose the nozzle diameter so that the compression process consists of a single pulse. We also assume that F_{st} = 2500 N and the device is evacuated down to $p_2 = 1.094 \times 10^4$ Pa (see table).

The ultimate aim of gas compression in the plasmatron is to produce radiation energy, which is liberated when the temperature reaches fairly high values ($T \cong$

The influence of the nozzle diameter on the number of pulses *n* and on the gas parameters in the first pulse

No.	*d*, m	*n*	p_{max}, atm	T_{max}, K
1	0.001	$\gg 9$	361	3036
2	0.002	>9	381	3096
3	0.003	5	424	3182
4	0.004	3	486	3320
5	0.005	2	609	3561
6	0.006	1	822	3814

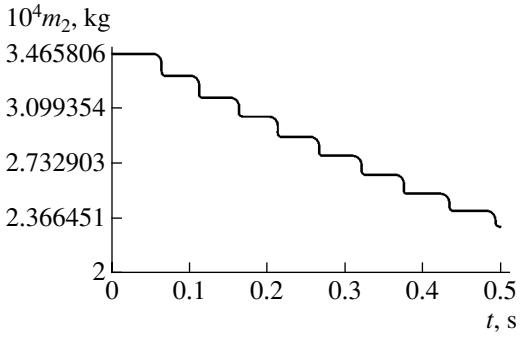

Fig. 4. Gas mass as a function of time for d_n = 1 mm for F_{st} = 2500 N and evacuation down to $p_2 = 1.094 \times 10^4$ Pa.

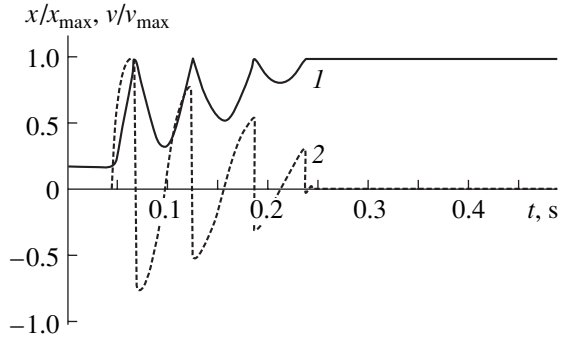

Fig. 5. Piston coordinate (*1*) and piston velocity (*2*) as functions of time for d_n = 3.5 mm. The maximum velocity is 57 m/s.

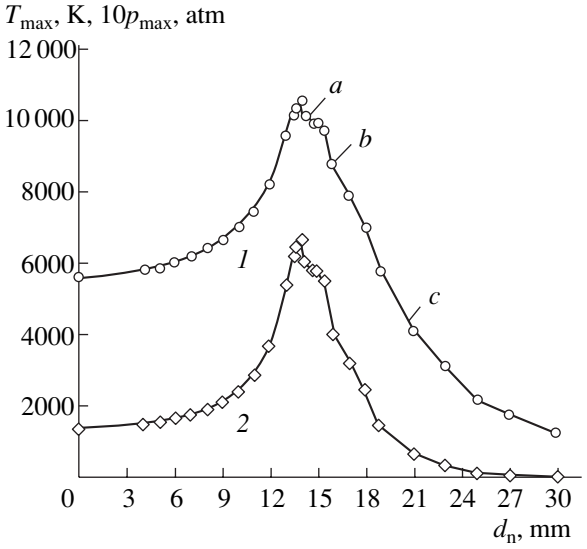

Fig. 6. Xenon temperature (*1*) and pressure (*2*) as functions of the plasmatron nozzle diameter d_n for F_{st} = 2500 N and evacuation down to $p_2 = 9.32 \times 10^3$ Pa.

10^4 K). However, attaining the temperature $T_{max} >$ 4000 K in air is rather problematic, because most of the energy is dissipated or is spent on the ionization of molecules. For this reason, noble gases (such as xenon and argon) are usually used as working gases in plasmatrons. Without evacuation, the maximum temperatures obtained in these device are still far from the temperatures requires for intense radiative heat exchange ($T >$ 6800 K for xenon).

Let us examine how the nozzle diameter affects the maximum temperature of xenon in the first pulse in the same device with the following initial parameters: $\gamma_2 =$ 1.67, μ_2 =0.131 kg/mol, and the radiation constants are $G' = 1.12 \times 10^{12}$ m^3/kg K and I = 140 602 K [7]. The device is evacuated down to $p_2 = 9.32 \times 10^3$ Pa. As d_n increases, the values of T_2 and p_2 in the first pulse increase (Fig. 6) until the nozzle diameter reaches a value corresponding to a single pulse. The temperature increases not as rapidly as the pressure does, which is explained by radiative losses.

As d_n increases further, a larger amount of the gas has time to flow into the chamber without being compressed; as a result, the compression process becomes inefficient. In the descending branch of the temperature curve, we can distinguish three segments. Segment *a* in Fig. 6 begins from the maximum of the curve and ends when surface radiative losses change to volume ones [7]. Since d_n here does not affect radiative losses, this segment of the curve has a relatively small slope. At segment *b*, volume radiative losses are predominant. These losses depend strongly on the device geometry and the pressure; as a result, this segment is the steepest. Finally, segment *c* corresponds to gas temperatures at which radiative heat exchange is absent. This segment has the smallest slope.

CONCLUSION

A mathematical model of a single-stage ballistic plasmatron has been developed. The model agrees well with the experimental data and allows one to quantitatively describe the compression process in the plasmatron. The model can be used to determine the optimal operating conditions, calculate the device parameters, and find ways of intensifying radiative heat exchange.

REFERENCES

1. J. A. Dowling, J. Shumsky, J. Eckerman, *et al.*, Appl. Phys. Lett. **12** (5), 184 (1968).
2. V. M. Shmelev, V. T. Volov, D. B. Volov, *et al.*, Zh. Tekh. Fiz. **68** (9), 67 (1998) [Tech. Phys. **43**, 1069 (1998)].
3. A. D. Margolin, N. Ya. Vasilik, V. M. Shmelev, *et al.*, in *Proceedings of the 1st All-Union Symposium on Radiation Plasma Dynamics, Moscow, 1989*, p. 33.
4. Yu. N. Ryabinin, *Gases at High Densities and Temperatures* (Moscow, 1959).
5. D. B. Volov, RF Patent No. 3419-V98, November 23, 1998.
6. S. V. Makarychev, G. D. Smekhov, and M. S. Yalovik, Izv. Akad. Nauk, Mekh. Zhidk. Gaza, No. 1, 155 (1992).
7. V. T. Volov, D. B. Volov, and Yu. L. Ratis, Zh. Vychisl. Mat. Mat. Fiz. **38**, 1919 (1998).
8. D. B. Volov, Candidate's Dissertation (Moscow, 1998).

Translated by E. Satunina

Technical Physics, Vol. 48, No. 5, 2003, pp. 557–562. Translated from Zhurnal Tekhnicheskoĭ Fiziki, Vol. 73, No. 5, 2003, pp. 35–40.

GAS DISCHARGES, PLASMA

Magnetohydrodynamic Instabilities of a Pinch Resonant Streamer Microwave Discharge

L. P. Grachev, I. I. Esakov, and K. V. Khodataev

State Unitary Enterprise Moscow Radiotechnical Institute, Russian Academy of Sciences, Moscow, 117519 Russia

e-mail: esakov@dataforce.net

Received September 19, 2002

Abstract—A pulsed freely localized resonant streamer microwave discharge in air and high-pressure hydrogen in the field of a linearly polarized standing electromagnetic wave in a two-mirror open cavity is investigated. The observed characteristic features of the discharge are treated as consequences of the sausage and wriggle instabilities of the plasma channel with a longitudinal microwave current contracted by its magnetic self-field.

INTRODUCTION

Pulsed freely localized spontaneous microwave gas discharges in quasi-optical traveling microwave beams have been studied actively [1–5]. In the focal region of such a beam, the electric field can be strong enough to provide breakdown at relatively high gas pressures p (e.g., at air pressures of up to $p \approx 0.2$ atm). At higher pressures (up to 1 atm and higher), this type of discharge was ignited by using a high-Q quasi-optical two-mirror open cavity in which a linearly polarized high-order longitudinal electromagnetic (EM) mode was excited [6–10].

Electrodeless discharge in atmospheric-pressure air under the above conditions was first observed in [6]. The discharge had the shape of a sole plasma channel with a bright central core. The channel was stretched along the electric field vector $\mathbf{E}_0$ of the initial microwave field. The results of these studies were published in more detail much later in [7]. It was found that the discharge developed from a seed plasmoid and grew along vector $\mathbf{E}_0$ due to the field amplification at the poles of the plasmoid; the characteristic time of discharge development was determined. It was supposed that a significant fraction of the EM energy accumulated in the cavity before breakdown was released in the core. The existence of the core was attributed to dissipation caused by the finite conductivity of the discharge channel.

The experimental results of [7] were confirmed in [8]. It was pointed out that the interaction between the discharge and the microwave field exhibited resonant features as the discharge length approached one-half of the field wavelength, $\lambda/2$. It was supposed that, at the final stage of the discharge development, the microwave pinch effect was responsible for the formation of a cumulative core. Further experiments on the time evolution of a discharge were carried out in [9]. It is shown that the discharge develops from a single free electron. Then, a small spherical plasmoid arises, which stretches along $\mathbf{E}_0$ in both directions from the point of origin due to the electrostatic interaction with the initial field. In this stage, the microwave discharge only slightly absorbs EM energy and, in many aspects, is similar to a streamer in a constant electric field. However, in contrast to the latter, both the current I in the microwave streamer and the effective cross section for the interaction between the discharge and the initial field increase resonantly as the streamer length approaches $\lambda/2$. As a result, a high-temperature core forms. In [9] (as well as in [7]), the existence of the core was related to dissipation in plasma, taking into account that the distribution of the current I along a resonant microwave streamer had a maximum in its central part. The doubts of the authors of [8, 9] on how to treat the final stage of the discharge development were mainly caused by the lack of experimental data because the discharge was rather difficult to diagnose. These difficulties are related to the large statistical scatter in the place and time of origin of the seed electron, the small size of the core, the significant distance not only from the nearest construction elements but also from the recording apparatus, and the fairly short durations of both the entire discharge and especially its final stage. These obstacles cause one to look for indirect verification of one or another version of the cumulative core formation.

In [10], this type of discharge was studied not only in air but also in hydrogen. Moreover, by that time, freely localized streamer microwave discharges in air and hydrogen were ignited in the field of a quasi-optical traveling microwave beam [11]. In a traveling wave, the initial streamer, which was stretched along $\mathbf{E}_0$, had a core in the case of hydrogen and had no core in air. In all the experiments, the core arose only when the initial gas pressure exceeded a certain threshold value and the corresponding amplitude of the EM field was larger than the breakdown amplitude E_{thres}. Estimates show

that, at EM field amplitudes close to E_{thres}, the magnetic pressure produced on the surface of the plasma channel by the longitudinal current I flowing through the channel begins to surpass the gas-kinetic pressure in the discharge channel. These experimental results indicate that the pinch effect plays a key role in the formation of a cumulative core.

In [10], two cores separated along the discharge axis were observed in the central region of a hydrogen discharge. This allows one to assume that a relatively large central region of the plasma channel, where the current I is the highest, undergoes self-contraction, whereas the cores arise due to sausage instability, which is characteristic of conventional Z-pinches [12]. Under certain conditions, a resonant microwave streamer may also undergo wriggle instability. This study is aimed at the experimental verification of these assumptions.

EXPERIMENTAL SETUP

A schematic of the experimental device is shown in Fig. 1. Microwave cavity *4* is placed in a high-pressure chamber. The cavity is fed by a quasi-optical microwave beam entering the chamber through a window that is transparent for microwave radiation. To control the field in the cavity, a fraction of the microwave energy escaping from the cavity is applied via a measurement circuit to an oscilloscope.

The beam feeding the cavity is a linearly polarized TEM wave with a central frequency (corresponding to the maximum beam power) of $f_0 = 7005$ MHz. The cavity is fed by single pulses with the duration $t_{pul} = 350$ μs. During a pulse, the field frequency is swept linearly at a rate of 2 kHz/μs within the range $f_0 \pm 350$ kHz.

The cavity is formed by two round coaxial spherical mirrors with a radius of curvature of 17.5 cm and diameter of 34 cm. The mirrors are made from a 0.2-cm-thick copper sheet. The cavity mirrors are coaxial with the microwave beam. The distance between the mirrors along the cavity axis is 29.6 cm. To tune to the central frequency f_0, this distance can be smoothly varied within the range 29.6 ± 0.5 cm. The mirror facing the microwave beam is perforated with holes and is partially transparent for microwave radiation. The cavity is excited at the simplest azimuthally symmetric mode with a transverse Gaussian profile; along the cavity axis, the microwave field forms a standing wave [13]. In the central focal plane, the distance from the cavity axis at which the field decreases e-fold is 3 cm. There are 13 variations in the field amplitude along the cavity axis; i.e., there is the field maximum in the center of cavity. For a Q factor of the cavity of 10^5, the maximum field amplitude in the focal plane was $E_{max} = 150$ kV/cm.

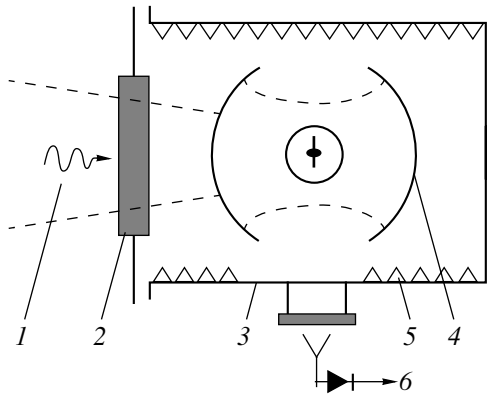

Fig. 1. Schematic of the experimental device: (*1*) microwave beam feeding the cavity, (*2*) microwave-transparent window, (*3*) sealed chamber, (*4*) open cavity, (*5*) coating absorbing microwave radiation, and (*6*) to an oscilloscope.

The cavity is placed along the axis of a cylindrical chamber with a diameter and length of about 50 cm. The inner surface of the chamber is covered with a coating absorbing microwave radiation. On one of the chamber ends, a 40-cm-diameter microwave-transparent quartz window is installed through which the microwave beam exciting the cavity enters the chamber. On the side surface of the chamber, against the cavity focal region, there are two mutually perpendicular 8-cm-diameter quartz windows that are transparent for optical and microwave radiation. The discharge is photographed through the window whose axis is perpendicular to both the chamber axis and the field vector $\mathbf{E}_0$. The chamber is designed so as to withstand a pressure of up to $p_{max} = 8$ atm. Before filling with air or hydrogen, the chamber is evacuated to a pressure of 0.1 torr.

The microwave energy escaping from the cavity over the mirror edges and leaving the chamber through the second side window is collected by a waveguide horn, and the rectified signal is applied to a storage oscilloscope. This signal is used to tune the cavity and monitor the time behavior of the field amplitude $E_0(t)$ in the cavity focal region.

EXPERIMENT

When tuning the cavity, the chamber was filled with air up to a pressure of $p_{max} = 8$ atm. At this pressure, the microwave field with the amplitude $E_{max} = 150$ kV/cm is insufficient for breakdown. For air, the breakdown field is $E_{cr}/p \approx 30$ kV/(cm atm) [14]; hence, for breakdown of air at a pressure of 8 atm, a field of $E_0 \geq 240$ kV is required, which is substantially higher than $E_{max} = 150$ kV/cm. Indeed, no breakdown of air occurred in the experiments at the pressure p_{max}. Provided that the cavity is tuned properly, a typical resonance curve with the full width $2\Delta f = 70$ kHz at the level of $1/\sqrt{2}$ (which corresponds to $Q = 10^5$) is displayed on the oscilloscope screen.

First, a series of reference experiments in which the chamber was filled with air at a pressure of $p \geq 1$ atm was carried out. These experiments gave important and somewhat surprising results.

Breakdown of air occurred in the focal plane of the cavity at pressures of no higher than 3 atm, which was less than the expected value, 5 atm. This phenomenon (which, however, was not thoroughly studied in these experiments) was most likely related to a small number of free electrons in air under natural conditions [15].

In the pressure range $1 \le p \le 3$ atm, breakdown may or may not occur during a microwave pulse. In the case of breakdown, only a part of the rising segment of the resonance curve up to the breakdown field $E_0 = E_{br}$ was observed on the oscilloscope screen; then, the signal sharply, in a time less than a fraction of a microsecond, dropped to zero. At a fixed pressure, the E_{br} value varied appreciably in successive pulses, being in the range $E_{cr} < E_{br} < E_{max}$ [15]. Hence, at a fixed pressure, the ratio of the breakdown field to the critical field, $\Psi = E_{br}/E_{cr}$, differed substantially from pulse to pulse.

At pressures of $1 \le p < 1.5$ atm, a known type of discharge in air was observed [10]: at E_{br} slightly higher than E_{cr}, the discharge channel was stretched along $\mathbf{E}_0$ and had no central core, whereas at higher Ψ, a core appeared in the channel.

At $p \ge 1.5$ atm, the discharge can occasionally have two cores, as is shown in Fig. 2a, which corresponds to $p = 1.5$ atm. Previously, this phenomenon was observed only in hydrogen [10]. The integral photographs shown in Figs. 2 and 3 were taken in a dark room with an exposure much longer than the discharge glow duration. In the figures, the cavity axis is horizontal and the vector $\mathbf{E}_0$ is vertical. The length of the plasma channel shown in Fig. 2a ($2l = 1.2$–1.3 cm) can serve as a typical scale. This length was estimated by using a control photograph of the construction elements located near the central region of the cavity; the control photograph was taken at the same viewing angle and distance as the photographs of the discharge itself.

The length $2l$ obtained from Fig. 2a is about one-half of the resonance length $\lambda/2 \approx 2$ cm. This fact reflects the discharge physics. In the streamer stage, the discharge only slightly absorbs microwave energy, and only the discharge ends glow intensely. They move along $\mathbf{E}_0$ with an exponentially increasing speed, which attains 10^8 cm/s [9]. It is most likely that this stage is not captured on the photographs at all. The central region of the plasma channel begins glowing intensely only in the resonant stage, when the current I substantially increases there. The self-contraction of this region leads to an extra release of microwave energy, which additionally increases the glow intensity. As a result, the integral glow of the discharge channel in an optical range varies along the channel by several orders of magnitude, so that the photographs capture only the discharge central region. The same is true for any gas. Indeed, in all the experiments described below, both in air and hydrogen, the discharge length $2l$ was approximately the same (1.2–1.4 cm) regardless of the Ψ value.

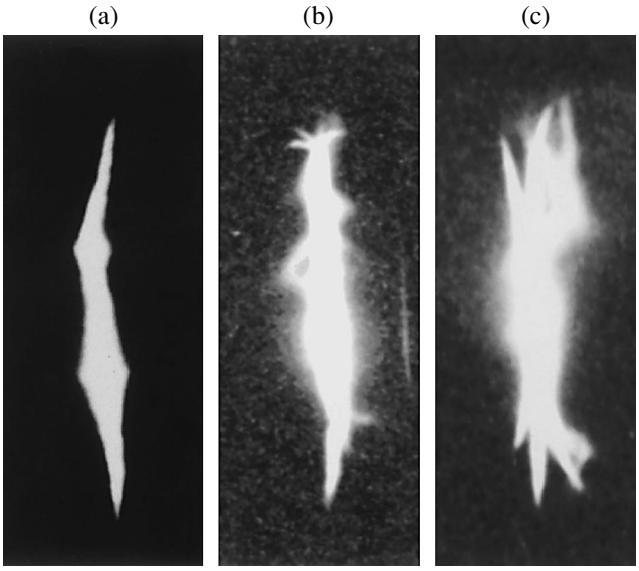

Fig. 2. Microwave discharge in air at p = (a) 1.5, (b) 2.5, and (c) 3 atm.

In Fig. 2a, the plasma channel diameter is equal to $2a \approx 6 \times 10^{-2}$ cm. It should be noted that, taking into account the integral nature of photorecording, this corresponds to the maximum value of the channel diameter in the course of discharge evolution.

At $p \ge 2.5$ atm, the discharge in air begins to exhibit a wriggle instability. Figure 2b shows a photograph of the discharge at $p = 2.5$ atm. The discharge central region, in which the core is usually located, is overexposed, and its structure is hardly resolvable. This indicates a significant excitation of air inside this region. The discharge channel is a source of intense ionizing radiation [16, 17], which excites air around the channel. Air is a rather complicated molecular gas, which, being excited, emits radiation in a wide spectral range. In the upper part of the channel, one can see wriggles with the characteristic wavelength of transverse perturbations $\Lambda \approx 0.25$ cm and the maximum displacement amplitude $A_{max} \approx 0.09$ cm.

At higher pressures, the discharge is blurred over almost its entire length, which does not allow us to examine its inner structure. It can only be seen in Fig. 2c, which shows the discharge photograph at $p =$ 3 atm, that the structure is rather complicated.

Most of the experiments were carried out in hydrogen, in which, as was expected, breakdown occurred within the entire pressure range $1 \le p \le 8$ atm. Indeed, for hydrogen, $E_{cr}/p = 10$ kV/(cm atm) [14]; hence, at $p_{max} = 8$ atm, the critical field is $E_{cr} = 80$ kV/cm $< E_{max}$. As in the case of air, breakdown in hydrogen occurred in the focal region and was irregular in character (i.e., during a pulse, breakdown may or may not occur). In successive pulses, the measured breakdown field E_{br} ranged from E_{cr} (corresponding to a given pressure) to

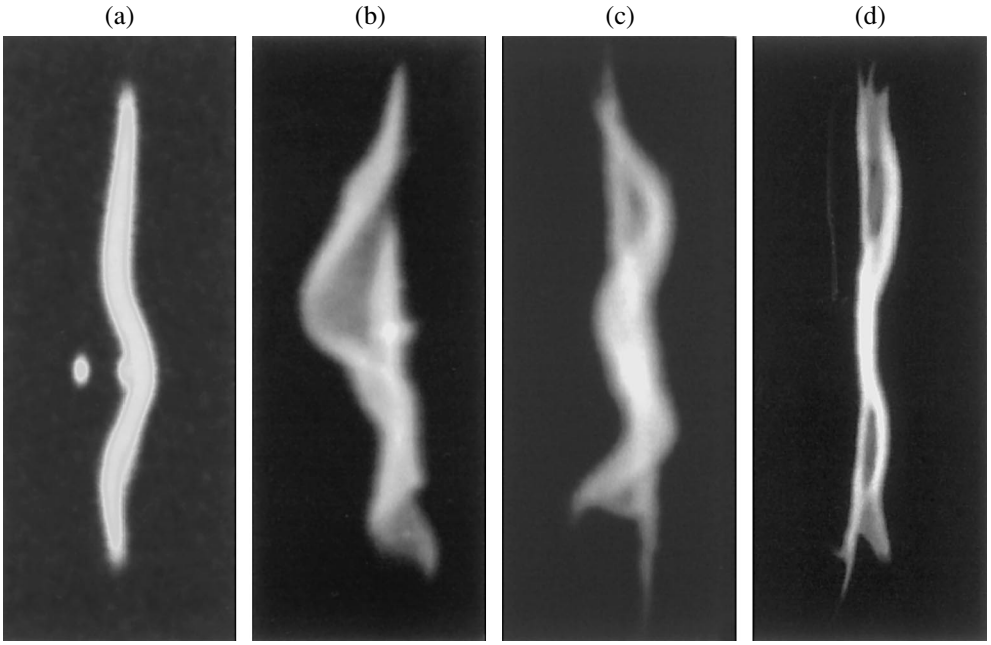

Fig. 3. Microwave discharge in hydrogen at p = (a) 2.5, (b) 4, (c) 5, and (d) 8 atm.

E_{max}. Thus, at a fixed hydrogen pressure, breakdown in different pulses occurred at different Ψ, as was the case with air.

In the case of breakdown in hydrogen at pressures of $1 \le p \le 3$ atm, an ordinary resonant streamer microwave discharge with one or two cores was observed. In almost any microwave pulse, a discharge in hydrogen at relatively low pressures develops from a few spatially separated centers. Figure 3a shows a photograph of the discharge at $p = 2.5$ atm. One can see three isolated discharge regions. One of them has developed to the full length, whereas the other two are in an embryonic state. The fields induced by the discharge regions affect each other. As a result, the developed channel bypasses the other discharge centers and inhibits their development.

At $p \ge 3$ atm, a discharge in hydrogen becomes unstable against wriggle perturbations. Figure 3b shows a photograph of the discharge at $p = 4$ atm. One can see two overlapped discharge channels developed from two seed centers. The channels are located in the same field antinode but are separated in depth. The shorter channel is straight and has a pronounced core, and the longer channel is curved. The characteristic wavelength of wriggles is $\Lambda \approx 0.6$ cm and their maximum amplitude is $A_{max} \approx 0.15$ cm. It can be seen that the channel was originally straight and then bowed down. The region under the wriggles turned out to be exposed as the wriggle amplitude progressively increased during the instability. At this pressure, both the number of the discharge channels and the wavy shape of the main channel can vary from pulse to pulse. Such a variability is characteristic of instabilities, because the initial perturbation, as well as the final shape of the perturbed channel, is not predetermined.

Figure 3c shows a photograph of the discharge at $p = 5$ atm. One can clearly see an original straight discharge channel and its final curved position with an exposed region under the wriggles. The diameters of the original and wriggled channels estimated by the photograph are nearly the same ($2a \le 3.2 \times 10^{-2}$ cm), and the wriggle wavelength and amplitude are $\Lambda \approx 0.4$ cm and $A_{max} \approx 8.4 \times 10^{-2}$ cm, respectively. Again, at this pressure, the discharge shape varies significantly from pulse to pulse, whereas the values of $2a$, Λ, and A_{max} remain nearly the same.

The wriggle wavelength Λ decreases as the pressure increases to p = 6–7 atm. A further increase in p results in an increase in Λ.

At $p \ge$ 5–6 atm, the probability of discharge development from several centers significantly decreases.

As an illustration, Fig. 3d shows a typical discharge at $p_{max} = 8$ atm. It can be seen that, at the final position, the discharge channel is wriggled over almost its entire length $2l \approx 1.3$ cm. This confirms the above assumption that, under the experimental conditions, only the bright part of the discharge, where the current I is high, is seen in the photographs, whereas its dim ends with a length of about 0.4 cm are not seen at all.

DISCUSSION OF THE RESULTS

The experiments revealed two important circumstances. First, the observed large-scale instabilities have a threshold with respect to the gas pressure. In

hydrogen, this threshold is about 3 atm. Second, the development of the instability is limited by the streamer lifetime, which is no longer than 10 ns [7–9]. Both of these circumstances can be interpreted based on the assumption that the instabilities observed are hydrodynamic in nature.

Estimates show that the ratio of the magnetic field pressure produced by the streamer current at the instant of resonance to the plasma pressure in the channel increases with increasing initial gas pressure and can become more than unity at $p > 1.5$–2.0 atm. Numerical simulations performed in the framework of a phenomenological model at hydrogen pressures of several atmospheres revealed the strong compression of a resonant microwave streamer discharge by the averaged magnetic pressure [18]. Hence, it is natural to expect that, at high pressures, magnetohydrodynamic effects, in particular, large-scale instabilities, will manifest themselves more explicitly.

To estimate the growth rates of magnetohydrodynamic instabilities, it is natural to employ the theoretical concepts developed for an ordinary linear Z-pinch (see, e.g., [12, 19–22]) and use a conception of the magnetic pressure averaged over the microwave field period.

According to the above theoretical studies, when the plasma pressure is balanced by the magnetic pressure, a cylindrical discharge with a longitudinal current is unstable against large-scale perturbations, such as constrictions and wriggles. The growth rates Γ of these instabilities are proportional to the magnetic field H_2 on the discharge surface and are inversely proportional to the square root of the plasma density ρ. For a microwave discharge, the r.m.s. magnetic field should be taken as the field H. In [21], expressions for the growth rate Γ were obtained for the case of an infinite skinned cylindrical pinch with a remote screen, homogeneous ρ distribution, and zero longitudinal magnetic field in vacuum. In our experiments, the microwave skin depth is of the same order of magnitude as the discharge radius a, and the distribution of ρ in the discharge is far from homogeneous. Hence, the above expressions are applicable only in the long-wavelength limit, $ka \le 1$, where $k = 2\pi/\Lambda$ is the perturbation wavenumber. For both types of perturbations, we obtain the following estimate for the instability growth rate:

$$\Gamma \cong \sqrt{\mu_0/\rho}\,Hk, \tag{1}$$

where $\mu_0 = 4\pi \times 10^{-7}$ H/m.

At the instant of resonance, the current I in a half-wave thin vibrator is distributed by the cosine law, whereas its maximum value is limited by the radiation resistance $R_w = 73\ \Omega$,

$$I = \lambda E_0/(\pi R_w). \tag{2}$$

Hence, the magnetic field on the discharge surface in its middle part is equal to

$$H = \lambda E_0/(2\pi^2 a R_w). \tag{3}$$

Taking into account Eq. (3), we obtain the instability growth rate

$$\Gamma(p) \cong \sqrt{\mu_0/\rho(p)}\lambda E_0(p)k/(2\pi^2 a R_w). \tag{4}$$

A spontaneous microwave discharge is feasible only when the amplitude of the external field exceeds the critical breakdown field $E_{cr}(p)$, which is proportional to the initial gas pressure p. Hence, in Eq. (4), we should assume that $E_0 \ge E_{cr}(p)$. Without allowance for possible compression, the gas mass density does not exceed its initial value, which is also proportional to the initial pressure.

The measured discharge radius as a function of air and hydrogen pressures in the range 70–760 torr [18] can be roughly approximated as

$$a(p) \approx 0.015/p, \text{ cm}, \tag{5}$$

where p is in atmospheres.

Extrapolating Eq. (5) to the range $p > 1$ atm, we have from Eqs. (4) and (5) that, for $\lambda = 4.3$ cm and $ka = 1$, the growth rate for the case of hydrogen is equal to

$$\Gamma(p) \approx 1.6 \times 10^7 p^{2.5}, \text{ s}^{-1}. \tag{6}$$

The measurements show that the resonant current exists in a streamer for a few tens of nanoseconds [8, 18]. Setting $\Gamma > 10^8\ \text{s}^{-1}$, we obtain the lower pressure threshold for the onset of instability:

$$p > (10^8/1.6 \times 10^7)^{(1/2.5)} \approx 3.3 \text{ atm}. \tag{7}$$

The estimated threshold pressure satisfactorily agrees with the experimental data. This allows us to assume with great confidence that the observed large-scale perturbations are the nonlinear stage of a magnetohydrodynamic instability of the discharge channel in which the plasma pressure is balanced by the averaged magnetic pressure produced by the microwave current flowing in a resonant streamer.

We note that the use of theoretical concepts developed for ordinary Z-pinches is rather limited because pinches differ from microwave discharges in many aspects. The main differences are the absence of a conducting envelope and ends, the presence of a dense surrounding gas, the fact that microwave wavelength is comparable with the discharge length and thus the current is nonuniform along the discharge, magnetic pressure pulsations, and so on. To develop an adequate theory of the process under study, it is necessary to take into consideration all these features.

CONCLUSION

Electrodeless microwave discharges in air at pressures of $1 < p \le 3$ atm and hydrogen at pressures of $p \le 8$ atm have been investigated experimentally. Break-

down occurs in the electric field of a linearly polarized standing EM wave in the focus of a quasi-optical high-Q two-mirror open cavity. The cavity is excited by microwave radiation with the wavelength $\lambda = 4.3$ cm. Breakdown leads to the development of a resonant streamer microwave discharge. The discharge is freely localized and stays apart from the nearest construction elements by no less than ten centimeters. In the final stage of the discharge, its central region with a length of 1.2–1.4 cm and diameter of several hundredth of a centimeter undergoes both sausage instability and clearly defined wriggle instability. In air, the wriggle instability develops at pressures of $p \geq 2.5$ atm, and, in hydrogen, it develops at pressures of $p \geq 3$ atm. The presence of large-scale instabilities unambiguously indicates the decisive role of the averaged magnetic field pressure produced by the resonant microwave current flowing in the streamer. These instabilities can develop only under the conditions of discharge self-contraction caused by the magnetic pressure. Thus, the processes observed should be classified as a microwave pinch effect.

The microwave pinch effect is of interest, first of all, as a manifestation of a known phenomenon under completely different conditions. The specific features of a microwave pinch allow one to consider it as a possible pulsed source of hard X-ray or neutron radiation.

REFERENCES

1. *High-Frequency Discharges in Wave Fields*, Ed. by A. G. Litvak (Inst. Prikl. Fiz. Akad. Nauk SSSR, Gorki, 1988).
2. A. S. Zarin, A. A. Kuzovnikov, and V. M. Shibkov, *Self-Localized Microwave Discharge in Air* (Neft' i Gaz, Moscow, 1996).
3. N. D. Borisov, A. V. Gurevich, and G. M. Milikh, *Artificial Ionized Region in Atmosphere* (Inst. Zemn. Magn., Ionos., Rasprostr. Radiovoln, Moscow, 1986).
4. K. V. Khodataev, in *Proceedings of the 20th International Conference on Phenomena in Ionized Gases, 1991*, p. 207.
5. K. V. Khodataev, Khim. Fiz. **12**, 303 (1993).
6. R. F. Avramenko, L. P. Grachev, and V. I. Nikolaeva, in *Electropuncture and Problems of Information–Energetic Regulation of Human Activity*, Ed. by V. G. Nikiforov and V. N. Pushkin (Inst. Ékonom. Nauch.-Tekh. Inform. Ugol'n. Prom., Moscow, 1976), p. 197.
7. R. F. Avramenko, G. M. Batanov, and V. I. Nikolaeva, in *A Quantum Key to Open the Future* (Khimiya, Moscow, 2000), p. 197.
8. L. P. Grachev, I. I. Esakov, G. I. Mishin, and K. V. Khodataev, Preprint No. 1577 (Ioffe Physicotechnical Institute, Russian Academy of Sciences, St. Petersburg, 1992).
9. L. P. Grachev, I. I. Esakov, G. I. Mishin, and K. V. Khodataev, Zh. Tekh. Fiz. **64** (2), 26 (1994) [Tech. Phys. **39**, 130 (1994)].
10. V. S. Barashenkov, L. P. Grachev, I. I. Esakov, *et al.*, Zh. Tekh. Fiz. **70** (11), 31 (2000) [Tech. Phys. **45**, 1406 (2000)].
11. L. P. Grachev, I. I. Esakov, G. I. Mishin, and K. V. Khodataev, Zh. Tekh. Fiz. **66** (7), 32 (1996) [Tech. Phys. **41**, 652 (1996)].
12. S. Yu. Luk'yanov and N. G. Koval'skiĭ, *Hot Plasma and Controlled Nuclear Fusion* (Mosk. Inzh.-Fiz. Inst., Moscow, 1977).
13. L. P. Grachev, I. I. Esakov, S. G. Malyk, and K. V. Khodataev, Zh. Tekh. Fiz. **71** (6), 66 (2001) [Tech. Phys. **46**, 709 (2001)].
14. A. MacDonald, *Microwave Breakdown in Gases* (Wiley, New York, 1966; Mir, Moscow, 1969).
15. V. S. Barashenkov, L. P. Grachev, I. I. Esakov, *et al.*, Zh. Tekh. Fiz. **70** (10), 34 (2000) [Tech. Phys. **45**, 1265 (2000)].
16. N. A. Bogatov, S. V. Golubev, and V. G. Zorin, Pis'ma Zh. Tekh. Fiz. **9**, 888 (1983) [Sov. Tech. Phys. Lett. **9**, 382 (1983)].
17. N. A. Bogatov, S. V. Golubev, and V. G. Zorin, Fiz. Plazmy **12**, 1369 (1986) [Sov. J. Plasma Phys. **12**, 793 (1986)].
18. L. P. Grachev, I. I. Esakov, and K. V. Khodataev, in *Proceedings of the International Workshop "Strong Microwaves in Plasmas," Nizhni Novgorod, 2000*, Vol. 1, p. 291.
19. A. Spitzer, *Physics of Fully Ionized Gases* (Interscience, New York, 1962; Mir, Moscow, 1965).
20. K. D. Sinel'nikov and B. T. Rutkevich, *Course of Plasma Physics* (Khar'kov, 1964).
21. B. A. Trubnikov, *Plasma Theory* (Énergoizdat, Moscow, 1998).
22. V. S. Imshennik and N. A. Bobrova, *Dynamics of Collisional Plasmas* (Énergoatomizdat, Moscow, 1997).

Translated by N. Ustinovskiĭ

Technical Physics, Vol. 48, No. 5, 2003, pp. 563–568. Translated from Zhurnal Tekhnicheskoĭ Fiziki, Vol. 73, No. 5, 2003, pp. 41–45.

GAS DISCHARGES, PLASMA

Cyclotron Drift along the Boundary between Regions of Differing Gyroradii

I. D. Dubinova

All-Russia Research Institute of Experimental Physics, Russian Federal Nuclear Center, Sarov, Nizhni Novgorod oblast, 607188 Russia

e-mail: dubinov@ntc.vniief.ru

Received July 25, 2002; in final form, October 30, 2002

Abstract—The cyclotron drift of charged particles along the boundary between regions of differing gyroradii is considered. Expressions for the drift velocity and drift current along a straight boundary, as well as for the drift velocity along a curvilinear boundary, are derived. The proportion between the parts into which the drift current divides along a branched boundary is estimated using a T-shaped boundary as an example. © *2003 MAIK "Nauka/Interperiodica".*

INTRODUCTION

It is well known that, in a plasma or a solid body placed in a magnetic field, the trajectories of the classical charged particles that move near a rigid wall and are specularly reflected from it are arcs of circles. In moving along the wall, the particles undergo multiple reflections, thereby creating an electric current of a drift nature [1, 2].

The drift current also arises at a metal–superconductor boundary in a magnetic field. In this case, the reflection law is different: when a charged particle is reflected, its total momentum reverses direction (i.e., the particle undergoes a so-called Andreev reflection) [3–5]. Because of the peculiar shape of the particle trajectories, the classical expression for the drift current in the case of Andreev reflections differs from that in the case of specular reflections.

These two examples refer to a class of phenomena that can be characterized by the common term "cyclotron drift along a boundary" or "cyclotron billiard." This paper is aimed at studying another example of cyclotron drift, specifically, that along the boundary between regions of differing gyroradii.

There are several physical reasons why the gyroradii of charged particles in adjoining regions may be different. Thus, they may be different on both sides of the surface at which the magnetic field parallel to it undergoes a jump. Such a structure of the magnetic field can arise near the current sheets in a plasma [6]; in this case, the sections of the sheets by a plane perpendicular to the field are just the boundaries in question. That cyclotron drift along a jump in the magnetic field is possible was pointed out in [6, 7], in which some features of the drift, such as the rounding ("wetting") of a boundary with breaks by particles and the division of the drift current into parts along a branched boundary, were analyzed at a qualitative level.

Cyclotron drift can also occur along the boundary between two semiconductors in which the effective electron masses are different. As may be seen from the list of the effective masses of the carriers in semiconductors [4], such a drift is comparatively easy to initiate by choosing materials with the longest possible mean free paths. There may be other physical examples of cyclotron drift along the boundary between regions of differing gyroradii.

The objective of this study is to calculate the drift current and estimate the proportion between the parts into which the drift current divides along a branched boundary.

In different physical situations, the parameters of the particles that cross the boundary between regions of differing gyroradii (which will be called simply "the boundary" for brevity) may change in different ways. For the boundary formed by a jump in the magnetic field in a plasma, the velocity and momentum vectors of a particle, as well as its energy, are conserved. In contrast, for the boundary between semiconductors, some of these parameters may not be conserved: the velocity may change in both magnitude and direction and the energy may be changed by the contact potential difference at the boundary and/or due to the excitation of transient phonons. Of course, these factors contribute to the resulting relationships for the current, but, in many situations, the final conclusions turn out to be qualitatively similar. In [8], it was also shown that, when the effective electron masses in adjoining semiconductors differ only slightly, the probability for the electrons to cross the boundary without scattering is close to unity. This circumstance allows us to exclude from consideration the particle dynamics when the boundary is crossed and to assume that the gyroradius of a particle in the ith region is equal to r_i.

1063-7842/03/4805-0563$24.00

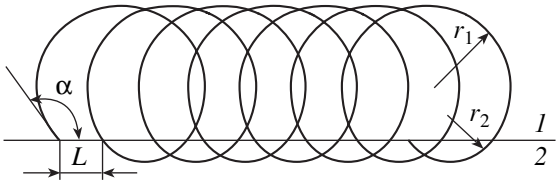

Fig. 1. Drift trajectory of a charged particle along a plane boundary between regions *1* and *2* with differing gyroradii. The magnetic field is perpendicular to the plane of the figure.

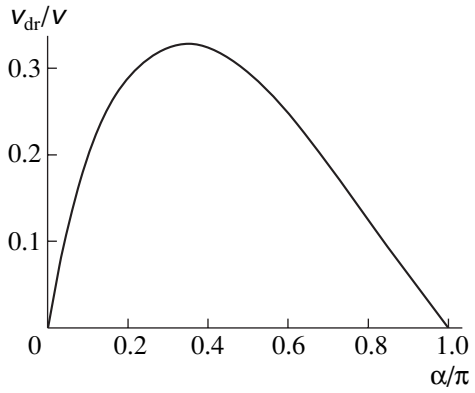

Fig. 2. Reduced drift velocity of a particle moving along a plane boundary vs. angle at which the particle trajectory intersects the boundary.

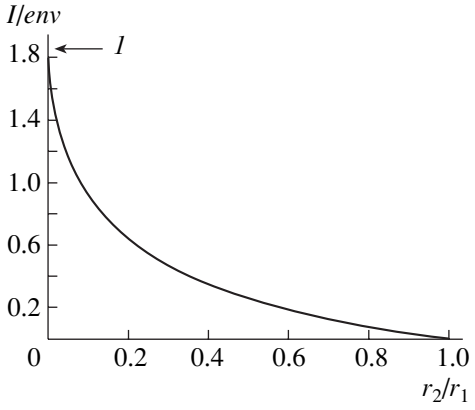

Fig. 3. Reduced drift current along a plane boundary vs. ratio of the gyroradii in the adjoining regions. The arrow indicates the maximum drift current (*1*) in the case of specular reflections.

We also make two additional assumptions. First, the velocities of all particles are the same and are equal to v. In deriving expressions for the currents, this assumption can easily be generalized to a particular particle velocity distribution function by performing the corresponding integration. Second, a charged particle moves without scattering both when crossing the boundary and at a distance from it. This assumption is valid under the condition $\omega_C\tau \gg 1$ (where ω_C is the gyrofrequency and τ is the mean free time of the particle), which indicates that the particle completes many Larmor revolutions without being scattered and which is equivalent to the condition $\tan\vartheta = \nu B \gg 1$, where ϑ is the Hall angle, ν is the mobility, and B is the magnetic field strength. The latter condition is known to hold, e.g., for an *n*-type InSb semiconductor in a magnetic field of 5 T or higher [9].

DRIFT ALONG A STRAIGHT AND A CURVED BOUNDARY

We consider two regions that are separated by a straight boundary and in which the gyroradii are equal to r_1 and r_2 (Fig. 1). For definiteness, we set $r_1 > r_2$. We will find the drift velocity of a particle along the boundary, assuming that the tangent to the particle trajectory at the point where it enters region *1* makes an angle α with the boundary. First, we determine the distance L that the guiding center of the particle travels along the boundary during one period of gyration:

$$L = 2(r_1 - r_2)\sin\alpha. \tag{1}$$

If the particle velocities in both regions are the same and are equal to v, then the period of gyration T is

$$T = \frac{2\alpha r_1 - (2\pi - 2\alpha)r_2}{v}. \tag{2}$$

It should be stressed that the period T is not equal to the period of gyration of a free particle far from the boundary. As a result, the sought expression for the drift velocity can be written as

$$v_{dr} = v\frac{(r_1 - r_2)\sin\alpha}{\alpha r_1 - (\pi - \alpha)r_2}. \tag{3}$$

The dependence of the drift velocity on the angle α is shown graphically in Fig. 2. The dependence is seen to be peaked: as the ratio r_1/r_2 increases, the peak shifts toward smaller α values.

We assume that, at each point at the boundary, the particles are distributed uniformly in the angle α over the closed interval $[0, \pi]$ and that the number of particles per unit length of the boundary is n. Under these assumptions, we can obtain the following expression for the drift current:

$$I = \int_0^\pi env_{dr}(\alpha)d\alpha = env\frac{r_1 - r_2}{r_1 + r_2}\left[\mathrm{Si}\frac{r_1}{\rho}\cos\frac{r_2}{\rho} + \mathrm{Ci}\frac{r_1}{\rho}\sin\frac{r_2}{\rho} + \mathrm{Si}\frac{r_2}{\rho}\cos\frac{r_2}{\rho} - \mathrm{Ci}\frac{r_2}{\rho}\sin\frac{r_2}{\rho}\right], \tag{4}$$

where Si and Ci are the integral sine and cosine, respectively, and $\rho = (r_1 + r_2)/\pi$.

It is easy to see that, for $r_1 = r_2$, the drift current vanishes and, for $r_2 \longrightarrow 0$, expression (4) reduces to the

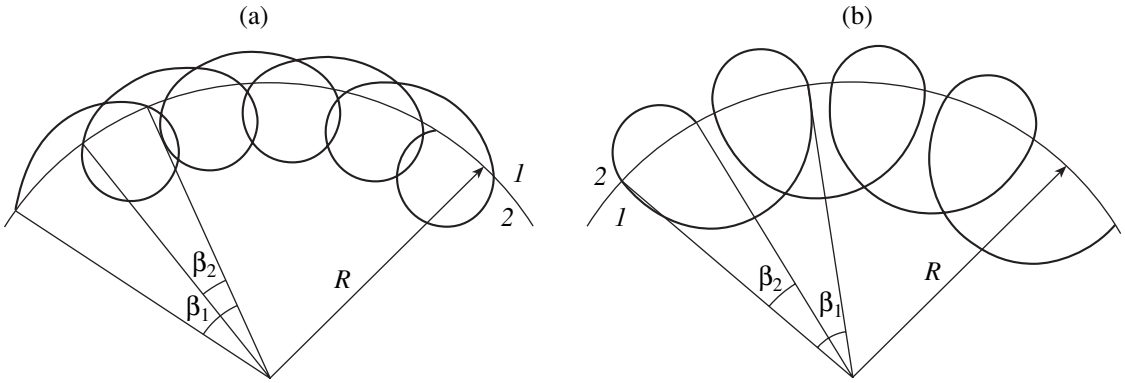

Fig. 4. Drift trajectories of a charged particle along a curvilinear boundary between regions *1* and *2* with differing gyroradii in the (a) diamagnetic and (b) paramagnetic cases. The magnetic field is perpendicular to the plane of the figure.

expression for the drift current in the case of specular reflections:

$$I_{SR} = env\mathrm{Si}(\pi) \approx 1.852\ env. \quad (5)$$

Figure 3 shows a plot of the drift current versus the ratio r_2/r_1 on the closed interval [0, 1], whose ends correspond to specular reflections ($r_2 \longrightarrow 0$) and to the absence of the drift current ($r_1 = r_2$).

Now, we consider the drift of charged particles along a curved boundary of radius $R > r_1 > r_2$. To do this, we must analyze two possible cases: the gyroradius is larger (r_1) on the outer side of a circle of radius R (Fig. 4a) and the gyroradius is larger on the inner side of the circle (Fig. 4b). In the first case, the drift current produces a diamagnetic effect, whereas in the second case, it produces a paramagnetic effect.

An expression for the drift velocity can be derived in a way analogous to that for a straight boundary. For this reason, we omit the derivation and give only the final expression, which is valid for both diamagnetic and paramagnetic cases:

$$v_{dr} = v\frac{R(\beta_1 - \beta_2)}{r_1(\alpha + \beta_1) + r_2(\pi - \alpha - \beta_2)}, \quad (6)$$

where α is the angle between the tangents to the boundary and to the trajectory at the point of their intersection and β_i are the angles at which the arcs between the points of successive intersections of the boundary by the trajectory passing in the *i*th region are seen from the center of curvature of the boundary,

$$\tan\beta_i = \frac{r_1}{R}\frac{\sin\alpha}{[1 - (r_i/R)\cos\alpha]}. \quad (7)$$

From expression (6), we can readily see that the direction of the drift is determined by the sign of the difference of the angles in the numerator, $\beta_1 - \beta_2$. It is also easily seen that, for $R \longrightarrow \infty$, expression (6) passes over to expression (3). Figure 5 shows a representative dependence of the drift velocity on the radius of curvature R of the boundary for fixed values of the parameters α and r_i. As R increases, the drift velocity decreases and approaches the steady-state value given by formula (3). Formally, the dependence has a maximum at $R \gtrsim r_1$; but, as R approaches r_1 from above, the phenomenon of drift as well as the magnitude and direction of the drift velocity all become physically meaningless. That is why the dependence to the left of the maximum is shown by the dashed curve.

In the general case, the currents resulting from the drift considered above are steady and undamped, provided that there is no friction between the moving current carriers. It is important that the boundary be either closed or infinite.

DIVISION OF THE DRIFT CURRENT INTO PARTS ALONG A BRANCHED BOUNDARY

Along the boundaries that have two, three, or more branches, the drift current divides into parts, the pro-

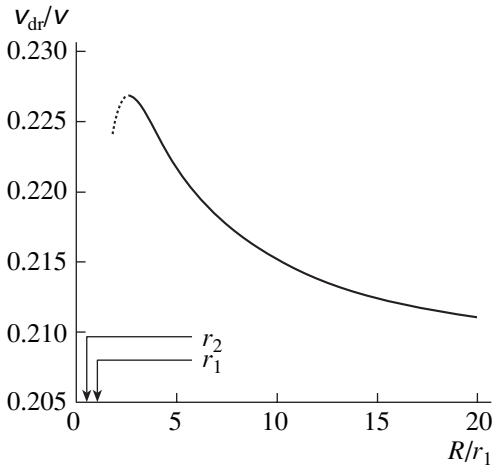

Fig. 5. Reduced drift velocity (6) of a particle moving along a curvilinear boundary vs. radius of curvature of the boundary for $\alpha = \pi/2$. The arrows indicate the values of the gyroradii r_1 and r_2.

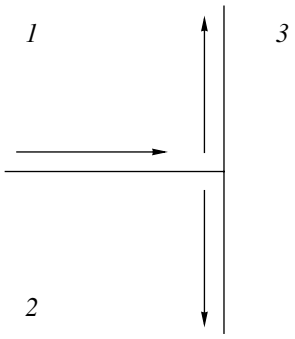

Fig. 6. Geometry of a T-shaped boundary separating regions *1*, *2*, and *3*. The arrows indicate the directions of the drift current.

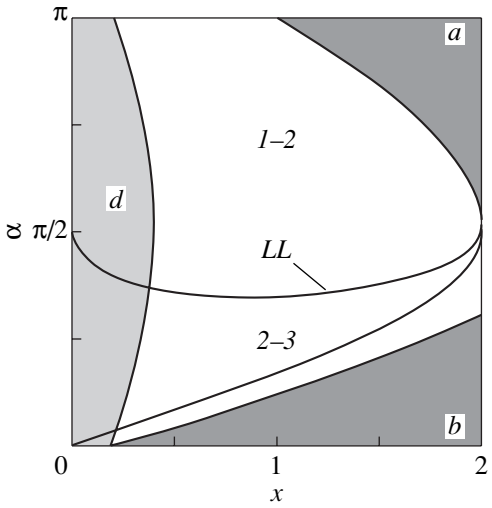

Fig. 7. Rectangle Ξ of the initial parameters of the trajectory of a charged particle. Portions *a*, *b*, and *d* refer to the trajectories shown in Figs. 8a, 8b, and 8d, respectively. Portions *1–2* and *2–3* refer to the particle trajectories that escape along the corresponding branches of the boundary. The line on which function (11) is equal to μ_2 is marked by *LL*.

portion between which depends both on the relationship between the gyroradii in different regions and on the geometry of the boundary. As an example, we calculate the proportion between the parts into which the drift current divides along a *T*-shaped boundary (Fig. 6).

For definiteness, we set $r_1 > r_2 > r_3$. In this case, the drift current flowing along the branch *1–3* divides between the branches *1–2* and *2–3* in accordance with Kirchhoff's law.

We consider all trajectories in region *1* that originate from the branch *1–3* and whose initial angle α and initial coordinate *l* span a rectangle Ξ, the base and height of which are closed intervals $x = l/r_1 \in [0, 2]$ and $\alpha \in [0, \pi]$ (Fig. 7).

Let us calculate the ratio of the number of trajectories that escape along the branch *1–2* to the number of all possible trajectories. In this case, the proportion sought is equal to the ratio of the areas of those portions in the rectangle Ξ that correspond to the trajectories escaping along different branches of the boundary. Further analysis will be aimed exclusively at determining the boundaries of these portions.

First, in the rectangle Ξ, we should eliminate from consideration the portions corresponding to the trajectories that cross the boundary before reaching the branches; otherwise we would take into account such trajectories two or even three times, because they inevitably reach the branches after several crossings of the boundary (Figs. 8a, 8b).

From Figs. 8a and 8b, we can see that, for acute and obtuse initial angles α, the boundaries of the eliminated portions should be determined by different formulas:

$$x = \begin{cases} 2\sin\alpha & \text{for} \quad 0 < \alpha < \pi/2 \\ 1 + \sin\alpha & \text{for} \quad \pi/2 < \alpha < \pi. \end{cases} \tag{8}$$

However, in order not to eliminate the trajectories that originate at certain acute initial angles α and immediately escape along branch *2–3* of the boundary (Fig. 8c), we should take into account the part of the lower eliminated portion corresponding to the trajectories that reach branch *2–3* immediately after they have crossed branch *1–3*. This part is bounded by two curves, one of which is described by Eqs. (8) and the other is given by the equation

$$x = \mu_3 + (\mu_3 + 2)\sin\alpha, \tag{9}$$

where $\mu_i = r_i/r_1$ for $i = 2, 3$.

In Fig. 7 (obtained for the particular case $\mu_3 = 0.2$), the resulting eliminated portions, except for the part that should be taken into account, are shaded in dark gray.

In the rectangle Ξ without the portions that have already been eliminated, there are points (corresponding to certain values of the initial angle α and the initial coordinate *l*) through which the trajectories may pass after they have originated from other points, crossed the boundary several times, and enclosed the branch point one or more times (Fig. 8d). Without taking this circumstance into account, it is likely that some trajectories will be included twice or more. That is why, in the rectangle Ξ, we should also eliminate from consideration the portion into which the trajectories originating from the same rectangle can arrive. The equation for the boundary of this portion has the form

$$\frac{x}{\mu_3} - \sin\alpha + \sqrt{1 - \left[(2\mu_2 - \mu_3 - 1)\sqrt{1 - \left(\frac{x}{\mu_3} - \sin\alpha\right)^2} + \mu_3\cos\alpha\right]^2} = 2. \tag{10}$$

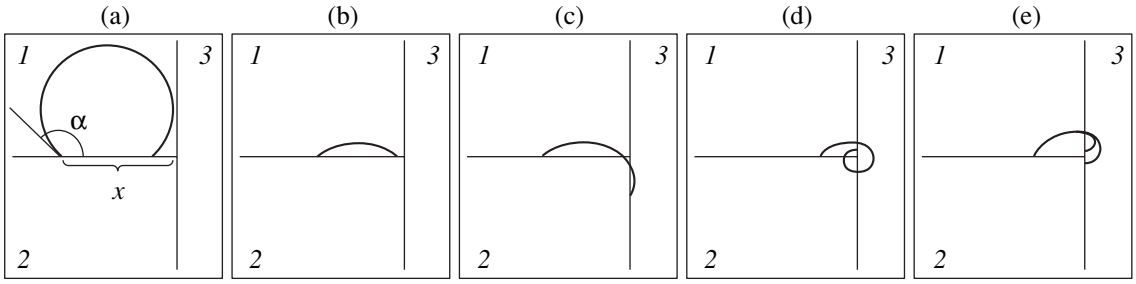

Fig. 8. Typical trajectories of a charged particle near a branched boundary.

In Fig. 7, the portion eliminated in accordance with Eq. (10) in the particular case $\mu_2 = 0.25$ and $\mu_3 = 0.2$ is shaded in light gray.

In the portion that remains in the rectangle Ξ after all the above portions have been eliminated (in Fig. 7, the remaining portion is unshaded), we determine the values of the initial angle α and the initial coordinate l that correspond to the trajectories escaping along branch *1–2* and to those escaping along branch *2–3*. To do this, we consider the trajectories that originate from branch *1–3* and immediately reach branch *1–2*. If, after reaching this branch, the trajectory crosses the boundary above the branch point, then the particle will move along branch *1–2*. If the crossing occurs below the branch point, then the particle will move along branch *2–3*. These two situations are illustrated in Fig. 8e. A simple calculation enables us to derive an equation for the boundary separating those values of the initial angle α and the initial coordinate l that correspond to the particles escaping along branch *1–2* and to the particles escaping along branch *2–3*. This boundary is the line on which the function $f(x, \alpha)$, given by the formula

$$f(x, \alpha) = \frac{1}{2}\left(1 - \frac{\cos\alpha}{\sqrt{\cos^2\alpha + 2x\sin\alpha - x^2}}\right) \qquad (11)$$

is equal to μ_2. For $\mu_2 \geq 0.5$, the line essentially coincides with the horizontal straight line $\alpha = \pi/2$. For μ_2 below 0.5, the line is convex downward. In Fig. 7, the line on which function (11) is equal to $\mu_2 = 0.25$ is denoted by *LL*.

Hence, the sought proportion between the parts into which the drift current divides along a T-shaped boundary is equal to the ratio of the areas of unshaded portions separated by the line on which function (11) is equal to μ_2.

Now, we should point out the following important circumstance. The total current along the branches satisfies Kirchhoff's law. The current along branch *1–3* satisfies relationship (4), while the currents along branches *1–2* and *2–3* do not. The reason for this is that relationship (4) was derived for a uniform distribution of particles over the initial angles. However, the distribution of the particles that have passed the branch point is nonuniform.

The last remark raises the problem of determining both the maximum drift current along a complex branched boundary and the branch along which the current is maximum. For a boundary in the form of a simply connected graph, the maximum current of magnitude (4) is that along the branch separating the regions for which the ratio of the gyroradii is the largest. From an electrotechnical standpoint, this indicates that there is a current source in the corresponding branch of a complex circuit.

CONCLUSION

An analysis has been performed of the cyclotron drift of charged particles along the boundary between regions of differing gyroradii. The expressions for the drift velocity and drift current along a straight boundary, as well as the expression for the drift velocity along a curvilinear boundary, have been obtained. The proportion between the parts into which the drift current divides along a branched boundary has been estimated using a T-shaped boundary as an example.

The processes analyzed above may serve as a basis for creating fundamentally new complex branched current structures in plasma and semiconductor systems. Thus, a closed curvilinear boundary (in the simplest case, a circle) may be used as a key element to implement a magnetic field detector, and a T-shaped branched boundary may underlie the operation of a device for separating particles (plasma ions) by mass or energy.

ACKNOWLEDGMENTS

I am grateful to Yu.B. Kudasov for valuable advice.

REFERENCES

1. S. V. Vonsovskiĭ, *Magnetism* (Nauka, Moscow, 1971).
2. V. Ya. Demikhovskiĭ and G. A. Vugal'ter, *Physics of Quantum Low-Dimensional Structures* (Logos, Moscow, 2000).

3. A. F. Andreev, Zh. Éksp. Teor. Fiz. **46**, 1823 (1964) [Sov. Phys. JETP **19**, 1228 (1964)].
4. V. F. Gantmakher and I. B. Levinson, *Scattering of Current Carriers in Metals and Semiconductors* (Nauka, Moscow, 1984).
5. I. Kosztin, D. L. Maslov, and P. M. Goldbart, Phys. Rev. Lett. **75**, 1735 (1995).
6. S. K. Zhdanov, V. A. Kurnaev, M. K. Romanovskiĭ, and I. V. Tsvetkov, *The Physical Basis of Processes in Plasma and Plasma Devices* (Mosk. Inzh.-Fiz. Inst., Moscow, 2000).
7. I. Y. Dodin and N. J. Fisch, Phys. Rev. E **64**, 016405 (2001).
8. V. I. Strikha, *Theoretical Backgrounds of Metal–Semiconductor Junction Operation* (Naukova Dumka, Kiev, 1974).
9. A. Kobus and Ya. Tushinskiĭ, *Hall Probes and Magnetoresistors* (Énergiya, Moscow, 1971).

Translated by O. Khadin

Technical Physics, Vol. 48, No. 5, 2003, pp. 569–575. Translated from Zhurnal Tekhnicheskoĭ Fiziki, Vol. 73, No. 5, 2003, pp. 46–52.

SOLIDS

Dependence of the Structure Period on the Interface Velocity upon Eutectic Solidification

A. P. Gus'kov

Institute of Solid-State Physics, Russian Academy of Sciences, Chernogolovka, Moscow oblast, 142432 Russia

e-mail: guskov@issp.ac.ru

Received June 24, 2002; in final form, October 28, 2002

Abstract—The period of eutectic structures is known to depend on the interface velocity (three types of this dependence are given in [1]). The form of this dependence is shown to depend on the growth mechanism of the solid phase and the surface tension coefficient. The calculated and experimental dependences are in good agreement. © *2003 MAIK "Nauka/Interperiodica".*

INTRODUCTION

Eutectic periodic structures that appear during the solidification of eutectic melts have attracted widespread interest for several decades from both the fundamental and applied viewpoints. Applied interest is provoked by the fact that the microstructure of eutectic composites consists of lamellas or rods of different phases simultaneously growing from the melt; therefore, the properties of such a material combine those of its constituents [2]. The practical application of eutectic composites is, however, limited, because they are difficult to grow. The complex space–time dynamics of the formation of a periodic two-phase structure from a homogeneous melt is still unknown. In particular, of fundamental importance in this process is the nature of morphologically unstable simple spatially periodic steady states, which make the dynamics complex [3]. The variety of the shapes and sizes of the structures solidified is specified by nonequilibrium processes at the solid–liquid interface. The current status of research on solidification is comprehensively reviewed in [4]. Among other things, this review considers the interface stability during the formation of three-dimensional dendritic structures (i.e., in the course of the oriented growth of the dendrite tip and the formation of dendrite branches) and during cellular solidification, as well as the morphological instability and oscillation of the interface during the formation of eutectic structures. The most popular theory describing the solidification of eutectic melts with the formation of periodic structures is the Jackson–Hunt theory [5]. This theory, however, does not explain the origin of the periodic structures and faces difficulties when selecting solutions to the equations derived [6]. Characterizing the state of the art in the theory of eutectic solidification, Hunt and Lu [7] indicated that, in spite of some progress in understanding eutectic, monotectic, and peritectic growth, most works are only qualitative. They also noted that a further advance can only be achieved by constructing a model of nonsteady-state growth and that it would be appropriate to develop a simpler analytical model for monotectic growth and check the stability of phase coexistence.

Many researchers believe that the basic cause of the periodic structure formation is the instability of the interface during solidification. Beginning from the classical work [8], numerous simulations of directional solidification that give qualitative agreement with experimentally observed structures have appeared [4]. However, quantitative results that provide a good fit to experimental data are very scarce. One of them is the dependence of the eutectic structure period on the interface velocity [9–11]. This dependence coincides exactly with the experimental dependences for a number of materials. An expression for the eutectic structure period was found from the dispersion relation:

$$\lambda = \frac{\pi(\chi' + \chi)}{\varepsilon|\Theta|}, \qquad (1)$$

where Θ is the kinetic parameter defined by a model of growth mechanism.

For growth by screw dislocations, Eq. (1) yields the dependence of the eutectic structure period on the steady-state interface velocity V_S [11, 12] that coincides with the experimental dependences. This coincidence may either be accidental or reflect the fact that the experimental dependences adequately describe the growth mechanism. The former possibility should not be ruled out, since the period squared may appear from the solution of many quadratic equations in the course of investigation. To tackle this problem, we introduce here surface tension, which was not taken into account in the previous models, and assume an exponential growth model. It will be shown that such a model gives dependences $\lambda(V_S)$ that, although being different from those found in [11, 12], also coincide with the known

1063-7842/03/4805-0569$24.00

experimental dependences. This result proves that the analytical dependence $\lambda(V_S)$ found previously is true and that the solidification model will also provide true $\lambda(V_S)$ dependences for eutectics of other compositions.

THE MODEL

Let T be temperature normalized to the phase transition temperature T_{e0} at an initial component concentration C_0; C, the component concentration normalized to its initial concentration; $y = \alpha y_r$, $z = \alpha z_r$, and $\tau = \alpha^2\chi_0\tau$ the dimensionless coordinates and time; $D = D_r/\chi_0$, the dimensionless diffusion coefficient in the liquid phase; $\chi = \chi_r/\chi_0$, the thermal diffusivity; ε, the heat of phase transition normalized to the specific heat and the phase transition temperature; ϕ, the heat transfer coefficient normalized to the specific heat; y_r, z_r, τ_r, D_r, χ_r, and ε_r, dimensional quantities; $\chi_0 = 10^{-5}$ m^2/s; and $\alpha = 10^2$ m^{-1}.

We take into account heat conduction in the liquid and solid phases and the diffusion of the component in the liquid phase. To shorten the mathematics, the x coordinate will hereafter be omitted. The primed quantities refer to the solid phase. Let $\bar{x}$, $\bar{y}$, $\bar{z}$ be the laboratory coordinate system in which the melt is motionless. Then, the equations for the temperatures $\bar{T}'(\bar{y}, \bar{z}, \tau)$ and $\bar{T}(\bar{y}, \bar{z}, \tau)$ in the liquid and solid phases, respectively, and for the concentration $\bar{C}(\bar{y}, \bar{z}, \tau)$ in the liquid phase have the form

$$\frac{\partial \bar{T}'}{\partial \tau} = \chi'\left(\frac{\partial^2 \bar{T}'}{\partial \bar{y}^2} + \frac{\partial^2 \bar{T}'}{\partial \bar{z}^2}\right) - \phi(\bar{T}' - \bar{T}_{\text{ext}}), \quad -\infty < z \le 0, \tag{2}$$

$$\frac{\partial \bar{T}}{\partial \tau} = \chi\left(\frac{\partial^2 \bar{T}}{\partial \bar{y}^2} + \frac{\partial^2 \bar{T}}{\partial \bar{z}^2}\right) - \phi(\bar{T} - \bar{T}_{\text{ext}}), \quad 0 \le z < \infty, \tag{3}$$

$$\frac{\partial \bar{C}}{\partial \tau} = D\left(\frac{\partial^2 \bar{C}}{\partial \bar{y}^2} + \frac{\partial^2 \bar{C}}{\partial \bar{z}^2}\right), \quad 0 \le z < \infty, \tag{4}$$

$$\chi'\frac{\partial \bar{T}'}{\partial n}\bigg|_{\text{solid}} - \chi\frac{\partial \bar{T}}{\partial n}\bigg|_{\text{liquid}} = \varepsilon V_n, \tag{5}$$

$$\bar{T}'\big|_{\text{solid}} = \bar{T}\big|_{\text{liquid}}, \tag{6}$$

$$\bar{T}'\big|_{z\to-\infty} = \bar{T}_{\text{ext}}(-\infty), \quad \bar{T}\big|_{z\to\infty} = \bar{T}_{\text{ext}}(\infty), \tag{7}$$

$$D\frac{\partial \bar{C}}{\partial n}\bigg|_{\text{liquid}} = V_n(k_u - 1)\bar{C}\big|_{\text{liquid}}, \quad \bar{C}\big|_{\bar{z}\to\infty} = 1, \tag{8}$$

$$V_n = V_n(\Delta T_k(\bar{T}(\bar{z}_{\text{int}}, \bar{y}, \bar{\tau}), \bar{C}(\bar{z}_{\text{int}}, \bar{y}, \bar{\tau}))). \tag{9}$$

Here, V_n is the interface velocity along the normal to the interface toward the liquid phase and ΔT_k is the kinetic supercooling, which is equal to the difference between the phase-transition temperature and the interface temperature at a given point of the interface.

The above set of equations is written with allowance for an external temperature field $\bar{T}_{\text{ext}}$. Such a formulation of the problem and the possible approximation of the external temperature field was analyzed in [12]. The expression for the kinetic supercooling has the form

$$\Delta\bar{T}_k = 1 + m(\bar{C}(\bar{z}_{\text{int}}, \bar{y}, \bar{\tau}) - 1) + \Gamma\kappa(\bar{T}(\bar{z}_{\text{int}}, \bar{y}, \bar{\tau}), \bar{C}(\bar{z}_{\text{int}}, \bar{y}, \bar{\tau})) - \bar{T}(\bar{z}_{\text{int}}, \bar{y}, \bar{\tau}), \tag{10}$$

where κ is the interface curvature, $\Gamma = \alpha\Gamma_r$, and Γ_r is the surface tension coefficient. In the problem of interface stability upon directional solidification, the curvature is usually introduced in explicit form via the dependence of the interface shape on space coordinates [8]. We do not introduce perturbations of a planar interface in explicit form. Instead, the interface velocity is considered to be a function of temperature and concentration, and the problem is solved with the use of only these perturbations. We will find the curvature of the perturbed interface in terms of temperature and concentration perturbations. The derivatives of $\bar{T}'$, $\bar{T}$, and $\bar{C}$ are taken along the vector **n** that is normal to the interface and directed toward the liquid phase. The segregation coefficient is defined as the ratio of the component concentration in the solid phase to that in the liquid phase. Assuming the concentration in the solid phase to be equal to the initial concentration in the melt, we find for the segregation coefficient

$$k = \frac{\bar{C}\big|_{\bar{z}\to\infty}}{\bar{C}\big|_{\text{liquid}}}.$$

Let $V(\bar{y}, \bar{z}, \tau)$ be the interface velocity along the $\bar{z}$ coordinate. Then, the interface coordinate $\bar{z}_{\text{int}}$ can be written as

$$z'_{\text{int}}(y', \tau) = \int V(y', z'_{\text{int}}, \tau)d\tau = F(y', z'_{\text{int}}, \tau). \tag{11}$$

The velocity $V(\bar{y}, \bar{z}, \tau)$ is related to V_n by the expression

$$V = \sqrt{1 + \left(\frac{\partial F}{\partial y}\right)^2}\, V_n.$$

Let us write this boundary-value problem in the moving coordinate system related to the interface. This coordinate system was used in [9, 10] and is curvilinear with respect to the laboratory coordinate system. It is related to the interface whose velocity, in general, depends on the component temperature and concentration rather than to the interface moving in the steady-state conditions, i.e., in the laboratory coordinate system with a constant velocity. The new variables are

$$y = \bar{y}, \quad z = \bar{z} - F(\bar{y}, \bar{z}_{\text{int}}, \tau).$$

Now, we recast Eqs. (2)–(9) into the form

$$\frac{\partial T'}{\partial \tau} = \chi'\left[\frac{\partial^2 T'}{\partial y^2} + \left(1 + \left(\frac{\partial F}{\partial y}\right)^2\right)\frac{\partial^2 T'}{\partial z^2} - 2\frac{\partial F}{\partial y}\frac{\partial^2 T'}{\partial y \partial z} - \frac{\partial^2 F}{\partial y^2}\frac{\partial T'}{\partial z}\right] + \frac{\partial F}{\partial \tau}\frac{\partial T'}{\partial z} - \phi(T' - T_{\text{ext}}), \quad (12)$$

$$-\infty < z \le 0,$$

$$\frac{\partial T}{\partial \tau} = \chi\left[\frac{\partial^2 T}{\partial y^2} + \left(1 + \left(\frac{\partial F}{\partial y}\right)^2\right)\frac{\partial^2 T}{\partial z^2} - 2\frac{\partial F}{\partial y}\frac{\partial^2 T}{\partial y \partial z} - \frac{\partial^2 F}{\partial y^2}\frac{\partial T}{\partial z}\right] + \frac{\partial F}{\partial \tau}\frac{\partial T}{\partial z} - \phi(T - T_{\text{ext}}), \quad (13)$$

$$0 \le z < \infty,$$

$$\frac{\partial C}{\partial \tau} = D\left[\frac{\partial^2 C}{\partial y^2} + \left(1 + \left(\frac{\partial F}{\partial y}\right)^2\right)\frac{\partial^2 C}{\partial z^2} - 2\frac{\partial F}{\partial y}\frac{\partial^2 C}{\partial y \partial z} - \frac{\partial^2 F}{\partial y^2}\frac{\partial C}{\partial z}\right] + \frac{\partial F}{\partial \tau}\frac{\partial C}{\partial z}, \quad (14)$$

$$0 \le z < \infty,$$

$$\left[1 + \left(\frac{\partial F}{\partial y}\right)^2\right]\left(\chi'\frac{\partial T'}{\partial z}\bigg|_{z=0-0} - \chi\frac{\partial T}{\partial z}\bigg|_{z=0+0}\right) - \frac{\partial F}{\partial y}\left(\chi'\frac{\partial T'}{\partial y}\bigg|_{z=0-0} - \chi\frac{\partial T}{\partial y}\bigg|_{z=0+0}\right) = \varepsilon V, \quad (15)$$

$$T'|_{z=0-0} = T|_{z=0+0} T'|_{z\to-\infty} = T_{\text{ext}}(-\infty) T|_{z\to\infty} = T_{\text{ext}}(\infty), \quad (16)$$

$$D\left[\left(1 + \left(\frac{\partial F}{\partial y}\right)^2\right)\frac{\partial C}{\partial z} - \frac{\partial F}{\partial y}\frac{\partial C}{\partial y}\right]\bigg|_{z=0+0} = V(k-1)C|_{z=0+0}, \quad (17)$$

$$v = v(\Delta T_{\text{k}}(T(0, y, \tau), C(0, y, \tau), \kappa)). \quad (18)$$

Let the flat solidification front move in the laboratory coordinate system with a constant velocity V_{S} when the melt solidifies under steady-state conditions. Here, we investigate the stability of the steady-state solidification conditions against temperature and concentration perturbations in the linear approximation. In order to obtain the linear approximation of boundary problem-value (12)–(18), we assume that its solutions are

$$T' = T'_{\text{S}}(z) + T'_m(z)\exp(\omega\tau + Ky) = T'_{\text{S}}(z) + f'_T,$$
$$T = T_{\text{S}}(z) + T_m(z)\exp(\omega\tau + Ky) = T_{\text{S}}(z) + f_T,$$
$$C = C_{\text{S}}(z) + C_m(z)\exp(\omega\tau + Ky) = C_{\text{S}}(z) + f_C,$$
$$\omega = \omega_1 + i\omega_2, \quad K = K_1 + iK_2.$$

In our case of infinite interface, we take $K_1 = 0$,

$$T'_m(z) \ll T'_{\text{S}}(z), \quad T_m(z) \ll T_{\text{S}}(z), \quad C_m(z) \ll C_{\text{S}}(z),$$

where $T'_{\text{S}}(z)$, $T_{\text{S}}(z)$, and $C_{\text{S}}(z)$ are the steady-state solutions to the problem.

The approximation linear in small perturbations then has the form

$$\chi'\frac{\partial^2 T'_m}{\partial z^2} + V_{\text{S}}\frac{\partial T'_m}{\partial z} + (\chi' K^2 - \omega)T'_m = \left[(\chi' K^2 - \omega)\frac{\partial T'_{\text{S}}}{\partial z} - \phi\frac{\partial T_{\text{ext}}}{\partial F}\right]\frac{V_m}{\omega}, \quad -\infty < z \le 0, \quad (19)$$

$$\chi'\frac{\partial^2 T_m}{\partial z^2} + V_{\text{S}}\frac{\partial T_m}{\partial z} + (\chi K^2 - \omega)T_m = \left[(\chi K^2 - \omega)\frac{\partial T_{\text{S}}}{\partial z} - \phi\frac{\partial T_{\text{ext}}}{\partial F}\right]\frac{V_m}{\omega}, \quad 0 \le z < \infty, \quad (20)$$

$$D\frac{\partial^2 C_m}{\partial z^2} + V_{\text{S}}\frac{\partial C_m}{\partial z} + (DK^2 - \omega)C_m = \frac{(DK^2 - \omega)}{\omega}V_m\frac{\partial C_S}{\partial z}, \quad 0 \le z < \infty, \quad (21)$$

$$\chi'\frac{\partial T'_m}{\partial z}\bigg|_{z=0-0} - \chi\frac{\partial T_m}{\partial z}\bigg|_{z=0+0} = \varepsilon V_m, \quad (22)$$

$$T'_m|_{z=0-0} = T_m|_{z=0+0}, \ T'_m|_{z\to-\infty} = 0, \ T_m|_{z\to\infty} = 0, \quad (23)$$

$$D\frac{\partial C_m}{\partial z}\bigg|_{z=0+0} = (k-1)(V_{\text{S}}C_m + C_{\text{S}}V_m), \quad C_m|_{z\to\infty} = 0. \quad (24)$$

Now consider the linearization of kinetic condition (18). This condition describes the dependence of the interface velocity on the rate of attachment of molecules to the growing surface. The form of the dependence $V(\Delta T_{\text{k}})$ is specified by a model of growth. In the new variables, kinetic supercooling (10) is given by the expression

$$\Delta T_{\text{k}} = 1 + m(C(0, y, \tau) - 1) + \Gamma\kappa(T(0, y, \tau), C(0, y, \tau)) - T(0, y, \tau),$$

which applies to any growth model. For the kinetic supercooling thus written, the Maclaurin expansion of velocity (18) in small temperature and concentration perturbations is

$$V \approx V_{\text{S}} + \Lambda\left(\frac{\partial \Delta T_{\text{k}}}{\partial T}dT + \frac{\partial \Delta T_{\text{k}}}{\partial C}dC + \frac{\partial \Delta T_{\text{k}}}{\partial \kappa}d\kappa\right)$$

$$+\frac{1}{2}\left[\psi\left(\frac{\partial\Delta T_k}{\partial\kappa}\right)^2+\Lambda\frac{\partial^2\Delta T_k}{\partial\kappa^2}\right]d\kappa^2$$

$$+\frac{1}{2}\left[\psi\frac{\partial\Delta T_k}{\partial\kappa}\frac{\partial\Delta T_k}{\partial T}+\Lambda\frac{\partial^2\Delta T_k}{\partial T d\kappa}\right]dTd\kappa$$

$$+\frac{1}{2}\left[\psi\frac{\partial\Delta T_k}{\partial\kappa}\frac{\partial\Delta T_k}{\partial C}+\Lambda\frac{\partial^2\Delta T_k}{\partial C d\kappa}\right]dCd\kappa.$$

Note that this expression applies to any growth model in which the velocity depends on the kinetic supercooling. After differentiating, we find for the linear approximation

$$V\approx V_S+\Lambda(-T_m+mC_m+\Gamma\kappa), \tag{25}$$

where

$$\Lambda=\frac{\partial V}{\partial\Delta T_k}.$$

For the model of normal growth [13], we have

$$V=h_n\Delta T_k,\quad \Lambda_n=h_n; \tag{26}$$

for growth by screw dislocations [13],

$$V=h_d\Delta T_k^2,\quad \Lambda_d=2\sqrt{h_d v_S}; \tag{27}$$

and for two-dimensional nucleation [13],

$$V=h_1\exp\left(-\frac{h_2}{\Delta T_k}\right),\quad \Lambda_d=\frac{V_S}{h_2}\ln^2\left(\frac{V_S}{h_1}\right). \tag{28}$$

In the linear approximation, Eq. (25) has the form

$$V\approx V_S+\Lambda(-f_{T0}+mf_{C0}+\Gamma\kappa)=V_S+V_m. \tag{29}$$

Here, V_m is the as yet unknown perturbation of interface velocity and the temperature and concentration perturbations are

$$f_{T0}=T_m(0)\exp(Ky+\omega\tau),$$

$$f_{C0}=C_m(0)\exp(Ky+\omega\tau).$$

We will seek V_m as the linear combination of the temperature and concentration perturbations:

$$V_m=\Theta f_{T0}+\gamma f_{C0}, \tag{30}$$

where Θ and γ are as yet unknown expressions. Substituting (30) into (29) yields

$$\Theta f_{T0}+\gamma f_{C0}=\Lambda(-f_{T0}+mf_{C0}+\Gamma\kappa). \tag{31}$$

By definition, the curvature is given by

$$\kappa=-\mathrm{div}(n)=-\mathrm{div}\left(\frac{(-F_y,1)}{\sqrt{1+F_y^2}}\right). \tag{32}$$

To explain the curvature in temperature and concentration perturbations, we first find an expansion for the function F. To this end, we pass to the curvilinear coordinates in (11):

$$F(0,y,\tau)=\int V\{\Delta T_k[T(0,y,\tau),C(0,y,\tau)]\}d\tau$$

$$=\int(V_S+\Theta f_{T0}+\gamma f_{C0})d\tau \tag{33}$$

$$=V_S\tau+\frac{\Theta f_{T0}+\gamma f_{C0}}{\omega}=F_S+f,$$

where

$$f=\frac{\Theta f_{T0}+\gamma f_{C0}}{\omega}. \tag{34}$$

Differentiating (33), we derive from (32)

$$\kappa=\frac{K^2 f(y,\tau)}{\sqrt{1+K^2 f(y,\tau)^2}}-\frac{K^4 f(y,\tau)^3}{(1+K^2 f(y,\tau)^2)^{\frac{3}{2}}}.$$

Expansion into series gives the expression

$$\kappa\approx K^2 f(y,\tau)-\frac{3}{2}K^4 f(y,\tau)^3+O(f(y,\tau)^7).$$

In the linear approximation,

$$\kappa=K^2 f. \tag{35}$$

Substituting (34) in (31) yields

$$\omega f=\Lambda(-f_{T0}+mf_{C0}+\Gamma\kappa). \tag{36}$$

From Eqs. (35) and (36), we find expressions for f and κ that are linear in temperature and concentration perturbations:

$$f=\frac{\Lambda(f_{T0}-mf_{C0})}{\Lambda\Gamma K^2-\omega}, \tag{37}$$

$$\kappa=\frac{K^2\Lambda(f_{T0}-mf_{C0})}{\Lambda\Gamma K^2-\omega}. \tag{38}$$

It follows from (37) and (34) that

$$\frac{\Lambda(f_{T0}-mf_{C0})}{\Lambda\Gamma K^2-\omega}=\frac{\Theta f_{T0}+\gamma f_{C0}}{\omega}. \tag{39}$$

Grouping the coefficients by the temperature and concentration perturbations, we derive a set of equations for the unknown coefficients. From this set, we find

$$\Theta=\Lambda\frac{\omega}{\Lambda\Gamma K^2-\omega}, \tag{40}$$

$$\gamma=-m\Lambda\frac{\omega}{\Lambda\Gamma K^2-\omega}=-m\Theta. \tag{41}$$

A dispersion relation is found in the same manner as in [12]. A solution to the problem stated by (19)–(24) and (39) is first found. At the interface, this solution is

represented by a linear set of equations for the coefficients $T_{m0} = T_m(0)$ and $C_{m0} = C_m(0)$:

$$(S_T' - S_T)T_{m0} - \eta V_{m0} = 0, \quad (42)$$

$$[S + 2(1-k)]C_{m0} - (k-1)\xi V_{m0} = 0, \quad (43)$$

where (42) is the solution to the heat conduction equation and (43) is that to the diffusion equation. Here, S_T', S_T, and S are the roots of the characteristic equations for Eqs. (19)–(21), and η and ξ depend on the system's parameters ($\xi \neq 0$ at $k = 1$). Substituting expansion (39) into (42) and (43) yields the dispersion relation

$$[(S_T' - S_T) - \eta\Theta][S + 2(1-k) + (1-k)\xi\gamma] + (1-k)\xi\eta\gamma\Theta = 0. \quad (44)$$

The procedure of deriving the dispersion relation is given in more detail in [9, 10, 12]. Note that, if the interface velocity is independent of temperature and concentration, then $\Theta = 0$ and $\gamma = 0$ and the problems of diffusion and heat conduction are mutually independent. In this case, Eq. (44) degenerates into the product of the dispersion relations for the problems of diffusion and heat conduction. If the component concentrations are close to the eutectic composition, k is close to 1. At small values of $k - 1$, Eq. (44) takes the form

$$[(S_T' - S_T) - \eta\Theta]S = 0. \quad (45)$$

This equation splits into two real equations for the imaginary and real parts of Eq. (45):

$$\begin{aligned} &\mathrm{Re}((S_T' - S_T) - \eta\Theta)\mathrm{Re}S - \mathrm{Im}[(S_T' - S_T) - \eta\Theta]\mathrm{Im}S = 0, \\ &\mathrm{Re}((S_T' - S_T) - \eta\Theta)\mathrm{Im}S - \mathrm{Im}[(S_T' - S_T) - \eta\Theta]\mathrm{Re}S = 0. \end{aligned} \quad (46)$$

The imaginary part of S has the form

$$\mathrm{Im}(S) = -0.5\sqrt{2\sqrt{(1 + Y + \delta)^2 + \Omega^2} - 2(1 + Y + \delta)}, \quad (47)$$

where

$$\delta = \frac{4D\omega_1}{V_S^2}, \quad \Omega = \frac{4D\omega_2}{V_S^2}, \quad Y = \frac{4D^2K_2^2}{V_S^2} \quad (48)$$

are the growth increment, temporal oscillation frequency, and spatial distortion frequency, respectively.

For further simplifications, numerical calculation is needed. To this end, the segregation coefficient is taken to be $k = 1.03$ and the liquidus slope, $m = -0.05$, i.e., the same as in [9–12], where k was used to simulate melt layering at the interface. The external temperature gradient is assumed to be $\phi_{0r} = 10^4$ K m^{-1}. For numerical calculation, we use, as in [11], the model of growth by screw dislocations with the kinetic coefficient $h = 2.2 \times 10^{11}$ and assume that $\Gamma = 10^{-5}$. With these values, solutions to our problem virtually coincide with those of the problem considered in [12]. It follows from the solutions obtained that the interface has a spatial oscillation mode with a frequency of $\log(Y) \approx 8.5$ at the given parameters. According to the role of selection, temporal oscillations at the interface are absent, since the trajectory $\delta(\Omega)$ increases monotonically at $\Omega \longrightarrow 0$. Hence, at the point of maximal growth increment, $\Omega = 0$ and Eq. (47) takes the form

$$\mathrm{Im}(S) = -0.5\sqrt{2\sqrt{(1 + Y + \delta)^2} - 2(1 + Y + \delta)} \equiv 0.$$

Similarly, it is easy to show that the expressions $\mathrm{Im}S_T'$ and $\mathrm{Im}S_T$ also vanish. Therefore, set (46) contains the only equation at the point of maximal growth increment, from which we obtain

$$\mathrm{Re}(S_T') - \mathrm{Re}(S_T) - \Theta\mathrm{Re}(\eta) = 0. \quad (49)$$

Here, Θ is a real coefficient, since the condition $\Omega = 0$ means that the imaginary part of the complex frequency ω goes to zero.

Consider the expression

$$\mathrm{Re}S_T = -1 + 0.5\sqrt{2\sqrt{\left(1 + \frac{\chi^2 Y}{D^2} + \frac{\chi\delta}{D}\right)^2} + 2\left(1 + \frac{\chi^2 Y}{D^2} + \frac{\chi\delta}{D}\right)}.$$

Substituting numerical values into this expression yields

$$1 \ll \frac{\chi\delta}{D} \ll \frac{\chi^2 Y}{D^2}.$$

Similar relationships are also valid for $\mathrm{Re}(S_T')$. $\mathrm{Re}(\eta)$ can be expressed as

$$\mathrm{Re}(\eta) = \frac{2\varepsilon}{V_S}(1 + \beta).$$

As in [12], it follows from the calculations that $\beta \ll 1$. Neglecting small quantities in $\mathrm{Re}(S_T)$, $\mathrm{Re}(S_T')$, and $\mathrm{Re}(\eta)$ and substituting them into (49), we come to the equation

$$|\chi_1 \pm \chi|\sqrt{Y} - \frac{2\varepsilon D\Theta}{V_S} = 0;$$

hence,

$$\sqrt{Y} = \frac{2D\varepsilon\Theta}{V_S(\chi' + \chi)}. \quad (50)$$

Substituting Eq. (40) for the kinetic coefficient into (50) and taking into account relation (48) between the wave number and Y, we arrive at the equation

$$(\chi' + \chi)V_S\Lambda\Gamma(\sqrt{Y})^3 + (\chi' + \chi)V_S\delta Y + 2D\varepsilon\Lambda\delta = 0. \quad (51)$$

At $\Gamma = 0$, it follows from (40) that $\Theta = \Lambda$ and Eq. (51) transforms into expression (50). However, it is impossible to obtain Eq. (50) for arbitrary parameters

Table

Curve no.	Composition	A_1	A_2	B	Expression
1	Al_2O_3–ZrO_2	3.50×10^{-3}	–	0	(57)
2	Pb–Sn	5.38×10^{-3}	–	0	(57)
3	ZrO_2–MgO	7.13×10^{-3}	–	0	(57)
4	MgO–$MgAl_2O_4$	12.10×10^{-3}	–	0	(57)
5	ZrO_2–Y_2O_3	24.30×10^{-3}	–	0	(57)
6	CaO–NiO	2.61×10^{-3}	–	2.085	(57)
7	$Zn_5B_4O_{11}$–ZnB_2O_4	–143.8	1.837	0	(58)

of the system if Γ is small. This is due to the fact that the growth increment δ remains in this equation at $\Gamma \neq 0$ and its presence does not allow the desired asymptotic solution (50). We can obtain (50) only by taking into account the condition

$$\delta \approx Y, \tag{52}$$

which was used to derive solution (50) in [11]. Substituting $\delta \approx Y$ into (51), we get

$$(\chi' + \chi)V_S\Lambda\Gamma(\sqrt{Y})^3 + (\chi' + \chi)V_S(\sqrt{Y})^3 + 2D\varepsilon\Lambda(\sqrt{Y})^2 = 0;$$

hence,

$$\lambda = \frac{2\pi(\chi' + \chi)}{\varepsilon\Lambda}(1 + \Lambda\Gamma). \tag{53}$$

Thus, condition (52) is necessary to obtain the desired solution. The validity of this condition follows from the numerical calculations of the solutions to the dispersion relation of the system [11, 12]. The factor multiplying the second parenthesis in Eq. (53) is structural period (1) obtained earlier without considering surface tension [10]. The term $\Lambda\Gamma$ is the contribution of surface tension. Substituting Eqs. (26) and (27) into (53), we find for normal growth

$$\lambda_n = \frac{2\pi(\chi' + \chi)}{\varepsilon h_n}(1 + h_n\Gamma)$$

and for growth by screw dislocations,

$$\lambda_d = \frac{\pi(\chi' + \chi)}{\varepsilon\sqrt{h_d V_S}} + \frac{2\pi(\chi' + \chi)\Gamma}{\varepsilon}. \tag{54}$$

From (28) for two-dimensional nucleation, we arrive at

$$\lambda_{2D} = \frac{2\pi(\chi' + \chi)h_2}{\varepsilon V_S \ln\left(\frac{V_S}{h_1}\right)^2} + \frac{2\pi(\chi' + \chi)\Gamma}{\varepsilon}. \tag{55}$$

For the value of the surface tension coefficient estimated from (53), the Gibbs–Thomson effect can be neglected:

$$\Gamma \ll \frac{1}{\Lambda}. \tag{56}$$

For numerical calculations in this work and in [11], we used $h_S = 2.2 \times 10^{11}$, $V_S = 10^{-2}$, and $\Lambda = 2\sqrt{h_S V_S} \sim 10^5$. For the Al_2O_3–ZrO_2 system studied, various estimates of Γ fall into the range 10^{-6}–10^{-5}; that is, condition (56) is fulfilled at $\Gamma = 10^{-6}$. For this system, the dependence $\lambda(V_S)$ was constructed in [11] without allowance for surface tension. Those dependences coincided completely with the experimental dependence found in [1], which means that, according to the theory developed here, the actual surface tension in the Al_2O_3–ZrO_2 system satisfies estimate (56). Let us compare our calculated dependence of the eutectic period with those found elsewhere. In [1], the eutectic period as a function of the interface velocity for several eutectic compositions was reported. These dependences can be divided into three families. Most of them are straight lines coming from the origin. For the CaO–NiO composition, the dependence is a straight line intersecting the axis of ordinates above the origin. For the $Zn_5B_4O_{11}$–ZnB_2O_4 composition, the dependence is an increasing nonlinear curve.

We rewrite Eqs. (54) and (55) as

$$\lambda_d = A_1 R + B, \tag{57}$$

$$\lambda_{2D} = \frac{R^2}{(A_1 + A_2 \ln R^{-2})} + B, \tag{58}$$

where $R = V_S^{-1/2}$. To compare our theory with experiment, we plotted the experimental dependences found in [1] for the eutectic compositions listed in the table (see figure).

The analytical dependences plotted in the figure coincide with the experimental data up to the accuracy of the construction.

This agreement can be explained as follows. The solidification model proposed is based on the heat-conduction and diffusion equations. The adequacy of these equations to actual processes is beyond question. The boundary conditions of the model describe successfully the separation of components during solidification and take into account mechanisms of crystal growth. In essence, we are dealing with a homogeneous dynamic

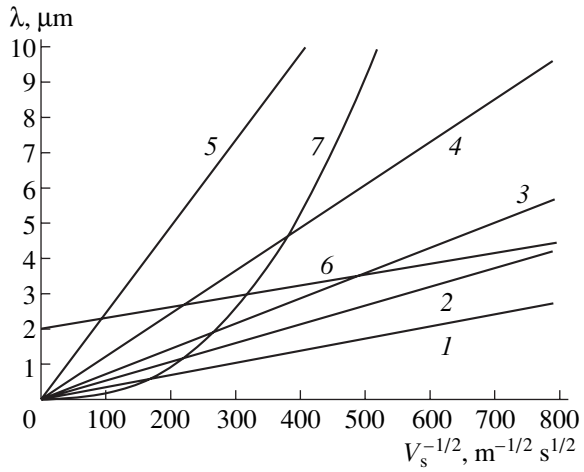

Figure.

system for the process under investigation, and the dependences obtained are resonance curves. Of course, it is difficult to imagine that structures that reflect only intermolecular interaction between materials grow in growth equipment. However, it was unclear why the period of a solidifying structure cannot be controlled by an external temperature field in experiments. It turns out [12] that the parameters describing external thermal conditions are far less than those reflecting the physical properties of materials and, thus, do not appear in the final solution. It should also be noted that the available growth models are adequate to the process studied. Generally speaking, these theories are not rigorous. Their experimental confirmation is, as a rule, only qualitative. For example, the qualitative confirmation of the theory of growth by screw dislocations is micrographs of growth spirals. This is because the kinetic supercooling is difficult to measure. The theory considered in this work is a direct support of the fact that the growth models also provide quantitatively correct results.

Apparently, the resonance curves obtained are akin to the resonance curves of an oscillating contour in the sense that an oscillating contour is the simplest circuit that quantitatively reflects the interaction between inductance, capacitor, and resistor. In terms of materials science, a eutectic structure is the simplest result of thermal, diffusion, and intermolecular interactions during directional solidification. Basically, experimental and theoretical $\lambda(V_S)$ dependences in combination allow one to find unknown thermophysical parameters of a material. However, the values of many parameters are today either unknown or greatly scattered. This is due to difficulties in determining the parameters of the system near the phase transition. A more comprehensive discussion of this problem is beyond the scope of this work.

CONCLUSIONS

(1) Within the model of directional solidification, solutions including the surface tension coefficient of the interface are found in the coordinate system related to the curvilinear interface.

(2) An analytical expression for the dependence of the eutectic structure period on the interface velocity is obtained with allowance for surface tension.

(3) The parameters involved in the dependence of the eutectic structure period on the interface velocity are calculated for a number of experimental curves. Good coincidence with the experiment is obtained.

(4) The dependence of the eutectic structure period on the interface velocity is shown to depend on a growth mechanism, namely, on the rate of attachment of molecules to the growing surface.

REFERENCES

1. W. J. Minford, R. C. Bradt, and V. S. Stubican, J. Am. Ceram. Soc. **62**, 154 (1979).
2. Yoshikawa, K. Hasegawa, T. Fukuda, *et al.*, in *Proceedings of the 23rd International Conference on Composites, Advanced Ceramics, Materials, and Structures: B, American Ceramic Society, Cocoa Beach, 1999*, Vol. 20, p. 275.
3. M. Plapp and A. Karma, Phys. Rev. E **60**, 6865 (1999).
4. W. J. Boettinger, S. R. Coriell, A. L. Greer, *et al.*, Acta Mater. **48**, 43 (2000).
5. K. A. Jackson and J. D. Hunt, Trans. Metall. Soc. AIME **236**, 1129 (1966).
6. R. Eliot, *Eutectic Solidification Control* (Metallurgiya, Moscow, 1987).
7. J. D. Hunt and S.-Z. Lu, *Handbook of Crystal Growth* (North Holland, 1994), Vol. 2, Part B, Chap. 17.
8. W. W. Mullins and R. F. Sekerka, J. Appl. Phys. **35**, 444 (1964).
9. A. P. Gus'kov, Dokl. Akad. Nauk **366**, 468 (1999) [Dokl. Phys. **44**, 330 (1999)].
10. A. P. Gus'kov, Izv. Akad. Nauk, Ser. Fiz. **63**, 1772 (1999).
11. A. Gus'kov, Comput. Mater. Sci. **17**, 555 (2000).
12. A. P. Gus'kov, Pis'ma Zh. Tekh. Fiz. **27** (11), 86 (2001) [Tech. Phys. Lett. **27**, 480 (2001)].
13. *Physical Metallurgy*, Ed. by R. W. Cahn and P. Haasen (North-Holland, New York, 1983, 3rd ed.; Metallurgiya, Moscow, 1987).

Translated by K. Shakhlevich

Technical Physics, Vol. 48, No. 5, 2003, pp. 576–579. Translated from Zhurnal Tekhnicheskoĭ Fiziki, Vol. 73, No. 5, 2003, pp. 53–56.

SOLID-STATE ELECTRONICS

Soliton Delay Line Based on a Semiconductor Superlattice

S. V. Kryuchkov and E. V. Kaplya

Volzhskiĭ Polytechnical Institute, Volgograd State Technical University, Volzhskiĭ, Volgograd oblast, 404121 Russia
e-mail: kaple_ev@newmail.ru

Received March 18, 2002; in final form, July 31, 2002

Abstract—A new type of delay line intended for soliton pulses is proposed. As a nonlinear medium, a semiconductor superlattice is taken. Solitons that propagate along the superlattice layers are confined in cells bounded by transverse inhomogeneity layers. Solitons are confined and released with the help of an external electric current passing inside the cell. © *2003 MAIK "Nauka/Interperiodica".*

INTRODUCTION

In recent years, a new type of fiber-optic communication, soliton communication lines (SCLs), which use electromagnetic solitons as information carriers, has been developed [1, 2]. SCLs feature a high transmission rate owing to the high stability of soliton pulses. However, the speed of transmitters, receivers, and analyzers of soliton pulses is limited. To provide their matched operation upon information overload, a soliton delay line may be necessary.

DESIGN OF A SOLITON DELAY LINE

The basic element of a soliton delay line (SDL) is a semiconductor superlattice. Relatively high nonlinear electric properties are offered by superlattices with a period of $d \sim 10^{-8}$ m and a volumetric carrier concentration of $n \sim 10^{20}$ m^{-3}. SDLs can be fabricated from various semiconductor materials, e.g., GaAs/AlGaAs superlattices, whose energy spectrum is fairly accurately described within the strong coupling approximation.

A soliton that has come from an SCL is amplified in an external high-frequency electric field created in the region U_1 by lateral plates (electrodes) O_1. The soliton is amplified to an amplitude that is necessary to overcome cell inhomogeneities N_m (m = 1 or 2) with a concentration $n_m \sim 10^{22}$ m^{-3}. The width of the inhomogeneity layers is $D \sim 10^{-7}$ m. The cell width r must exceed the soliton width: $r \sim 10^{-5}$ m. The cell is equipped with two electrodes O_2 (Fig. 1), to which an electric current that controls the confinement (writing) and release of electromagnetic solitons is applied. The electrodes must be wide enough to almost entirely cover the cell. Between each of the electrodes and the adjacent transverse inhomogeneities N_1 and N_2, a narrow gap should be provided in order to prevent the effect of the electric field created by the electrodes on these inhomogeneities.

The transverse dimension (along the x axis) of the SDL must equal ~10^{-6} m, i.e., several tens or several hundreds of the superlattice period d in order to exclude the edge effects.

PROPAGATION OF AN ELECTROMAGNETIC SOLITON IN THE SUPERLATTICE

A soliton (kink) is a localized solitary wave [3] with the electric field intensity given by

$$E_x = (-(\hbar\omega_{pl})/ed)[\partial\varphi/\partial\tau], \quad (1)$$

where

$$\varphi(\tau, \zeta, u(\tau)) = 4\arctan(\exp(Q\xi(\tau, \zeta, u(\tau))/\Gamma(u(\tau)))) \quad (2)$$

is a dimensionless function.

The above formulas involve dimensionless variables: $\zeta = z\omega_{pl}/c$ is the space variable, $\tau = t\omega_{pl}$ is the time variable, $u(\tau) = v(\tau)/c$ is the dimensionless soliton velocity, $\xi(\tau, \zeta, u(\tau)) = \xi_0 + \zeta - u(\tau)\tau$ is the soliton phase, and $\Gamma(u(\tau)) = (1 - u(\tau)^2)^{1/2}$ is the soliton half-width.

The electric field intensity of a soliton that propagates in a superlattice is proportional to the plasma frequency $\omega_{pl} = \sqrt{[(4\pi)/\varepsilon_0][e^2/m_e]n}$ of electrons in the minizone of the superlattice.

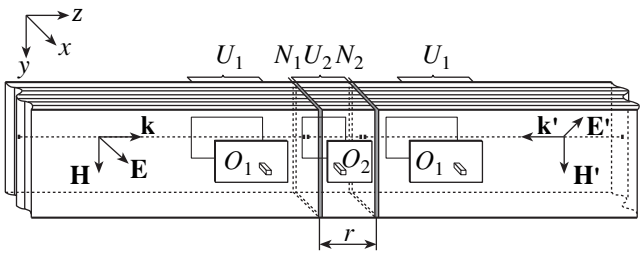

Fig. 1. Design of a one-cell soliton delay line based on a semiconductor superlattice.

1063-7842/03/4805-0576$24.00 © 2003 MAIK "Nauka/Interperiodica"

The propagation of an electromagnetic soliton in a superlattice with inhomogeneities under the action of an applied electric current can be described in terms of the disturbed sine-Gordon equation with singularity [4–6]

$$\frac{\partial^2\varphi}{\partial\tau^2} - \frac{\partial^2\varphi}{\partial\zeta^2} + \Theta(\zeta)\sin(\varphi) = -\alpha\frac{\partial\varphi}{\partial\tau} - \beta(\zeta,\tau) + \Theta(\zeta)\chi\gamma(\tau,\varphi,\varphi'). \quad (3)$$

The attenuation of a soliton because of the minizone structure of a superlattice [7] is allowed for in (3) by the coefficient

$$\alpha = 4\pi\frac{c}{\omega_{pl}}\eta, \quad (4)$$

where η is a constant that is responsible for soliton energy losses due to interminizone electron transitions.

The density of the applied electric current in (3) is given by the dimensionless function of the space coordinate and time

$$\beta(\zeta,\tau) = \frac{4\pi ed}{\varepsilon_0}\frac{1}{\hbar}\frac{1}{\omega_{pl}^2}J_x(z,t), \quad (5)$$

where $J_x(z, t)$ is the density of the applied electric current.

Transverse inhomogeneities can be specified in terms of the delta function [8]:

$$\Theta(\zeta) = 1 + \sum_m(\mu_m\delta(\zeta - \zeta q_m)), \qquad \mu_m = D_m\frac{\Delta n_m}{n}\frac{\omega_{pl}}{c}\ (m = 1; 2). \quad (6)$$

The parameter μ_m of the inhomogeneity N_m, in the ζq_m plane depends on the width D_m of the inhomogeneity and on the excess Δn_m of the carrier concentration in it over the concentration n in the superlattice.

Electron–inhomogeneity collisions enter (3) through the integral

$$\gamma(\tau,\varphi,\varphi') = \int_{-\infty}^{\tau}\exp[-\chi(\tau-\tau')][\sin(\varphi'-\varphi) + \sin(\varphi)]d\tau', \quad (7)$$

where $\chi = (1/\omega_{pl})\nu$ and ν is the collision rate.

CONTROL CURRENTS

A soliton is written by applying a short external current pulse $j_x^W(t, z) < 0$ inside the cell when the soliton passes through it.

A soliton is read (released) from the cell with the help of a current pulse $j_x^R(t, z) > 0$. The current value depends on the energy necessary before an electromagnetic soliton leaves the cell.

The main problem in designing an SDL is to determine the time instant a soliton passes through inhomogeneities and the required value of the control currents. The soliton possesses the static and kinetic energies

$$W_{ss} = 8; \quad Wks(u(\tau)) = 8(\Gamma(u(\tau))^{-1} - 1). \quad (8)$$

If integral (7) is ignored, the soliton velocity $u(\tau)$ at a time instant τ can be found from the energy equation

$$Wks(u(\tau)) = Wks(u(\tau_0)) - \sum_{m=1}^{2}[Wq_m(\tau, \zeta q_m, u(\tau))] - Wp(\tau, \zeta, u(\tau)), \quad (9)$$

where $Wq_m(\tau, \zeta q_m, u(\tau))$ is the energy given up by the soliton at an mth inhomogeneity by the time instant τ and $Wp(\tau, \zeta, u(\tau))$ is the soliton energy loss due to interminizone transitions:

$$Wq_m(\tau, \zeta q_m, u(\tau)) = \int_{\tau_0}^{\tau}\mu_m[1 - \cos(\varphi(\tau', \zeta q_m, u(\tau')))]d\tau', \quad (10)$$

$$Wp(\tau, \zeta, u(\tau)) = \alpha\int_{\tau_0}^{\tau}\int_{\zeta_0}^{\zeta}\left[\frac{\partial\varphi(\tau', \zeta', u(\tau'))}{\partial\tau'}\right]^2 d\zeta' d\tau'. \quad (11)$$

The time instant τ_k the soliton passes a kth inhomogeneity satisfies the equation

$$\int_{\tau_0}^{\tau_k}u(\tau')d\tau' = \zeta q_k. \quad (12)$$

The soliton is written when it is confined between the inhomogeneities by applying a current pulse $j_x^W(t, z) < 0$. When the soliton is confined in the cell, the electric current has to be locally applied to the region $\zeta q_1 < \zeta < \zeta q_2$. The instants the current is switched on and off must meet the condition $\tau_1 \le \tau j_1 < \tau j_2 \le \tau_2$.

A soliton passes through an inhomogeneity N_m in the absence of external actions if its energy and velocity away from the inhomogeneity are

$$Wks > 2\mu_m, \quad u > u_0 = \frac{\sqrt{\mu_m(\mu_m + 8)}}{\mu_m + 4}. \quad (13)$$

Otherwise, the soliton reflects from the inhomogeneity [9], regaining its energy.

For a soliton that has passed through the first inhomogeneity, the condition for reflection from the second

one is given by the inequality

$$Wks(\tau j_1) + Wq_1(\tau_1, \zeta q_1, u(\tau_1)) \le Wj(\tau j_2) + 2\mu_2 + \Delta Wp_{1,2}. \quad (14)$$

The energy $Wj(\tau j_2)$ gained by a soliton from the electric current in the time interval $(\tau j_1; \tau j_2)$ is given by the integral

$$Wj(\tau j_2) = \int_{\tau j_1 \zeta q_1}^{\tau j_2 \zeta q_2} [\beta^W(\tau', \zeta')\varphi(\tau', \zeta', u(\tau'))] d\zeta' d\tau', \quad (15)$$

where

$$\beta^W(\tau', \zeta') = (4\pi/\varepsilon_0)(ed/\hbar)(1/\omega_{pl}^2) j_x^W(t', z').$$

When a soliton propagates in the cell, its energy losses due to interminizone transitions in the time interval $(\tau_1; \tau j_2)$ are

$$\Delta Wp_{1,2} = Wp(\tau j_2, \zeta(\tau j_2)) - Wp(\tau_1, \zeta q_1). \quad (16)$$

By equating the left and right of (14), we obtain an integral equation a solution to which, being solved with (15) and (16), yields the minimum write current $j_x^W(t, z)$.

A soliton reflected from the inhomogeneity N_2 remains confined in the SDL cell. The soliton written executes oscillatory motion between the cell walls, exchanging energy with them. While stored in the cell, the oscillating soliton loses part of the energy given by (11).

To leave the cell, the soliton must gain the energy of a local current pulse $j_x^R(t, z) > 0$. The read current value is calculated similar to that of $j_x^R(t, z)$, which amounts to solving an integral equation.

INTERACTION BETWEEN SOLITONS

Interaction between solitons (kinks) does not change their amplitudes u_1 and u_2 but causes phase shifts [9, 10]

$$\Delta\xi_1 = 2\Gamma_1 \ln[P], \quad \Delta\xi_2 = -2\Gamma_2 \ln[P],$$

where

$$P = \frac{\sqrt{(1+u_1)(1-u_2)} + \sqrt{(1+u_2)(1-u_1)}}{\sqrt{(1+u_1)(1-u_2)} - \sqrt{(1+u_2)(1-u_1)}}. \quad (17)$$

The total phase shift of a soliton scattered by a set of other solitons is the sum of the partial phase shifts. This fact allows for the use of an SCL in two directions simultaneously and increases its transmission rate [1, 2]. Due to the stability of solitons upon interaction, trains of soliton pulses can be delayed and confined solitons can be released in an arbitrary order. To this end, an SDL must contain several cells. Solitons that pass through adjacent cells do not damage those confined therein.

RESULTS OF SIMULATION

The possibility of solitons being confined and released was tested in terms of one-cell and four-cell SDL models. The stability of a soliton is independent of the number of cells, because it is localized within one cell. The simulation of soliton propagation in a superlattice with inhomogeneities was carried out by solving disturbed sine-Gordon equation with singularity (3) subject to appropriate initial and boundary conditions with the finite-difference method.

Consider the operation of a one-cell SDL based on a superlattice with $d = 10^{-8}$ m, $\Delta = 10^{-2}$ eV, $n = 10^{20}$ m^{-3}, $\eta = 10^{-2}$ m^{-1}, $\alpha \approx 1.887 \times 10^{-5}$, and $\omega_{pl} \approx 1.998 \times 10^{12}$ Hz. Let the cell be formed by two inhomogeneities with $D = 10^{-7}$ m, $\Delta n_m/n = 10^2$, $\mu_m = 0.067$, and $\Omega_{pl}^m \approx 1.998 \times 10^{13}$ Hz located in the planes $zq_1 = 7.2 \times 10^{-3}$ m and $zq_2 = 9.6 \times 10^{-3}$ m. The cell size is $r = 2.4 \times 10^{-3}$ m. The initial parameters of a soliton (kink) are $v_0 = 10^8$ m/s, $u \approx 0.333$, $E_0 = 9.303 \times 10^4$ V/m, $\Gamma = 0.943$, $W \approx 0.485$, and $\xi_0 = -13.318$.

The soliton is confined in the cell by applying a trapezoidal current pulse with a steepness $a = \pi/50$. The time instants the soliton passes through the inhomogeneities (they specify the time interval of application of the write current $j_x^W(z, t)$) are determined from (12): $t_1 = 4.2 \times 10^{-11}$ s and $t_2 = 6.8 \times 10^{-11}$ s. The minimum current value needed to confine the soliton with the above amplitude is found from (14): $j_x^W \approx -0.441 \times 10^3$ A/m^2 with $\beta \approx -2.382 \times 10^{-3}$.

The soliton confined in the cell executes oscillatory motion. The oscillation period in the cell with the above parameters is $T \approx 0.1$ ns. The permissible time of soliton storage in the cell is defined by the parameter η of semiconductor materials making up the superlattice and by the write quality required. At $\eta = 0.01$, the logarithmic decrement is $\delta \approx 1.121 \times 10^{-3}$.

The soliton delay is quantized in time. The delay quantum is approximately equal to the soliton's oscillation period in the cell.

Due to attenuation and the action of the electric current, the intensity of the soliton's electric field changes. The variation of the electric field in the principal maximum of the soliton when it is confined for a period and then released is shown in Fig. 2.

To read out the soliton from the cell means to supply an additional energy. For a long delay in the cell, soliton energy loss (11) must be taken into account.

In the case illustrated in Fig. 2, the soliton is amplified by applying the current $j_x^R \approx 1.5 \times 10^3$ A/m^2 after one oscillation period. The current is fed to the cell when the soliton moves along the z axis.

The corresponding space–time distribution of the field extrema when the soliton is confined and released

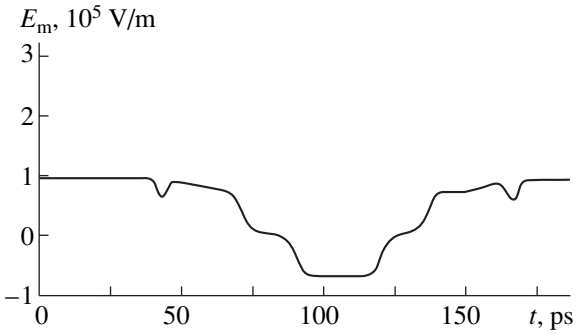

Fig. 2. Time variation of the electric field intensity in the principal maximum of a soliton upon confinement and release.

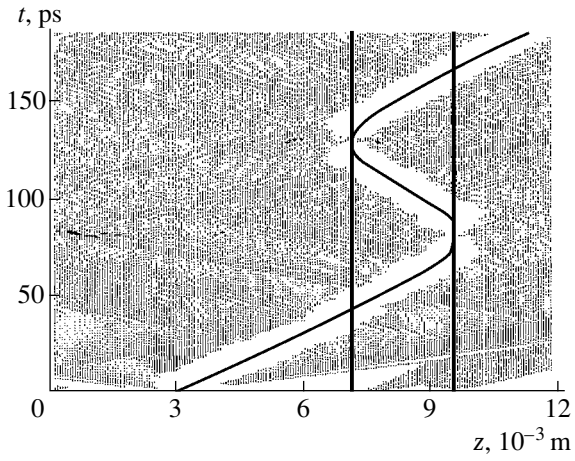

Fig. 3. Space–time distribution of the electric field extrema for a soliton delayed by one period.

is shown in Fig. 3. The positions of the inhomogeneities bounding the cell are shown by thick vertical lines. The soliton pulse moves along the bright curve.

CONCLUSION

The model proposed in this paper makes it possible to produce an SCL with a time-quantized SDL. The delay quantum is specified by the longitudinal dimension of the cell.

To delay a train of soliton pulses, one should use an SDL with several cells provided with control electrodes. It is possible to release solitons from the cell in an order other than the order of their arrival at the SDL. It is reasonable to release the solitons according to the priority of information received.

An SDL (Fig. 1) and control elements can be based on the $Al_xGa_{1-x}As$ superlattice [12, 13] grown by molecular beam epitaxy [10, 11]. Inhomogeneities in the superlattice are usually created in the process of the epitaxy by doping (with a separate beam) or by changing the content of the constituents.

REFERENCES

1. *Fiber-Optics Technology: History, Advances, and Prospects*, Ed. by S. A. Dmitriev and N. N. Slepov (Connect, Moscow, 2000).
2. N. N. Slepov, Seti, No. 3, 90 (1999).
3. É. M. Épshteĭn, Fiz. Tverd. Tela (Leningrad) **19**, 3456 (1977) [Sov. Phys. Solid State **19**, 2020 (1977)].
4. S. A. Gabov, *Introduction to the Theory of Nonlinear Waves* (Mosk. Gos. Univ., Moscow, 1988).
5. M. J. Ablowitz and H. Segur, *Solitons and the Inverse Scattering Transform* (SIAM, Philadelphia, 1981; Mir, Moscow, 1987).
6. G. L. Lamb, Jr., *Elements of Soliton Theory* (Wiley, New York, 1980; Mir, Moscow, 1983).
7. É. M. Épshteĭn, Izv. Vyssh. Uchebn. Zaved. Radiofiz. **24**, 1293 (1981).
8. G. S. Kazacha and S. I. Serdyukova, Zh. Vychisl. Mat. Mat. Fiz. **33**, 417 (1993).
9. S. V. Kryuchkov and K. A. Popov, Fiz. Tekh. Poluprovodn. (St. Petersburg) **30**, 2168 (1996) [Semiconductors **30**, 1130 (1996)].
10. *Molecular Beam Epitaxy and Heterostructures*, Ed. by L. L. Chang and K. Ploog (Martimus Nishoff, Amsterdam, 1985; Mir, Moscow, 1989).
11. L. V. Golubev and E. I. Leonov, Izv. Vyssh. Uchebn. Zaved. Fiz., No. 8, 24 (1997).
12. I. Ya. Gerlovin, Yu. K. Dolgikh, S. A. Eliseev, *et al.*, Fiz. Tekh. Poluprovodn. (St. Petersburg) **33**, 302 (1999) [Semiconductors **33**, 305 (1999)].
13. G. B. Galiev, V. É. Kaminskiĭ, V. G. Mokerov, *et al.*, Fiz. Tekh. Poluprovodn. (St. Petersburg) **34**, 769 (2000) [Semiconductors **34**, 741 (2000)].

Translated by A. Khzmalyan

Technical Physics, Vol. 48, No. 5, 2003, pp. 580–586. Translated from Zhurnal Tekhnicheskoĭ Fiziki, Vol. 73, No. 5, 2003, pp. 57–63.

SOLID-STATE ELECTRONICS

Effect of Oxidizing Environments on the Diffusion–Segregation Boron Distribution in the Thermal Silicon Dioxide–Silicon System

O. V. Aleksandrov* and N. N. Afonin**

** St. Petersburg State Electrotechnical University, ul. Prof. Popova 5, St. Petersburg, 197376 Russia*
e-mail: aleks_ov@maibox.alkor.ru
*** Voronezh State Pedagogical University, ul. Lenina 86, Voronezh, 394043 Russia*
e-mail: nafonin@vspu.ac.ru
Received June 10, 2002

Abstract—The diffusion–segregation boron distribution in the silicon dioxide–silicon system upon oxidation in different environments is studied by secondary-ion mass spectrometry and numerical simulation. The coefficient of boron segregation at the SiO_2/Si interface and the enhancement of boron diffusion in silicon as functions of the type of oxidizing environment (dry oxygen, wet oxygen, and the presence of hydrochloric acid vapor), the orientation of the silicon surface, and the temperature of oxidizing annealing are obtained. A qualitative model is proposed based on the assumption that the segregation mass transfer of boron through the SiO_2/Si interface is associated with the generation of nonequilibrium intrinsic interstitials. *© 2003 MAIK "Nauka/Interperiodica".*

INTRODUCTION

Thermal oxidation, which is widely used in the technology of silicon semiconductor devices and integrated circuits, is accompanied by the segregation of doping impurities at the moving SiO_2/Si interface. Studies of this phenomenon concentrate mainly on the determination of the impurity segregation coefficient m_{seg}, which characterizes the interface properties in terms of segregation mass transfer ($m_{seg} = C''/C'$, where C'' and C' are the impurity concentrations at the SiO_2/Si interface on the side of SiO_2 and Si, respectively). In most of the experimental studies concerned with boron segregation at the SiO_2/Si interface, dry oxygen was used as an oxidizing medium [1–6]. It was found that the coefficient of boron segregation increases with temperature and depends on the orientation of the silicon substrate. It also appeared that even a small amount (2×10^{-3}%) of steam in dry oxygen has an effect on m_{seg} and its temperature dependence [7].

The considerable difference in the values of m_{seg} obtained in different studies under similar experimental conditions [2–7] is noteworthy. The boron segregation coefficient at the SiO_2/Si [1–5] interface was determined indirectly from the design and process parameters of the devices (the sheet resistance R_s and the p–n junction depth x_j) [1–3] or from the concentration profile of boron in silicon [4, 5] in terms of analytical models for diffusion–segregation impurity distribution in silicon. In order to obtain an analytical solution in the simulation of impurity diffusion in a system with moving interfaces, a number of simplifications were adopted. In particular, in [5], the motion of the interface was ignored, and in [1, 2, 4, 5], the kinetics of thermal silicon oxidation was assumed to be parabolic, the impurity diffusion coefficient in silicon was taken to be constant, and a certain profile of the initial impurity distribution was specified.

Secondary-ion mass spectrometry (SIMS) allows for the direct determination of the segregation coefficient from a jump of the signal at the SiO_2/Si interface [6, 7]. However, attendant effects (the difference in the yields of elements of the same mass from silicon and its dioxide, the difference in the ion-etching rates, the presence of charge on the sample surface, etc. [8]) may reduce the reliability of SIMS data. The above disadvantages of the indirect [1–5] and direct [6, 7] methods can be a reason for the great spread in m_{seg} obtained by different authors.

The reliability of experimental results can be improved by applying a complex approach where the concentration distribution of boron in the SiO_2/Si system obtained by SIMS is analyzed in terms of a numerical diffusion–segregation model that is free of restrictions inherent in analytical models and takes into account the accelerating effect of thermal oxidation on impurity diffusion in silicon.

It was shown experimentally that the addition of gaseous HCl to dry oxygen affects the boron distribution in silicon [9]; however, boron segregation upon oxidation in halogen-containing environments has not been investigated. The aim of this work is to study the

1063-7842/03/4805-0580$24.00

effect of an oxidizing environment (dry oxygen, wet oxygen, and an HCl-containing atmosphere) on diffusion–segregation boron distribution in the SiO_2/Si system upon the thermal oxidation of silicon.

EXPERIMENTAL

Dislocation-free KÉF-5[1] (111)Si wafers precoated with a thermal silicon dioxide layer of thickness W_{ox} = 0.1 μm were used as test objects. The wafers were irradiated by boron ions with an energy of 75 keV and a dose of 5.3×10^{14} cm^{-2}. Then the dioxide mask was removed by etching and the samples were thermally oxidized in the temperature range 1000–1100°C in dry O_2, wet O_2, and wet HCl. The oxidizing environment "dry O_2" was produced by cooling oxygen to its dew point 213 K with liquid-nitrogen traps. The wet O_2 was produced by passing oxygen through a bubbler with water held at a temperature of 95°C. The "wet HCl" oxidizing environment was produced by the evaporation of a weak (1–3%) solution of hydrochloric acid on the hot filament of a gas generator through which dry oxygen was passed. The duration of oxidizing annealing was chosen such that the thickness W_{ox} of the dioxide grown varied between 0.1 and 0.2 μm: 1–3 h in the dry oxygen and 3.5–12 min in the wet O_2 and wet HCl environment.

SIMS studies were performed with a Cameca IMS-300 ion microanalyzer equipped with a 100-eV-pass-band energy analyzer. O_2^+ ions were used as primaries. The instrument errors involved in quantitative SIMS analysis were minimized with special approaches described in [8].

Along with these data, we used SIMS data for boron concentration profiles [9] in silicon layers irradiated by B^+ ions with an energy of 50 keV and dose of 1×10^{15} cm^{-2} and oxidized in dry oxygen where the HCl vapor content was varied from 0 to 4%.

MATHEMATICAL MODEL OF DIFFUSION–SEGREGATION IMPURITY DISTRIBUTION

Experimental boron concentration profiles obtained by SIMS were analyzed in terms of a model of diffusion–segregation impurity distribution in the SiO_2/Si system with the moving gas/SiO_2, $x_1(t)$, and SiO_2/Si, $x_2(t)$, interfaces. With diffusion mass transfer in SiO_2 ignored, the impurity distribution is described by the boundary-value Stefan problem stated as

$$\partial C'/\partial t = \nabla((1-\alpha)U_{ox}C'), \quad x_1 < x < x_2, \qquad (1)$$

$$\partial C''/\partial t = \nabla(D(C'')\nabla C''), \quad x_2 < x < l, \qquad (2)$$

where t is time; x is the coordinate measured from the position of the SiO_2/Si interface at zero time, $x_2(0)$, and directed inward to the silicon; l is the extent of the solution domain in the silicon within which the impurity concentration is assumed to be constant throughout annealing; α is the ratio of the thickness of oxidized silicon to that of silicon dioxide W_{ox} (α = 0.44); $U_{ox} = dW_{ox}/dt$ is the silicon oxidation rate; $\nabla \equiv \partial/\partial x$ is the gradient operator; and D is the impurity diffusion coefficient in silicon.

The system of Eqs. (1) and (2) was supplemented by the fitting condition at the SiO_2/Si interface, which reflects the conservation of the total amount of the impurity transferred through the interface due to the motion of the interface and concentration gradient. If the segregation process is assumed to be equilibrium, this condition has the form

$$D\nabla C'' + U_{ox}(\alpha - 1/m_{seg})C'' = 0, \qquad (3)$$

where $m_{seg} = (C''/C')_{eq}$ is the equilibrium segregation coefficient, which is defined as the ratio of the impurity concentrations on the Si and SiO_2 sides of the interface when the system is in thermodynamic equilibrium.

The impurity diffusion coefficient in silicon depends on the impurity concentration and oxidation rate (so-called oxidation-enhanced diffusion (OED)). In simulating OED, we will assume that boron in the silicon lattice diffuses by the dual vacancy–interstitial mechanism. In this case, the impurity diffusion coefficient is given by [10]

$$D = D^*(f_v a_v + f_{int} a_{int}), \qquad (4)$$

where D^* is the impurity diffusion coefficient for the equilibrium distribution of intrinsic point defects; f_v and f_{int} are the relative fractions of the vacancy and interstitial mechanisms of diffusion, respectively ($f_v + f_{int} = 1$); $a_v = V/V_{eq}$ and $a_{int} = I/I_{eq}$ are the coefficients of supersaturation (or undersaturation) by vacancies and intrinsic interstitials, respectively; and V_{eq}, I_{eq} and V, I are the concentrations of equilibrium and nonequilibrium vacancies and intrinsic interstitials, respectively.

Under local equilibrium conditions, $a_v = 1/a_{int}$ according to the law of mass action. From recent results [11], $f_{int} \cong 0.9$. Because of the weak time dependence of OED [12], in (4) we used the average, $a_{int} = \langle I \rangle / I_{eq}$, instead of instantaneous, concentration of intrinsic interstitials and assumed that averaging is coordinate-invariant in the region of impurity localization.

Under equilibrium conditions, the coefficient of boron diffusion via intrinsic point defects in silicon was calculated from the concentration dependence [13]

$$D^* = h_e(D_i^0 + D_i^+ p/n_i), \qquad (5)$$

where h_e is the factor of diffusion enhancement by the internal electric field; D_i^0 and D_i^+ are the partial coefficients of diffusion via neutral and positively charged

[1] Phosphorus-doped with a resistivity of 5 Ω cm.

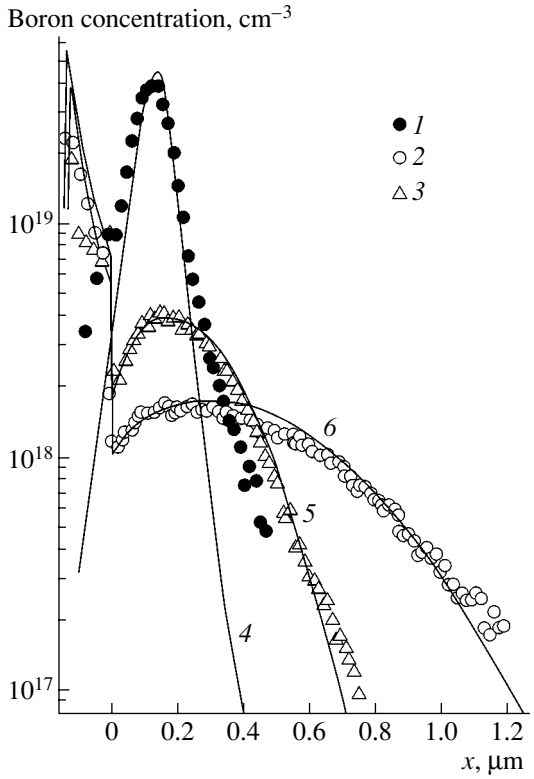

Fig. 1. Boron concentration profiles in the SiO_2/Si system after (*1*, *4*) implantation (B^+, 75 keV, 5.31×10^{14} cm^{-2}) through the 0.1-μm-thick oxide and annealing at 1050°C in (*2*, *5*) dry O_2 for 2 h and (*3*, *6*) wet HCl for 5 min. Symbols, data points (SIMS); curves, simulation. (*5*) $m_{seg} = 0.19$, $a_{int} = 2.4$ and (*6*) $m_{seg} = 0.28$, $\alpha = 11$.

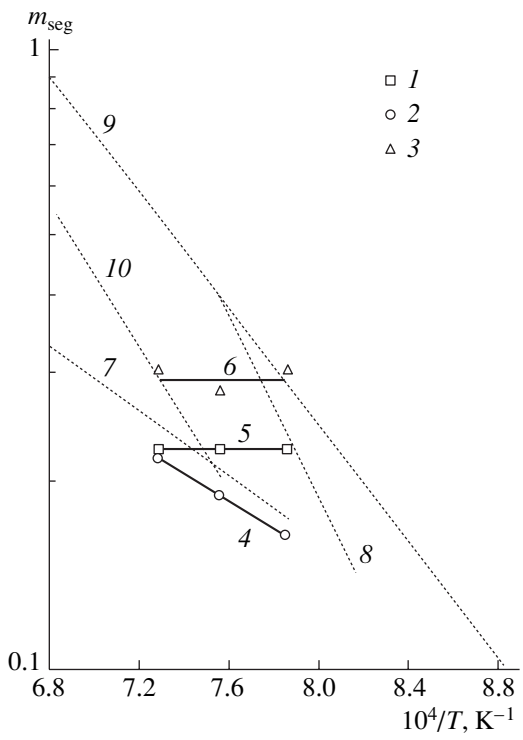

Fig. 2. Temperature dependence of m_{seg} for boron at the SiO_2/Si(111) interface. The symbols refer to oxidation in (*1*) dry O_2, (*2*) wet O_2, and (*3*) wet HCl. The curves are analytical $m_{seg}(T)$ dependences: (*4*) relationship (*7*), (*5*) $m_{seg} = 0.22$, (*6*) $m_{seg} = 0.29$, (*7*) from [6], (*8*) from [5], (*9*) from [3], and (*10*) from [1].

intrinsic point defects, respectively; $p = 1/2[(C'' - C_d'') + \sqrt{(C'' - C_d'')^2 + 4n_i^2}]$ is the hole concentration; n_i is the intrinsic carrier concentration at the temperature of diffusion; and C_d is the donor concentration in the substrate.

The oxidation kinetics was described by the linear–parabolic dependence

$$t = W_{ox}^2/k_p + W_{ox}/k_l, \quad (6)$$

where k_p and k_l are, respectively, the parabolic and linear rate constants of silicon oxidation (for the values of k_p and k_l, see [14]).

The experimental or model impurity distribution arising immediately after the ion implantation into silicon or the two-phase SiO_2/Si system was taken as the starting distribution. The simulation of the ion implantation process was carried out by using the four-parameter Pearson function with its moments given in [15].

To numerically solve Eqs. (1) and (2) with equilibrium boundary condition (3), we reduced the problem, by changing the variables, to the fixed-interface problem. The latter was solved by factorization with uniform implicit conservative difference schemes [16].

EXPERIMENTAL RESULTS

The boron segregation coefficient m_{seg} and the OED parameter $a_{int} = \langle I \rangle / I_{eq}$ for boron were determined from the best fit of the solution to problem (1)–(3) to experimental boron concentration profiles in the SiO_2/Si system. Figure 1 compares the experimental boron profiles (data points *1–3*) with the results of simulation (curves *4–6*) for oxidation at 1050°C in (*2*, *5*) dry O_2 and (*3*, *6*) wet HCl.

The SIMS measurements demonstrate that, in the temperature range considered, the coefficients of boron diffusion and segregation in the SiO_2/Si system depend on experimental conditions, particularly, on the oxidizing environment, surface orientation of the silicon, and temperature. Figure 2 illustrates the temperature dependence of the boron segregation coefficients at the SiO_2/Si(111) interface upon oxidation in the media under study. As follows from Fig. 2, the boron segregation coefficients in the temperature range T = 1000–1100°C meets the inequality m_{seg} (dry O_2) < m_{seg} (wet O_2) < m_{seg} (wet HCl). After annealing in the dry O_2 atmosphere, the segregation coefficient varies from 0.16 to 0.22 and its temperature dependence can be

approximated by

$$m_{seg} = 8.2\exp(-0.43\ \text{eV}/kT). \quad (7)$$

Upon oxidation in the wet O_2 and in wet HCl, $m_{seg} \cong 0.22$ and 0.3, respectively, and is practically independent of the temperature in both cases. The dotted lines in Fig. 2 show dependences obtained elsewhere for the oxidation of Si(111) in dry O_2 [3, 5, 6] and steam [1]. Note that dependence (7) for dry O_2 is close to the corresponding dependence in [6] also obtained by SIMS. On the other hand, both differ substantially from the corresponding dependences for dry O_2 [3, 5] and steam [1] obtained by indirect methods.

Figure 3 compares the temperature dependence of m_{seg} at the SiO_2/Si(100) interface under oxidation in the dry O_2–HCl vapor (0–4%) atmosphere that is obtained from the experimental boron profiles in silicon [9] with the corresponding curves [2, 3, 5–7] (dotted lines) for the oxidation of Si(100) in dry O_2. In the absence of HCl vapor, the experimental data are described by the relationship

$$m_{seg} = 2.3\times10^{2}\exp(-0.74\ \text{eV}/kT). \quad (8)$$

The addition of HCl vapor to dry oxygen decreases m_{seg} and changes the slope of the curve $m_{seg}(T)$; namely,

$$m_{seg} = 1.92\times10^{3}\exp(-1.01\ \text{eV}/kT) \quad (9)$$

for 2% of HCl and

$$m_{seg} = 1.7\times10^{3}\exp(-1.01\ \text{eV}/kT) \quad (10)$$

for 4% of HCl.

Note that dependence (8) for dry O_2 is similar to the corresponding dependences from [6, 7] obtained by SIMS. However, these curves differ substantially from those found in [2, 3, 5] by indirect methods.

The temperature dependences of the OED parameter a_{int} on the oxidation of Si(111) and Si(100) are shown in Fig. 4. In the environments under study, the relationship a_{int} (dry O_2) < a_{int} (wet HCl) < a_{int} (wet O_2) is fulfilled for Si(111) (curves *1–3*). The increase in the HCl content in dry O_2 decreases a_{int} in Si(100) (curves *4*, *5*) despite an increase in the oxidation rate by a factor of 1.5 and 1.6 when 2 and 4% of HCl vapor, respectively, are added to dry O_2 at T = 1000°C [9], as follows from the kinetic dependences $W_{ox}(t)$ found experimentally in [14].

Figure 5 demonstrates the a_{int} vs. oxidation rate U_{ox} dependences under different oxidation conditions. It is seen that data points *1–1*" for annealing in dry O_2 fit fairly closely the relationship $a_{int} \sim U_{ox}^{0.3}$ obtained in [5] (curves *6–6*"). Oxidation in wet HCl and wet O_2 (data points *2–2*" and *3–3*") is described adequately by the relationship $a_{int} \sim U_{ox}^{0.25}$ (curve *5*), which was found in [12] for steam oxidation. For all the environments, an increase in the temperature of oxidative annealing causes a_{int} to decrease, although the average oxidation rate $\langle U_{ox}\rangle$ grows.

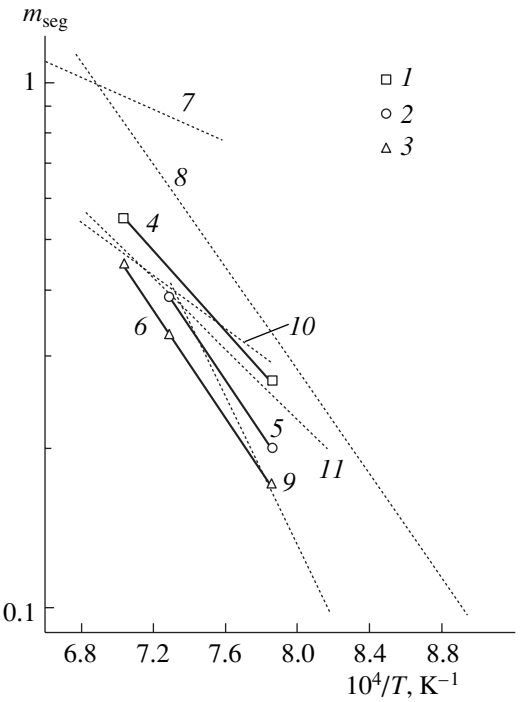

Fig. 3. Temperature dependence of m_{seg} for boron at the SiO_2/Si(100) interface. The symbols refer to oxidation in dry O_2 with the addition of HCl vapor: (*1*) 0, (*2*) 2, and (*3*) 4%. The curves are analytical $m_{seg}(T)$ dependences: (*4*) relationship (8), (*5*) (9), and (*6*) (10). Curves *7–11* are taken from [2], [3], [5], [6], and [7], respectively.

DISCUSSION

From the boron profiles obtained by SIMS and their numerical analysis, it is found that the segregation coefficient of boron m_{seg} and the OED parameter a_{int} depend on oxidation conditions, in particular, on the oxidizing atmosphere, silicon surface orientation, and temperature. At the same temperature, m_{seg} (dry O_2) < m_{seg} (wet O_2) < m_{seg} (dry wet HCl) (Fig. 2), m_{seg} (dry O_2) > m_{seg} (dry O_2 + 2% HCl) > m_{seg} (dry O_2 + 4% HCl) (Fig. 3), a_{int} (dry O_2) < a_{int} (wet HCl) < a_{int} (wet O_2) (Fig. 4), and a_{int} (dry O_2) > a_{int} (dry O_2 + 2% HCl) > a_{int} (dry O_2 + 4% HCl). Also, for dry O_2, m_{seg} (100) > m_{seg} (111) (cf. Figs. 2, 3) and a_{int} (111) < a_{int} (100) (Fig. 4).

The increase in a_{int} upon annealing in wet O_2 in comparison with annealing in dry O_2 is explained merely by the increase in the oxidation rate. Earlier, it was found that the supersaturation by intrinsic interstitials, a_{int}, which is responsible for the enhancement of B and P diffusion in Si and an increase in the number of stacking faults upon oxidation, varies as $(U_{ox})^b$, where b = 0.25–0.5 [5, 12]. Our data confirms this result, giv-

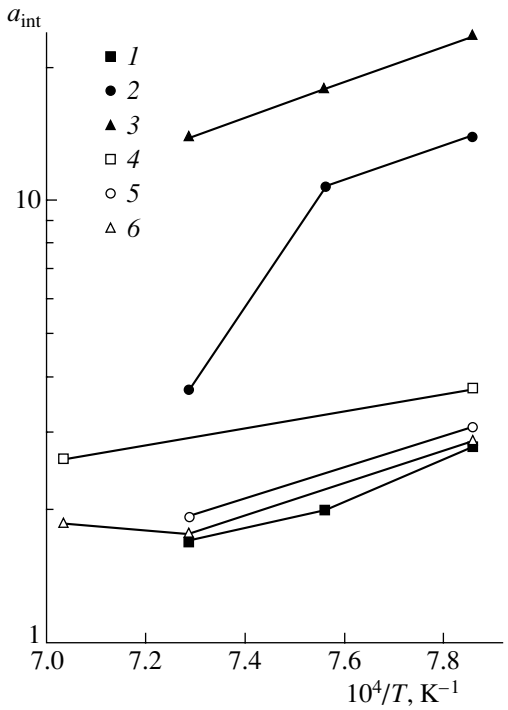

Fig. 4. Temperature dependence of a_{int} upon the oxidation of Si(111) in (*1*) dry O_2, (*2*) wet HCl, and (*3*) wet O_2 and upon the oxidation of Si(100) in dry O_2 with the addition of HCl: (*4*) 0, (*5*) 2, and (*6*) 4%.

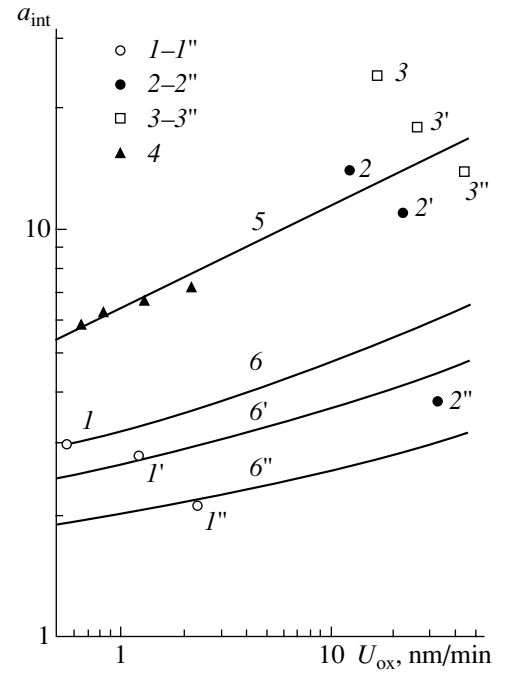

Fig. 5. a_{int} as a function of oxidation rate for annealing in (*1*–*1*") dry O_2, (*2*–*2*") wet HCl, (*3*–*3*") wet O_2, and (*4*) H_2O vapor [12]. Annealing temperature is (*1*–*5*) 1000, (*1*'–*6*') 1050, and (*1*"–*6*") 1100°C. The symbols are data points; the curves, empirical dependences from [5] (*6*–*6*") and [12] (*5*).

ing $b \cong 0.3$ in dry O_2 and $b \cong 0.25$ in wet O_2 and wet HCl (Fig. 5).

When explaining the variation of m_{seg} for boron with the addition of steam to oxygen, Fair and Tsai [7] suggested that metaboric acid HBO_2, instead of boron oxide B_2O_3, forms in SiO_2 at the interface. Chemical transformations in solid phases assume the presence of some free volume V_f when the molecular volume of a parent material ($\Omega(Si) \cong 0.02$ nm^3) is smaller than the molecular volume of a reaction product ($\Omega(SiO_2) \cong 0.044$ nm^3). Therefore, the effect of the oxidation medium on m_{seg} can be explained if we assume the presence of a free space in silicon dioxide at the interface that provides the chemical interaction of silicon and boron with the oxidant. This free space is also necessary for a forming structural fragment, a silicon–oxygen tetrahedron SiO_4, and boron oxide to be built into the network structure of silicon dioxide. The reactions of silicon oxidation in dry O_2 and wet O_2 then have the form

$$Si + O_2 + V_f \rightleftharpoons SiO_2, \quad (11)$$

$$Si + 2H_2O + V_f \rightleftharpoons SiO_2 + 2H_2. \quad (12)$$

According to today's concept [12, 17], the free volume arises when silicon atoms occupy interstices with the formation of excess silicon interstitials in silicon dioxide and nonequilibrium intrinsic interstitials in silicon. The addition of HCl vapor to dry O_2 accelerates oxidation. A possible reason for this effect is the etching of the silicon surface by HCl vapor, as a result of which silicon atoms are removed from regular lattice sites at the interface on the side of silicon dioxide, forming vacancies and thereby providing an additional free space for silicon oxidation. The concentration of silicon interstitials decreases due to their interaction with the vacancies, as evident by the decay of the OED of boron in silicon as the HCl content increases (Fig. 4, curves *4*–*6*). Upon oxidation in wet oxygen, where steam is the major oxidant, the presence of HCl vapor effectively diminishes the oxidation rate presumably because of a decrease in the steam pressure [18]. Eventually, the OED of boron in silicon in wet HCl becomes less pronounced than in wet O_2 (Fig. 4; curves *2*, *3*).

Let us assume that impurity boron atoms interact with free particles of the oxidant to form native oxide B_2O_3 regardless of the oxidizing atmosphere. Since the molecular volume of boron oxide ($\Omega(B_2O_3) \cong 0.063$ nm^3) per boron atom is larger than the silicon atomic volume upon the formation of boron oxide and also silicon oxide, the presence of a free volume V_f' is necessary. If oxygen as the major oxidant, boron oxide forms according to the reaction

$$4B + 3O_2 + V_f' \rightleftharpoons 2B_2O_3. \quad (13)$$

With HCl vapor added to dry oxygen, the free volume V_f' increases and boron oxidation at the interface on the side of silicon dioxide is accelerated according to reaction (13). Therefore, the segregation mass transfer of boron from silicon to silicon dioxide through the SiO_2/Si interface is intensified. This shows up as the decrease in m_{seg} with increasing HCl content in the oxidizing medium (Fig. 3).

In wet O_2, where H_2O molecules are major oxidizing particles, boron oxidation also needs a free volume:

$$4B + 6H_2O + V_f' \rightleftharpoons 2B_2O_3 + 6H_2. \quad (14)$$

The addition of HCl vapor to wet oxygen reduces the vapor pressure of the oxidant and, according to reaction (12), decreases the oxidation rate. This causes a free volume to appear. As follows from reaction (14), the same reason retards the formation of B_2O_3 and makes the segregation mass transfer of boron from silicon to silicon dioxide through the SiO_2/Si interface difficult. This shows up in the increase in the segregation coefficient: m_{seg} (wet HCl) > m_{seg} (wet O_2) (Fig. 2). Because of the reduced oxidation rate and the etching effect observed, the density of intrinsic interstitials and the OED parameter a_{int} in wet HCl are lower than in HCl-free wet oxygen: a_{int} (wet HCl) < a_{int} (wet O_2).

Note that boron oxidation at the interface may go in parallel with boron reduction from B_2O_3 by free silicon interstitials:

$$2B_2O_3 + 3Si \rightleftharpoons 3SiO_2 + 4B. \quad (15)$$

The equilibrium constant of reaction (15) is given by

$$K = C_{SiO_2}^3 C_B^4 / C_{Si}^3 C_{B_2O_3}^2, \quad (16)$$

where C_{SiO_2}, C_B, C_{Si}, $C_{B_2O_3}$ are the concentrations of particles involved in the reaction.

The thermodynamic calculation [19] showed that the equilibrium constant of reaction (15) decreases with increasing temperature; accordingly, the reduction of boron by silicon slows down. This is expected to increase the boron oxidation rate in concurrent reactions (13) and (14) and to decrease m_{seg} with growing temperature of oxidation annealing. As a result, the temperature dependence of m_{seg} changes. The increase in the concentration of silicon interstitials with oxidation rate must increase, according to reaction (15), the rate of boron reduction by silicon and suppress the segregation mass transfer of boron from silicon to silicon dioxide through the interface. This explains the increase in m_{seg} and the weakening of its temperature dependence upon annealing in wet O_2 compared with annealing in dry O_2.

The effect of the silicon surface orientation on the boron segregation coefficient in the SiO_2/Si system, m_{seg} (100) > m_{seg} (111), upon oxidation in dry O_2, which is revealed in this paper, is in agreement with the results obtained in [3, 6]. Note that the reverse inequality found in [4, 5] may be related to the indirect determination of m_{seg} and the neglect of the effect of surface orientation on boron diffusion enhancement by oxidation.

The effect of orientation on m_{seg} was explained [6] under the assumption that m_{seg} measured is nonequilibrium for at least one of the surface orientations. The character of the segregation process may really change in the case of kinetic impurity trapping by growing dioxide; however, this effect occurs at relatively low temperatures and high oxidation rates [20, 21]. In our case, this would mean that m_{seg} increases for the (111) orientation with a higher oxidation rate, which is inconsistent with the data of [3, 6] and ours.

The segregation theory based on the equilibrium dynamics of interfacial chemical reactions [7] does not predict the orientation dependence of m_{seg}. It is taken into account formally by including the orientation dependence of the boron activity coefficient in silicon dioxide. Reasons for the phenomenon are not considered.

The oxidation of Si(111) proceeds at a higher rate than that of Si(100), $U_{ox}(111) > U_{ox}(100)$, due to a higher density of available bonds on the (111) surface. However, for the OED parameter of boron, we have a_{int} (111) < a_{int} (100) (Fig. 4; curves *1*, *4*). This result may be explained, on the one hand, by the loss of the orientation dependence of the oxidation rate in the parabolic oxidation regime and, on the other hand, by an increased surface density of traps on the Si(111) surface, which act as sinks for excess silicon interstitials [17]. Therefore, the SiO_2/Si(111) interface will have a lower effective rate of generation of intrinsic interstitials and, correspondingly, a higher rate of free volume generation than the SiO_2/Si(100) interface. In view of reaction (13), this will accelerate boron oxidation at the interface on the side of silicon dioxide and, thus, favor the segregation mass transfer of boron from silicon to silicon dioxide through the SiO_2/Si interface; as a result, m_{seg} (111) < m_{seg} (100).

CONCLUSIONS

Thus, we studied the diffusion–segregation boron distribution upon the thermal oxidation of silicon in different environments, using the complex approach. It combines taking concentration impurity profiles in the SiO_2/Si system by SIMS and their analysis in terms of the numerical diffusion–segregation model. The dependence of the boron segregation coefficient at the SiO_2/Si interface and oxidation-enhanced diffusion parameter of boron in silicon on the type of the oxidizing medium (dry O_2, wet O_2, and the presence of HCl vapor in them), the orientation of the silicon surface, and the annealing temperature was found. HCl vapor present in dry oxygen and in wet oxygen increases and

decreases, respectively, the segregation mass transfer of boron from silicon to silicon dioxide through the interface, while OED is suppressed in both cases. Based on the experimental data obtained, we suggested a qualitative model that relates the segregation mass transfer of boron through the SiO_2/Si interface to the generation of nonequilibrium intrinsic interstitials under thermal oxidation.

ACKNOWLEDGMENTS

We thank A.P. Kovarskiĭ for taking boron concentration profiles by SIMS.

REFERENCES

1. J. L. Prince and F. N. Schwettmann, J. Electrochem. Soc. **121**, 705 (1974).
2. S. P. Murarka, Phys. Rev. B **12**, 2502 (1975).
3. D. A. Antoniadis, A. G. Gonzales, and R. W. Dutton, J. Electrochem. Soc. **125**, 813 (1978).
4. G. Masetti, S. Solmi, and G. Soncini, Solid State Electron. **19**, 545 (1976).
5. M. Miyake and H. Harado, J. Electrochem. Soc. **129**, 1097 (1982).
6. J. W. Colby and L. E. Katz, J. Electrochem. Soc. **123**, 409 (1976).
7. R. B. Fair and J. C. C. Tsai, J. Electrochem. Soc. **125**, 2050 (1978).
8. O. A. Aleksandrov, N. N. Afonin, and A. P. Kovarskiĭ, Kondens. Sredy Mezhfaz. Granitsy **1** (2), 181 (1999).
9. R. Sabrahmanyan, Z. Hishman, and R. B. Fair, J. Appl. Phys. **61**, 4804 (1987).
10. P. M. Fahey, P. B. Griffin, and J. D. Plummer, Rev. Mod. Phys. **61**, 289 (1989).
11. A. Ural, P. B. Griffin, and J. D. Plummer, J. Appl. Phys. **85**, 6440 (1999).
12. N. Jeng and S. T. Dunham, J. Appl. Phys. **72**, 2049 (1992).
13. C. P. Ho, J. D. Plummer, S. E. Hansen, *et al.*, IEEE Trans. Electron Devices **30**, 1438 (1983).
14. D. W. Hess and B. E. Deal, J. Electrochem. Soc. **124**, 735 (1977).
15. A. F. Burenkov, F. F. Komarov, M. A. Kumakhov, *et al.*, *Spatial Distributions of Energy Released in Cascade Collisions of Atoms in Solids* (Énergoizdat, Moscow, 1985).
16. A. A. Samarskiĭ, *The Theory of Difference Schemes* (Nauka, Moscow, 1977).
17. S. M. Hu, J. Appl. Phys. **45**, 1567 (1974).
18. B. E. Deal, J. Electrochem. Soc. **125**, 576 (1978).
19. V. Ya. Zaĭtsev, Izv. Akad. Nauk SSSR, Neorg. Mater. **14**, 963 (1978).
20. O. A. Aleksandrov and N. N. Afonin, Fiz. Tekh. Poluprovodn. (St. Petersburg) **32** (1), 19 (1998) [Semiconductors **32**, 15 (1998)].
21. O. A. Aleksandrov and N. N. Afonin, Kondens. Sredy Mezhfaz. Granitsy **2** (2), 128 (2000).

Translated by M. Lebedev

Technical Physics, Vol. 48, No. 5, 2003, pp. 587–591. Translated from Zhurnal Tekhnicheskoĭ Fiziki, Vol. 73, No. 5, 2003, pp. 64–68.

SOLID-STATE ELECTRONICS

Thermal Expansion and Thermal Conductivity of $CuGa_{1-x}In_xTe_2$ Solid Solutions

I. V. Bodnar

Belarussian State University of Information Science and Radio Engineering, ul. Brovki 17, Minsk, 220072 Belarus
e-mail: chemzav@gw.bsuir.unibel.by

Received July 10, 2002; in final form, November 13, 2002

Abstract—The thermal expansion coefficients and the thermal conductivity of Bridgman-grown crystals of $CuGa_{1-x}In_xTe_2$ solid solutions are investigated. It is found that the thermal expansion coefficient varies with x linearly, while the thermal conductivity is minimal when $x = 0.5$. The Debye temperature and the rms dynamic atomic displacements are calculated from experimental data. It is shown that the Debye temperature decreases and the rms displacements in the crystal lattice sharply increase as the In content in the solid solutions grows.

INTRODUCTION

$CuInTe_2$ and $CuGaTe_2$ compounds, as well as $CuGa_{1-x}In_xTe_2$ solid solutions, crystallize into the chalcopyrite structure (space group D_{2d}^{12}–142d) and are the electronic chemical analogues of II–VI compounds [1]. Such properties as the absence of the inversion center, high nonlinear susceptibility, natural photopleochroism, and many others make these semiconductors promising for quantum and solid-state electronics [2–4]. These semiconductors were studied at length in [5–8].

The physicochemical and optical properties of $CuGa_{1-x}In_xTe_2$ solid solutions were examined in [9, 10]. In this work, we for the first time investigate their electrical and thermal properties.

EXPERIMENTAL

$CuInTe_2$ and $CuGaTe_2$ ternary compounds, as well as $CuGa_{1-x}In_xTe_2$ solid solutions, were grown by the horizontal Bridgman method. The metals and tellurium were contained at opposite ends of an evacuated quartz ampoule. The ampoule was placed in a two-zone horizontal furnace. The zone with the metal charge was heated to 1100–1170 K (depending on the composition of the compound or solid solution), and the zone with tellurium was heated to 1000 K with a rate of ≈100 K/h and kept at this temperature for 3 h. Then, oriented crystallization was accomplished by decreasing the melt temperature to 1000 K with a rate of ≈2 K/h. At the same temperature, the homogenizing annealing of the crystals grown was carried out for 500 h. After the annealing, the $CuGa_{1-x}In_xTe_2$ ingots had large blocks with maximal dimensions of $10 \times 4 \times 4$ mm.

The compositions of the $CuInTe_2$ and $CuGaTe_2$ ternary compounds, as well as the $CuGe_{1-x}In_xTe_2$ solid solutions, were determined by electron probe X-ray spectrum microanalysis with a Camera-MBX X-ray microanalyzer (Fig. 1). Calculated and experimental data are seen to be in good agreement.

The equilibrium state of the compounds and the homogeneity of the solid solutions were checked by X-ray diffraction analysis by means of a DRON-3M diffractometer (CuK_α radiation) with a nickel filter. Dif-

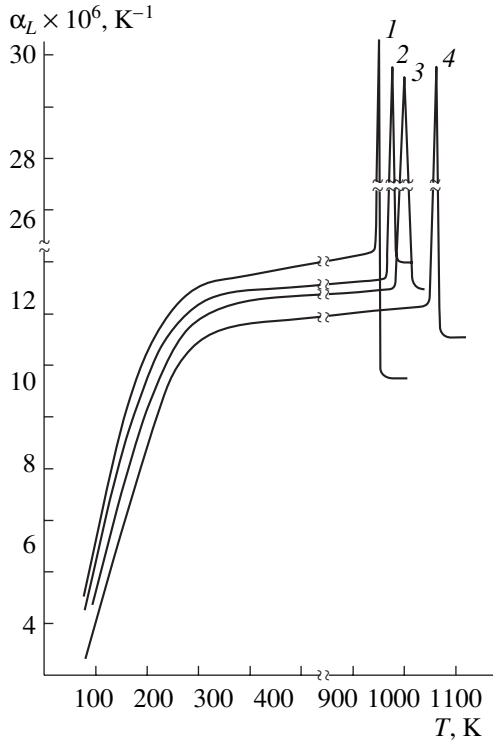

Fig. 1. Temperature dependence of the thermal expansion coefficient for (*1*) $CuInTe_2$, (*2*) $CuGa_{0.4}In_{0.6}Te_2$, (*3*) $CuGa_{0.6}In_{0.4}Te_2$, and (*4*) $CuGaTe_2$.

1063-7842/03/4805-0587$24.00 © 2003 MAIK "Nauka/Interperiodica"

fractograms taken from different parts of ingots of both the compounds and solid solutions contained a set of lines characteristic of the chalcopyrite structure. From the diffraction angles measured, we calculated the interplanar spacings for various planes of diffraction and from the interplanar spacings, the cell parameters by the least-squares method. The cell parameters were found to be $a = 6.184 \pm 0.002$ Å, $c = 12.371 \pm 0.005$ Å for $CuInTe_2$ and $a = 6.024 \pm 0.002$ Å, $c = 11.924 \pm 0.005$ Å for $CuGaTe_2$, which agrees with data in [5–8]. These values vary with x linearly (in accordance with the Vegard law).

The homogeneity of the $CuGa_{1-x}In_xTe_2$ solid solutions was judged from the resolution of high-angle ($2\Theta > 60°$) lines in the diffractograms.

The Hall effect on the crystals grown and their resistivity ρ were measured by the standard technique [11, 12]. Specimens measuring $6 \times 2 \times 1$ mm on average were cut from the crystals. Contacts to the specimens were made of silver paste (Kontaktol) fired-in at a temperature of 520 K in the hydrogen atmosphere. The measurements were performed in a vacuum at 300 K. The electrical parameters were calculated by formulas given in [11, 12]. To eliminate stray effects, four measurements at two directions of the current through the specimen and two directions of the magnetic field were made. As follows from the measurements of the resistivity and Hall effect that were made with different pair of probes, the crystals were electrically uniform: the spread in the measurands did not exceed 4%.

RESULTS AND DISCUSSION

As follows from the measurements, all the crystals have the conductivity of the p type. For the $CuInTe_2$ and $CuGaTe_2$ ternary compounds and also for the $CuGe_{1-x}In_xTe_2$ solid solutions, $\rho = (1.5–10)\ \Omega$ cm; the hole mobility, 20–50 $cm^2/(V\ s)$; and the hole concentration, $(2–8) \times 10^{17}$ cm^{-3}. The decreased mobility (to 20 $cm^2/(V\ s)$) and the increased carrier concentration (8×10^{17} cm^{-3}) for x in the intermediate range ($x = 0.4–0.6$) are noteworthy. This can be explained by scattering by lattice defects.

The thermal expansion of the ternary compounds and solid solutions was measured with a quartz dilatometer, where the thermal expansion of solids is measured relative to the thermal expansion of quartz [13]. Prior to the measurements, the instrument was evacuated and filled with an inert gas to prevent the decomposition and oxidation of the specimen. The temperature was measured by a Chromel–Copel thermocouple with an accuracy of no worse than 5%. The specimen was heated with a rate of 3–5 K/min, which provided reproducible results. The temperature dependence of the relative elongation $\Delta l/l_0$ was taken from the specimens with average dimensions of $3 \times 3 \times 8$ mm.

Both for $CuInTe_2$ and $CuGaTe_2$ ternary compounds and for the solid solutions, the temperature curves $\Delta l/l_0(T)$ exhibit a step near the α–β phase transition. The phase transition temperatures for these materials that were obtained in this work from the thermal expansion measurements are in agreement with differential thermal analysis (DTA) data [9].

The temperature dependences of the linear thermal expansion coefficient α_l for the ternary compounds and solid solutions are shown in Fig. 1. Both for the compounds and the solid solutions, α_l linearly grows with temperature in the range 80–290 K. Then, the growth of α_l slows down up to the phase transition temperature. Near the phase transition, the thermal expansion coefficient changes λ-wise.

Thus, as follows from the DTA data [9] and our experimental dependences $\alpha_l = f(T)$, the phase transitions in $CuInTe_2$ and $CuGaTe_2$ ternary compounds and in $CuGa_{1-x}In_xTe_2$ solid solutions are first-order transitions, since they are accompanied by thermal effects. However, unlike typical first-order phase transitions, which occur at a constant temperature, the phase transitions in these materials are observed in a temperature range with a λ-wise change in α_l; in this respect, they are akin to second-order phase transitions.

At the same time, it is known that I–III–VI_2 ternary compounds exhibit phase transitions of two types [14], which are due to cation–cation and cation–anion disorder. High-temperature X-ray studies [15, 16] showed that, due to cation–cation disorder, these ternary compounds experience the transition from the chalcopyrite to sphalerite (zinc blende) structure. Therefore, we may assume that the solid-phase transformations observed in $CuGa_{1-x}In_xTe_2$ solid solutions are also the chalcopyrite sphalerite phase transition by analogy with I–III–VI_2 ternary compounds.

Physically, the solid-phase transformations observed in these substances (which, as was indicated above, are likely to be the phase transition from ordered lower symmetry chalcopyrite to random higher symmetry sphalerite) can be represented as follows. In the case of cation–cation disorder, which takes place in the range 15–30 K, some of the atoms in the cation sublattice exchange sites. As long as the probabilities of occupation of different sites by cations are unequal, these sites remain nonequivalent and the structure remains unchanged (chalcopyrite). When these probabilities are equalized, all the sites in the cation sublattice become equivalent and the chalcopyrite structure turns to the higher symmetry sphalerite structure. To substantiate the above considerations, the ternary compounds and solid solutions heated above the temperature of the phase transition corresponding to cation–cation disorder were quenched by immersing in liquid nitrogen. The high-temperature sphalerite modification was retained in none of the materials. This fact also indicates that the phase transformations observed in the

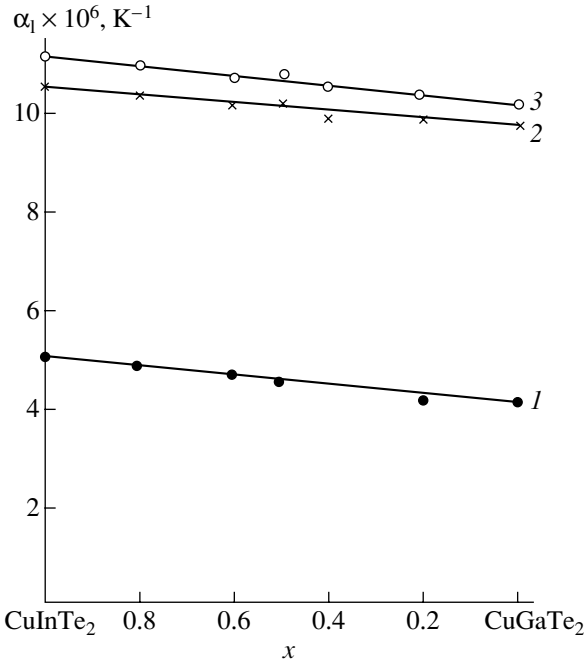

Fig. 2. Concentration dependence of the thermal expansion coefficient for $CuGa_{1-x}In_xTe_2$ solid solutions at (*1*) 100, (*2*) 300, and (*3*) 600 K.

materials studied are close to second-order phase transitions, since they are accompanied by overheating and overcooling.

Figure 2 shows isotherms for the concentration dependencies of the thermal expansion coefficient. It is seen that α_l grows linearly with the gallium content in the solid solutions.

From the melting points and thermal expansion coefficients found experimentally, we calculated the Debye temperatures Θ and rms atomic displacements $\sqrt{\bar{u}}$ using the following formulas [17, 18]:

$$\Theta^{\alpha} = 14.3/\alpha_l^{1/2}\bar{A}^{1/2}V^{1/3}, \quad (1)$$

$$\Theta^{T_m} = 137T_m^{1/2}/\bar{A}^{1/2}V^{1/3}, \quad (2)$$

$$\bar{u}^2 = 4.3\times10^{-14}[D(\Theta/T)/\Theta/T + 1/4]/\bar{A}\Theta, \quad (3)$$

where α_l is the thermal expansion coefficient, $\bar{A}$ is the mean atomic mass, V is the mean atomic volume, T_m is the melting point, and $D(\Theta/T)$ is the Debye function.

The results of calculation are listed in Table 2, from which it follows that the Debye temperature decreases and the rms atomic displacements in the lattice increase as the gallium content in the solid solutions rises. Such behavior of these parameters suggests that chemical bonds in $CuGa_{1-x}In_xTe_2$ solid solutions loosen with increasing gallium concentration.

The thermal conductivity χ of the compounds and solid solutions was measured with the absolute stationary method [19] at temperatures between 300 and 350 K on specimens with the dimensions mentioned above. The accuracy of measurement was 6%. The temperature dependence of χ is depicted in Fig. 3. The thermal conductivity of the compounds varies as T^{-1} in the range 300–400 K, which is typical of three-phonon scattering processes. This result agrees with the Peierls theory, according to which χ is inversely proportional to temperature at temperatures above the Debye temperature. In this case, three-phonon scattering takes place, during which the phonons exchange energy. As a

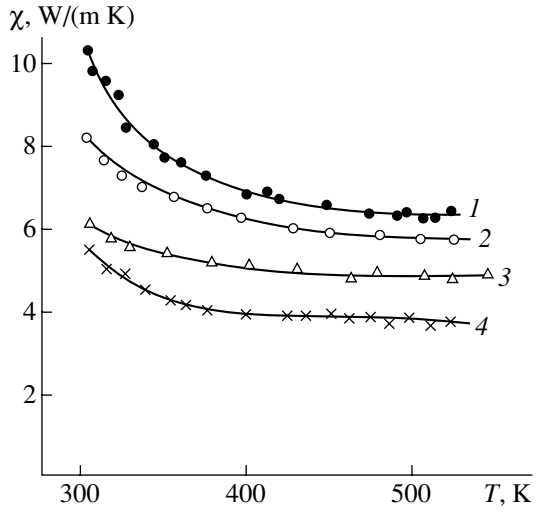

Fig. 3. Temperature dependence of the thermal conductivity for $CuGa_{1-x}In_xTe_2$ solid solutions at x = 0.0 (*1*), 0.1 (*2*), 0.2 (*3*), and 1.0 (*4*).

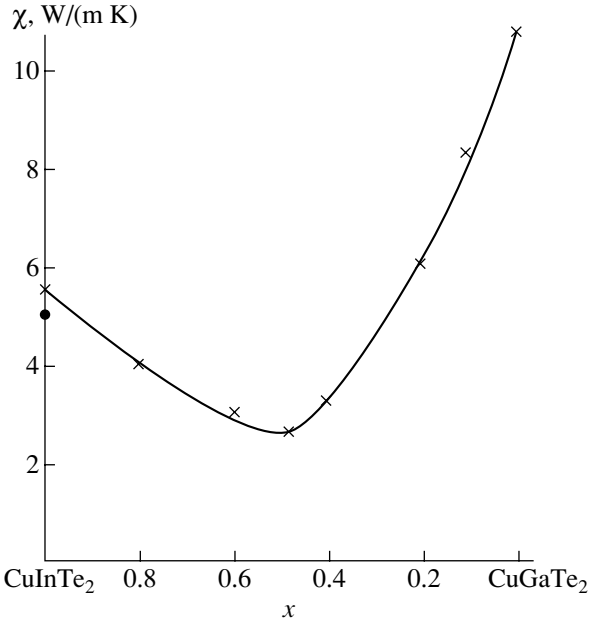

Fig. 4. Concentration dependence of the thermal conductivity for $CuGa_{1-x}In_xTe_2$ solid solutions.

Table 1. Electron probe microanalysis data for $CuInTe_2$ and $CuGaTe_2$ compounds and $CuGa_{1-x}In_xTe_2$ solid solutions

x	Cu, at. %		Ga, at. %		In, at. %		Te, at. %	
	I	II	I	II	I	II	I	II
1.0	25.0	25.4	25.0	24.8	–	–	50.0	49.8
0.9	25.0	25.3	22.5	22.4	2.5	2.4	50.0	49.9
0.8	25.0	25.1	20.0	19.8	5.0	5.4	50.0	49.7
0.6	25.0	24.8	15.0	15.3	10.0	9.4	50.0	50.5
0.5	25.0	25.2	12.5	12.7	12.5	12.2	50.0	49.9
0.4	25.0	24.7	10.0	10.1	15.0	14.8	50.0	50.4
0.2	25.0	24.8	5.0	5.1	20.0	20.3	50.0	49.8
0.0	25.0	24.9	–	–	25.0	24.7	50.0	50.4

Note: I, calculation; II, experiment.

Table 2. Debye temperatures and rms dynamic atomic displacements for $CuInTe_2$, $CuGaTe_2$, and $CuGa_{1-x}In_xTe_2$

x	$\bar{A}$, g	V, cm^3	Θ^{α}, K	Θ^{T_m}, K	$\sqrt{\bar{u}}$, Å
0.0	108.4	17.9	163	165	0.214
0.2	106.1	17.6	166	168	0.210
0.4	103.9	17.3	171	171	0.207
0.5	102.8	17.1	173	173	0.206
0.6	101.6	17.0	175	175	0.205
0.8	99.4	16.7	179	180	0.202
1.0	97.1	16.4	185	185	0.198

result of this process, one phonon disappears and two new phonons appear or two phonons disappear and one new phonon originates. At higher temperatures, χ varies as T^n, where $0 < n < 1$, which means that scattering by impurities and lattice defects dominates. Accordingly, the temperature dependence of χ is weak. In the solid solutions, the power law T^{-n} is observed throughout the temperature range studied; hence, the basic scattering mechanism is scattering by lattice defects.

Figure 4 shows the concentration dependence of the thermal conductivity for the $CuGa_{1-x}In_xTe_2$ solid solutions. This curve has a minimum near $x = 0.5$. Such behavior (i.e., the considerable decrease in χ of the solid solutions compared with that of the compounds) is due to the disturbance of the lattice periodicity in the solid solutions because of the random distribution of the atoms over equivalent sites. In the solid solutions, dissimilar atoms, though occupying regular lattice positions (sites), are ordered improperly. Because of this, the atomic masses and force constants vary randomly from site to site, causing phonon scattering. Therefore, the solid solutions can be viewed as intermediates between the crystalline state (the crystal lattice persists) and the amorphous state (the disordered arrangement of the atoms). For the solid solutions, the disorder is maximal at x near 0.5; hence, the thermal conductivity is also minimal at this point.

CONCLUSIONS

The thermal expansion and thermal conductivity of $CuInTe_2$ and $CuGaTe_2$ compounds, as well as of Bridgman-grown $CuGe_xIn_{1-x}Te_2$ solid solutions, were measured. It was found that $\Delta l/l_0(T)$ experiences a jump near the α–β phase transition, while α_l changes λ-wise. It is shown that the thermal expansion coefficient varies linearly with x, while the thermal conductivity has a minimum at $x = 0.5$.

REFERENCES

1. N. A. Goryunova, *Compound Diamond-Like Semiconductors* (Khimiya, Moscow, 1968).
2. R. Diaz, J. M. Merino, and M. Leon, J. Phys. D **28**, 1162 (1995).
3. V. Yu. Rud', Yu. V. Rud', I. V. Bodnar', *et al.*, Fiz. Tekh. Poluprovodn. (St. Petersburg) **33**, 824 (1999) [Semiconductors **33**, 757 (1999)].
4. V. F. Gremenok, R. W. Matrin, I. V. Bodnar, *et al.*, Thin Solid Films **394**, 24 (2001).
5. B. Kuhn, W. Kaefer, K. Fess, *et al.*, Phys. Status Solidi A **162**, 661 (1997).
6. S. Roy, P. Guha, S. Chaudhuri, *et al.*, Phys. Status Solidi A **189**, 209 (2002).
7. L. Essaleh, S. M. Wasim, G. Marin, *et al.*, Phys. Status Solidi B **225**, 203 (2001).

8. J. Krustok, H. Collan, H. Hjelt, *et al.*, J. Appl. Phys. **83**, 7867 (1998).
9. I. V. Bodnar', I. A. Viktorov, and I. A. Zabelina, Zh. Neorg. Khim. **38**, 871 (1993).
10. I. V. Bodnar' and I. A. Zabelina, J. Appl. Spectrosc. **60**, 320 (1994).
11. E. V. Kuchis, *Methods for Study of the Hall Effect* (Sov. Radio, Moscow, 1974).
12. S. I. Rembeza, *Measurements of Basic Parameters of Semiconductors* (Voronezh, 1989).
13. S. I. Novikova, *Thermal Expansion of Solids* (Nauka, Moscow, 1974).
14. L. S. Palatnik, V. M. Koshkin, and L. P. Gal'chinetskiĭ, Fiz. Tverd. Tela (Leningrad) **4**, 2365 (1962) [Sov. Phys. Solid State **4**, 1732 (1962)].
15. L. S. Palatnik and E. I. Rogacheva, Dokl. Akad. Nauk SSSR **174**, 80 (1967) [Sov. Phys. Dokl. **12**, 503 (1967)].
16. J. J. L. Binsma, L. J. Giling, and J. Bloem, J. Cryst. Growth **50**, 429 (1980).
17. I. V. Bodnar, B. V. Korzun, and A. P. Chernyakova, Phys. Status Solidi A **101**, 409 (1987).
18. I. I. Frantsevich, *Powder Metallurgy and Material Strength* (Izd. Akad. Nauk SSSR, Kiev, 1956).
19. B. M. Mogilevskiĭ and A. F. Chudnovskiĭ, *Heat Conduction in Semiconductors* (Nauka, Moscow, 1972).

Translated by V. Isaakyan

Technical Physics, Vol. 48, No. 5, 2003, pp. 592–597. Translated from Zhurnal Tekhnicheskoĭ Fiziki, Vol. 73, No. 5, 2003, pp. 69–74.

SOLID-STATE ELECTRONICS

Effect of Surface Modification on the Properties of Hydrogen-Sensitive GaAs-Based Schottky Diodes

S. V. Tikhov, E. L. Shobolov, S. B. Levichev, and N. V. Baidus

Lobachevski State University, pr. Gagarina 23, Nizhni Novgorod, 603950 Russia

e-mail: fdp@phys.unn.ru

Received July 22, 2002

Abstract—The surface of hydrogen-sensitive GaAs Schottky diodes is modified by nonpolishing etching and by producing quantum wells and quantum dots in the space-charge region of the semiconductor. The sensitivity to hydrogen is found to increase by a factor of 8–37 after the etching and by two or three orders of magnitude after the introduction of quantum wells and dots. It is shown that the increased sensitivity is associated with the lowering of the barrier at the Pd/GaAs interface, the retardation of hydrogen diffusion into GaAs due to the presence of strained quantum-size layers, and an increase in the recombination current. The presence of the recombination component is supported by luminescence from the quantum wells and quantum dots, as well as from the GaAs substrate. The etch composition is shown to be a decisive factor in raising the sensitivity. © *2003 MAIK "Nauka/Interperiodica".*

INTRODUCTION

Microelectronic hydrogen sensors can be made of various MIS structures (including MIS transistors) and Schottky diodes (SDs) with a catalytically active Pd electrode [1]. MIS diodes and Si-based transistors offer the highest sensitivity to hydrogen: the maximal shift of the hydrogen response reaches 0.6 V, and the detectivity is as low as 10^{-5} vol % [2, 3]. These sensors are, however, difficult to fabricate (an elaborate technology is needed to provide a low density of surface states at the Si/SiO_2 interface), and, in addition, they require sophisticated instruments for detecting the response (by the capacitance or the shift of the flat-band voltage at the semiconductor surface). SDs with a thin oxide spacer are easier to fabricate and offer wider possibilities in detecting the signal (by the capacitance, current, or photovoltage). However, their sensitivity to hydrogen is lower: the maximal voltage shift of the *I–V* forward branch is ≈0.2 V, and the detectivity is ~10^{-2}% in terms of current and ~10^{-4}% in terms of photovoltage [4–7].

This work was aimed at improving the hydrogen sensitivity of Pd/thermal oxide/GaAs SDs. The adsorptivity of the hydrogen-sensitive surface was expected to be enhanced owing to the developed surface relief obtained by nonpolishing etching [8] and the retardation of hydrogen diffusion into the GaAs substrate by strained quantum-size layers with InAs/GaAs quantum dots (QDs) and InGaAs/GaAs quantum wells (QWs) introduced into the space-charge region (SCR) of GaAs [9].

EXPERIMENTAL

SDs were fabricated on ≈1-μm-thick epitaxial *n*-GaAs layers with an electron concentration $n_0 \approx 10^{16}$ cm^{-3}. The layers were grown by atmospheric-pressure metallorganic vapor-phase epitaxy on *n*-GaAs substrates ($n_0 \approx 10^{16}$ cm^{-3}) misoriented by +3° relative to the (100) plane. Prior to the evaporation of the metallic electrode, the GaAs surface of several diodes was modified by etching in a nonpolishing ferrocyanide etch of composition ($0.8MK_3[Fe(CN)_6]$ in a 0.3M solution of KOH) : H_2O : glycerol = 1 : 5 : 8 and in a Sirtl etch (CrO_3 (30%) : HF = 1 : 1). The etch rate of GaAs in the ferrocyanide etch was 2–4 nm/min, and the etch time was varied from 10 to 30 min. The etch rate of GaAs in the Sirtl etch was ≈4 μm/min, and the etch time was ≈3, 11, and 30 s. In some of the structures, 5-nm-thick $In_xGa_{1-x}As$ (x = 0.2) QWs and InAs QDs (five monolayers) were introduced into the SCR of the semiconductor at a distance of 15 nm from the surface through a 10-nm-thick spacer. The sequence of the quantum-size layers was either QW/spacer/QD or QD/spacer/QW, starting from the epitaxial film surface. The QWs and QDs were produced following the technology described in [10, 11]. Before Pd was applied, the structures had been heated in air to 300°C for 30 min to grow 3- to 4-nm-thick thermal oxide. Semitransparent Pd electrodes of thickness ≈20 nm were applied on the oxidized semiconductor surface by thermal evaporation *in vacuo*. The evaporation conditions were standard for GaAs SDs: preheating to 200°C and the deposition of Pd on the substrate heated to 100°C [12]. Such conditions are known to provide good *I–V* characteristics. The size of the Pd electrode was $\approx 2.35 \times 10^{-2}$ cm^2.

We took the *I–V* characteristics in the dark and under illumination by undecomposed light at room temperature and a temperature of 100°C that is optimal

1063-7842/03/4805-0592$24.00

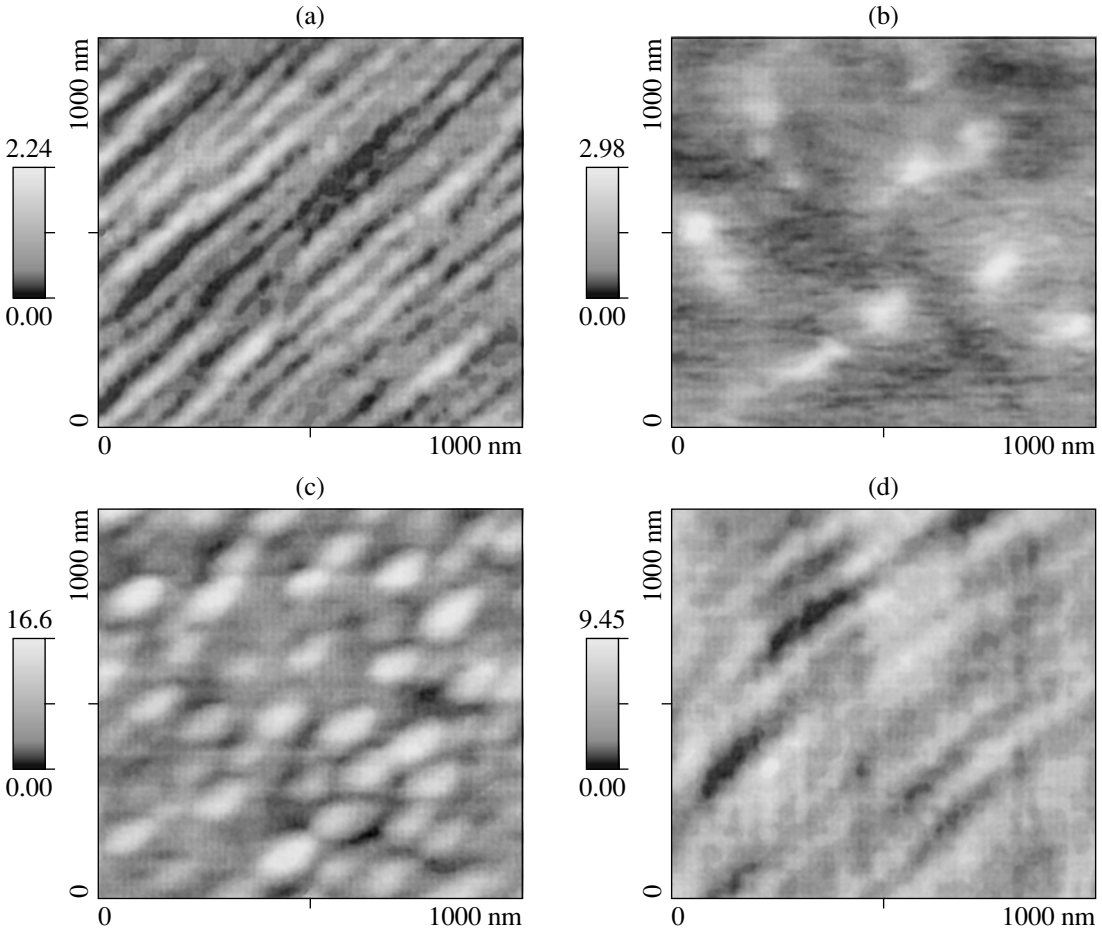

Fig. 1. AFM images of the oxidized surfaces of the semiconductor and metal. (a) GaAs surface before etching, (b) surface of Pd applied on the original GaAs surface, (c) semiconductor surface after etching in the ferrocyanide etch, and (d) semiconductor surface after etching in the Sirtl etch.

for gas sensors [5]. The measurements were made in an air flow and in the flow of a hydrogen-containing (0.6 vol %) air–argon mixture by the technique described in [5]. The photosensitivity S of the small-signal photovoltage was measured as a function of the photon energy $h\nu$ at room temperature. The spectral curves of electroluminescence, $I_{EL}(h\nu)$, were taken at a pulsed forward bias of amplitude ≈1 V and current ≈30 mA, and those of photoluminescence, $I_{PL}(h\nu)$, were recorded at 77 K.

The surface relief of the Pd and semiconductor was examined with a Topometrix® Accurex™ TMX-2000 atomic force microscope (AFM) in the noncontact mode. To quantitatively characterize the surface topography, we calculated the mean roughness h of the surface and its fractal dimension F. According to [13], fractal dimension describes surface more adequately and allows one to identify various types of surfaces by using the only number lying in the interval from 2.00 (perfectly smooth surface) to 3.00 (highly irregular porous surface). The fractal dimension was found by calculating the number of cells [14].

RESULTS AND DISCUSSION

1. Surface Morphology

Figure 1 shows the AFM image of the (a) oxidized and (b) Pd-coated GaAs surface. Growth steps in the form of ridges are clearly seen. The mean roughness of the oxidized surface of the epitaxial film is ≈0.5 nm, and its fractal dimension is ≈2.54. The Pd surface almost copies the microrelief of the oxidized surface ($h \approx 0.6$ nm, $F \approx 2.50$). The ridges on the Pd surface are somewhat broadened, because the Pd film rounds irregularities on the GaAs surface. The broadening correlates with the metal film thickness.

Figure 1 also shows the morphology of the oxidized GaAs surface after etching in the (c) ferrocyanide and (d) Sirtl etchs. From Figs. 1a, 1c, and 1d, it follows that the etching modifies greatly the surface morphology: the ridges give way to 160×100-nm hills with a density of 10^{10} cm^{-2} and ~10^9 cm^{-2} on the surfaces etched in the ferrocyanide and Sirtl etchs, respectively. For the former surface, $h \approx 8.0$ nm and $F \approx 2.33$; for the latter, $h \approx 4.0$ nm and $F \approx 2.31$. As for the as-prepared GaAs

Table 1. Effect of substrate etching in the Sirtl etch on the parameters of hydrogen-sensitive GaAs SDs at $T = 27°C$

Δd, μm	φ_b, V	m	N_{ss}, (eV cm)$^{-1}$	V_{oc}, V	j_{sc}, A/cm^2
0	0.89	1.17	2.6×10^{12}	0.5	9.5×10^{-3}
0.2	0.76	1.36	5.8×10^{12}	0.37	9.5×10^{-3}
0.7	0.67	1.44	7.1×10^{12}	0.29	6.7×10^{-3}
2.0	0.61	1.83	1.4×10^{13}	0.22	4.5×10^{-3}

Table 2. Effect of substrate etching in the Sirtl etch on the parameters of hydrogen-sensitive GaAs SDs at $T = 100°C$

Δd, μm	φ_b, V	$\Delta\varphi_b$, V	ΔV_{oc}, V	Δj, A/cm^2	$\Delta j_e/\Delta j_o$, experiment	$\Delta j_e/\Delta j_o$, theory
0	0.86	0.17	0.16	4.9×10^{-4}		
0.2	0.80	0.16	0.23	4.0×10^{-3}	8	3
0.7	0.75	0.13	0.20	4.5×10^{-3}	9	3
2.0	0.70	0.14	0.15	1.8×10^{-2}	37	60

Table 3. Effect of substrate etching in the ferrocyanide etch on the parameters of hydrogen-sensitive QW/spacer/QD and QD/spacer/QW GaAs SDs at $T = 27°C$

Device structure	Δd, nm	φ_b, V	m	N_{ss}, (eV cm)$^{-1}$	V_{oc}, V	j_{sc}, A/cm^2
QW/spacer/QD	0	0.64	1.17	2.8×10^{12}	0.20	8.9×10^{-3}
	25	0.74	1.95	1.6×10^{13}	0.23	4.2×10^{-5}
	50	0.81	1.4	6.4×10^{12}	0.48	8.1×10^{-3}
QD/spacer/QW	0	0.67	1.17	2.8×10^{12}	0.23	7.6×10^{-3}
	25	0.73	1.83	1.4×10^{13}	0.21	3.6×10^{-4}
GaAs	0	0.86	1.15	2.3×10^{12}	0.5	9.5×10^{-3}

Table 4. Effect of substrate etching in the ferrocyanide etch on the parameters of hydrogen-sensitive QW/spacer/QD and QD/spacer/QW GaAs SDs at $T = 100°C$

Device structure	Δd, nm	φ_b, V	$\Delta\varphi_b$, V	ΔV_{oc}, V	j_{sc}, A/cm^2	$\Delta j_e/\Delta j_o$, experiment	$\Delta j_e/\Delta j_o$, theory
QW/spacer/QD	0	0.69	0.09	0.18	7.4×10^{-2}		
	25	0.86	0.10	0.12	1.0×10^{-4}	740	292
	50	0.89	0.26	0.26	1.7×10^{-3}	43	32
QD/spacer/QW	0	0.75	0.20	0.19	9.0×10^{-2}		
	25	0.84	0.12	0.12	4.8×10^{-4}	187	
GaAs	0	0.86	0.17	0.16	4.9×10^{-4}		60

surface, the Pd surface almost copies the microrelief of the etched GaAs substrate. The morphology of the etched GaAs surface is practically independent of the etch time.

2. Electrophysical Characteristics

Measured and calculated data obtained from the *I–V* characteristics obtained with and without illumination are summarized in Tables 1–4. In the tables, φ_b is the barrier height at the Pd/GaAs interface (estimated by extrapolating the exponential portion of the forward branch to $V = 0$ under the assumption that Schottky emission prevails), m is the ideality factor of the diode that is found from the slope of the exponential portion [11], V_{oc} is the open-circuit voltage, and j_{sc} is the short-circuit current. The density of surface states (SSs), which exchange charge carriers with the semiconductor, was calculated from the experimental value of m by the formula [12]

$$m = 1 + \frac{d_{ox}}{\varepsilon_{ox}}\frac{\varepsilon_s}{w} + \frac{q^2 N_{ss} d_{ox}}{\varepsilon_0 \varepsilon_{ox}}, \quad (1)$$

where q is the charge of an electron; N_{ss} is SS density in $(\text{eV cm})^{-1}$; d_{ox} is the oxide thickness; ε_{ox}, ε_s, and ε_0 are the relative permittivity of the oxide, relative permittivity of the semiconductor, and the absolute dielectric constant of free space, respectively; and w is the thickness of the SCR in the semiconductor. When calculating N_{ss}, we put $\varepsilon_{ox} = 9$ (the value for gallium arsenate [6]) and $d_{ox} = 3$ nm.

The other parameters listed in the tables reflect the effect of hydrogen with a concentration of 0.6% at a temperature of ≈100°C: $\Delta\varphi_b$ is the change in the barrier height, ΔV_{oc} is the change in the open-circuit voltage (photovoltage), and Δj is the hydrogen-related change in the reverse current of the diode when a voltage $V = -0.3$ V is applied to the Pd electrode.

2.1. GaAs Schottky diodes. Etching in the ferrocyanide solution does not change φ_b, m, V_{oc}, N_{ss}, and the sensitivity to hydrogen. Consequently, the variation of the microrelief of the GaAs and Pd surfaces (cf. Figs. 1a, 1c) does not change the catalytic activity of the Pd surface with respect to hydrogen.

Tables 1 and 2 list the parameters of the diodes etched in the Sirtl etch for 3, 11, and 30 s. It is seen that all the parameters (φ_b, m, V_{oc}, N_{ss}, and the sensitivity to hydrogen) change considerably after the etching. The absolute sensitivity to hydrogen in terms of the change Δj in the reverse current through the diode increases by a factor of 8 to 37 depending on the thickness Δd of the etched-off layer (column 5 in Table 2).

The increase in the sensitivity goes in parallel to the decrease in the potential barrier. The barrier photovoltage decreases by 0.28 V, which is consistent with the decrease in φ_b (columns 2 and 5 in Table 1).

As follows from Table 2, the decrease in the barrier height $\Delta\varphi_b \approx \Delta V_{oc}$ is almost independent of its initial value. However, a relative hydrogen-related increase in the current that is associated with a decrease in φ_b can be found (under the assumption that Schottky emission prevails) from the obvious relationship

$$\frac{\Delta j_e}{\Delta j_o} = \exp\left\{q\frac{(\varphi_{b,o} - \varphi_{b,e}) + (\Delta\varphi_{b,e} - \Delta\varphi_{b,o})}{kT}\right\}, \quad (2)$$

where the subscripts e and o refer to the etched and original surfaces, respectively.

Relationship (2) is valid when Δj is much larger than the difference in the current densities before and after exposure to hydrogen (which was fulfilled in practice). The calculated data are given in column 7 (Table 2). In column 6 of this table, this ratio is obtained by directly dividing the hydrogen-related changes in the reverse current for the diodes with the etched and original surfaces by each other. The ratios in columns 6 and 7 are seen to agree only by one order of magnitude. When $m < 1.5$, the increase in the sensitivity exceeds that predicted from the change in the barrier height; when $m \approx 1.8$, the situation is reverse. In both cases, the presence of the oxide and an increase in the SS density (corresponding to the increase in m) must suppress to an extent the effect of hydrogen due to a decrease in the barrier height: because of the influence of the oxide resistance in the former case [6] and the enhanced screening of surface states in the latter. With $m \approx 1.8$, the screening is so effective that the increase in the sensitivity is actually smaller than predicted from the decrease in the barrier height. The substantial decline in the short-circuit current, which is observed in this case, is an indication of enhanced recombination in the diode.

Since the increase in the sensitivity to hydrogen after etching is, as a rule, higher than predicted from the decrease in the barrier height, one might assume that another reason is a change in the catalytic activity of the Pd surface and oxide/Pd interface, which is associated with the modified surface relief. However, this argument has little force, because the GaAs surface etched in the Sirtl solution is smoother than the original surface, as judged from the fractal dimension, and the surface etched in the ferrocyanide solution. The postetching increase in the reverse current and sensitivity may be partially related to the growth of the recombination component of the current. The presence of the recombination component is directly evident from interband electroluminescence observed in the diodes (Fig. 2, curve *2*). Thus, it can be concluded that the reason for the postetching increase in the hydrogen sensitivity is the modification of the GaAs surface by semiconductor–etch chemical interaction.

Figure 3 shows the small-photovoltage photosensitivity spectra before and after etching the GaAs surface. From these spectra, according to [15], one can detect surface states localized in the lower half of the energy gap or deep levels. The photosensitivity range is rather wide, extending from 0.9 to 1.35 eV. In this range, the photosensitivity grows with energy nearly exponen-

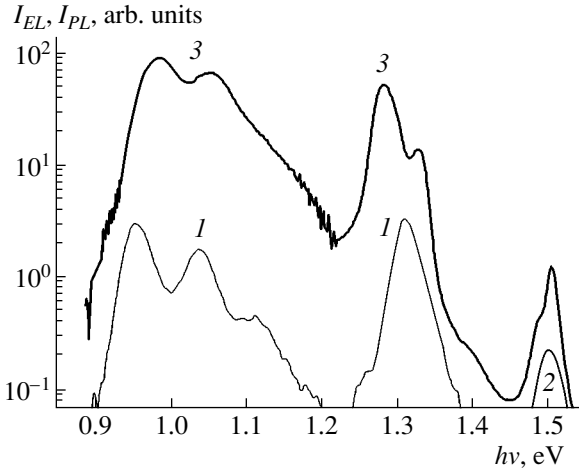

Fig. 2. (*1*, *2*) Electroluminescence and (*3*) photoluminescence spectra: (*1*) QW/spacer/QD GaAs diode, (*2*) GaAs diode, and (*3*) semiconductor with QWs and QDs.

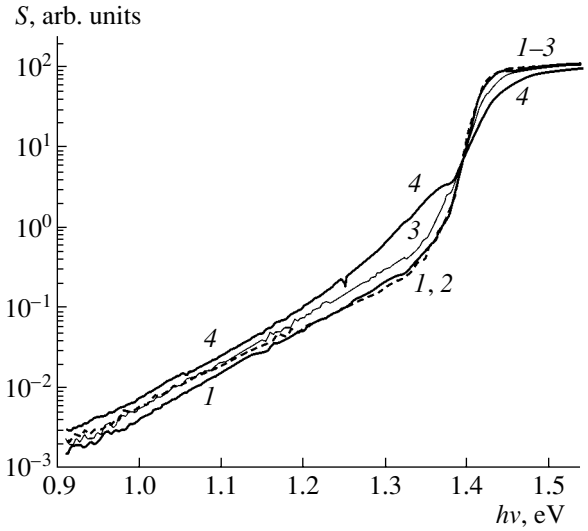

Fig. 3. Effect of etching in the Sirtl etch on the photosensitivity spectra of GaAs SDs. Δd = (*1*) 0, (*2*) 0.2, (*3*) 0.7, and (*4*) 2.0 μm.

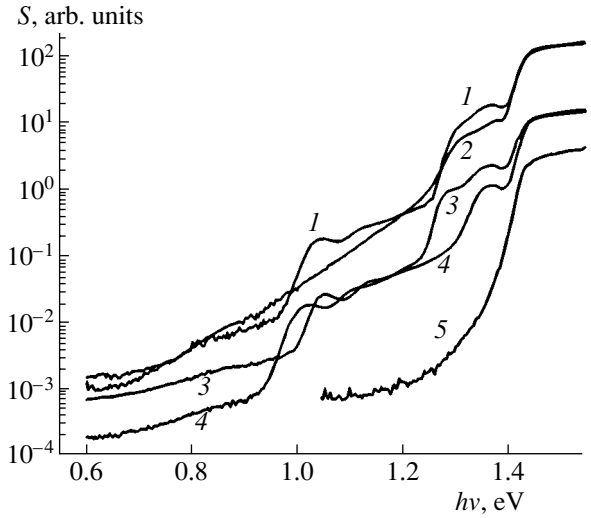

Fig. 4. Spectral sensitivity of the photovoltage in (*1*, *2*) QD/spacer/QW and (*3*–*5*) QW/spacer/QD SDs: (*1*, *3*) before and (*2*, *4*) after etching-off a layer of thickness $\Delta d \approx$ 25 nm in the ferrocyanide etch. (*5*) $\Delta d \approx$ 50 nm.

tially, as usually does the SS density on the real GaAs surface (toward the valence band top) [6]. With increasing etch time, the photosensitivity somewhat rises. When the barrier passes into the substrate (the thickness of the etched-off layer is ≈2 μm), the photosensitivity grows four times in the range 1.28–1.38 eV possibly because of an increase in the density of donor surface states. This qualitatively agrees with the increase in *m* mentioned above.

2.2. Schottky diodes with quantum wells and quantum dots. The effect of QWs and QDs incorporated into the SCR of the GaAs substrate was elucidated after etching in the ferrocyanide etch. As was noted above, this etch leaves the basic parameters of the GaAs diodes and, specifically, the sensitivity to hydrogen unchanged.

Figure 4 demonstrates the photosensitivity spectra for the diodes with the sequence QD/spacer/QW and QW/spacer/QD that were taken before and after etching in the ferrocyanide etch, which allows the fine etching of thin layers from the semiconductor surface. After removing a layer ≈25 nm thick, the QD-related signal (in the range 1.0–1.2 eV) disappears but the QW-related signal (1.30–1.37 eV) persists in the QD/spacer/QW diodes (curves *1*, *2*). For the QW/spacer/QD devices, the reverse is true (curves *3*, *4*). With a ≈50-nm-thick layer removed, both the QW and QD signals are absent (curve *5*).

Tables 3 and 4 illustrate the effect of ferrocyanide etching on the parameters of the diodes with the QWs and QDs. With the QDs or QWs removed, the values of φ_b, V_{oc}, *m*, and N_{ss} increase (φ_b to 0.1 V), while the short-circuit current density j_{sc} drops. In this case, the decrease in j_{sc} may be associated with the growth of the oxide thickness (and, hence, resistance) due to the oxidation of indium present in the residual InAs and InGaAs surface layers. After removing the 50-nm-thick layer, when both QDs and QWs completely disappear, the short-circuit current increases again to the value responsible for the oxidized GaAs surface.

The removal of the QWs and QDs resulted in the decrease in the hydrogen sensitivity (Δj) by a factor of 740 (after the removal of the QWs) and 187 (after the removal of the QDs). The effect of the barrier change on the sensitivity in terms of the current was estimated by formula (2). Note that the calculated ratios $\Delta j_o/\Delta j_e$ (Δj_o and Δj_e are the sensitivities to H_2 before and after etching, respectively) were on the same order of magnitude as, but always less than, those measured experimentally (Table 4; columns 7, 8). Earlier, it was demonstrated [16] that the hydrogen sensitivity of a planar resistive structure with Pd electrodes on semi-insulating GaAs can be improved by one or two orders of magnitude by introducing QWs and QDs into the SCR of the semiconductor. As follows from our findings, the removal of QWs and QDs, conversely, deteriorates the device's sensitivity to hydrogen by more than two orders of magnitude, which agrees qualitatively with results of [16].

After QW (or QD) removal, the decrease in the hydrogen sensitivity that is associated with a change in the barrier height was found to be larger than expected. It is likely that the strained InGaAs and InAs layers on the semiconductor surface retard hydrogen diffusion into the substrate [9] and, thereby, improve the sensitivity, since a rise in the sensitivity of the diodes with unstrained (non-quantum-size) $In_{1-x}Ga_xAs$ and InAs layers was much less pronounced.

The presence of QWs and QDs may also increase the recombination component of the current through

the diode. The electroluminescence spectra displayed in Fig. 2 suggest that recombination through QWs and QDs in the SCR is essential. Curve *3* in Fig. 2 shows intense luminescence from QDs (the energies 0.95, 1.025, and 1.11 eV for the fundamental, first, and second excited quantizing levels) and QWs (≈1.31 eV). It is of interest that the electroluminescence spectra were resolved better (especially for the QD luminescence) than the photoluminescence spectra from the semiconductor of which the diodes were made (cf. curves *1* and *3* in Fig. 2).

The etching of the substrate surface and the introduction of the quantum-size layers did not change the speed of the diodes as hydrogen sensors but improved conside-rably their detectivity from 10^{-2} to 10^{-3} and even 10^{-4}%. It should also be noted that, at low hydrogen concentrations (no more than 10^{-2}%), Δj grows linearly with hydrogen concentration, which is of interest for sensor applications.

CONCLUSIONS

It is found that the modification of the semiconductor surface in SDs with a catalytically active Pd electrode by nonpolishing etching or by introducing InGaAs QWs and InAs QDs into the SCR at a distance of 15 nm from the substrate surface may improve the sensitivity to hydrogen by a factor of 10–40 in the former case and by more than two orders of magnitude in the latter. This increase may be associated with a decrease in the potential barrier height at the Pd/GaAs interface, the retardation of hydrogen diffusion into the semiconductor by strained QW and QD layers, and the effect of the recombination current. The introduction of QWs and QDs into the SCR increases the recombination current and causes electroluminescence due to recombination via QWs and QDs. The postetching reverse current in GaAs SDs grows, causing interband electroluminescence in GaAs.

ACKNOWLEDGMENTS

The authors thank I.A. Karpovich for valuable discussions and B.N. Zvonkov for assistance in the experiments.

This work was financially supported by the Russian Foundation for Basic Research (grant no. 00-02-17598).

REFERENCES

1. A. V. Evdokimov, M. N. Murshudli, A. Yu. Podlepetskiĭ, *et al.*, Zarubezhn. Élektron. Tekh., No. 2 (321), 3 (1988).
2. L. G. Petersson, H. M. Dunnetum, J. Fogelbery, *et al.*, J. Appl. Phys. **58**, 404 (1985).
3. M. Johansson, I. Lundstrom, and L. D. Ekedahi, J. Appl. Phys. **84**, 44 (1998).
4. V. I. Gaman, P. I. Drobot, M. O. Duchenko, *et al.*, Poverkhnost, No. 11, 64 (1996).
5. S. V. Tikhov, V. P. Lesnikov, V. V. Podol'skiĭ, *et al.*, Zh. Tekh. Fiz. **65** (11), 120 (1995) [Tech. Phys. **40**, 1154 (1995)].
6. V. I. Gaman, M. O. Duchenko, and V. M. Kalygina, Izv. Vyssh. Uchebn. Zaved. Fiz., No. 1, 69 (1988).
7. S. V. Slobodchikov and K. N. Salikhov, Fiz. Tekh. Poluprovodn. (St. Petersburg) **34**, 290 (2000) [Semiconductors **34**, 284 (2000)].
8. S. V. Tikhov, D. A. Pavlov, P. A. Shilyaev, *et al.*, Pis'ma Zh. Tekh. Fiz. **28** (9), 1 (2002) [Tech. Phys. Lett. **28**, 355 (2002)].
9. I. A. Karpovich, S. V. Tikhov, B. N. Shobolov, *et al.*, Fiz. Tekh. Poluprovodn. (St. Petersburg) **36**, 582 (2002) [Semiconductors **36**, 552 (2002)].
10. I. A. Karpovich, A. V. Anshon, and D. O. Filatov, Fiz. Tekh. Poluprovodn. (St. Petersburg) **32**, 1089 (1998) [Semiconductors **32**, 975 (1998)].
11. B. I. Zvonkov, I. A. Karpovich, N. V. Baidus, *et al.*, Fiz. Tekh. Poluprovodn. (St. Petersburg) **35**, 92 (2001) [Semiconductors **35**, 93 (2001)].
12. E. H. Rhoderic, *Metal–Semiconductor Contacts* (Clarendon, Oxford, 1988, 2nd ed.; Radio i Svyaz', Moscow, 1982).
13. S. Chesters *et al.*, in *Proceedings of the 36th Annual Technical Meeting of the Institute of Environmental Sciences, New Orleans, 1990*, Vol. 316.
14. J. Feder, *Fractals* (Plenum, New York, 1988; Mir, Moscow, 1991).
15. I. A. Karpovich, N. V. Baidus, B. I. Zvonkov, *et al.*, Nanotechnology, No. 12, 405 (2001).
16. I. A. Karpovich, S. V. Tikhonov, E. L. Shobolov, *et al.*, Pis'ma Zh. Tekh. Fiz. **28** (8), 28 (2002) [Tech. Phys. Lett. **28**, 320 (2002)].

Translated by V. Isaakyan

Technical Physics, Vol. 48, No. 5, 2003, pp. 598–601. Translated from Zhurnal Tekhnicheskoĭ Fiziki, Vol. 73, No. 5, 2003, pp. 75–78.

SOLID-STATE ELECTRONICS

Effect of Microwave Annealing on Silicon Dioxide/Silicon Carbide Structures

Yu. Yu. Bacherikov*, R. V. Konakova*, A. N. Kocherov, P. M. Lytvyn*, O. S. Lytvyn*, O. B. Okhrimenko*, and A. M. Svetlichnyi****

** Institute of Semiconductor Physics, National Academy of Sciences of Ukraine, pr. Nauki 45, Kiev, 03028 Ukraine*
e-mail: olga@isp.kiev.ua
*** Taganrog State Radioengineering University, Nekrasovskiĭ pr. 39, Taganrog, 347928 Russia*
e-mail: svetlich@tsure.ru
Received July 24, 2002

Abstract—The methods of atomic force microscopy and optical absorption spectroscopy are applied to study the effect of microwave treatment on the properties of SiO_2/SiC structures obtained by rapid thermal annealing and conventional thermal oxidation in steam. From the variation of the sample optical density with total time of microwave treatment, it is concluded that the structures prepared by rapid thermal annealing are more stable against microwave radiation. It is shown that long-term microwave treatment flattens the oxide film surface at the nanolevel regardless of the method of silicon carbide oxidation. © *2003 MAIK "Nauka/Interperiodica".*

INTRODUCTION

The stability and reliability of MIS devices depend to a great extent on the presence of localized states in the insulating layer and at the insulator–semiconductor interface. This is especially true for silicon carbide structures, which are designed for higher temperature operation than silicon and gallium arsenide devices.

Among traditional radiation treatments, microwave irradiation is finding ever increasing use in the fabrication of electron devices. Microwave irradiation may cause fluctuations in the distribution of dopants and defects at the surface and in the bulk [1]. Sometimes these physical effects may affect the electrical performance and functionality of semiconductors. The effect of microwave irradiation on semiconductor structures can be studied by nondestructive techniques, such as optical methods and atomic force microscopy.

The aim of this paper is to study the influence of microwave irradiation on SiO_2/SiC structures.

EXPERIMENTAL

We examined the optical transmission spectra and the surface morphology of SiO_2/SiC structures prepared by the oxidation of *n*-type silicon carbide (polytype 6H-SiC, the free electron density $(2–3)\times 10^{17}$ cm^{-3}) grown by the Lely method. SiO_2 films were grown on silicon carbide by two methods: conventional thermal steam oxidation (SO) at a temperature of 1373 K for 30 to 180 min and rapid thermal annealing (RTA) in dry oxygen at a temperature of 1273K for 60 to 180 s. Before oxidation, silicon carbide samples were chemically cleaned by the standard technique. The (0001) and $(000\bar{1})$ faces were oxidized simultaneously. The thickness of the silicon carbide substrate was 450 ± 5 μm. The oxide film thickness estimated by ellipsometry was found to be 6–10 nm.

The SiO_2/SiC structures thus obtained were subjected to multiple microwave (frequency $f = 2.45$ GHz, power density 1.5 W/cm^2) annealing in a magnetron chamber. The time of single microwave annealing was 10 s. Then, the optical properties and surface morphology of the samples were examined.

Surface morphology studies were performed with a NanoScope IIIa atomic force microscope in the contact mode.

The transmission spectra were recorded on an SDL-2 setup at room temperature in the range 400–800 nm. An SIRSh-200 lamp was used as a source of continuous radiation.

Atomic force microscopy in combination with optical transmission studies allows one to gain information on the effect of microwave irradiation on the oxide film surface and clarify processes occurring in the bulk of the sample under microwave radiation treatment.

RESULTS AND DISCUSSION

The study of the oxide film surface showed that the growth of the oxide film starts at nucleation centers (as is typical of oxide growth [2, 3]) that are, as a rule, extended linear defects on the silicon carbide surface. Characteristic crystalline conical brushes of diameter up to 10 μm were found on the surface of the continuous film. In addition, the surface of the samples obtained by SO for 60 to 120 min and by RTA for 180 s

1063-7842/03/4805-0598$24.00

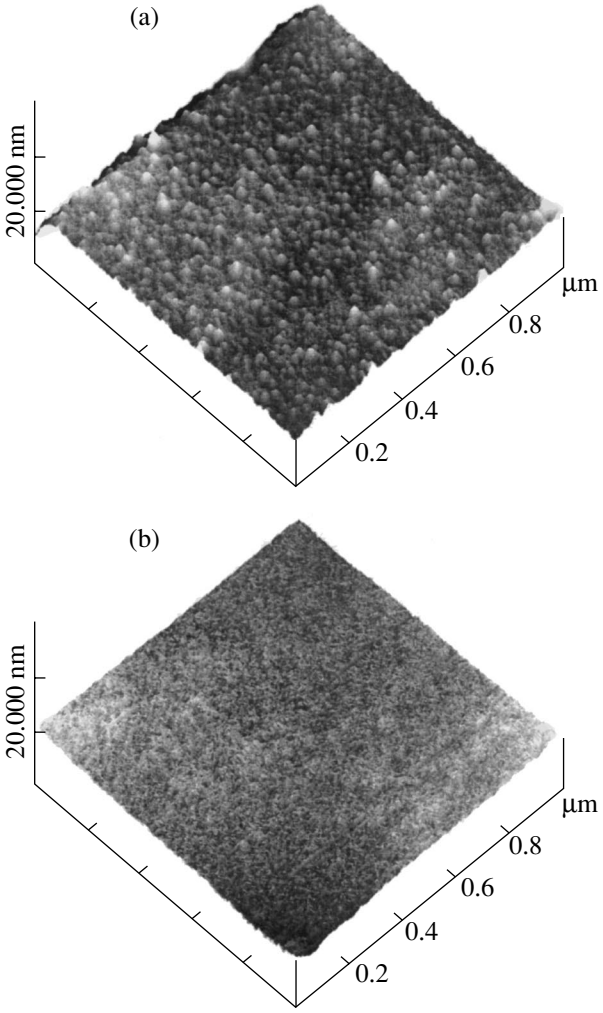

Fig. 1. Modification of the surface microrelief on the SO-grown sample (temperature 1373 K, oxidation time 120 min). Surface morphology (a) after and (b) before microwave treatment (total time of the treatment 30 s).

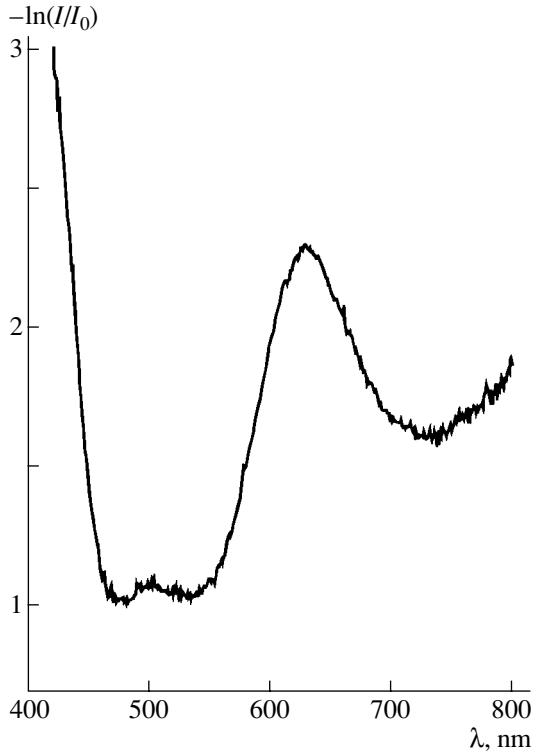

Fig. 2. Typical wavelength dependence of the optical density ($-\ln(I/I_0)$) at T = 300 K for nonirradiated samples.

exhibited a microrelief (imposed on the original macrorelief): most likely SiO_x nanoislands with their size and density depending on the oxidation method (Fig. 1a).

The optical absorption spectra (Fig. 2) for all the samples are similar and do not depend on the SiC oxidation conditions.

It should be noted that the absorption spectrum of the SiO_2/SiC structure in the range λ 400–800 nm is a specific integral characteristic; i.e., the resulting spectrum reflects the absorption in the SiC bulk, in the oxide film, and at the SiO_2/SiC interface. The component with the highest absorption in this spectral range makes a major contribution to the overall absorption spectrum of such a complicated system. At present, this component is silicon carbide.

The broad band near 630 nm (Fig. 2) is a typical feature of the spectrum presented. This band is usually associated [4–7] with the ground state of donor centers caused by the presence of nitrogen impurity in silicon carbide crystals [4–7]. Note that this band is observed against the extended background. According to [7], the background absorption (like that in Fig. 2) arises when the broad band with a maximum near 630 nm partly overlaps with two other absorption bands: a more intense broad near-edge band and an IR absorption band with a short-wave tail. Both bands result from the photoionization of nitrogen with electron transitions to different minima of the conduction band.

As is seen from Fig. 3a, the total dose of microwave radiation variously affects the optical density of the structures in the range 400–800 nm, depending on the SiC oxidation method.

After the first microwave irradiation, the optical density of the absorption band with a maximum near 630 nm decreases for all the samples regardless of the oxidation method (Fig. 3a). After the second microwave irradiation, the optical density of this absorption band either remains almost unchanged or slightly decreases. For such doses, the structure morphology does not change. The third microwave treatment (the total time of treatment is 30 s) leads to an increase in the optical density of the absorption band (Fig. 3a) and removes nanoislands (if any) on all the samples without affecting the SiO_2 film macrorelief (Fig. 1b). The modification of the surface microrelief on a number of the samples may indicate that the oxide film on these samples undergoes phase or structural transformations

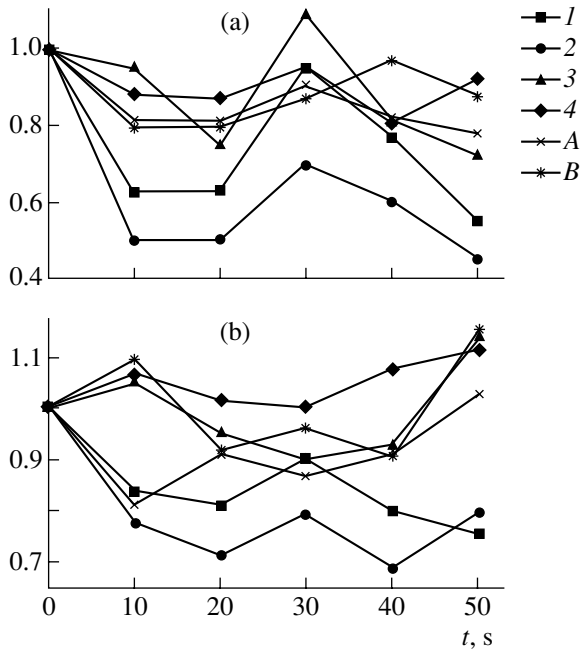

Fig. 3. (a) Relative change in the optical density and (b) 630-nm band half-width vs. total time (*t*) of microwave irradiation. Unity on the vertical axes corresponds to the optical density and half-width of nonirradiated samples. Curves *1–4* correspond to the samples grown by steam oxidation at a temperature of 1373 K. Oxidation time is (*1*) 30, (*2*) 60, (*3*) 120, and (*4*) 180 min. Curves *A* and *B* correspond to the samples grown by rapid thermal annealing in dry oxygen at a temperature of 1273 K for 60 and 180 s, respectively.

when the total time of microwave treatment reaches 30 s. This shows up in the reduction of the surface roughness at the nanolevel down to 0.3 nm. As the total time of treatment increases further, the optical density of the absorption band decreases again in this case, but both the macrorelief and microrelief patterns remain unchanged. However, in the framework of this paper, it is impossible to infer a correlation between the optical density of the structure and the nanorelief of oxide films on the silicon carbide surface.

The SiO_2/SiC samples for which the oxidation time was maximum (Fig. 3a) show different behavior of the optical density. For example, for the oxide grown by RTA for 180 s and irradiated by microwaves for 40 s, the absorption grows only slightly, while for the oxide obtained by SO for 180 min, the optical density increases when the total microwave treatment time is 50 s.

Unlike the case of optical density, any correlation between the half-width of the absorption band with a maximum near 630 nm and the total time of microwave treatment is absent. The dependence of the half-width on the total microwave dose is nonmonotonic.

The change in the background absorption level correlates well with that in the optical density in the maximum of the 630-nm band. This result is in agreement with the data of [7], where it was noted that the background against which this band is observed and the band itself are of the same chemical nature and are caused by the presence of nitrogen impurity in silicon carbide.

As was mentioned earlier [4–7], the 630-nm band is due to the photoionization of three nonequivalent nitrogen donors with the hexagonal and cubic coordinations of the nearest neighbors. In essence, the band consists of three nearby subbands, which merge into one broad band [7]. Microwave treatment apparently leads to fluctuations in the distribution of dopants and defects at the surface and in the bulk, which, in turn, affects impurity interaction between absorption centers [8] and, as a consequence, changes the absorption band intensity. The variation of the absorption band half-width may be explained by the disturbed defect distribution as a result of microwave irradiation (a similar effect was observed for the half-width of diffraction reflection curves [9]). Besides, the appearance and disappearance of structure defects under microwave irradiation must be accompanied by a change of symmetry in the neighborhood of nitrogen atoms. This results in the intensity redistribution between the subbands constituting the 630-nm band and eventually affects its half-width and intensity.

The presence of three nonequivalent absorption centers allows one to assume that their stability against microwave irradiation is different. The nonmonotonic dependences of the absorption band half-width and intensity on the total time of microwave treatment may be a consequence of the donor concentration redistribution due to a different degree of interaction with microwave radiation. One can assume that the samples where donor-microwave radiation interaction is the weakest are the most stable against microwave treatment. However, additional investigation is needed to clarify the type of such donors. The dependences of the 630-nm absorption band intensity and half-width on the total time of microwave treatment indicate that the structures with the RTA oxide offer the highest stability.

CONCLUSIONS

As follows from the experimental results, the structures made by rapid thermal annealing in dry oxygen are the most stable against microwave treatment. It is shown that certain microwave doses (the total microwave treatment time is 30 s or more) cause a decrease in the density of nanoislands in oxide films on silicon carbide up to their disappearance and flatten the surface.

REFERENCES

1. V. V. Antipin, V. A. Godovitsin, D. V. Gromov, *et al.*, Zarubezhn. Élektron., No. 1, 37 (1995).

2. Ya. E. Geguzin and Yu. S. Kaganovskiĭ, *Diffusion Processes on Crystal Surface* (Énergoatomizdat, Moscow, 1984).

3. L. S. Palatnik, M. Ya. Fuks, and V. M. Kosevich, *Formation Mechanisms and Substructure of Condensed Films* (Nauka, Moscow, 1972).

4. G. B. Dubrovskiĭ and E. I. Radovanova, Fiz. Tverd. Tela (Leningrad) **11**, 680 (1969) [Sov. Phys. Solid State **11**, 549 (1969)].

5. I. S. Gorban', V. P. Zavada, and A. S. Skirda, Fiz. Tverd. Tela (Leningrad) **14**, 3095 (1972) [Sov. Phys. Solid State **14**, 2652 (1972)].

6. I. S. Gorban' and A. S. Skirda, Ukr. Phys. J. **26**, 228 (1981).

7. I. S. Gorban' and A. P. Krokhmal', Fiz. Tekh. Poluprovodn. (St. Petersburg) **35**, 1299 (2001) [Semiconductors **35**, 1242 (2001)].

8. I. S. Gorban', Yu. A. Marazuev, and A. S. Skirda, Fiz. Tverd. Tela (Leningrad) **14**, 780 (1972) [Sov. Phys. Solid State **14**, 664 (1972)].

9. L. M. Sorokin, A. S. Tregubova, M. P. Shcheglov, *et al.*, Fiz. Tverd. Tela (St. Petersburg) **42**, 1384 (2000) [Phys. Solid State **42**, 1422 (2000)].

Translated by M. Astrov

Technical Physics, Vol. 48, No. 5, 2003, pp. 602–606. Translated from Zhurnal Tekhnicheskoĭ Fiziki, Vol. 73, No. 5, 2003, pp. 79–83.

OPTICS, QUANTUM ELECTRONICS

Absorption and Scattering of Infrared Radiation by Vanadium Dioxide Nanoparticles with a Metallic Shell

O. P. Mikheeva and A. I. Sidorov

Research Institute of Laser Physics, St. Petersburg, 199034 Russia

Received August 15, 2002

Abstract—The numerical simulation of the absorption and scattering cross sections of vanadium dioxide nanoparticles with silver and gold shells are presented. The cross sections are evaluated for the spectral intervals 1–1.2, 1.3–1.7, and 9–12 μm both before and after the semiconductor–metal phase transition in VO_2. It is demonstrated that the transition of VO_2 to the metallic state near (or away from) plasmon resonances leads to a decrease (or increase) in the absorption and scattering cross sections for a given wavelength. The decrease is related to the shift of the plasmon resonance band, whereas the increase is directly related to the growth of the VO_2 absorption upon the phase transition. © *2003 MAIK "Nauka/Interperiodica".*

Nonlinear optical media with semiconductor and metal nanoparticles are promising for fast optical switches. A distinctive feature of the media containing metal nanoparticles is the excitation of a plasmon resonance at an optical frequency equal or close to the plasma frequency of free electron oscillations in the metal. The plasmon resonance is accompanied by an increase in the absorption and scattering cross sections of the nanoparticles and by a local enhancement of the electromagnetic wave field inside and near nanoparticles [1–4]. The nonlinear response of the medium with nanoparticles can increase by several orders of magnitude owing to the local field enhancement. Plasmon resonances in homogeneous spherical nanoparticles of noble metals (Ag, Au, and Pt) lie in the visible spectral range [2]. More complex nanoparticles with the dielectric core surrounded by a continuous metal shell (e.g., an Au_2S core covered by an Au shell [5–7] or a CdS core with an Ag shell [8]) exhibit additional plasmon resonances in the near-IR range. Today's technologies enable one to coat a particle with a diameter of several tens to several hundreds of Angströms by a thin metallic or semiconductor shell of controlled thickness [5, 9]. An additional plasmon resonance can be observed in the near-IR range if the dielectric core of a particle is coated by a discontinuous metal film [10]. Optical limitation takes place near the plasmon resonance in the 10-μm spectral range for silver halide nanoparticles coated by a discontinuous silver film. Nanoparticles with such a structure are of great practical interest. First, by varying their geometrical parameters, one can control the wavelength of plasmon resonance and the range of high nonlinearity of a material. Second, by properly selecting the core material, it is possible to create nonlinear optical media with desired properties.

Vanadium dioxide exhibits the reversible semiconductor–metal phase transition (PT), resulting in a significant change in its permittivity [11, 12]. With photon energies $h\nu > E_g$ ($E_g = 0.7$ eV is the energy gap of VO_2 in the semiconductor phase [11, 12]), the PT in VO_2 can be induced within several hundreds of femtoseconds by nonequilibrium electronic processes due to the photogeneration of charge carriers [13]. If $h\nu \ll E_g$, the PT is initiated by thermal processes [11]. The unique properties of polycrystalline VO_2 films allow their use in visualizers of IR radiation [11]; reversible holographic media [11]; and modulators, switches, and limiters of IR radiation [14, 15]. It is therefore expedient to investigate the optical properties of VO_2 nanoparticles with the aim of expanding the possibilities of controlling optical devices. In this work, we analyze the optical properties of nanoparticles with a VO_2 core and an Ag or Au shell both near and away from the basic plasmon resonance and also the effect of the PT on these properties. The analysis is carried out in the spectral intervals 1–1.2, 1.3–1.7, and 9–12 μm.

We performed the numerical simulation of the optical properties of nanoparticles in the Rayleigh scattering approximation (the size of nanoparticles is much less than the radiation wavelength) and assumed that a nanoparticle consists of a spherical core and a thin absorbing shell. For low concentrations of such particles, the condition for the plasmon resonance is given by [16]

$$\mathrm{Re}(A) = \mathrm{Re}(\varepsilon_s\varepsilon_a + \varepsilon_{env}\varepsilon_b) = 0. \quad (1)$$

Here,

$$\varepsilon_a = \varepsilon_c(3-2P) + 2\varepsilon_s P;$$

$$\varepsilon_b = \varepsilon_c + \varepsilon_s(3-P); \quad P = 1-\left(\frac{r_c}{r_s}\right)^3;$$

ε_c, ε_s, and ε_{env} are the permittivities of the core, shell, and the environment, respectively; and r_c and r_s are the radii of the core and the shell, respectively. The effec-

1063-7842/03/4805-0602$24.00 © 2003 MAIK "Nauka/Interperiodica"

tive permittivity of the medium containing such nanoparticles is given by [16]

$$\varepsilon = \varepsilon_{env} + 3g\delta, \quad (2)$$

where

$$\delta = \frac{\varepsilon_s\varepsilon_a - \varepsilon_{env}\varepsilon_b}{\varepsilon_s\varepsilon_a + 2\varepsilon_{env}\varepsilon_b},$$

and g is the volume concentration of the particles.

For coated nanoparticles, the absorption (σ_a) and scattering (σ_{sc}) cross sections are [7]

$$\sigma_a = \frac{8\pi^2\sqrt{\varepsilon_{env}}r_s^3}{\lambda}\mathrm{Im}(\delta), \quad (3)$$

$$\sigma_{sc} = \frac{128\pi^5\varepsilon_{env}^2 r_s^6}{3\lambda^4}|\delta|^2. \quad (4)$$

Narrow plasmon resonances are observed in the mid-IR spectral range if the metallic shell is discontinuous [10]. The effective permittivity of a discontinuous metal film may significantly differ from the permittivity of the bulk metal. The former is defined by the dipole–dipole interaction between the islands, which, in turn, depends on the shape of the islands, island spacing, and permittivity of the environment [17]. The components of the effective permittivity of a discontinuous film can be written as [17]

$$\varepsilon_{eff}^* = \chi^* + \varepsilon_c, \quad \frac{1}{\varepsilon_{eff}^{**}} = \frac{1}{\varepsilon_c} - \chi^{**}\frac{d}{\varepsilon_c^2}. \quad (5)$$

Here, ε_{eff} is the effective permittivity of the film, ε_c is the permittivity of the nanoparticle core, χ is the effective polarizability, and d is the packing density of the particles in the film. The upper asterisks correspond to the parallel (*) and perpendicular (**) orientations of the electric field vector relative to the interface.

With allowance for the dipole–dipole interaction, the polarizability has the form [17]

$$\chi^{*,**} = \frac{2\varepsilon_{env}\varepsilon_c}{\varepsilon_{env} + \varepsilon_c}\left[F^{*,**} + \left(\frac{\varepsilon_m}{\varepsilon_c} - 1\right)^{-1}\right]^{-1}, \quad (6)$$

where

$$F^* = f^* - \frac{\pi^2}{24}\frac{2\varepsilon_c}{\varepsilon_{env} + \varepsilon_c}\frac{d_w}{a},$$

$$F^{**} = f^{**} + \frac{\pi^2}{12}\frac{\varepsilon_{env}}{\varepsilon_{env} + \varepsilon_c}\frac{d_w}{a}.$$

Here, ε_m is the permittivity of the metal, ε_{env} is the permittivity of the environment, f is the depolarization factor depending on the particle shape ($f^* = 0.5(1 - f^{**})$), d_w is the weight thickness of the metal film, and a is the mean particle spacing in the film.

When simulating, we employed the spectral dependences of the optical constants for continuous Ag and Au films from [18] and for polycrystalline VO_2 films from [19, 20]. The table shows the complex refractive indices ($n^* = n - ik$) of the polycrystalline VO_2 film below ($T < 50$°C) and above ($T > 70$°C) the PT temperature.

Optical constants of VO_2 before and after the phase transition [19, 20]

λ, μm	$n^*(T < 50°C)$	$n^*(T > 70°C)$
10.6	$2.55 - i \times 0.08$	$8 - i \times 9$
1.55	$3.26 - i \times 0.17$	$1.7 - i \times 2.5$
1.06	$3.1 - i \times 0.5$	$1.7 - i \times 1.8$

It is seen from the table that the PT-related variation of the optical constants of VO_2 films is the greatest at a wavelength of 10.6 μm. Note that dn/dT and dk/dT at this wavelength are positive. In the near-IR range, the variations of n and k due to the PT are relatively small, the absorption coefficient of the semiconductor phase is high, and the derivative dn/dT is negative.

In each of the spectral intervals, the simulation was performed for two types of nanoparticles. For nanoparticles of type 1, the parameters of the core, continuous shell, and environment were taken such that plasmon resonance in the semiconductor phase of VO_2 occurs approximately at the center of the spectral interval. For nanoparticles of type 2, the parameters were such that the plasmon resonance condition is not satisfied in all the spectral intervals. The characteristics of the particles of both types for each of the spectral intervals were as follows.

For the interval λ = 9–12 μm, the parameters of the nanoparticles of type 1 were $r_c = 200$ nm, $r_s = 202$ nm, $n_{env} = 1.4$, $f^* = 0.0073$, $d_w = 0.105$, and $a = 0.1$. The shell was a discontinuous Ag film. In the calculation, the effective thickness and the permittivity of the continuous and discontinuous films were assumed to be equal. The best conditions for plasmon resonance turned out to arise when the discontinuous film covers a medium with a refractive index $n = 1$. This can be realized, for example, if the nanoparticles are embedded in a fine-grain nonabsorbing powder (KCl, KBr, or BaF_2). The parameters of the nanoparticles of type 2 were $r_c = 200$ nm, $r_s = 208$ nm, $n_{env} = 1.4$, $f^* = 0.06$, $d_w = 0.1$, and $a = 0.1$. The shell was a discontinuous Ag film.

For the interval λ = 1.3–1.7 μm, the parameters of the nanoparticles of type 1 were $r_c = 15$ nm, $r_s = 16.2$ nm, and $n_{env} = 1.5$. The shell was a continuous Au film. For the nanoparticles of type 2, $r_c = 30$ nm, $r_s = 31$ nm, and $n_{env} = 1.8$. The shell was a solid Au film.

For the interval λ = 1–1.2 μm, the parameters of the nanoparticles of type 1 were $r_c = 10$ nm, $r_s = 11.5$ nm, and $n_{env} = 1.5$. The shell was a continuous Au film. For

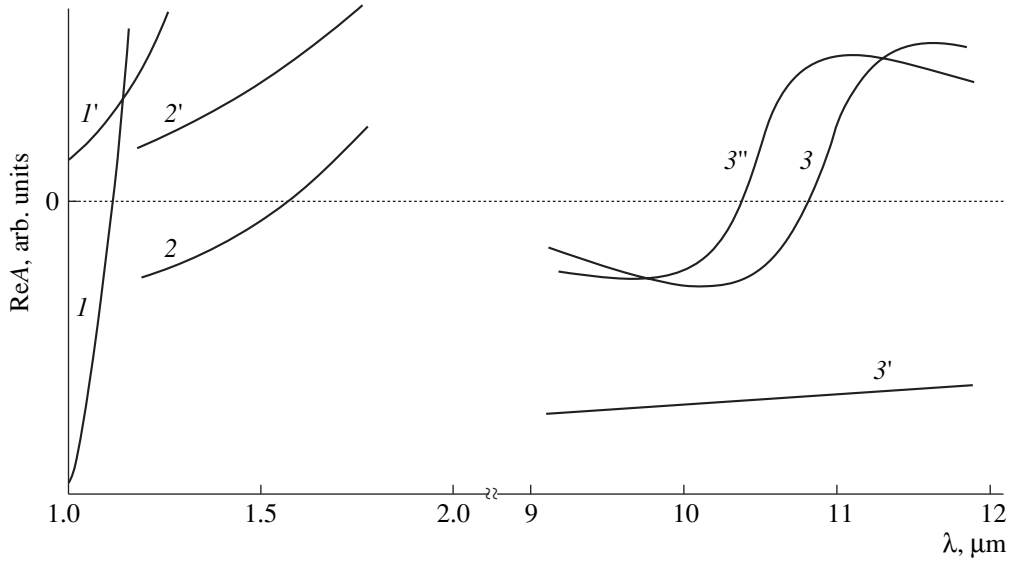

Fig. 1. Excitation of the plasmon resonance (ReA = 0) in type-1 metal-coated VO_2 nanoparticles (*1*–*3*) prior to the PT, (*1*'–*3*') after the PT, and (*3*") at the initial stage of the PT.

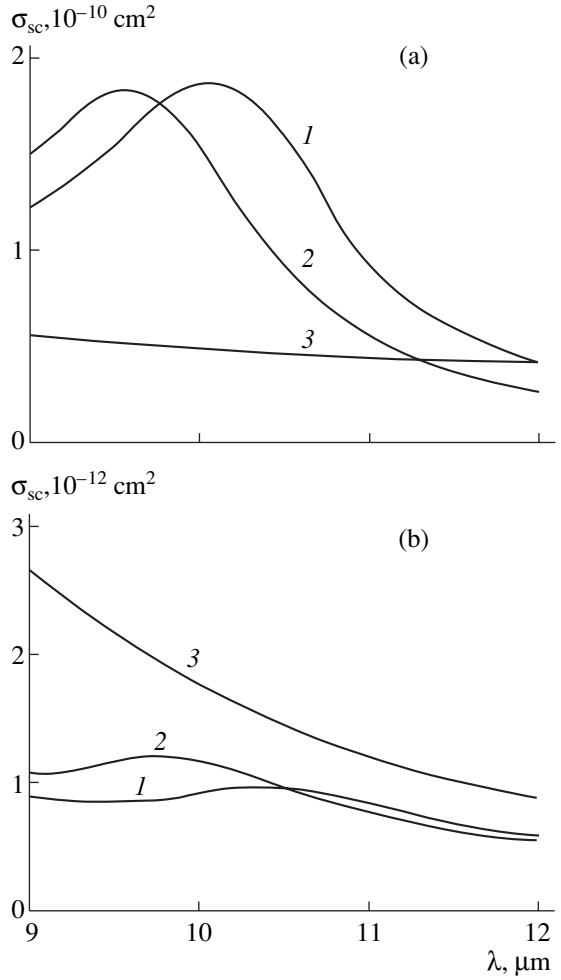

Fig. 2. (a) Absorption and (b) scattering cross sections of VO_2 nanoparticles coated by a discontinuous Ag film (nanoparticles of type-1): (*1*) before PT, (*2*) initial stage of PT, and (*3*) after PT.

the nanoparticles of type 2: r_c = 10 nm, r_s = 10.7 nm, and n_{env} = 1.8. The shell was a continuous Au film.

For the nanoparticles of type 1 prior to the PT, the plasmon resonance condition (ReA = 0) is satisfied approximately at the center of each of the spectral intervals (Fig. 1). At the initial stage of the PT, the plasmon resonance shifts toward smaller wavelengths (curve *3*"). After the transition to the metallic state, the plasmon resonance is absent in the entire spectral interval.

Figure 2 demonstrates the spectral dependences of the absorption and scattering cross sections for the nanoparticles of type 1 in the interval 9–12 μm. It is seen from Fig. 2a that, prior to the PT, the absorption cross section has a distinct maximum at λ = 10.1 μm, which is related to the plasmon resonance. At the initial stage of the PT, the maximum shifts to λ = 9.6 μm. Therefore, the absorption at the latter wavelength first increases and then decreases. After the PT, the absorption cross section $\sigma_a(\lambda)$ decreases monotonically with increasing wavelength in the entire spectral interval. For the wavelength λ = 10.1 μm, the ratio of the absorption cross sections prior to and after the PT equals four. Figure 2b shows weak resonance-related maxima in the spectral dependences of the scattering cross section prior to the PT and at its initial stage. The weak effect of the resonance on the scattering cross sections reflects a low absorption coefficient of semiconductor VO_2 in the given spectral range. The transition of VO_2 to the metallic state increases the scattering cross section in the entire spectral interval. Note that, for the wavelength λ = 12 μm, the PT affects the absorption and scattering only slightly. At the same time, the calculation shows that the effective refractive index of the medium with nanoparticles of type 1 changes by 0.01 at this wavelength when the volume concentration of the

particles equals 1%. This effect can be used for recording light-induced phase gratings and for phase conjugation.

In the absence of the plasmon resonance for nanoparticles of type 2, the PT in VO_2 increases the absorption (Fig. 3) and scattering cross sections (the spectral curves for the scattering cross section are similar to those for the absorption cross section shown in Fig. 3). For the wavelength $\lambda = 10$ μm, the absorption, σ_a, and scattering, σ_{sc}, cross sections increase by a factor of 2.5 and 4, respectively. In this given case, the optical parameters of the shell weakly affect the optical properties of the nanoparticles: the absorption and scattering both before and after the PT grow insignificantly. For such nanoparticles, both σ_a and σ_{sc} depend only on the increase in the VO_2 absorption coefficient upon the PT. Thus, plasmon resonance in metal-coated VO_2 nanoparticles substantially affects their optical properties during the PT.

Figure 4 shows the spectral curves of the absorption and scattering cross sections for VO_2 nanoparticles with a continuous Au shell (type-1 nanoparticles) in the presence of plasmon resonance for the spectral interval 1.3–1.7 μm. Prior to the PT, clearly cut maxima are observed in both the σ_a and σ_{sc} curves near the plasmon resonance. This is because the absorption of semiconductor VO_2 in the given spectral interval is high. As a result of the PT, the plasmon resonance first shifts to smaller wavelengths and then disappears. For the wavelength $\lambda = 1.5$ μm, this process is accompanied by a decrease in the absorption and scattering cross sections (eleven and ten times, respectively). For the wavelength $\lambda = 1.3$ μm, the PT first increases the absorption and scattering cross sections owing to the shift of the plasmon resonance and then decreases these parameters. For $\lambda = 1.7$ μm, σ_a and σ_{sc} diminish slightly with the PT.

For the nanoparticles of type 2, the PT in VO_2 leads to a growth of the absorption and scattering cross sections in the entire spectral interval 1.3–1.7 μm. Figure 5 shows the spectral curves for the absorption cross section for this case. The PT results in a tenfold increase in σ_a at the wavelength $\lambda = 1.5$ μm. The spectral curves for the scattering cross section have a similar shape, but the increase in the scattering cross section at the wavelength $\lambda = 1.5$ μm is 30-fold. As in the case of $\lambda = 10$ μm, the PT-induced variations of σ_a and σ_{sc} for particles of this type depend only on the increase in the absorption coefficient of VO_2.

The calculations for the spectral interval 1–1.2 μm show that the PT-related variations of the optical properties of type-1 and type-2 VO_2 nanoparticles with a solid Au shell are qualitatively similar to those observed in the spectral interval 1.3–1.7 μm. The curves $\sigma_a(\lambda)$ and $\sigma_{sc}(\lambda)$ for $\lambda = 1$–1.2 μm are similar to those shown in Figs. 4 and 5. In the presence of the plasmon resonance, the maxima of the cross sections are observed at a wavelength of 1.13 μm. As a result of the

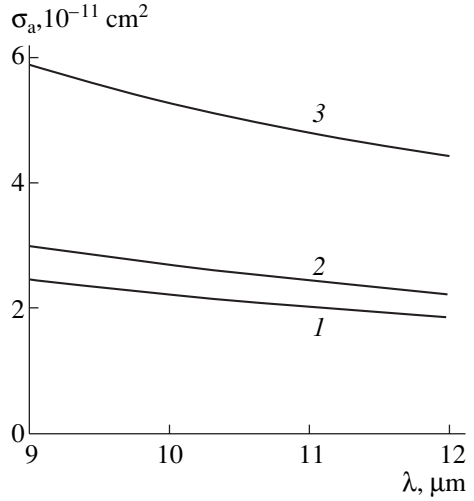

Fig. 3. Absorption cross section of VO_2 nanoparticles coated by a discontinuous Ag film (nanoparticles of type-2): (*1*) prior to PT, (*2*) initial stage of PT, and (*3*) after PT.

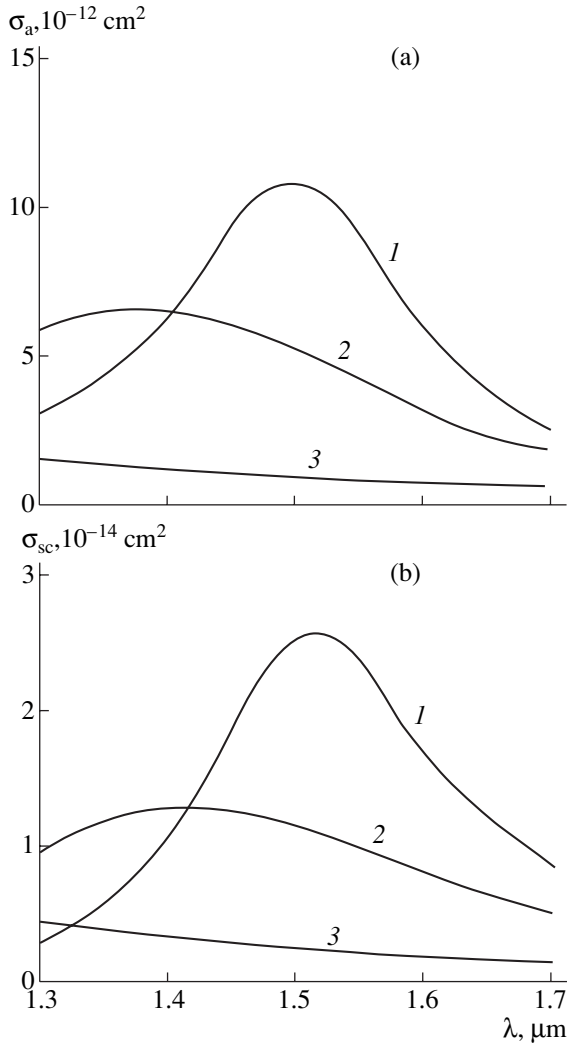

Fig. 4. (a) Absorption and (b) scattering cross sections of VO_2 nanoparticles with the Au shell (nanoparticles of type-1): (*1*) prior to PT, (*2*) initial stage of PT, and (*3*) after PT.

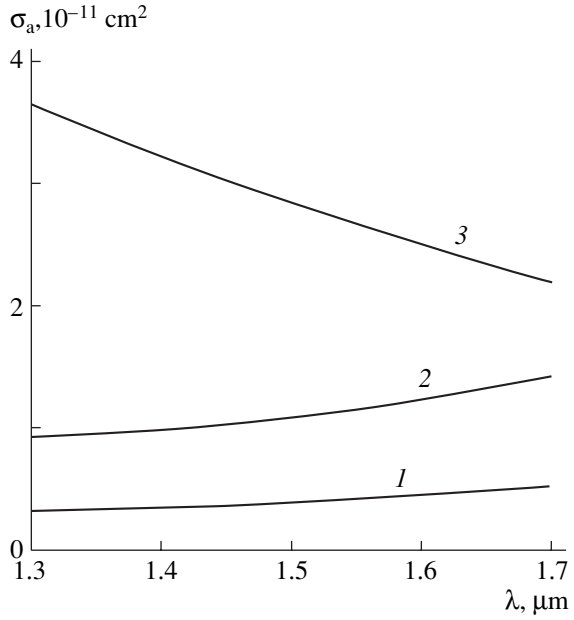

Fig. 5. Absorption cross section of VO_2 nanoparticles with Au the shell (nanoparticles of type-2): (*1*) prior to PT, (*2*) initial stage of PT, and (*3*) after PT

PT in VO_2, the absorption and scattering cross sections at a wavelength of 1.13 μm decrease five and four times, respectively. In the absence of the plasmon resonance, nanoparticles of type-2 exhibit a fourfold and a tenfold PT-induced increase in σ_a and σ_{sc}, respectively, at λ = 1.13 μm. The variations of σ_a and σ_{sc} at this wavelength are less than those at λ = 1.5 μm because of the less significant variation of the VO_2 absorption coefficient upon the PT at smaller wavelengths (see table).

The results presented show that the plasmon resonance condition can be satisfied in the near- and mid-IR ranges for the case of VO_2 nanoparticles coated with a thin continuous and a discontinuous noble-metal film, respectively. Plasmon resonance substantially affects the optical properties of such nanoparticles and the variation of these properties during the PT in VO_2. In particular, in the absence (or presence) of the plasmon resonance, the PT leads to an increase (or decrease) in the absorption and scattering cross sections of the nanoparticles. Thus, the light-induced PT may cause both enhanced transmission and optical limitation in a medium containing metal-coated VO_2 nanoparticles. By varying the volume concentration of nanoparticles, one can create nonlinear optical materials with desired linear and nonlinear optical properties and control these properties over wide limits. Such media containing VO_2 nanoparticles can be used in nonlinear optical switches and modulators of infrared laser radiation.

REFERENCES

1. G. Jadonisi, V. Mmarigliano, and G. P. Zuchelli, Phys. Rev. B **23**, 5163 (1981).
2. M. J. Bloemer, M. C. Buncick, R. J. Warmack, *et al.*, J. Opt. Soc. Am. B **5**, 2552 (1988).
3. W. H. Weber and G. W. Ford, Opt. Lett. **6** (3), 122 (1981).
4. L.-C. Chu and S. Wang, Phys. Rev. B **31**, 693 (1985).
5. H. S. Zhou, I. Honma, H. Komiyama, *et al.*, Phys. Rev. B **50**, 12052 (1994).
6. R. D. Averitt, S. L. Westcott, and N. J. Halas, J. Opt. Soc. Am. B **16**, 1814 (1999).
7. R. D. Averitt, S. L. Westcott, and N. J. Halas, J. Opt. Soc. Am. B **16**, 1824 (1999).
8. J. W. Haus, H. S. Zhou, S. Takami, *et al.*, J. Appl. Phys. **73**, 1043 (1993).
9. M. Y. Han, W. Huang, C. H. Chew, *et al.*, J. Phys. Chem. B **102**, 1884 (1998).
10. A. I. Sidorov, Opt. Zh. **70** (2), 20 (2003).
11. A. A. Bugaev, B. P. Zakharchenya, and F. A. Chudnovskiĭ, *Semiconductor–Metal Phase Transition and Its Applications* (Nauka, Leningrad, 1979).
12. W. Bruckner, H. Opperman, W. Reichelt, *et al.*, *Vanadiumoxide* (Akademie-Verlag, Berlin, 1983).
13. M. F. Becker, A. B. Buckman, R. M. Walser, *et al.*, J. Appl. Phys. **79**, 2404 (1996).
14. F. C. Case, Appl. Opt. **30**, 4119 (1991).
15. O. P. Mikheeva and A. I. Sidorov, Opt. Zh. **68** (4), 48 (2001).
16. A. E. Neeves and M. H. Birnboim, J. Opt. Soc. Am. B **6**, 787 (1989).
17. T. Yamaguchi, H. Takahashi, and A. Sudoh, J. Opt. Soc. Am. **68**, 1039 (1978).
18. V. M. Zolotarev, V. N. Morozov, and E. V. Smirnova, *Optical Constants of Natural and Engineering Media* (Khimiya, Leningrad, 1984).
19. O. P. Konovalova, A. I. Sidorov, and I. I. Shaganov, Opt. Zh. **66** (5), 13 (1999).
20. M. Tazawa, P. Jin, and S. Tanemura, Appl. Opt. **37**, 1858 (1998).

Translated by A. Chikishev

Technical Physics, Vol. 48, No. 5, 2003, pp. 607–611. Translated from Zhurnal Tekhnicheskoĭ Fiziki, Vol. 73, No. 5, 2003, pp. 84–89.

**OPTICS,
QUANTUM ELECTRONICS**

X-ray Phase-Contrast Method and Its Application to the Study of Blood Vessels with a Model Object

A. P. Petrakov

Syktyvkar State University, Syktyvkar, Komi Republic, 167001 Russia
e-mail: petrakov@ssu.komi.com

Received June 26, 2002; in final form, October 2, 2002

Abstract—Studies of the phase-contrast method are reviewed. The principles of phase-contrast image formation are considered. The potentialities of the method are demonstrated using a model object as an example: a capillary tube filled with air and paraffin. *© 2003 MAIK "Nauka/Interperiodica".*

INTRODUCTION

X-ray imaging of an object's internal structure is an important diagnostic tool in medicine, biology, and materials science owing to the high penetrability of X rays and the possibility of nondestructive testing. Conventional methods of medical and industrial radiography, tomography, microscopy, etc., are based on the fact that the X-ray absorption factor depends on the density, composition, and thickness of an object.

Problems arise when weakly absorbing carboniferous objects, such as soft biological tissues, are investigated. However deep X-ray radiation penetrates into such materials, the image contrast is low because of the small absorption factor gradient. By means of X-ray tomography and radiography techniques, hard patterns can be obtained by introducing contrast-enhancing agents containing barium salts or iodine for the study of internals or blood vessels, respectively.

Circulating with the body fluids (in particular, with blood) in a living organism, contrast-enhancing agents fluoresce under the action of X-ray radiation, i.e., emit highly penetratable beams, which leave the object and fall on a photographic film or an appropriate detector. Thus, by imaging the internals or blood vessels at definite time intervals, one can locate a pathological site that makes fluid circulation difficult. The application of hard X rays in contact radiography and tomography methods enables one to display internal structures that are impossible to visualize by any other nondestructive methods.

To reduce the radiation load in medical diagnostics, soft X rays should be used. However, when studying large objects by absorption methods, hard X rays are necessary, since the radiation will otherwise be completely absorbed. Hence, refractive techniques must be developed to reduce the radiation load (dose).

The refraction of X rays has not long been used for the investigation of the internal macrostructure of objects, because refraction angles are small (from several tenths of a second of arc to several seconds of arc). The possibility of detecting small refraction angles has appeared with the advances in high-resolution X-ray diffractometry. The technique that enables the hard imaging of weakly absorbing materials by combining the refraction and diffraction of X rays is known as the X-ray phase-contrast method.

This technique visualizes the internal structure of a weakly absorbing object with a small density gradient with a high spatial resolution [1–3]. It is based on the fact that refraction distorts the phase front of the X-ray wave transmitted through the object. As a result, the X-ray wave deflects from its initial direction by small angles, which depend on the spatial distribution of the object density.

The transmitted radiation is detected by a perfect crystal analyzer placed in the neighborhood of the Bragg angle. With such an arrangement, even a small variation in the angle of incidence of X rays on the analyzer significantly changes the diffracted intensity, which is recorded on a photographic film or by a position-sensitive detector. It should be mentioned that diffraction reflection is dissimilar to reflection from a mirror surface. The difference is that diffraction takes place in the bulk of a crystal, with the diffraction volume defined by the extinction length, which is wavelength dependent. Diffraction reflection results in the convolution of waves and produces image points.

The refraction angle of X rays depends on their energy and the electron density of an object. For example, the refraction angle of 8.048-keV radiation (copper tube) at the protein–water interface is $\approx 0.2''$, which is comparable to the angular width of the diffraction reflection curve of the analyzer. Therefore, the phase-contrast technique allows the image contrast to be increased by one or two orders of magnitude [4–6] compared with the conventional absorption methods. This is of special value for studying medical and biological objects [7, 8]. The spatial resolution of the

1063-7842/03/4805-0607$24.00

method is limited only by the X-ray beam divergence and diffraction in crystal.

In terms of wave optics, phase-contrast images result from the interference of the incident wave with the waves transmitted through an object. Such an approach to imaging weakly absorbing materials has been used for many years; however, the development of similar devices designed for operation in the hard X-ray range was impeded by the lack of lenses appropriate for short-wavelength radiation. The feasibility of high-resolution angular analysis of monochromatic X rays by using diffraction from perfect crystals has given impetus to phase-contrast investigations. This idea was first applied to measuring the thickness of walls of small-radius spheres [9]. Later, the potentialities of the method were demonstrated with various model and biological objects [1–3, 8, 10].

Of high importance is the ultimate sensitivity of the method to a change in the refractive index. According to the theory developed in [4], the least detectable change in the refractive decrement is $\Delta\delta \sim 10^{-9}$, which is three orders of magnitude less than the value $\delta \sim 10^{-6}$ for most soft tissues in medical and biological objects.

The technique considered here makes it possible to obtain hard images from weakly absorbing objects in their natural state without using contrast-enhancing agents, which are a potential health hazard, especially for those suffering from allergic reactions. Another advantage of phase-contrast methods for safe clinical diagnostics is that the sensitivity of these methods decreases with increasing radiation energy as E^{-2} against E^{-3} for the absorption techniques [11]. Therefore, phase-contrast diagnostics is more sensitive at high energies. Owing to this circumstance, the phase-contrast method and conventional radiography provide the same information but an absorbed dose is lower and, hence, a health hazard is less severe in the former case. The phase-contrast technique may also find applications in other fields of X-ray diagnostics [12].

The basic distinction in the X-ray units is that radiation from an X-ray tube first falls not on the object, as in conventional methods, but on a perfect single crystal and reach the object only after diffraction reflection from the crystal. Having passed through the object, X-ray radiation strikes a photographic film or the photosensitive area of a detector after it has undergone diffraction reflection from another perfect single crystal.

Note that the phase-contrast method differs from Bonse–Hart interferometry [13], since the latter technique uses one single crystal. An X-ray beam is halved and, after several Laue reflections, is brought to one again to give an interference pattern. Placing an object in the path of one of the beams results in a change in the interference pattern. A weak point of Bonse–Hart interferometry is that the wave phase shifts by 2π at a length of $\approx$100 μm; therefore, only the images of thin objects can be uniquely identified. For comparison, the phase-contrast method is effective for weakly absorbing objects of size from 0.1 mm to 10 cm.

The radiation source plays an essential role in phase-contrast imaging. If the spatial coherence of an X-ray beam is high, a phase-contrast image can be obtained by placing a highly sensitive film immediately behind the object [14]. In this way, the images of small objects with sizes ranging from 0.1 to 50 μm can be obtained.

Sharp-focused tubes ($\approx$20 μm) provide good contrast from the boundaries of a weakly absorbing object at a distance of $\approx$1 m even in bremsstrahlung [11]. Combining a sharp-focused tube with a slit monochromator allows one to improve the angular resolution to 0.2″ [15].

There exist a number of other methods that do not involve the optics of crystal diffraction. In such techniques, an incident beam is formed by a highly coherent source provided with an aperture, and the transmitted beam is detected by a precision analyzer.

PHASE-CONTRAST IMAGE FORMATION

Let an X-ray beam propagate in air. For X rays, air can be closely approximated by a vacuum. An object placed in the path of the beam causes refraction at its boundary. The refractive index can be expressed as $n = 1 - \delta - i\tau$, where δ is the unit decrement of the refractive index:

$$\delta = (e^2/2\pi mc^2)\lambda^2 Nf.$$

Here, $e^2/\pi mc^2 = r_e = 2.812 \times 10^{-13}$ cm is the electron classical radius; λ is the wavelength; N is the atomic density; and f is the atomic scattering function, which is almost equal to the effective atomic number. In carboniferous compounds, the decrement of refractive index at wavelengths of $\approx$1 Å is very small but nonzero (on the order of 10^{-6}).

The transmitted wave phase is given by $\varphi = 2\pi\delta l/\lambda$, where l is the travel in the object. The difference in the optical paths for different X rays gives rise to a phase difference and, consequently, to a phase gradient. This is equivalent to a change in the direction of wave propagation. Any optical scheme that is sensitive to the direction of X-ray propagation can resolve a phase gradient and, hence, can be used for phase-contrast imaging. Phase gradient is detected by diffraction from a perfect crystal (analyzer) positioned behind the object.

Phase-contrast technology places stringent requirements upon the monochromatism and divergence of the incident beam. An X-ray tube generates continuous and characteristic radiations. The most intense K_{α_1} radiation can be separated out with the help of a monochromator, i.e., a perfect single crystal set at the Bragg angle to one of the crystal planes. In a symmetric monochromator, the diffraction plane is parallel to the surface. However, after single diffraction reflection, the K_{α_2} component is

still present. Its intensity may be considerably reduced relative to that of K_{α_1} by using a slit monochromator with multiple reflections of the wave. The more the number of reflections in the monochromator, the narrower the diffraction curve at its exit.

Usually, monochromatic radiation with an angular width of less than one angular second is generated with the help of an asymmetric monochromator. The angular width of asymmetric reflection is defined by the expression $\Delta\vartheta_B = \Delta\vartheta_0 b^{-1/2}$, where $\Delta\vartheta_0 = C|\chi_{hr}|/\sin 2\vartheta_B$ is the width of the diffraction reflection curve (DRC) for symmetric reflection, C is the polarization factor ($C = 1$ and $C = \cos 2\vartheta_B$ for σ and π polarizations, respectively), χ_{hr} is the real part of the polarizability of a crystal, ϑ_B is the Bragg angle, $b = \gamma_0/\gamma_h$ is the asymmetry parameter, $\gamma_0 = \sin(\vartheta_B + \psi)$, $\gamma_h = \sin(\vartheta_B - \psi)$, and ψ is the angle between the reflecting plane and crystal surface (for symmetric reflection, $\psi = 0$).

Passing through an object results in a change in the X-ray wave front. Within the approximation of geometrical optics, the transmitted wave phase can be written [11] as

$$\varphi(x, y, z, k) = -k\int_{-\infty}^{z}\delta(x, y, z', k)dz'$$

$$= -(r_e/k)\int_{-\infty}^{z}\rho(x, y, z')dz',$$

where ρ is the electron concentration and $k = 2\pi/\lambda$.

The spatial dependence of the phase leads to the refraction of the beam. The angular deflection in the direction perpendicular to the wave front is given by

$$\beta \approx (1/k)|\nabla_{xy}\varphi(x, y, z)| = \left|\nabla\int_{-\infty}^{z}[\delta(x, y, z')]dz'\right|.$$

The setup for phase-contrast imaging is schematically shown in Fig. 1. Two silicon single crystals form the wave front of X rays and ensure a high angular sensitivity to refraction. The crystal monochromator specifies the wave front and collimates the beam incident on the sample. The second single crystal, crystal analyzer, directs (by means of diffraction the plane waves transmitted through the sample to a detector or a photographic film.

Since the refractive index changes, the wave front appears to be distorted. This distortion influences the wave leaving the analyzer, because its intensity depends on the convolution of the wave transmitted through the object with the DRC of the analyzer. The paths of three X rays are indicated by letters *A*, *B*, and *C*. Beam *A* falls on the analyzer without refraction. This case is realized if a beam passes through the center of a cylindrical object. When meeting an interface, such a beam is deflected by an angle $\beta = \Delta n \cot\Theta$, where Δn is the change in the refractive index and Θ is the glancing angle.

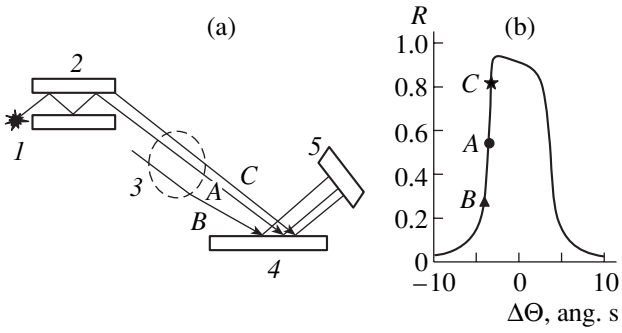

Fig. 1. (a) Experimental scheme: (*1*) X-ray source, (*2*) monochromator, (*3*) sample, (*4*) crystal analyzer; and (*5*) detector or photographic film. *A*, *B*, and *C* indicate the X-ray beam paths. (b) DRC of the analyzer.

Refracted beams *B* and *C* are deflected to the opposite sides and, hence, fall on the analyzer at, respectively, smaller and larger angles than the nonrefracted beam. The refraction sensitivity of the analyzer can be improved by rotating it from the precise Bragg position $\Delta\vartheta = 0$ towards negative (smaller) angles, since the small-angle slope of the DRC is steeper than its positive (large-angle) one (Fig. 1b). The peak intensity is close to unity when $|\Delta\vartheta| \le \Delta\vartheta_B$ and drops abruptly outside this region. The maximal intensity gradient is observed at the point $|y| = 1.0$–1.5, where $y = \Delta\vartheta/\Delta\vartheta_B$.

The image intensity is defined as the product of the intensity I_0 incident on the analyzer by the diffraction reflection coefficient $P(\Delta\vartheta - \beta)$, where the offset $(\Delta\vartheta - \beta)$ is determined by the angle of rotation of the analyzer and the refraction angle. For low-absorption object imaging, the image contrast $K = \Delta I_h/I_h$ (where I_h is the initial intensity and ΔI_h is the intensity change) rather than the intensity of the detected radiation is of importance. The image contrast depends on the angle of rotation of the analyzer. Bright- and dark-field phase-contrast images with contrast reversal are possible to obtain. A dark object against light background appears when the analyzer is turned so that it cannot reflect the beams deflected from the initial direction. Contrast reversal occurs when the analyzer reflects only the deflected beams.

Let us consider the phase-contrast image of a homogeneous rod of radius R. In this case, the phase and the volume absorption of the wave are found from the following formulas: $\varphi(x) = -k\delta l(x)$ and $\mu_v(x) = 0.5\mu l(x)$, where $l(x) = 2(R^2 - \gamma_0^2 x^2)^{1/2}$ is the path of X rays in the rod. The refraction angle $\beta(x) = 2\gamma_0\delta x/l(x)$ for $|\gamma_0 x| \le R$ and $\beta = 0$ for $|\gamma_0 x| > R$. Close to the rod surface, the angle is expected to sharply increase, since $|\beta| \longrightarrow \infty$ at $|x| \longrightarrow R/\gamma_0$. Experimentally, the X-ray intensity at the rod surface was shown to depend on its roughness. This

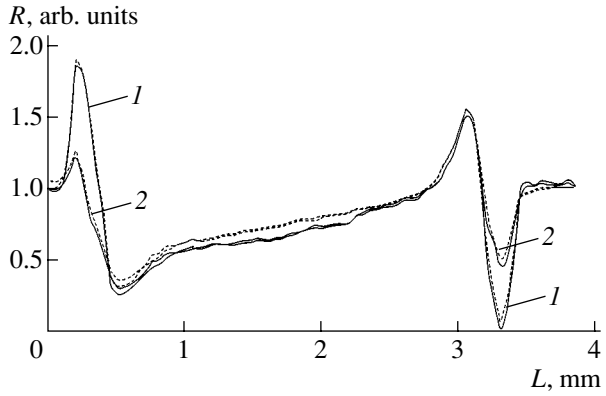

Fig. 2. Experimental (solid line) and calculated (dashed line) intensity of the transmitted X-ray radiation vs. the position of the capillary with (*1*) smooth and (*2*) rough external surface relative to the beam.

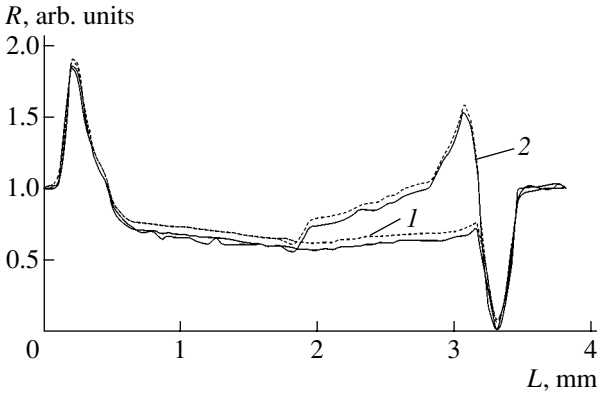

Fig. 3. Experimental (solid line) and calculated (dashed line) intensity of the transmitted X-ray radiation vs. the position of the capillary (*1*) entirely or (*2*) partially filled with paraffin relative to the beam.

factor can be taken into account by introducing a transition layer with the smoothing function [16]

$$F(\rho) = \{1 + \exp[(\rho - R)/\Delta R]\},$$

where $\rho = (x^2 - z^2)^{1/2}$ and ΔR is the transition layer thickness.

It is seen that $F(\rho) \longrightarrow 1$ at $\rho < R$, $F(R) = 0.5$, and $F(\rho) \longrightarrow 0$ at $\rho - R \gg \Delta R$. With regard for the transition layer, $\delta(x, z) = \delta F(\rho)$ and $\mu(x, z) = \mu F(\rho)$. The thicker the transition layer, the smoother the curves.

EXPERIMENTAL

The test samples were polyethylene capillaries with an outer radius and a wall thickness of 1.6 and 0.3 mm, respectively. Phase-contrast images were obtained with the help of a triple-crystal X-ray diffractometer with a copper tube. X-ray radiation from the tube passed through a 0.1-mm-wide vertical slit and entered a slit silicon monochromator with triple symmetric reflection from the (111) plane.

Cu$K_{\alpha 1}$ radiation separated out by the monochromator fell on the object mounted on a support that could move in the direction perpendicular to the beam. After the beam had been transmitted through the object, it entered a silicon analyzer and experienced the single symmetric (111) reflection. The analyzer was offset from the exact Bragg position towards smaller angles by the DRC half-width to enhance the contrast [12]. A scintillation detector picked up the radiation reflected from the analyzer after each move of the sample (0.05 mm^{-1}). The radiation intensity in the absence of the object was taken to be unity.

Several modifications of the object were considered. First, we studied an air-filled capillary with a smooth or rough outer surface. The surface was made rough by ruling the capillary surface at regular intervals (25 mm^{-1}). Then, the smooth-surface capillary was twice filled with paraffin: in one case, paraffin occupied the entire volume of the capillary; in the other, half the inner space along the capillary with the other half occupied by air. In the latter case, the air–paraffin interface coincided with the diameter aligned with the direction of the nonrefracted X-ray beam.

RESULTS AND DISCUSSION

The intensity of the radiation transmitted through the capillaries with the smooth and rough surfaces is shown in Fig. 2. The vertical axis plots the intensity measured by the detector, and the horizontal axis is the position of the object. Curve *1* has two peaks and two dips. Movement along the abscissa axis from left to right is equivalent to the travel of the beam across the capillary. The first peak corresponds to the external boundary of the capillary wall. The dip next to it indicates the internal boundary of the wall. Going on traveling across the capillary, the beam meets the internal and external walls again, giving rise to the second peak and the second dip, respectively, in the curve. Curve *2* is similar to curve *1* with the only difference that the peak at the entrance to, and the dip at the exit from, the capillary are less pronounced.

The intensity distribution in the phase-contrast image of the paraffin-filled capillary is shown in Fig. 3. Curve *1* has one peak at the entrance to the medium and one dip at the exit from it. Curve *2* can be divided into two parts. The left part coincides with the corresponding portion of curve *1* in Fig. 3, and the right one is similar to the right portion of curve *1* in Fig. 2. The left half-space inside the capillary was filled with paraffin; the right, with air. The step in curve *2* near 1.8 mm corresponds to the paraffin–air interface.

The peaks in curve *1* (Fig. 2) appear due to the refraction of the beam first at the external and then at the internal capillary wall as the beam scans the capillary. At these interfaces, the beam from the lower density medium (air) passes into the higher density

medium (polyethylene); therefore, the refracted beams fall on the analyzer surface at a larger angle approaching the exact Bragg angle. Because of this, the reflectivity of the analyzer increases. The right peak is weaker than the left one because of the partial absorption of X rays in the capillary.

The minima in curve *1* correspond to the interfaces crossed by the beam passing from the higher-density to the lower density medium. In this case, the refraction of the beam reduces the angle of incidence on the analyzer and its reflectivity drops.

The shape of the peaks and dips depends on the surface condition [16]. The boundary of any object is not perfectly abrupt: there is always the transition layer due to, e.g., the surface roughness. The theoretical curves constructed similarly to [12] are in good agreement with the experiment if the transition layer thickness is taken to be 0.005 and 0.03 mm for the initial and grooved surfaces, respectively. The decrement of the refractive index and the absorption factor of polyethylene walls with a density of 0.92 g/cm^3 were taken to be $\delta = 0.444 \times 10^{-6}$ and $\mu = 0.333$ cm^{-1}, respectively.

Filling the capillary with paraffin leads to the disappearance of the dip and peak related to the internal boundaries (curve *1* in Fig. 3). This is explained by the higher optical density of paraffin compared with that of air and, accordingly, by the smaller refraction angle of the beam at the interfaces. According to the calculation where the density of paraffin was taken to be 0.82 g/cm^3; δ, 0.396×10^{-6}; and μ, 0.297 cm^{-1}, such an interface may also be detected with the help of highly asymmetric monochromators and analyzers [6]. With these devices, the contrast at the paraffin–air interface inside the capillary will be raised, though this boundary is discernible in curve *2* even with symmetric reflections. The theoretical curve fits closely the experimental data in the presence of the 0.01-mm-thick transition layer on the paraffin surface.

CONCLUSIONS

The results of our investigations can be generalized to objects with a more intricate shape and to several objects arbitrarily arranged in space. The 3D image of a real object may be obtained by recording several phase-contrast images at different rotations of the object about one or several axes. The experimental data presented above clearly demonstrate the possibilities offered by the phase-contrast imaging technique for the diagnostics of soft tissues and blood vessels. This method holds promise for the early recognition of pathologies in the soft-tissue internals of living organisms and vascular diseases, such as atherosclerosis, ischemia, and strokes.

REFERENCES

1. V. A. Somenkov, A. K. Tkalich, and S. Sh. Shil'shteĭn, Zh. Tekh. Fiz. **61** (11), 197 (1991) [Sov. Phys. Tech. Phys. **36**, 1309 (1991)].
2. V. N. Ingal and E. A. Beliaevskaya, J. Phys. D **28**, 2314 (1995).
3. T. J. Davis, T. E. Gureyev, D. Gao, *et al.*, Phys. Rev. Lett. **74**, 3173 (1995).
4. V. A. Bushuev, V. N. Ingal, and E. A. Beliaevskaya, Kristallografiya **41**, 808 (1996) [Crystallogr. Rep. **41**, 766 (1996)].
5. V. A. Bushuev, E. A. Beliaevskaya, and V. N. Ingal, Nuovo Cimento D **19**, 513 (1997).
6. V. A. Bushuev, V. N. Ingal, and E. A. Beliaevskaya, Kristallografiya **43**, 586 (1998) [Crystallogr. Rep. **43**, 538 (1998)].
7. V. N. Ingal and E. A. Beliaevskaya, Phys. Medica **12** (2), 75 (1996).
8. S. Sh. Shil'shteĭn, K. M. Podurets, V. A. Somenkov, *et al.*, Poverkhnost, Nos. 3–4, 231 (1996).
9. E. Forster, K. Goetz, and P. Zaumseil, Krist. Tech. **15**, 937 (1980).
10. D. Gao, T. J. Davis, and S. W. Wilkins, Aust. J. Phys. **48**, 103 (1995).
11. S. W. Wilkins, T. E. Gureyev, D. Gao, *et al.*, Nature **384**, 335 (1996).
12. V. A. Bushuev and A. P. Petrakov, Kristallografiya **46**, 209 (2001) [Crystallogr. Rep. **46**, 171 (2001)].
13. U. Bonse and M. Hart, Appl. Phys. Lett. **7**, 99 (1965).
14. A. Snigirev, I. Snigireva, V. Kohn, *et al.*, Rev. Sci. Instrum. **66**, 5486 (1995).
15. T. E. Gureyev and S. W. Wilkins, Nuovo Cimento D **19**, 545 (1997).
16. V. A. Bushuev and A. Kone, Poverkhnost, No. 10, 5 (1998).

Translated by A. Sidorova

Technical Physics, Vol. 48, No. 5, 2003, pp. 612–615. Translated from Zhurnal Tekhnicheskoĭ Fiziki, Vol. 73, No. 5, 2003, pp. 90–93.

**OPTICS,
QUANTUM ELECTRONICS**

Nonthermal Glow of Thin Metal Plates and Films Exposed to Pulsed Laser Radiation

A. F. Banishev, V. Ya. Panchenko, and A. V. Shishkov

Institute of Problems of Laser and Information Technologies, Russian Academy of Sciences, Shatura, Moscow oblast, 140700 Russia

e-mail: banishev@laser.nictl.msk.su

Received October 22, 2000

Abstract—Nonthermal glow excited in molybdenum plates and films as a result of temperature stresses arising under the action of laser pulses is investigated. A relation between the glow excitation threshold and the sample thickness is established. A possible mechanism of nonthermal glow is discussed. © *2003 MAIK "Nauka/Interperiodica".*

Nonthermal glow induced by the failure (cleavage) of a metal (copper) was first reported in [1]. Later, it was found [2–4] that the nonthermal glow of copper and other metals can also be observed under plastic deformation. Considerable attention has been given to the study of ductile metals, such as Cu, Pt, Au, and Ag. In recent works [5, 6], samples were deformed by laser pulses. In [7–9], a possible mechanism of such a glow was proposed. It was argued [1–9] that nonthermal glow in these metals is similar to luminescence and is caused by the radiative recombination of electrons localized on surface levels and holes generated in the *d* band. The hole generation is due to the overlap of electronic terms (lying above the Fermi level) and *d* states near the dislocation core when dislocations cross the surface during failure. According to this mechanism, plastic-deformation-induced luminescence in a metal is related to the presence of mobile (weakly pinned) dislocations, the probability of hole generation, and the probability of radiative electron–hole recombination.

In terms of this mechanism, in fine-grained brittle metals, the luminescence would be expected to be very weak because of the low concentration of dislocations in the grains and their low mobility in intergranular regions. Therefore, the possibility of luminescence excitation in such materials is of particular interest.

In this study, we investigate deformation-initiated luminescence in thin fine-grained Mo plates and films exposed to laser pulses. Molybdenum is a relatively brittle metal characterized by high values of elastic constants and a low mobility of dislocations.

We managed to detect nonthermal glow (luminescence) from the materials under investigation. A relation between the excitation threshold of luminescence and the sample thickness was found. Possible mechanisms of luminescence excitation are discussed.

EXPERIMENTAL

The experimental setup is schematically shown in Fig. 1. Test sample *3* was placed into vacuum chamber *2*, where the pressure was varied in the range from 10^{-2} torr to 1 atm. The samples were exposed to laser pulses from free-running YAG : Nd laser *1*. The lasing parameters were $\tau_p = 1.4$ ms and $E_{max} = 3.5$ J. The radiation was focused into a spot 1.2 to 2 mm in size on the sample surface. In our experiments, we investigated the glow from the back surface of the samples. For this purpose, photomultiplier *4* was mounted coaxially with the laser beam on the back surface. The sample–photomultiplier spacing was approximately 0.8 cm. The sample temperature was not measured. Instead, using another photomultiplier (*5*), which was mounted in front of the sample at an angle of 45° to its surface, and a set of light filters, we kept track of thermal glow from the irradiated region on the surface in the spectral range of 0.5–0.7 μm and the threshold of plasma formation. The signals from both photomultipliers were applied to a digi-

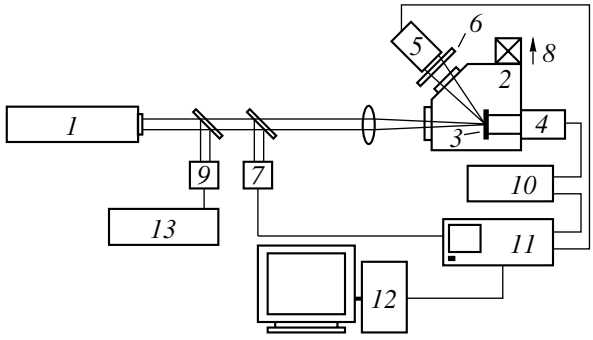

Fig. 1. Experimental setup: (*1*) YAG : Nd laser, (*2*) vacuum chamber ($P = 10^{-2}$ torr), (*3*) sample, (*4*, *5*) FÉU-79 photomultiplier, (*6*) set of light filters, (*7*) photodetector, (*8*) to vacuum pump, (*9*) energy meter, (*10*) amplifier, (*11*) digital oscilloscope, (*12*) PC, and (*13*) pulse voltmeter.

1063-7842/03/4805-0612$24.00 © 2003 MAIK "Nauka/Interperiodica"

tal oscilloscope and then to a PC. We investigated the glow of 100-, 200-, 300-, 400-, and 500-μm-thick Mo plates (thin foils). They were prepared by rolling at a temperature of about 300°C and were textured. In addition, Mo, Cu, Al, and Ti films with a thickness of about 1–2 μm deposited on quartz substrates were examined. Prior to measurements, the plates were polished by diamond powder and cleansed in ethanol. To measure the grain sizes and to visualize the dislocation pattern, the plates were treated in the $5HNO_3 + 3H_2SO_4 + 2H_2O$ etchant and then rinsed in the $10NaOH + 250H_2O_2 + 750H_2O$ solution. The surface structure was examined with optical and atomic-force microscopes.

RESULTS

The intensity I_{ML} of the mechanoluminescence (ML) signal as a function of the power density of a laser pulse, I_{las}, was studied, and the dependences of the threshold temperature stress for luminescence on the sample thickness were constructed.

Figure 2 shows the luminescence signals from the Mo plates of various thicknesses and from the thin Mo film under the action of laser pulses with a threshold power density $I_{las, th}(h)$ ($I_{las, th}(h)$ is the minimum (threshold) power density necessary to initiate luminescence for a given sample thickness). It is seen that the signals appear as a set of spikes nearly identical in amplitude and, generally, similar in shape. Figure 3 shows the experimental dependence $I_{las, th}(h)$ and analytical dependences $T_{th}(I_{las, th}(h))$ and $\sigma_{th}(T_{th})$, where T_{th} and σ_{th} are, respectively, the temperature and thermal stresses on the back surfaces of the plates and film that are reached when $I_{las} = I_{las, th}(h)$. As is seen, T_{th} and σ_{th} are virtually independent of the plate thickness and equal $T_{th} = 50–70$°C and $\sigma_{th} = (4.0–5.5) \times 10^7$ N/m^2. However, for the thin Mo film, both values are noticeably higher: $T_{th} \approx 150$°C and $\sigma_{th} \approx 12.3 \times 10^7$ N/m^2 (Fig. 4). For comparison, the values of T_{th} and σ_{th} for other films are also presented in Fig. 4.

Figure 5 shows the surface relief of the samples that is observed in a SMENA-B atomic-force microscope. It is known that the low-temperature (at $T < 0.5T_{fus}$, where T_{fus} is the fusion point) deformation (rolling) of molybdenum leads to the formation of a fine-grained structure with a small concentration of dislocations in the grain volume. The dislocations are concentrated in intergranular regions, producing cellular structures [10]. The majority of the cells are seen to be 0.1–0.5 μm in size. The characteristic property of the Mo samples thus obtained is the absence of dislocations inside the cells and their localization along the cell boundaries [10]. The surface relief of the Mo film is also shown in Fig. 5. The film also has a fine-grained structure with grain sizes of about 0.05–0.20 μm.

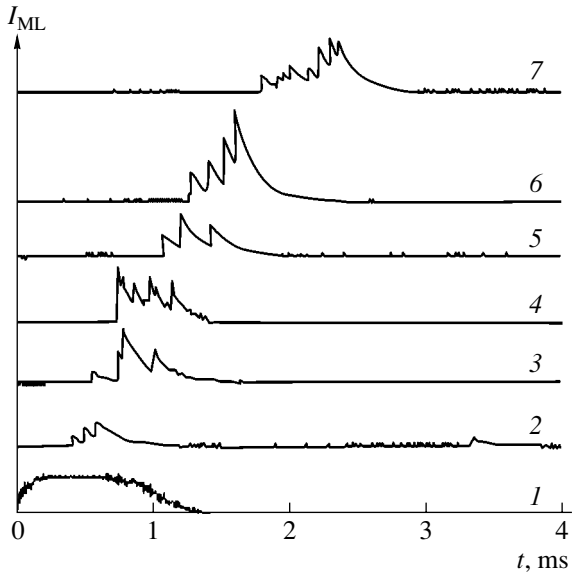

Fig. 2. Waveforms of the ML signals from the Mo samples. (*1*) Laser pulse, (*2*) $h = 2$ μm and $I_{las} = 2.3 \times 10^3$ W/cm^2, (*3*) $h = 0.1$ mm and $I_{las} = 1.3 \times 10^4$ W/cm^2, (*4*) $h = 0.2$ mm and $I_{las} = 3.4 \times 10^4$ W/cm^2, (*5*) $h = 0.3$ mm and $I_{las} = 7.6 \times 10^4$ W/cm^2, (*6*) $h = 0.4$ mm and $I_{las} = 11.0 \times 10^4$ W/cm^2, and (*7*) $h = 0.5$ mm and $I_{las} = 21.4 \times 10^4$ W/cm^2.

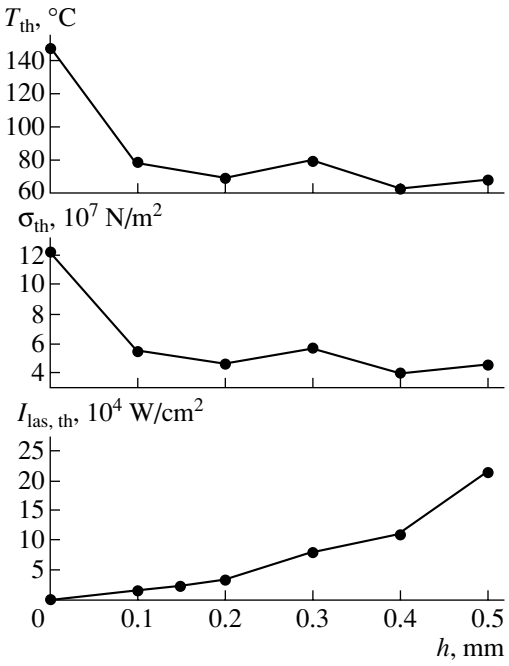

Fig. 3. Experimental dependence $I_{las, th}(h)$ and calculated dependences $T_{th}(I_{las, th}(h))$ and $\sigma_{th}(I_{las, th}(h))$ for the Mo plates.

DISCUSSION

Today, mechanisms behind luminescence mechanoluminescence in metals under plastic deformation still remain unclear. Therefore, the questions as to

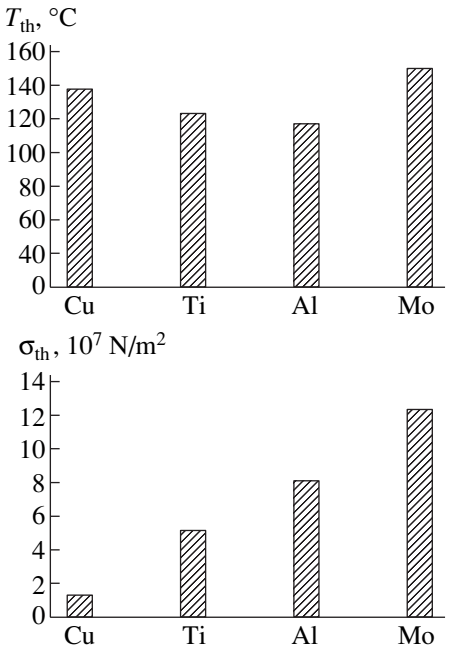

Fig. 4. $T_{th}(I_{las,\,th}(h))$ and $\sigma_{th}(I_{las,\,th}(h))$ for the thin Cu, Ti, Al, and Mo films.

which electron transitions are responsible for ML in a particular metal and what mechanism is responsible for their excitation are still to be attacked. At present, one can only argue that the ability of metals to luminesce is specified by the presence of mobile dislocations [1–9]. In terms of the dislocation model of ML, the threshold value of temperature stress $\sigma_{th}(T_{th})$ at which the ML signal appears when $I_{las} = I_{las,\,th}(h)$ must depend on the strength of dislocation pinning. One may thus expect that the amount of mobile (weakly pinned) dislocations in micrometer- or sub-micrometer-thick samples is low.

For example, in thin samples (whiskers and thin films [11]) and ultra-fine-grained materials (with grain sizes of $d < 100$ nm) [12–15], dislocations are practically absent. Therefore, according to the dislocation model, ML in such materials is expected to be initiated at high $\sigma(T_{th})$. This agrees completely with the experimental results obtained by us for the thin fine-grained films, where the increase in σ_{th} is observed (Fig. 4). At the same time, with the mechanism proposed in [1–9], it is difficult to explain why the glow of Mo and W [16, 17] is observed in the entire visible range 0.4–0.8 μm, where there are no maxima typical of transitions between particular electron levels.

As was mentioned above, the materials investigated have a fine-grained cellular structure and dislocations in the cells are absent. Therefore, the emergence of dislocations on the grain (cell) surface is unlikely and, consequently, the plastic deformation of these materials occurs mainly via grain boundary glide (i.e., by means of grain-boundary dislocations). According to [11, 18], the presence of grain-boundary dislocations and large-angle boundaries does favor intergranular slip and leads to the formation of intergranular microcracks during plastic deformation.

Based on our experimental results and the structural features of the test samples, we suggest the following mechanism behind the nonthermal deformation-induced glow of fine-grained metals. Temperature stresses lead to grain boundary glide, which activates the interaction between grain-boundary dislocations and impurity atoms, which are usually always present in the material and concentrated mainly along dislocations and grain boundaries. The materials used in our experiments were of 3*N* purity, and the concentration of

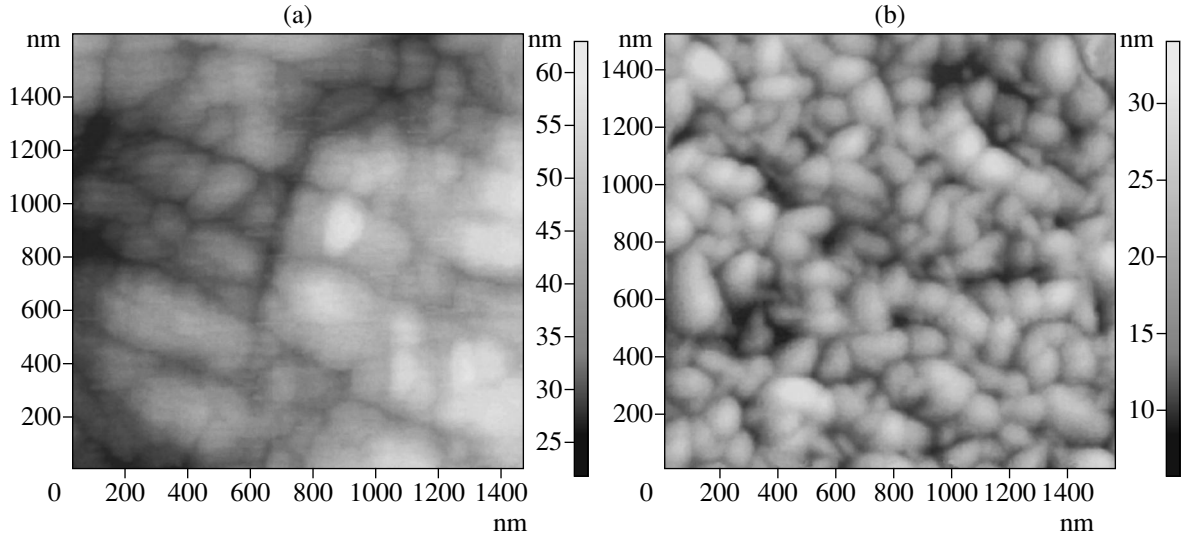

Fig. 5. Surface topograms obtained with the atomic force microscope: (a) Mo plate with a thickness $h = 0.2$ mm and (b) Mo film with a thickness $h = 2$ μm.

impurities (oxygen, nitrogen, carbon, hydrogen, etc.) was on the order of 10^{17}–10^{18} cm^{-3}. In this case, the excitation mechanism of luminescence is likely to be related to tunnel transitions in impurity atoms subjected to the field of a charged dislocation. Since there is a variety of impurity atoms, which are in different coordination environments, it may be expected that luminescence will have a wide spectrum, which is the case, as revealed experimentally. Therefore, such a glow must be observed in any metal containing impurities and mobile dislocations.

ACKNOWLEDGMENTS

We are grateful to K.B. Abramova for submitting the program used to compute temperature stresses in metal plates under laser action.

This work was supported by the Russian Foundation for Basic Research (grant no. 02-02-17028).

REFERENCES

1. K. B. Abramova, V. P. Valitskiĭ, N. A. Zlatin, *et al.*, Zh. Éksp. Teor. Fiz. **71**, 1873 (1976) [Sov. Phys. JETP **44**, 983 (1976)].
2. K. B. Abramova, A. B. Pakhomov, B. P. Peregud, *et al.*, Zh. Tekh. Fiz. **58**, 817 (1988) [Sov. Phys. Tech. Phys. **33**, 497 (1988)].
3. K. B. Abramova, A. B. Pakhomov, B. P. Peregud, *et al.*, Zh. Tekh. Fiz. **60** (6), 186 (1990) [Sov. Phys. Tech. Phys. **35**, 752 (1990)].
4. K. B. Abramova and I. P. Shcherbakov, Zh. Tekh. Fiz. **64** (9), 75 (1994) [Tech. Phys. **39**, 901 (1994)].
5. K. B. Abramova, I. P. Shcherbakov, I. Ya. Pukhonto, *et al.*, Zh. Tekh. Fiz. **66** (5), 190 (1996) [Tech. Phys. **41**, 511 (1996)].
6. K. B. Abramova, A. I. Rusakov, A. A. Semenov, *et al.*, Fiz. Tverd. Tela (St. Petersburg) **40**, 957 (1998) [Phys. Solid State **40**, 877 (1998)].
7. M. I. Molotskiĭ, Fiz. Tverd. Tela (Leningrad) **20**, 1651 (1978) [Sov. Phys. Solid State **20**, 956 (1978)].
8. M. I. Molotskiĭ, Fiz. Tverd. Tela (Leningrad) **23**, 2171 (1981) [Sov. Phys. Solid State **23**, 1269 (1981)].
9. M. I. Molotskiĭ, Fiz. Met. Metalloved. **55** (1), 43 (1983).
10. V. I. Trefilov, Yu. V. Milman, R. K. Ivashchenko, *et al.*, *Structure, Texture, and Mechanical Properties of Strained Molybdenum Alloys* (Naukova Dumka, Kiev, 1983).
11. O. A. Kaĭbyshev and R. Z. Valiev, *Grain Boundaries and Properties of Metals* (Metallurgiya, Moscow, 1987).
12. R. A. Andrievskiĭ and A. M. Glezer, Fiz. Met. Metalloved. **88** (1), 50 (1999).
13. R. A. Andrievskiĭ and A. M. Glezer, Fiz. Met. Metalloved. **89** (1), 91 (2000).
14. V. A. Pozdnyakov and A. M. Glezer, Fiz. Tverd. Tela (St. Petersburg) **44**, 705 (2002) [Phys. Solid State **44**, 732 (2002)].
15. V. A. Pozdnyakov and A. M. Glezer, Dokl. Akad. Nauk **384** (2), 177 (2002) [Dokl. Phys. **47**, 363 (2002)].
16. A. F. Banishev, V. Ya. Panchenko, and A. V. Shishkov, Poverkhnost, No. 6, 48 (2002).
17. A. F. Banishev, V. Ya. Panchenko, and A. V. Shishkov, in *Technical Digest of the Conference on Lasers, Applications, and Technologies, LAT-2002, Moscow, 2002*, p. 261.
18. N. I. Novikov and V. A. Ermishkin, *Micromechanisms of Fracture in Metals* (Nauka, Moscow, 1991).

Translated by Yu. Vishnyakov

Technical Physics, Vol. 48, No. 5, 2003, pp. 616–620. Translated from Zhurnal Tekhnicheskoĭ Fiziki, Vol. 73, No. 5, 2003, pp. 94–98.

ACOUSTIC, ACOUSTOELECTRONICS

Thermally Stimulated Acoustic Splitting of an Elastic Wave in Polycrystalline Niobium Subjected to Electron-Beam Remelting

Yu. A. Burenkov

Ioffe Physicotechnical Institute, Russian Academy of Sciences, Politekhnicheskaya ul. 26, St. Petersburg, 194021 Russia

e-mail: pgpt@mail.ioffe.ru

Received September 27, 2002

Abstract—The effect of temperature on the Young's modulus of electron-beam-remelted polycrystalline niobium is studied in the temperature range 20–1000°C. The impurity content in the material is Ta < 0.5 wt% and O_2 < 0.1 wt%. The acoustic split of the resonant frequency is found in the temperature range 60–180°C, which makes the determination of the Young's modulus uncertain. Mechanisms behind the thermally stimulated splitting of an elastic wave and the behavior of the Young's modulus over a wide temperature interval are discussed. *© 2003 MAIK "Nauka/Interperiodica".*

INTRODUCTION

Niobium has a number of unique properties [1], making it an extremely promising structural material in many areas of technology, including nuclear power. That is why the physicomechanical properties of niobium have been the subject of much investigation. There is a large body of data for the effect of temperature on the elastic properties of Nb [1–3], but the spread in data obtained by different authors is significant. Possibly, this is related to the various structures of the samples studied. In addition, most of the data are incomplete; that is, the initial state of the material or the type of preliminary heat treatment was not indicated.

In this work, we study the behavior of the Young's modulus in electron-beam-remelted niobium (the content of impurities is Ta < 0.5 wt% and O_2 < 0.1 wt%) over a wide temperature range. Emphasis is on the effect of acoustic splitting of the resonance frequency, which has been discovered in imperfect specimens.

EXPERIMENTAL

Specimens used were 20-mm-long rectangular rods with a 3 × 3-mm cross section that were made of an as-prepared ingot by arc cutting.

The Young's modulus E was determined by the resonance method upon the electrostatic excitation of longitudinal elastic waves in the specimen [4] $E = 4\rho l^2 f^2 n^{-2}/(1 + \Delta l/l)$, where ρ is the density of the material, l is the length of the specimen, f is the resonance frequency of longitudinal vibrations in the specimen, n is the number of an excited harmonic (n = 1 in our case), and Δl is the specimen elongation due to thermal expansion.

The room-temperature density, which was determined by hydrostatic weighing, was found to be 8570 kg/m^3.

The experiments were carried out at T = 20–1000°C. To improve heat exchange, the specimen, together with the furnace, was placed in a chamber filled with pure helium at a pressure 0.1 MPa. For T above 300°C, the measurements were made at a pressure of 1.33×10^{-2} Pa. The rates of heating and cooling were about 2°C/min. Each data point in the curves $E(T)$ was taken after the temperature in the chamber had been stabilized. The thermal expansion parameters for Nb are available from [5].

RESULTS AND DISCUSSION

At T = 20°C, the modulus E of the rods cut from the side and central parts of the as-prepared ingot was equal to 103.4 and 103.8 GPa, respectively. The decrease in E by about 0.4% is likely to be associated with defects (nanopores, dislocations, grain boundaries, etc.) concentrated near the central area of the ingot surface.

Since the electrostatic method of exciting resonant mechanical vibrations is very sensitive to lattice defects, the curves $E(T)$ were taken from both as-prepared and annealed specimens.

When heated from 20 to 300°C, some of the as-prepared specimens show, along with the fundamental resonance, weaker (hereafter additional) resonances. The additional resonance appear at frequencies f_2 higher and lower than the fundamental vibration frequency f_1. Such a splitting of the resonance frequency in the curves $f(T)$, which makes the determination of E uncertain and has been called acoustic splitting (AS), is

1063-7842/03/4805-0616$24.00

observed in the interval 60–180°C. At higher temperatures, the AS effect is absent. Therefore, the modulus E of rods cut from different parts of the as-prepared ingot was examined precisely in this temperature interval.

Rods cut from the central part did not exhibit the AS effect. The curves $E(T)$ for these rods are shown in Fig. 1. For specimens *1–3*, the curves are similar to each other and run anomalously, with their minimum corresponding to 180°C. The forward (heating) and backward (cooling) curves coincide.

In specimens *4* and *5*, which were cut from the opposite ends of the as-prepared ingot, AS at low fixed temperatures and the anomalous behavior of f_1 in the form of successive jumps are observed in the dependences $f(T)$. Such jumps are typical of first-order phase transitions and occur when the resonances in the range of resonant frequency splitting are equal in amplitude at a certain temperature. The temperature dependences of the resonant frequency in the coordinates f^2–T are shown in Fig. 2. The values of f_2 (filled circles) are connected to the corresponding values of f_1 (open circles) by vertical dashed lines. For specimen *4*, the jumps of f_1 are observed at 63 and 113°C (Fig. 2a); for specimen *5*, at 97, 128, and 154°C (Fig. 2b).

Figure 3 depicts frequency responses (FRs) taken from specimen *4* in the AS range (Fig. 3a) before the jump of f_1 at 61.5°C, (Fig. 3b) at the instant of the jump at 63°C, and (Fig. 3c) after the jump at 64 and 66.5°C. At the instant of the jump, the peaks have equal amplitudes, while near the jump (Figs. 3a, 3c), the additional peaks are much lower. Before the jump of f_1, the amplitude of the additional peak grows with temperature; after the jump, the additional peak decays rapidly and disappears at a temperature 5 to 15°C higher than the jump temperature. Similar FRs with resonant frequency splitting were also observed at other temperatures. It is remarkable that the peaks in the FRs are stable: they persist after room-temperature storage of the specimens for several days, and their amplitudes do not change. Moreover, they are reproduced on both cooling and repeat heating and do not shift in the temperature scale.

The split of the FRs observed experimentally is consistent with the standard response of a resonator with several degrees of freedom [6]. According to the vibration theory, an FR has two peaks in the case of induced vibration of a system with two degrees of freedom. It was shown [7] that two types of longitudinal waves with various velocities may propagate in an elastic isotropic medium. The mechanical and thermal parameters of such waves are interrelated, which may cause the AS effect. However, a self-consistent theory of AS in solids is still lacking.

The split of the resonance frequency of specimens, as well as the oscillations of the velocity and attenuation of ultrasonic waves, was observed many times in experimentally studying the temperature dependences

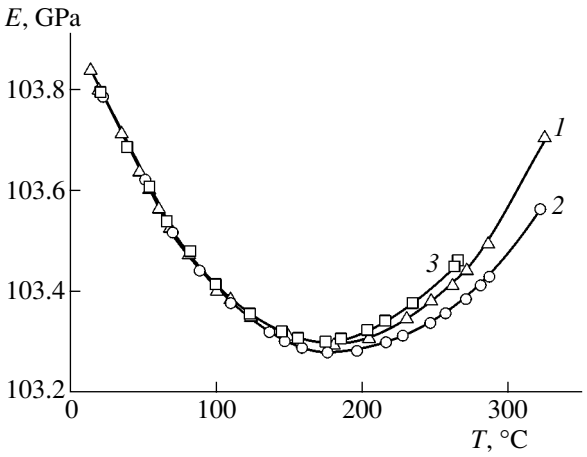

Fig. 1. Temperature dependence of the Young's modulus for Nb specimens cut from the central part of the as-prepared ingot. The figures by the curves are specimen numbers.

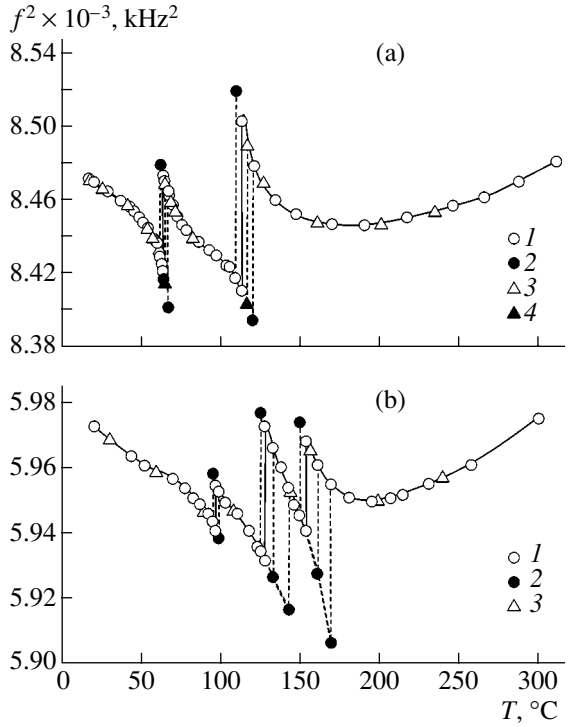

Fig. 2. AS effect in the curves $f^2(T)$ for Nb specimens cut from the surface part of the as-prepared ingot. (a) Specimen *4* and (b) specimen *5*. (*1*, *2*) Heating and (*3*, *4*) cooling.

of the elastic moduli and internal friction of different materials by the resonance method. As was noted in [8, 9], the effect of splitting the resonance frequency was originally discovered by Belomestnykh and Botaki as early as in 1976 [10]. These authors simultaneously measured the velocities of elastic waves propagating in two modifications of CsN_3 near the phase transition temperature. However, in even earlier works [11–14], the dispersion of mechanical resonance and the split of

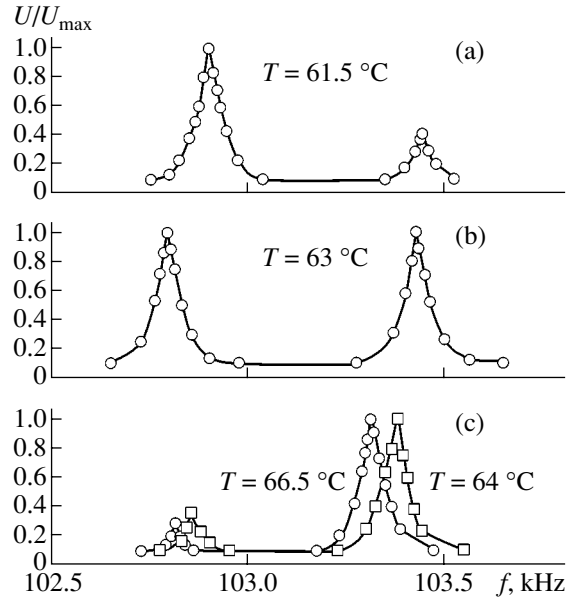

Fig. 3. Frequency responses taken upon the heating of specimen *4* at four temperatures. U, output voltage amplitude; U_{max}, output voltage amplitude in resonance. (a) Before the jump of the fundamental resonant frequency (61.5°C), (b) at the instant of the jump (63°C), and (c) after the jump (64 and 66.5°C).

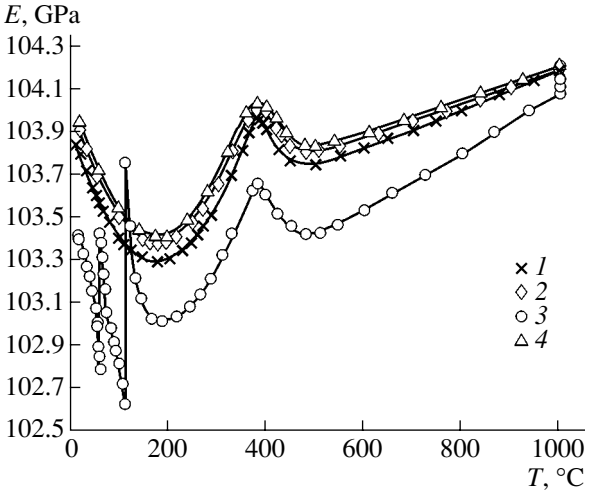

Fig. 4. Temperature dependence of the Young's modulus for specimens *1* (*1*, *2*) and *4* (*3*, *4*). (*1*, *3*) Heating and (*2*, *4*) cooling after annealing.

the resonance frequency of longitudinal and torsional vibrations in polycrystalline metals, alloys, quartz, and a number of single crystals were observed at different temperatures. Later, the thermally stimulated AS of elastic waves was found in barium titanate [15] and in many ionic metastable molecular crystals [16]. This phenomenon was attributed to the coexistence of various solid phases in the specimens. In [14, 17], AS was observed during the loading (deformation) of single-crystal copper and silicon bronze. This phenomenon was explained by the presence of second-phase particles in the specimens [17]. Upon the annealing of ultrafine-grain copper produced by intense plastic deformation, the shape memory effect for the Young's modulus was found [18]. After each annealing at a new temperature, the material changed its structural state. On subsequent cooling, two or three resonant frequencies were simultaneously detected. The authors of [18] believe that several resonances reflect the coexistence of new and old phases. AS in high-temperature superconductors, which was observed many times, was analyzed in [8]. It was related to the lattice instability and restructuring near the superconducting transition temperature, formation of long-period soliton-like structures, waveguide propagation of ultrasonic waves, etc.

From results of works [8–18], it follows that the AS effect showing up in different materials cannot yet be described comprehensively. Mechanisms behind the FR splitting have not been clearly understood up to now. Specifically, the influence of defects on resonance frequency splitting remains to be elucidated.

It is known [18, 19] that the elastic moduli of metals are very sensitive to lattice defects and change substantially after heat treatments. As is known [20], structural defects may cause new-phase precipitates to arise around a defect. It seems plausible that, in imperfect Nb rods cut from the surface part of the massive ingot, heat treatments favor the relaxation of high internal stresses through the movement of already existing defects and the generation of new ones. These processes are accompanied by material restructuring with the formation of various modifications.

It is natural to suppose that the AS effect observed in the curves $f^2(T)$ (Fig. 2) is due to the existence of macroregions with various structures in the Nb specimens. Elastic waves in these regions propagate with various velocities. The phenomenon observed can, therefore, be explained by the fact that induced vibrations with additional internal degrees of freedom arise near diffuse phase transitions in imperfect specimens. It is of interest that the values of f_2 fall on the extensions of the curve $f^2(T)$ before and after the jump, i.e., corresponding to the old and new structural states. These tails of the resonant frequencies are related to new-phase nuclei in the old phase and old-phase residues in the new one. The rearrangement of the structure takes place in a rather narrow (within several degrees) temperature range on both sides of the jump temperature. It was also found [21] that regions with a structure close to the new-phase structure nucleate well before the phase transition temperature in various materials. In [22], the coexistence of several regions with fluctuating structures was explained by the "thermodynamically uncertain" temperature dependence of the free energy. At each temperature when f_1 experiences a jump, the material changes its structure. Reversible structural relaxation occurs in this case, since the jumps are reproduced on both cooling and repeat heating of the speci-

men. The appearance of each new phase causes stresses, which increase the resonant frequency and, hence, the elastic wave velocity and Young's modulus, as follows from Fig. 2.

The annealing of specimen *4* at 500°C for 2 h and subsequent uniform cooling somewhat suppress the jumps and shift them toward higher temperatures. Also, the annealing partially relieves the stresses, and the modulus E slightly grows at room temperature.

In the following experiments, specimens *1* and *4* were heated to 1000°C, then annealed for 2 h, and cooled to room temperature. The results of such a heat treatment are shown in Fig. 4. The curves $E(T)$ for these specimens are seen to differ quantitatively. For specimen *1* isothermally annealed at 1000°C, the cooling and heating curves run in a similar manner and the hysteresis loop for the modulus is insignificant. During the annealing of specimen *4* at 1000°C, the value of E increases with time. The heat treatment completely suppresses the jumps of the fundamental resonant frequency on cooling. AS is absent in this case. The cooling curve runs above the heating curve and almost coincides with the curve $E(T)$ for specimen *1*. There is no doubt that such behavior of $E(T)$ upon the heating of as-prepared specimen *4* is due to its imperfect structure.

It is known [23] that annealing improves the specimen structure, alters the velocity of elastic waves, and increases the elastic modulus to a value observed in a perfect specimen. The fact that the annealing of specimen *4* causes an irreversible increase in E clearly demonstrates a significant modification in its structure. However, such a heat-treatment-assisted structural modification does not change the density of the material at room temperature. It was also demonstrated [11] that additional resonances observed in polycrystalline metals are removed after high-temperature annealing. This substantiates our supposition that the reasons for thermally stimulated AS are the instability of the imperfect structure of the Nb specimens and its complex reconstruction, causing the formation and coexistence of various material modifications. Note, however, that mechanisms behind AS in polycrystalline niobium are still little understood, because the problem of oscillatory states in imperfect crystals is complicated and calls for special theoretical and experimental investigation.

As follows from Figs. 1–4, E decreases only in the range 20–180°C. At higher temperatures, it even slightly grows rather than drops as in most crystals. At 380°C, the dependences $E(T)$ show a broad peak of unknown nature. In general, the dependence $E(T)$ is rather weak: in the range 20–1000°C, E varies by less than 1.5%.

The minor variation of E up to 1200°C was also observed by other authors; only above this point, E starts slowly decreasing. The dependences $E(T)$ for Nb obtained in various works are summarized in [1]. Almost all the curves differ from one another, since they were taken from specimens with different structures and an uncontrollable impurity composition.

Because of the complicated variation of binding forces, a unified mechanism describing the effect of temperature on the elastic properties of Nb has not worked out to date. Today, there are several viewpoints concerning the specific variation of the Nb elastic moduli. It was hypothesized [1] that the unusual behavior of the Young's modulus and shear modulus of Nb on heating reflects the specific configuration of electronic shells in this metal. Impurities (primarily oxygen) present in it may strengthen atomic bonds by producing a solid solution at high temperatures. Foreign atoms may have a twofold effect: (1) atomic interactions start to depend on the free electron concentration (electronic factor) and (2) static distortions, which change the lattice parameter, arise because of a radius mismatch between an impurity and the solvent (dimension factor). In [2], the variation of E upon heating is accounted for by the anisotropy of Nb grain properties. Relations between elastic properties, anisotropy, and texture have not yet been studied at length. We can only note that the difference in the elastic moduli of isotropic and textured polycrystals may reach several tens of percent [19].

CONCLUSIONS

Our investigation clearly demonstrates that the AS effect for a longitudinal ultrasonic wave in polycrystalline Nb is reproducibly observed in a limited temperature range, depends on the concentration of defects in specimens and their thermal history, and disappears after annealing at 1000°C.

It is shown that traces of new and previous (thermally broken) substructures can be detected by measuring the Young's modulus of imperfect specimens. The possibility of simultaneously finding the FR amplitudes at two resonant frequencies corresponding to two different structural states (phases) makes it possible to judge a quantitative relationship between these phases near the phase transition. A detailed study of the AS of elastic waves may give rise to a new method for investigating the phase transition kinetics in materials, since there appears the possibility of keeping track of phase relations with a high accuracy as the temperature varies.

Our experimental data for the elastic properties of Nb over a wide temperature range and the behavior of ultrasonic waves in defect structures might be helpful in analyzing component parts of machines and constructions; in equations of mechanics of rigid bodies; and in the analytical apparatus of the physical theory of deformation and fracture, which involves contemporary concepts of imperfections in crystalline materials.

ACKNOWLEDGMENTS

The author thanks V.I. Kopylov for the material submitted and also B.I. Smirnov and S.P. Nikanorov for the valuable advice and discussions.

This work was supported by the Russian Foundation for Basic Research (grant no. 00-01-00482).

REFERENCES

1. Yu. A. Kashtalyan, *High-Temperature Elasticity of Materials* (Naukova Dumka, Kiev, 1970).
2. P. E. Armstrong, J. M. Dickinson, and M. L. Brown, Trans. Metall. Soc. AIME **236**, 1404 (1966).
3. Y. Talmor, E. Walker, and S. Steinemann, Solid State Commun. **23**, 649 (1977).
4. Yu. A. Burenkov, S. P. Nikanorov, and A. V. Stepanov, Izv. Akad. Nauk SSSR, Ser. Fiz. **35**, 525 (1971).
5. S. I. Novikova, *Thermal Expansion of Solids* (Nauka, Moscow, 1974).
6. F. S. Crawford, Jr., *Waves* (McGraw-Hill, New York, 1968; Nauka, Moscow, 1974).
7. A. Rudgers, J. Acoust. Soc. Am. **88**, 1078 (1990).
8. V. N. Belomestnykh, Supercond., Phys. Chem. Technol. **6**, 1219 (1993).
9. V. N. Belomestnykh, *Physicochemical Acoustics of Crystals* (Tomsk. Politekhn. Univ., Tomsk, 1998).
10. V. N. Belomestnykh and A. A. Botaki, Fiz. Tverd. Tela (Leningrad) **18**, 313 (1976) [Sov. Phys. Solid State **18**, 186 (1976)].
11. E. Fitzgerald, Phys. Rev. **112**, 1063 (1958).
12. R. J. Wasilewski, Trans. Metall. Soc. AIME **233**, 1691 (1965).
13. U. T. Hochli, Solid State Commun. **8**, 1487 (1970).
14. D. Weiner, A. van den Beukel, and P. Penning, Acta Metall. **23**, 783 (1975).
15. I. T. Perro and V. Ya. Fritsberg, Fiz. Tverd. Tela (Leningrad) **21**, 3176 (1979) [Sov. Phys. Solid State **21**, 1832 (1979)].
16. V. N. Belomestnykh, Pis'ma Zh. Éksp. Teor. Fiz. **51**, 526 (1990) [JETP Lett. **51**, 596 (1990)].
17. K. V. Sapozhnikov, S. B. Kustov, P. Kopanya, *et al.*, Fiz. Tverd. Tela (St. Petersburg) **35**, 83 (1993) [Phys. Solid State **35**, 44 (1993)].
18. A. B. Lebedev, Yu. A. Burenkov, V. I. Kopylov, *et al.*, Fiz. Tverd. Tela (St. Petersburg) **38**, 1775 (1996) [Phys. Solid State **38**, 978 (1996)].
19. S. A. Golovin, A. Pushkar, and D. M. Levin, *Elastic and Damping Properties of Structural Metallic Materials* (Metallurgiya, Moscow, 1987).
20. F. J. Bartis, Phys. Lett. A **55**, 311 (1975).
21. V. K. Semenchenko, Zh. Fiz. Khim. **48**, 450 (1974).
22. A. R. Ubbelohde, Colloq. Int. C. N. R. S., No. 205, 393 (1972).
23. R. W. K. Honeycombe, *The Plastic Deformation of Metals* (Arnold, London, 1968; Mir, Moscow, 1972).

Translated by V. Isaakyan

Technical Physics, Vol. 48, No. 5, 2003, pp. 621–625. Translated from Zhurnal Tekhnicheskoĭ Fiziki, Vol. 73, No. 5, 2003, pp. 99–103.

RADIOPHYSICS

Q Factor of a Millimeter-Wave Sapphire Disk Resonator with Conductive End Plates

A. A. Barannik, Yu. V. Prokopenko, Yu. F. Filipov, N. T. Cherpak, and I. V. Korotash

Usikov Institute of Radiophysics and Electronics, National Academy of Sciences of Ukraine, ul. Akad. Proscura 12, Kharkov, 61085 Ukraine

e-mail: cherpak@ire.kharkov.ua, prokopen@ire.kharkov.ua

Received August 27, 2002; in final form, November 25, 2002

Abstract—The quality factor of a sapphire disk resonator with conductive end plates is studied theoretically and experimentally. The feasibity of measuring the sheet resistance of copper, titanium, and $YBa_2Cu_3O_{7-\delta}$ high-temperature superconductor films in the 8-mm range is shown. *© 2003 MAIK "Nauka/Interperiodica".*

INTRODUCTION

Dielectric resonators are widely used for measuring the microwave characteristics of insulators [1, 2] and, in recent years, high-temperature superconductor films [3]. A method for the measurement of the microwave sheet resistance of these films that uses conductive-end-plate resonators with lower volume modes has recently been suggested [4]. Such resonators are designed for microwave frequencies below 25 GHz. In the millimeter-wave band, they become too small to be effective. The basic power parameter of a dielectric resonator is its quality factor. In this band, the highest quality factor is featured by quasi-optical dielectric resonators with higher azimuthal wave modes ("whispering gallery" modes) [5]. For millimeter waves, these resonators have a reasonable size and show promise for resonant structures that employ high-temperature superconductor films [6].

The electrodynamic analysis of quasi-optical dielectric resonator properties and the theoretical and experimental identification of resonator modes were carried out in [7, 8]. It was shown that the sheet resistance R_S of normal conductors can basically be measured in the millimeter-wave band. The value of R_S superconductors is, however, difficult to measure, since losses in superconductors, which define R_S, are much smaller than all other losses in the resonator.

In this paper, we measure the radiation quality factor, determine the contribution of dielectric and conduction losses to the total loss of a sapphire disk resonator with conductive end plates, and estimate the value of R_S for normal metals and thin high-temperature superconductor films.

THEORETICAL RELATIONSHIPS FOR THE INTRINSIC AND RADIATION QUALITY FACTORS

The general design of the resonator is given in Fig. 1. Its loaded quality factor Q_L is given by

$$Q_L^{-1} = k\tan\delta + \frac{1}{2}A_N R_S^{(n)} + \frac{1}{2}A_S R_S^{(sc)} + Q_{rad}^{-1} + Q_C^{-1}, \quad (1)$$

where $Q_{rad} = \omega'/2\omega''$ is the radiation quality factor of the resonator ($\omega = \omega' - i\omega''$ is the complex circular eigenfrequency of the resonator, which is a solution to the dispersion relation given in [8, 9]); Q_C is the coupling quality factor; $\tan\delta$ is the dielectric loss tangent; $R_S^{(n)}$ and $R_S^{(sc)}$ are the sheet resistances of the normal conductor and superconductor, respectively; and k, A_N, and A_S are the weight factors of the dielectric, conduction, and superconductivity losses.

The coefficients $\Gamma_N = 2A_N^{-1}$ and $\Gamma_S = 2A_S^{-1}$ are often referred to as geometrical factors. In sheet resistance measurements, the coupling to the resonator is usually

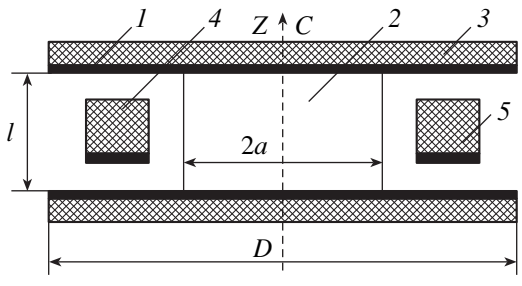

Fig. 1. Dielectric disk resonator with conductive end plates: (*1*) high-temperature superconductor film (or copper disk), (*2*) sapphire disk, (*3*) dielectric Al_2O_3 substrate, and (*4*, *5*) input and output waveguides.

1063-7842/03/4805-0621$24.00 © 2003 MAIK "Nauka/Interperiodica"

very weak; i.e., $Q_C^{-1} \ll Q_0^{-1}$, where Q_0 is the resonator's unloaded quality factor. For a quasi-optical dielectric resonator with conductive end plates, the following inequality is valid:

$$Q_{\text{rad}}^{-1} \ll k\tan\delta + \frac{1}{2}A_N R_S^{(n)} + \frac{1}{2}A_S R_S^{(sc)}.$$

In such a resonator, $A_S = A_N = A$ and expression (1) simplifies to

$$Q_0^{-1} = k\tan\delta + \frac{1}{2}A(R_S^{(n)} + R_S^{(sc)}). \quad (2)$$

When the end plates are made of the same material,

$$Q_0^{-1} = k\tan\delta + AR_S. \quad (2a)$$

For *Y* modes (by *Y* modes, we mean *HE* or *EH* modes), the resonator's unloaded quality factor, in this case, is given by [7, 8]

$$(Q_0^Y)^{-1} = \frac{1}{1+R_0^Y}\tan\delta + \frac{2}{\omega\mu_0 l R_Y}R_S, \quad (3)$$

where μ_0 is the permeability and l is the longitudinal size of the resonator.

Formulas (3) and (2a) yield

$$k = 1/(1+R_0^Y), \quad (4)$$

$$A = 2/\omega\mu_0 l R_Y. \quad (5)$$

We experimentally studied a quasi-optical dielectric resonator with HE_{nsm} modes, where $n = 0, 1, 2, \ldots$ is the azimuthal subscript; $s = 1, 2, \ldots$ is the radial subscript; and $m = 0, 1, 2, \ldots$ is the axial subscript. It turned out that, in resonators with conductive end plates, it is relatively easy to excite axially uniform HE_{ns0} modes, for which [8]

$$R_0^{HE} = \frac{\dfrac{|J_n(z_E)|^2}{|H_n^{(1)}(z_0)|^2}\left[\Phi_1(z_0) + \frac{1}{2}\Phi_2(z_0)\right]}{\varepsilon_\parallel\left[F_1(z_E) + \frac{1}{2}F_2(z_E)\right]},$$

$$R_{HE} = \frac{\varepsilon_\parallel\left[F_1(z_E) + \frac{1}{2}F_2(z_E)\right] - \dfrac{|J_n(z_E)|^2}{|H_n^{(1)}(z_0)|^2}\left[\Phi_1(z_0) + \frac{1}{2}\Phi_2(z_0)\right]}{\varepsilon_\parallel[F_1(z_E) + F_2(z_E)] - \dfrac{|J_n(z_E)|^2}{|H_n^{(1)}(z_0)|^2}[\Phi_1(z_0) + \Phi_2(z_0)]}. \quad (6)$$

Here, a is the radius of the dielectric disk, $z_0 = k_0 a$, $k_0 = \omega/c$, c is the velocity of light, $z_E^2 = \varepsilon_\parallel z_0^2$, $\varepsilon_\parallel$ is the component of the permittivity tensor along the resonator,

$$F_1(z) = \left(1 - \frac{n^2}{z^2}\right)J_n^2(z) + J_n'^2(z),$$

$$F_2(z) = \frac{1}{z}[J_n(z)J_n'^*(z) + J_n^*(z)J_n'(z)],$$

$$\Phi_1(z) = \left(1 - \frac{n^2}{z^2}\right)H_n^{(1)^2}(z) + H_n^{(1)'^2}(z),$$

$$\Phi_2(z) = \frac{1}{z}[H_n^{(1)}(z)H_n^{(1)'^*}(z) + H_n^{(1)^*}(z)H_n^{(1)'}(z)],$$

and $J_n(z)$ and $H_n^{(1)}(z)$ are the nth-order cylindrical Bessel and Hankel functions of the first kind. The primed quantities are derivatives with respect to the argument, and the asterisk denotes complex conjugation.

EXPERIMENTAL

In the experiments, we used a leucosapphire cylinder with a diameter $2a = 14.4$ mm and a length $l = 2.4$ mm. The optical axis of the crystal was aligned with its longitudinal axis (Fig. 1). The diameter D of the end plates satisfied the condition $D > 2a$; therefore, the eigenfrequency ω and the radiation quality factor Q_{rad} were diameter independent. The leucosapphire was synthesized at the Institute of Single Crystals, National Academy of Sciences of Ukraine, by directed crystallization. The surface of the dielectric cylinder was lapped, and the optical axis was aligned with the longitudinal axis within ±50'. The end plates were made of oxygen-free copper (unannealed and annealed), titanium, and $YBa_2Cu_3O_{7-\delta}$ high-temperature superconductor films applied onto a single-crystal Al_2O_3 substrate by laser ablation technology.

The measurements were taken in the 35–37 GHz frequency range. The resonance frequencies were measured by an electronic frequency meter accurate to 10^{-7}. In practice, the error was ≈0.5 MHz, which is due to the instability of the microwave oscillator. The resonator's quality factor was measured by two methods [10]:

(i) the transmission method, which measures the width Δf of the resonant response function and the resonance frequency f_0, with the quality factor calculated as $Q = f_0/\Delta f$, and (ii) the decrement method, which measures the transient time period τ in the resonator after it has been excited by a rectangular pulse at a carrier frequency f_0, with the quality factor calculated as $Q = 2\pi f_0\tau/\ln(P_1/P_2)$, where P_1 and P_2 are the powers released in the load at time instants t_1 and $t_2 = t_1 + \tau$ after the beginning of the relaxation process. The latter method was used when the quality factor was high: $Q = 10^4$–10^8. In the measurements, resonator–feed line coupling was weak; i.e., $Q \approx Q_0$.

The resonator was coupled to the feed lines through rectangular dielectric waveguides one side of which was metallized. The input and output waveguides were set at an angle (10°–15°) to each other, which allowed us to vary the coupling between the transmission lines and resonator by moving the latter in the plane of the waveguides. The waveguides were fabricated from a special organic polymer with a permittivity $\varepsilon \approx 9$.

RESULTS AND DISCUSSION

As follows from (1) and (2), to calculate the contributions of dielectric and conduction losses to the total energy loss Q_0^{-1} in the resonator, one should find the weight factors k and A, dielectric loss tangent $\tan\delta$, and R_S. If one of the end plates is made of a normal metal, it becomes possible to find $R_S^{(sc)}$ from the quality factor Q_0 measured and k, A, and $R_S^{(n)}$ known.

We studied a quasi-optical dielectric resonator with the axially uniform mode $HE_{141 0}$. Table 1 lists the calculated values of k, A, and Q_{rad}, as well as the resonance frequency f_0 found experimentally. In the experiments at 77 K, both end disks of the resonator were made of copper-based materials: one, of the high-temperature superconductor; the other, of pure copper. At 300 K, the end plates were either copper or titanium disks.

Al_2O_3 single crystals feature the lowest value of $\tan\delta$ among solid insulators currently known. Microwave absorption in this material was studied, e.g., in [2, 11, 12]. However, $\tan\delta$ depends strongly on the quality of the crystal. It should also be taken into account that $\tan\delta$ is determined from the measured quality factor, which, in turn, depends on the surface finish, deviation from the cylindrical shape, and accuracy of the optical axis adjustment. Therefore, it is necessary to measure $\tan\delta$ immediately on the material of which the resonator is made. In this paper, we determined $\tan\delta$ from Q_0^{HE} measured for an open resonator with the $HE_{141\delta}$ mode at the subscript $\delta \approx 0$ and obtained $Q_0^{HE} = 3.2 \times 10^4$ at 300 K and $Q_0^{HE} = 3.4 \times 10^5$ at 77 K. Figure 2 shows that the dependence $\log(Q_0^{-1})$ is well fitted by a straight line, which complies with results reported elsewhere [11, 12]. The lower values of the unloaded quality factor Q_0 that are observed in our study may be attributed to a number of reasons: low-grade sapphire, poor surface condition, or misalignment between the crystal's optical axis and the geometrical axis of the disk.

Table 1

T, K	f_0, GHz	k	A, Ω^{-1}	Q_{ran}
300	35.12	0.992	2.961×10^{-3}	5.3×10^9
77	35.57	0.992	2.924×10^{-3}	5.3×10^9

Table 2 lists R_S for a number of conductors, including high-temperature superconductors.

As follows from Table 2, at 300 K, the sheet resistances measured on oxygen-free hydrogen-annealed copper and pure titanium are in good agreement with those found by the formula $R_S^{(n)} = \sqrt{\omega\mu_0/2\sigma}$, which is valid in the case of the normal skin effect. Here, σ is the conductivity of the material. This agreement means that our analysis of the field structure and the associated method for determining the coefficients k and A are correct.

For titanium, the experimental temperature dependence of $R_S^{(n)}$ is also in good agreement with the model of the normal skin effect in the millimeter-wave band. Unlike copper, the agreement is observed down to liquid nitrogen temperature.

The sheet resistances $R_S^{(sc)}$ of the two $YBa_2Cu_3O_{7-\delta}$ films measured in this work are noticeably different.

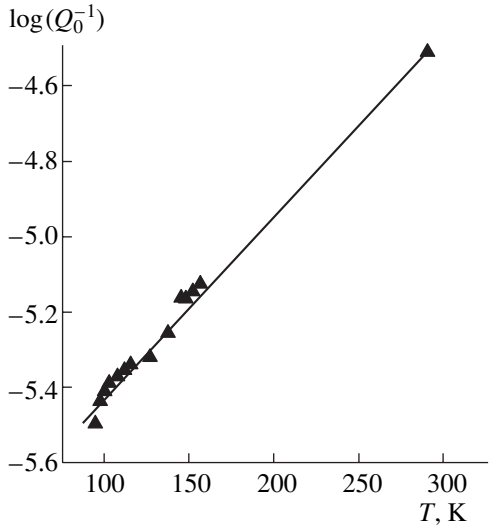

Fig. 2. Microwave absorption in the open sapphire disk resonator versus temperature.

Table 2

Conductors		Cu			Ti	$YBa_2Cu_3O_{7-\delta}$	
		unannealed		annealed		film 1	film 2
T, K		300	77	300	300	77	77
Q_0^{HE}		5100	10 380	5730	1250	13 110	16 270
$R_S^{(sc)}$, mΩ		–	–	–	–	17.8	8.2
$R_S^{(n)}$, mΩ	experiment	54.9	31.8	48.8	261	–	–
	calculatation	48.4	–	48.4	264	–	–

Table 3

T, K	$k\tan\delta$	$\frac{1}{2}AR_S^{(sc)}$	$\frac{1}{2}AR_S^{(n)}$	Q_{rad}^{-1}
77	2.94×10^{-6}	1.97×10^{-5}	5.39×10^{-5}	1.89×10^{-10}
300	3.07×10^{-5}	–	1.44×10^{-4}	1.89×10^{-10}

Three circumstances may cause film 1 (Table 2) to have a higher sheet resistance: (i) the film is not large enough (18×20 mm), which basically may increase the diffraction loss; (ii) the film was synthesized long (about two years) ago and might degrade; and (iii) the resonant frequency response of the doubly degenerate mode might have an extended width due to weak splitting. At present, it seems impossible to discriminate between these factors: figuring out the reasons for the increase in (or the overestimation of) the sheet resistance is the subject of subsequent investigation.

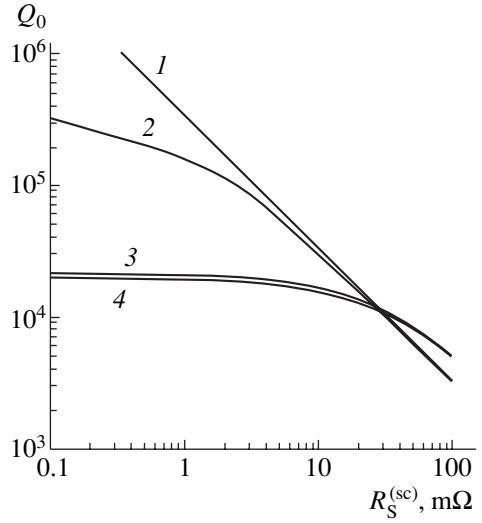

Fig. 3. Resonator's quality factor versus sheet resistance of the high-temperature superconductor film: (*1*, *2*) two films and (*3*, *4*) film and copper end plate. (*1*, *3*) $\tan\delta = 0$ and (*2*, *4*) $k\tan\delta = 2.94\times10^{-6}$.

The data gathered allow us to evaluate and compare the loss components in the sapphire resonator. Table 3 summarizes the data obtained upon using the high-temperature superconductor film and copper disk at 77 K and two copper disks at $T = 300$ K.

The Q factor of the resonator increases with decreasing temperature, because the losses in the sapphire and conductor decrease. A sharp change in the quality factor is observed when the high-temperature superconductor film (used as the end plate) passes into the superconducting state. At $T = 77$ K, the decrements are related as follows:

$$\frac{1}{2}AR_S^{(n)} > \frac{1}{2}AR_S^{(sc)} > k\tan\delta \gg Q_{rad}^{-1}.$$

It is clear that the sensitivity of superconductor sheet resistance measurements will be improved if both end plates are made of high-temperature superconductor films (Fig. 3). The accuracy of measuring $R_S^{(sc)}$ will depend only on the accuracy with which the quality factor and dimensions of the resonator are measured. Upon using modern approaches to the measurement of Q_0, this accuracy can approach ≈1% [4].

CONCLUSIONS

Thus, based on the theoretical analysis of the field structure in a conducting-end-plate sapphire disk resonator, the radiation quality factor and weight factors of the dielectric and conductors are evaluated. When the geometrical parameters of the resonator, the sheet resistance of the conductor, and the dielectric loss tangent are known, the above parameters specify the quality factor Q_0. On the other hand, the measurement of the unloaded quality factor Q_0 allows one to solve the

inverse problem for the microwave characteristics of materials. The feasibity of measuring the sheet resistances of conductors and superconductors in the millimeter wave band is shown. Good agreement between the measured sheet resistances and those calculated under the condition of the normal skin effect is demonstrated with oxygen-free copper and titanium. The sensitivity and accuracy of sheet resistance measurements as applied to high-temperature superconductor films is improved when these films cover both end plates of the resonator.

ACKNOWLEDGMENTS

We thank E.M. Ganapol'skĭ for valuable discussions and also É.V. Izhik, A.I. Tishchenko, and V.A. Novikov for assistance in the experiments.

REFERENCES

1. S. J. Fiedziuszko and S. Holme, IEEE Microwave Magazine **2** (3), 51 (2001).
2. J. Krupka, K. Derzakowki, A. Abramowicz, *et al.*, IEEE Trans. Microwave Theory Tech. **47**, 752 (1999).
3. Z.-Y. Shen, *High-Temperature Superconductivity Microwave Circuits* (Artech House, Boston, 1994).
4. J. Mazierska and C. Wilker, IEEE Trans. Appl. Supercond. **11**, 4140 (2001).
5. M. E. Il'chenko, V. F. Vzyatyshev, L. G. Gassanov, *et al.*, *Dielectric Resonators* (Radio i Svyaz', Moscow, 1989).
6. N. T. Cherpak, in *Proceedings of the 4th International Symposium on Physics and Engineering of Millimeter and Submillimeter Waves (MSMW'2001), Kharkov, Ukraine, 2001*, Vol. 1, pp. 63–67.
7. Yu. V. Prokopenko, Yu. F. Filipov, and N. T. Cherpak, in *Radiophysics and Electronics: Collection of Scientific Works* (Inst. Radiofiz. Élektron. Akad. Nauk Ukr., Khar'kov, 1999), Vol. 4, No. 2, pp. 50–54.
8. A. A. Barannik, Yu. V. Prokopenko, Yu. F. Filipov, *et al.*, in *Radiophysics and Electronics: Collection of Scientific Works* (Inst. Radiofiz. Élektron. Akad. Nauk Ukr., Khar'kov, 2000), Vol. 5, No. 3, pp. 104–109.
9. V. N. Egorov and I. N. Mal'tseva, Élektron. Tekh., Ser. Élektron. SVCh, No. 1, 3 (1984).
10. F. F. Mende and A. I. Spitsyn, *Surface Impedance of Superconductors* (Naukova Dumka, Kiev, 1985).
11. V. B. Braginskiĭ, Kh. S. Bagdasarov, F. V. Bulygin, *et al.*, Pis'ma Zh. Tekh. Fiz. **11**, 247 (1985) [Sov. Tech. Phys. Lett. **11**, 177 (1985)].
12. E. M. Ganapol'skiĭ, Fiz. Nizk. Temp. **26**, 1162 (2000) [Low Temp. Phys. **26**, 862 (2000)].

Translated by A. Khzmalyan

Technical Physics, Vol. 48, No. 5, 2003, pp. 626–630. Translated from Zhurnal Tekhnicheskoĭ Fiziki, Vol. 73, No. 5, 2003, pp. 104–108.

**SURFACES,
ELECTRON AND ION EMISSION**

Current–Voltage Characteristics of Poly(diphenylenephthalide) Thin Films

A. A. Bunakov*, A. N. Lachinov, and R. B. Salikhov***

** Bashkir State Pedagogical University, Ufa, 450000 Bashkortostan, Russia*

*** Institute of Molecular and Crystal Physics, Ufa Scientific Center, Russian Academy of Sciences, Ufa, 450075 Bashkortostan, Russia*

e-mail: gen_phys@bspu.ru

Received February 11, 2002; in final form, September 24, 2002

Abstract—Charge transfer near the threshold of polymer film transition (induced by a low uniaxial pressure) to the high-conductivity state is studied in an attempt to tackle the question of how the energy band structure of a wide-gap organic insulator varies near this threshold. The *I–V* characteristics of poly(diphenylenephthalide) films of various thickness versus uniaxial pressure are analyzed. The results obtained are treated within the model of space-charge-limited injection currents. The parameters of the injection model, such as the equilibrium concentration of electrons, electron mobility, the occupation of traps, etc., are estimated. It is concluded that deep traps due to an excess charge may appear in the energy gap of the polymer near the imref. This probably causes a narrow subband to arise, and charge transfer via this subband increases the charge carrier mobility and, hence, conductivity. © *2003 MAIK "Nauka/Interperiodica".*

When subjected to an electric field [1], low uniaxial pressure [2], high temperature [3], etc., thin films of a number of electroactive polymers are known to pass from the dielectric to high-conductivity state. A feature of this phenomenon is that the conductivity of the latter state varies with temperature as in metals and may be very high ($>10^5$ $(\Omega\ \mathrm{cm})^{-1}$) [4]. At the same time, the parameters characterizing the initial dielectric state are as follows: the energy gap equals ≈4.3 eV; electron work function, ≈4.2 eV; and the first ionization potential, ≈6.2 eV [5]. To date, it still remains unclear how the energy band structure of a wide-gap organic insulator varies near the transition to the high-conductivity state.

A possible reason for this situation is that researchers have concentrated on charge transfer in the high-conductivity state of a polymer and on constructing models accounting for the transfer features. In [6], a model of pressure-induced charge carrier injection from a metal to the conduction band of an insulator was developed. According to this model, the compression of the material causes the decay of surface states acting as electron acceptors [7].

Later [8], the conductivity of oxidized polypropylene films as a function of electric field, temperature, pressure, specimen geometry, and substrate material was studied. The film thickness was varied from 5 to 40 μm. It was assumed [8] that there exist conducting regions, narrow channels, whose spread resistance governs the conductivity of a polymer–metal system.

The occurrence of the high-conductivity state was explained by the formation of conducting channels (in the polymer film) made of an electrode material [9, 10]. It was also speculated that there are lower limits of the voltage and current in the high-conductivity state below which a continuous metallic filament does not form and conduction is associated with a more complicated configuration of the metallic channel. For example, metal particles separated by tunnel-transparent barriers may form a conducting chain between the electrodes.

It was also hypothesized [11, 12] that mobile dipole groups (with a concentration $C_{\mathrm{dip}} < 10^{20}$ cm^{-3}) arise in an elastomer upon oxidation. In this case, the ratio between the high- and low-frequency permittivities of the medium becomes low: $K = \varepsilon_\infty/\varepsilon_0 \ll 1$. As a result, some functional groups of the elastomer readily ionize and immobile ions and low-mobility polarons appear in the polymer. In this situation, specific high-conductivity domain structures may appear.

In [13], a high conductivity of polymer films was explained by the formation of channels with waveguide energy levels, via which electrons may penetrate from metallic electrodes into the channels and travel with a negligible energy dissipation. A simple model of such a channel was suggested, and estimates that clarify the nature of a waveguide level were made.

Eagles [14] made an attempt to apply the idea put forward in [15] to quasi-one-dimensional systems. According to this idea, in a narrow cylindrical region of thickness less than the magnetic field penetration depth, pairing is possible at a very high drift velocity. Calculations [14] based on the theory worked out in [16] showed that, if the Fermi level E_F lies higher than the energy $h\omega$ of phonons, plasmons, or excitons, super-

conductivity may arise, with the superconductivity energy gap higher than, or comparable to, that in the absence of current. However, straightforward calculations demonstrate that, if $E_F \ll h\omega$, superconductivity with strong pairing is possible.

Popov and Tséndin [17] proposed the model of high-temperature superconductivity in low-coordinated semiconductors and polymers. In this model, the state with an anomalously high conductivity at ambient temperature is described through the superconducting properties of a set of localized electron pairs. Superconductivity here is due to bipolaron transfer over a band formed by localized pairs occupying U^- centers (i.e., intrinsic defects with a negative effective correlation energy).

Ponomarev and Shikhovtseva [18] suggested the formation mechanism for conducting channels in thin films of oxygen-containing polymers. Here, the channels result from the soliton-like propagation of some excited state along a polymer molecule. This state arises when C–O bonds between quaternary carbon of a primary molecule and oxygen of a side group break. It is assumed that the polymer's structure has a doubly degenerate ground state. The transition between these states takes place when the excited state moves along the polymer chain.

Clearly, the phenomenon being discussed obeys some general laws irrespective of the polymer nature. It follows that a model to be elaborated must also adequately describe and predict the basic features of charge transfer in polymers near the transition to the high-conductivity state. However, a variety of available models apparently indicates the scantiness of experimental data upon which the models rely. Specifically, the variation of charge transfer parameters in the pretransition range is still an uncovered issue.

In view of the aforesaid, this work is devoted to the study of charge transfer near the threshold of polymer film transition to the high-conductivity state induced by a low uniaxial pressure. We took the *I–V* characteristics from poly(diphenylenephthalide) films [19] of different thickness under various pressures.

The *I–V* characteristics of highly conductive polymers were analyzed, e.g., in [20–24]. However, data for the pretransition range were not systematized there.

Poly(diphenylenephthalide) was selected as an object of investigation because it offers good film-forming properties on metallic substrates. It was shown [25] that 0.05- to 10-μm-thick continuous homogeneous films of this polymer are feasible if particular process conditions are met. In addition, the conductivity of poly(diphenylenephthalide) does not have temperature singularities up to the softening point (360°C in air). Finally, conditions for the occurrence of the high-conductivity state in this material are better understood [1, 26, 27]. The film quality and homogeneity were studied by optical microscopy methods (see [28]).

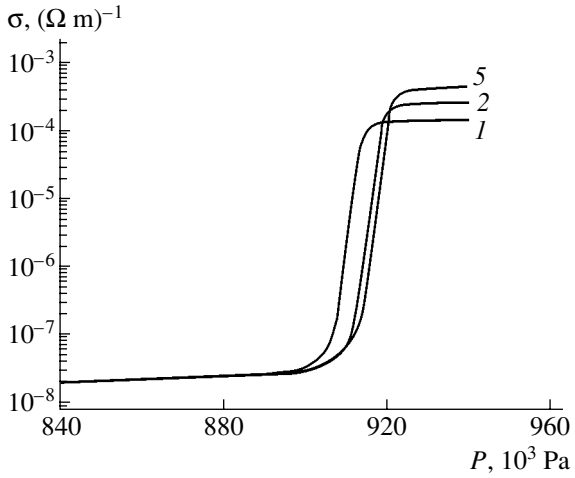

Fig. 1. Conductivity σ of the polymer film vs. uniaxial pressure *P* (excess pressure relative to atmospheric value). The figures by the curves are voltages (in V) applied to the film.

Our experiments were carried out on a setup that consisted of a uniaxial mechanical pressure controller, a pressure transducer built around a strain-sensitive resistive bridge, and a measuring circuit to record the *I–V* characteristics. The pressure was varied between 0 and 1000 kPa.

Test specimens were metal–polymer–metal sandwiches. A thin polymer film was applied on the lower electrode by spinning. The upper electrode was applied on the polymer film by thermal diffusion deposition *in vacuo*. The contact area was $S \approx 2$ mm^2. The film thicknesses were specified by the solution concentration and were checked by an MII-4 interferometer. They were found to vary between 0.8 and 1.5 μm. A total of more than 50 specimens were investigated.

Switching to the high-conductivity state was observed at a certain threshold pressure. Figure 1 shows the conductivity of the polymer film vs. voltage applied to the measuring cell. The run of the curves is typical of all the specimens studied in this work. The threshold pressure at which the conductivity grows sharply is extremely low. This may indicate that energy levels in the valence and conduction bands are not displaced, since such a displacement requires a considerable pressure. According to [29], the proportionality coefficient between the energy needed to displace a level and pressure is 10^{-10}–10^{-11} eV/Pa. It should be noted that the conductivity varies with the applied voltage: the higher the voltage, the higher the conductivity.

Typical *I–V* characteristics taken from the 1-μm-thick polymer films in the subthreshold range under different pressures are given in Fig. 2. These curves are well approximated by power functions of type $I \approx U^n$. In the absence of pressure, the curves can be divided into two regions: linear with $n = 1$ (low voltages) and quadratic with $n = 2$ (high voltages). The transition

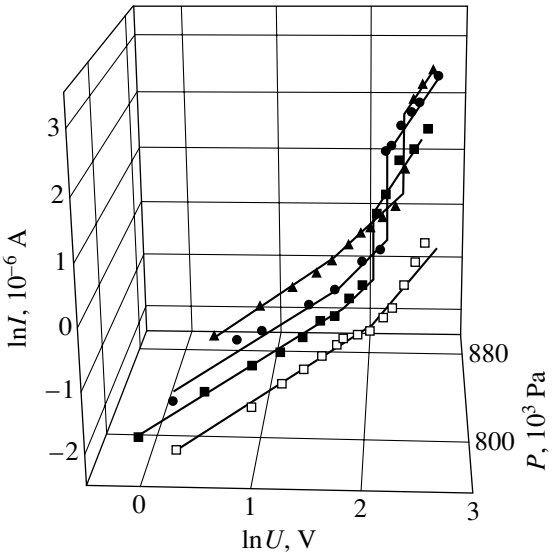

Fig. 2. *I–V* characteristics of the polymer film at (□) 0, (■) 780, (●) 820, and (▲) 860 kPa.

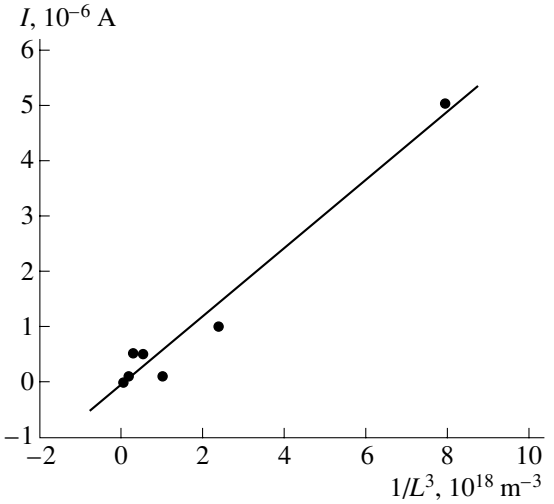

Fig. 3. Current vs. polymer film thickness.

between the two regions takes place at a certain voltage U_1.

From Fig. 2, it follows that U_1 decreases with pressure. After the voltage has reached the value U_2, the quadratic region is changed to a region where the curves run nearly vertically. As the pressure grows, U_2 tends toward higher values. At voltages higher than U_2, the vertical portion is followed by another quadratic region. A further increase in the pressure electronically switches the polymer to the high-conductivity state.

The *I–V* characteristics were treated within the model of space-charge-limited injection currents [30], which provides information on localized states in the energy gap and allows one to explain the shape of the *I–V* curves. Before proceeding to the discussion of the results obtained, we note that traps in this model are assumed to be monoenergetic. The discussion that follows demonstrates that, even with this limitation, it becomes clear how the model parameters depend on external conditions.

This model implies that, at low voltages (up to U_1) (Fig. 2), the *I–V* characteristic is well described by Ohm's law. At U_1, the equilibrium concentration of thermionic free electrons becomes comparable to the concentration of injected charges:

$$J \approx en_0\mu\frac{U}{L}, \tag{1}$$

where e is the charge of an electron, n_0 is the equilibrium concentration of free charges, μ is the electron mobility, and L is the film thickness.

Next, the *I–V* curve obeys the trap-related quadratic law

$$J \approx \theta\varepsilon\varepsilon_0\mu\frac{U^2}{L^3}, \tag{2}$$

where ε is the relative permittivity, ε_0 is the dielectric constant, and θ is a constant taking into account the degree of trap occupation.

The first quadratic portion of the curve is followed by the region where the current rises nearly vertically (Fig. 2). This voltage range is treated as that where the occupation of traps reaches a maximum ($U_2 = U_{t,\,max}$). Since the occupation of traps becomes maximal when the imref crosses trap levels in the energy gap, the injected charge density and, accordingly, the current in the polymer increase substantially. As the voltage rises further, the *I–V* curve is described, as a rule, by the trap-unrelated quadratic law (Fig. 2):

$$J \approx \varepsilon\varepsilon_0\mu\frac{U^2}{L^3}. \tag{3}$$

From the above formulas, it follows that, in terms of the injection model, the current varies with the specimen thickness as L^{-3} provided that the voltage remains the same. It was, therefore, of interest to check the fulfillment of this dependence for our polymer films. The curves $I = f(L^{-3})$ constructed in this work are shown in Fig. 3. The thickness of the films was varied by successively pouring the solution of the same concentration over the same substrate. In view of errors arising at different stages of this experiment, the curves are well fitted by a straight line. This indicates that the injection model may be used for treating the *I–V* characteristics.

The table lists the values of U_1 and $U_{t,\,max}$, as well as the basic parameters of the model: μ, electron mobility; n_0, the equilibrium concentration of thermionic electrons; and $p_{t,\,0}$, the concentration of empty traps (which is proportional to the total concentration N_t of traps), for

Effect of uniaxial pressure on injection model parameters

P, 10^3 Pa	μ, 10^{-9} m^2/(V s)	n_0, 10^{20} m^{-3}	U_1, V	$U_{t,\max}$, V	$p_{t,0}$, 10^{21} m^{-3}	θ
780	1.39	3.68	6.14	8.13	1.37	0.36
820	1.65	2.41	5.55	9.18	1.52	0.26
860	1.77	2.18	5.22	10.68	1.79	0.25

different uniaxial pressures. We used the following estimators [30]:

$$n_0 \approx \frac{\theta\varepsilon\varepsilon_0 U_1}{eL^2}; \quad \mu = \frac{JL^3}{\theta\varepsilon\varepsilon_0 U_1^2}; \quad p_{t,0} = \frac{\varepsilon\varepsilon_0 U_{t,\max}}{eL^2}. \quad (4)$$

It should be noted that the conductivity σ calculated from the current and voltage values within the linear portion of the curve coincides with that found by the formula $\sigma = en_0\mu$ up to order of magnitude.

From the tabulated data, it follows that an increase in the pressure decreases the equilibrium carrier concentration, which is probably related to a change in the imref position. The shift of the voltage U_1 toward lower values with increasing pressure supports our supposition that deep traps, the concentration of which grows, begin to play a primary role. The carrier mobility also rises presumably because of the increase in the trap concentration and the decrease in their occupation.

Thus, the preliminary conclusions are as follows. A rise in the pressure alters conditions for carrier injection into the polymer film. This process may be associated with the decay of electron surface states [6], which raises the injection level. The charge injected also grows with the electric field applied to the specimen; as a result, the conductivity of the highly conductive state increases (Fig. 1). When interacting with a poly(diphenylenephthalide) macromolecule, an excess injected charge may produce deep levels by the mechanism described in [31]. It was also shown that this interaction may increase the polarizability of a macromolecule fragment [32]. The result is an unstable high-permittivity polymer state that relaxes after a time with the electrons passing to deeper traps. It seems that there exists a certain critical injection level above which the processes mentioned above lead to the formation of a narrow band of traps near the imref in the energy gap. The possibility of charge transfer over this band improves significantly the charge carrier mobility and favors the transition of the polymer film into the high-conductivity state.

ACKNOWLEDGMENTS

The authors thank E.E. Churlina for assistance in the experiments.

REFERENCES

1. A. N. Lachinov, A. Yu. Zherebov, and V. M. Kornilov, Zh. Éksp. Teor. Fiz. **102**, 187 (1992) [Sov. Phys. JETP **75**, 99 (1992)].
2. A. N. Lachinov, A. Yu. Zherebov, and V. M. Kornilov, Pis'ma Zh. Éksp. Teor. Fiz. **52**, 742 (1990) [JETP Lett. **52**, 103 (1990)].
3. A. N. Lachinov, A. Yu. Zherebov, and M. G. Zolotukhin, Synth. Met. **59**, 377 (1993).
4. A. N. Ionov, A. N. Lachinov, M. M. Rivkin, *et al.*, Solid State Commun. **82**, 609 (1992).
5. B. G. Zykov, V. N. Baydin, Z. Sh. Bayburina, *et al.*, J. Electron Spectrosc. Relat. Phenom. **61**, 123 (1992).
6. Yu. A. Berlin, S. I. Beshenko, V. A. Zhorin, *et al.*, Sov. Phys. Dokl. Ser. Fiz. Khim., 1386 (1981).
7. F. Gutmann and L. Lyons, *Organic Semiconductors* (New York, 1967; Mir, Moscow, 1970).
8. V. M. Arkhangorodskiĭ, E. G. Guk, A. M. El'yashevich, *et al.*, Dokl. Akad. Nauk SSSR **309**, 603 (1989) [Sov. Phys. Dokl. **34**, 1016 (1989)].
9. A. M. El'yashevich, A. N. Ionov, M. M. Rivkin, *et al.*, Fiz. Tverd. Tela (St. Petersburg) **34**, 3457 (1992) [Sov. Phys. Solid State **34**, 1850 (1992)].
10. L. N. Grigorov, T. V. Dorofeeva, A. V. Kraev, *et al.*, Vysokomol. Soedin., Ser. A **38**, 2011 (1996).
11. S. G. Smirnova, L. N. Grigorov, N. M. Galashina, *et al.*, Dokl. Akad. Nauk SSSR **283** (14), 176 (1985).
12. L. N. Grigorov, Pis'ma Zh. Tekh. Fiz. **17** (10), 45 (1991) [Sov. Tech. Phys. Lett. **17**, 368 (1991)].
13. A. M. Elyashevich, A. A. Kiselev, A. V. Liapzev, *et al.*, Phys. Lett. A **156**, 111 (1991).
14. D. M. Eagles, Physica C **225**, 222 (1994).
15. R. H. Parmenter, Phys. Rev. **116**, 1390 (1959).
16. G. M. Éliashberg, Zh. Éksp. Teor. Fiz. **38**, 966 (1960) [Sov. Phys. JETP **38**, 696 (1960)].
17. B. P. Popov and K. D. Tséndin, Pis'ma Zh. Tekh. Fiz. **24** (7), 45 (1998) [Tech. Phys. Lett. **24**, 265 (1998)].
18. O. A. Ponomarev and E. S. Shikhovtseva, Zh. Éksp. Teor. Fiz. **107**, 637 (1995) [JETP **80**, 346 (1995)].
19. S. N. Salazkin, S. R. Rafikov, G. A. Tolstikov, *et al.*, Dokl. Akad. Nauk SSSR **262**, 355 (1982).
20. A. V. Kraev, S. G. Smirnova, and L. N. Grigorov, Vysokomol. Soedin., Ser. A **35**, 1308 (1993).
21. A. M. El'yashevich, A. N. Ionov, V. M. Tuchkevich, *et al.*, Pis'ma Zh. Tekh. Fiz. **23** (14), 8 (1997) [Tech. Phys. Lett. **23**, 538 (1997)].
22. S. Tagmouti, A. Oueriagli, A. Outzourhit, *et al.*, Synth. Met. **88**, 109 (1997).
23. P. Somani, R. Marimuthu, and A. B. Mandale, Polymer **42**, 2991 (2001).

24. P. Somani, D. Amalnerkar, and S. Radhakrishnan, Synth. Met. **110** (3), 181 (2000).
25. J. R. Rasmusson, Th. Kugler, R. Erlandsson, *et al.*, Synth. Met. **76**, 195 (1996).
26. A. N. Lachinov, M. G. Zolotukhin, A. Yu. Zherebov, *et al.*, Pis'ma Zh. Éksp. Teor. Fiz. **44**, 6 (1986) [JETP Lett. **44**, 349 (1986)].
27. A. Yu. Zherebov and A. N. Lachinov, Synth. Met. **44**, 99 (1991).
28. O. A. Skaldin, A. Yu. Zherebov, V. V. Delev, *et al.*, Pis'ma Zh. Éksp. Teor. Fiz. **51** (3), 141 (1990) [JETP Lett. **51**, 159 (1990)].
29. M. Lampert and P. Mark, *Current Injection in Solids* (Academic, New York, 1970; Mir, Moscow, 1973).
30. C. B. Duke and T. J. Fabish, Phys. Rev. Lett. **37**, 1075 (1976).
31. A. N. Lachinov, T. G. Zagurenko, V. M. Kornilov, *et al.*, Fiz. Tverd. Tela (St. Petersburg) **42**, 1882 (2000) [Phys. Solid State **42**, 1935 (2000)].

Translated by V. Isaakyan

Technical Physics, Vol. 48, No. 5, 2003, pp. 631–635. Translated from Zhurnal Tekhnicheskoĭ Fiziki, Vol. 73, No. 5, 2003, pp. 109–114.

**SURFACES,
ELECTRON AND ION EMISSION**

Single-Ion-Beam Experimental Setup for Combined Implantation and Deposition

F. F. Komarov*, A. A. Kamarou, P. Zukowski***, Cz. Karwat***, J. Sielanko****, K. Kiszak****, and A. F. Komarov***

** Sevchenko Research Institute of Applied Physical Problems, Minsk, 220064 Belarus*
e-mail: komarAF@bsu.by
*** Institute of Solid-State Physics, Schiller University of Jena, D-07743 Jena, Germany*
**** Technical University, 20-618 Lublin, Poland*
***** Institute of Physics, Sklodowska-Curie University of Lublin, 20-031 Lublin, Poland*
Received July 22, 2002; in final form, November 13, 2002

Abstract—An original approach and a single-ion-beam experimental setup for *in situ* ion implantation combined with the deposition of various materials on metals are suggested. The simulation system developed makes it possible to characterize ion-assisted deposition, as well as to analyze the radial and depth distributions of atoms deposited and implanted. The results of the simulation allow us to conclude that the ion beam energy, the mass and fluence of the ions, and especially the target geometry have a noticeable effect on the processes. Experimental data for the depth profiles of atoms implanted and for the thicknesses of films applied are also reported. The variation of the film thickness, the uniformity of the films, and the efficiency of mixing in the film–substrate system are discussed based on the results of simulation and experimental data. © *2003 MAIK "Nauka/Interperiodica"*.

INTRODUCTION

Ion-beam-assisted deposition (IBAD) of various materials has been widely used in recent years for the modification of mechanical, electrical, optical, tribological, barrier, anticorrosive, and catalytic properties of surface layers. The basic difference between IBAD and conventional ion implantation is that, in the former case, ion irradiation is accompanied by the deposition of an additional atomic or molecular component from a magnetron, ion–plasma, arc, or any other source, as well as from the residual atmosphere in the implantation chamber.

For example, titanium nitride (TiN) or cubic boron nitride (β-BN) deposits on the surface of steel parts greatly improve their wear resistance and corrosion resistance and, hence, extend their service life [1, 2]. Therefore, IBAD can be viewed as a promising means for the production of advanced mechanical and electrical engineering products and also as a promising technology for layered microelectronic devices.

Recent publications (see, e.g., [3]) have indicated that the structural, tribological, adhesive, and mechanical properties of IBAD films depend to a great extent on ion irradiation conditions (ion current density, ion energy, cumulative dose, and target temperature). In particular, the mechanical properties, adhesion to the substrate, and structural perfection of the coatings are appreciably improved if the ion beam density is sufficiently high.

During IBAD, the depth profiles of atoms both deposited and implanted are governed not only by the rate of early component deposition and atomic collision kinetics. They also depend on many other factors, such as the accumulation of impurities in the target, the sputtering of the target, the diffusion of impurities, atomic mixing (here both the ballistic and diffusion components of this process are essential), the nucleation of new phases during IBAD, and the swelling of the coating and substrate. In terms of physicochemical properties, nitride films are of greatest interest for applications [4]. Therefore, in this work, we concentrate mainly on the IBAD of nitrogen-containing coatings.

It should be noted, however, that, in a number of cases, IBAD (e.g., when used to improve the service properties of metal surfaces) requires expensive, energy-consuming, and sophisticated equipment (an ion accelerator plus a magnetron, ion–plasma, or any other source). Therefore, the search for novel original IBAD concepts that allow designers to simplify the technology and make the associated equipment less expensive, while retaining the advantages of the process, seems to be topical.

DESIGN OF IBAD EQUIPMENT AND IBAD SIMULATION

We suggest an original IBAD version for the modification of the surfaces of metals (specifically, copper as a promising material for electrical commutators) and

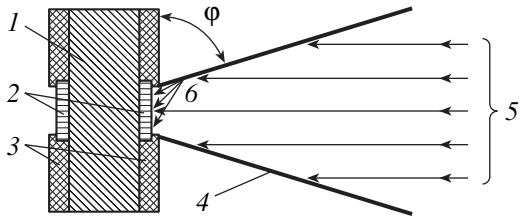

Fig. 1. Axisymmetric design of the IBAD setup. (*1*) Casing, (*2*) sample (substrate), (*3*) sample holder, (*4*) material to be sputtered, (*5*) ion beam, and (*6*) sputtered atom flux.

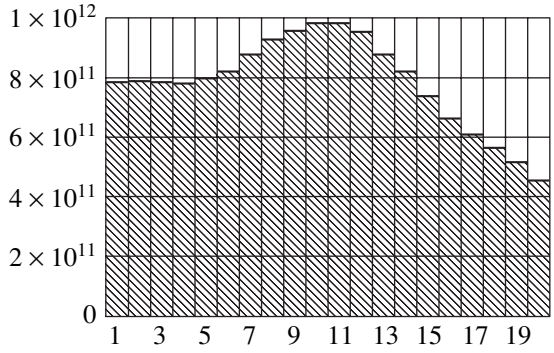

Fig. 2. Radial distribution of atoms deposited in 1 s as a function of the ring number (the largest number corresponds to the outermost ring).

other materials. The specific feature of our approach is that the *in situ* implantation of ions (e.g., nitrogen ions) and the deposition of metals (gold, nickel, etc.) are performed with the same ion beam (Fig. 1). The basic unit of the setup suggested is the target in the form of a truncated cone that is made of a desired material or of any material coated by a layer of a desired material. A diaphragm (with the diameter coincident with that of the substrate (sample)) in the upper part of the conical unit serves to provide one of the possible operating conditions: ion-assisted deposition (without the diaphragm), deposition of layers (with the diaphragm), or repetitive deposition with subsequent IBAD and ion-beam mixing of the layers. Thus, when the diaphragm is open, the central part of the beam acts on the sample surface, while the circumferential part of the beam strikes the lateral surface of the cone. Some of the sputtered particles reach the sample surface. Thus, during the ion irradiation of the truncated cone, we are dealing with ion implantation, sputtering, and deposition of cone atoms proceeding simultaneously.

The general problem of IBAD simulation can be subdivided into three independent stages: (i) the simulation of the spatial distribution of the sputtered particle flux as a function of azimuth and polar angles (because of the oblique incidence of the beam on the target); (ii) the calculation of the radial distribution of the sputtered particle flux reaching the substrate per unit time; and (iii) the simulation of IBAD with regard for the sputtering of the coated substrate, impurity diffusion, and motion of the surface because of deposition and sputtering (the deposition rate is found from the two preceding stages).

The first stage was solved by applying the latest modification of the SATVAL program [5, 6]. Stage (ii) of the simulation was performed by using our original program. Finally, stage (iii) of this work was solved with the program suite developed by us [7–13] for the simulation of conventional ion-assisted deposition [7–10] and high-dose ion implantation into layered structures (the BEAM2HD program [11–13].

The BEAM2HD program allows one to describe one- and two-beam high-dose implantation into multilayer or multicomponent systems. Each of the beams is characterized by the initial energy and dose, as well as by the number of Monte Carlo-simulated trajectories. Each of the trajectories is assigned a "pseudoparticle," i.e., a certain interval of the bombarding ion dose, and the ion trajectories for each of the beams are simulated in turn.

The description of high-dose ion implantation includes a number of additional factors compared with low-dose implantation: the scattering and energy loss of implanted ions by impurity atoms embedded earlier, the scattering of the target surface, the effect of the mobile surface boundary, and target swelling due to high-dose implants.

The simulation based on the program suite makes it possible to gain information on the radial and depth profiles of deposited and/or implanted atoms as functions of the ion type, energy, and fluence, and the geometry of the conical target [14, 15]. The efficiency of the simulation process is provided by splitting the cone and sample surfaces into a set of equiareal rings in order to obtain equal fluences per ring. Then, the double-angle spatial distribution of ion-beam-sputtered particles (obtained with the SATVAL program) is processed with the aim of finding the specific number of sputtered particles per ring and general radial distribution of deposited atoms. The histogram in Fig. 2 shows the distribution of deposited atoms vs. the ring number (the rings are numbered from the center toward the periphery).

RESULTS OF SIMULATION

The efficiency of the ion-beam material deposition and modification suggested in this article depends on the conical target material, cone geometry, ion type and energy, and substrate temperature. In our experiments, the substrate was kept at room temperature. The ion energy is a highly essential factor. Figure 3 shows the number of deposited chromium atoms per unit substrate area upon irradiation by N_2^+ ions with energies of 20 and 60 keV as a function of the distance from the sample axis (the diaphragm is closed). As for the normal incidence of ions on the target [3, 4], the coefficient of target sputtering depends considerably on the ion

energy. In our case, however, the net effect also includes the energy dependence of the angular (spatial) particle distribution. In general, ion energies that are optimal for depositing thicker layers shift toward lower energies compared with the case of normal incidence. The sample region near the cone wall has a maximal thickness. For the range $9° \le \theta \le 21°$, where $\theta = 90° - \varphi$ is the angle at which the beam enters into the cone, the thickness of the central part of the film varies with θ insignificantly (by less than 20%). However, along the substrate diameter, the thickness d of the film depends strongly on θ (Fig. 4). The thickness d is the most uniform when $\theta = 15°–16°$ (Fig. 3).

As for normal bombardment upon the ion sputtering of materials, the efficiency of target sputtering and, accordingly, of film deposition depends on the ion mass. Thick films that are uniform along the diameter of the sample are obtained with beams of heavy ions (Ar^+, Kr^+, or Xe^+). As follows from Fig. 5, the deposition efficiency in the case of Xe^+ ions is more than one order of magnitude higher than in the case of N_2^+ ions.

Generally, the deposition yield,

$$K\left(\frac{\text{atom}}{\text{ion}}\right) = \frac{dS_0}{S'D} \qquad (1)$$

(where S_0 and S' are the surface areas of the exposed parts of the entrance and exit faces of the truncated cone (Fig. 1), respectively), is more informative than the value of d.

This yield is an integral test for the optimality of the experiment geometry, ion type, and ion energy.

EXPERIMENTAL RESULTS

The distribution of deposited atoms across the substrate depends on several factors. The main ones are the energy of bombarding ions, the presence (or absence) of the diaphragm, the substrate temperature during the bombardment (hence, the density of the ion current to the sample), and the equilibrium and radiation-induced diffusions of impurities. To simplify the pattern, we will compare analysis and experiment via the integral thickness d (atoms/cm^2) of the film deposited. The experiment on the deposition of molybdenum on the copper substrate when the cone is irradiated by N_2^+ ions with $E = 110$ keV and $D = 1 \times 10^{17}$ cm^{-2} (Fig. 6) illustrates the effect of dynamic substrate–film mixing when not only ballistic mixing but also diffusion stimulated by a high concentration of nonequilibrium defects may be a factor. The substrate temperature during the deposition was no higher than 100°C (water cooling).

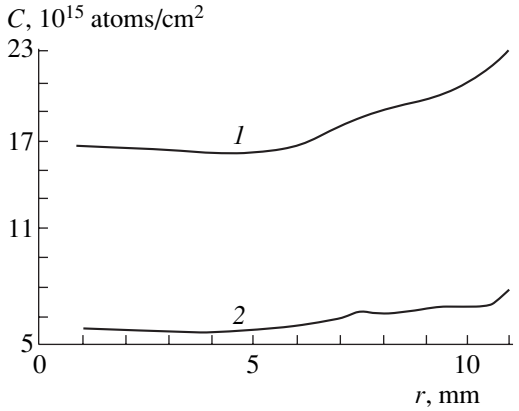

Fig. 3. Concentration of deposited chromium atoms vs. distance from the sample axis for a nitrogen ion beam energy E = (*1*) 20 and (*2*) 50 keV with $D = 2 \times 10^{17}$ cm^{-2}. The half-angle of the truncated cone is $\theta = 15°$.

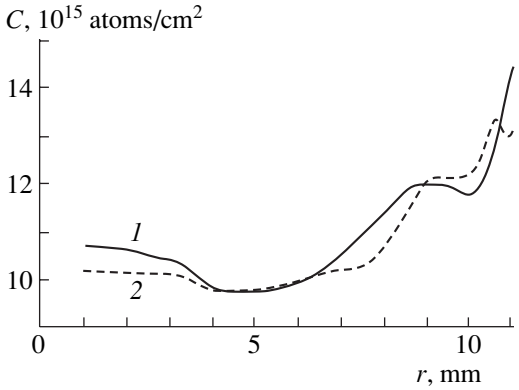

Fig. 4. Concentration of deposited chromium atoms vs. distance from the sample axis for N_2^+ ion irradiation with $D = 2 \times 10^{17}$ cm^{-2}. $E = 40$ keV and θ = (*1*) 11° and (*2*) 21°.

The effective thickness of the molybdenum layer, given by

$$d = \int_0^\infty N_{\text{Mo}}(x)dx, \qquad (2)$$

equals 2.64×10^{16} atoms/cm^2, according to Fig. 6. The simulation gives for the molybdenum layer thickness 1.8×10^{16} atoms/cm^2. The depth profile of the nitrogen in the copper is somewhat modified by the molybdenum coating. The projected range of nitrogen ions remains close to the theoretical value ($R_{\text{p, theor}} = 505$ Å, $\Delta R_{\text{p, theor}} = 290$ Å for N^+ ions with $E = 55$ keV in Cu). The yield K for irradiation by light fast nitrogen ions is as low as 0.26 atoms/N_2^+. The concentration of the embedded nitrogen far exceeds the molybdenum concentration in the modified layer on the copper surface.

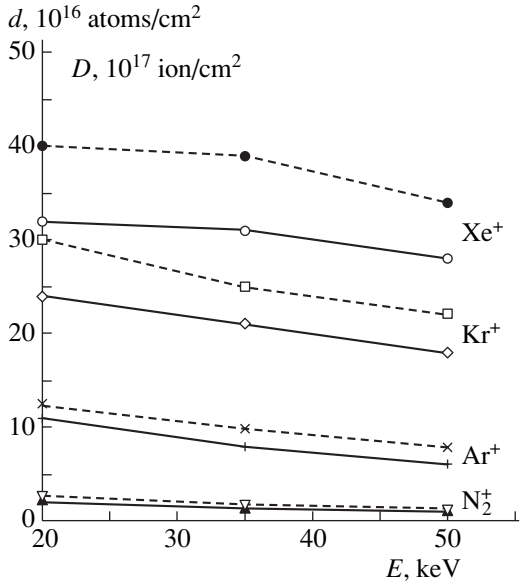

Fig. 5. Thickness of the deposited gold film vs. ion type and energy. The continuous curve shows the thickness in the central part of the sample; the dashed line shows the maximal thickness.

As was already noted, the behavior of a material applied depends on its diffusion mobility. In the case of copper deposited on the surface of bulk aluminum, the nonequilibrium concentration of structural defects due to ion irradiation causes a pronounced impurity redistribution (Fig. 7). The long tail extending from a depth of ≈30 nm to more than 3 μm (Fig. 7) corresponds to a concentration of 2.5 at.% (or 1.56×10^{21} atoms/cm^3). The equilibrium solubility of copper in aluminum is exactly 2.5 at.% [16], as follows from the Al–Cu phase diagram. The substrate temperature during the deposition was lower than 100°C. The integral content of copper is 5.25×10^{17} atoms/cm^2 (K = 0.71 atoms/ion), according to (2) and Fig. 7. Under the experimental conditions mentioned above, the simulation for this Cu/Al system gives $d = 2.8 \times 10^{17}$ atoms/cm^2. As a whole, agreement between the simulation and experiment must be taken as satisfactory. If the radiation-enhanced diffusion of a material deposited is appreciable, agreement may be worse, since exact data for the diffusion coefficient under various conditions of ion irradiation are lacking.

The fact that the experimental values of d and K are in excess of those obtained by the simulation may be associated with such factors as the surface roughness of the cone and the variation of the binding energy of surface atoms during irradiation (because of implant accumulation in the cone wall). These factors are disregarded in the analysis. The simulation is performed on the assumption that the surface of the cone is perfectly smooth, and the binding energy U_0 of surface atoms that is used in the SATVAL program is assumed to remain constant for a given material.

It should be noted that the experimental data for the thickness d of the coating, deposition yield K, and depth profiles of impurities, as well as those data not included in this paper, are highly reproducible from experiment to experiment.

Experiments with a fairly smooth cone obtained by the electrolytic deposition of gold showed better agree-

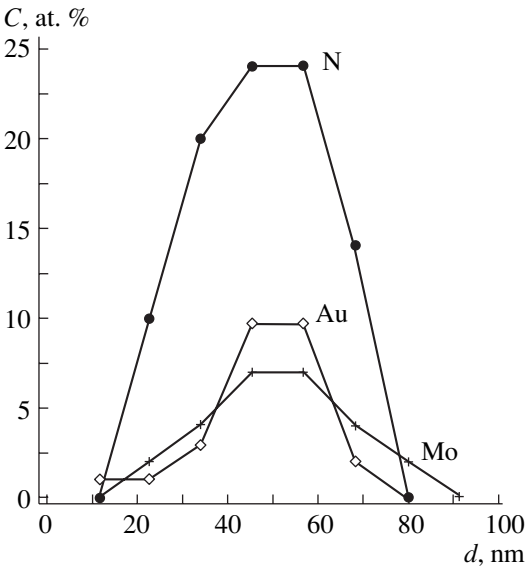

Fig. 6. Depth profiles of molybdenum, gold, and nitrogen atoms in copper that are obtained from RBS spectra. Cones made of these materials were irradiated by N_2^+ ions with E = 110 keV, $D = 1 \times 10^{17}$ cm^{-2}, and J = 10 μA/cm^2.

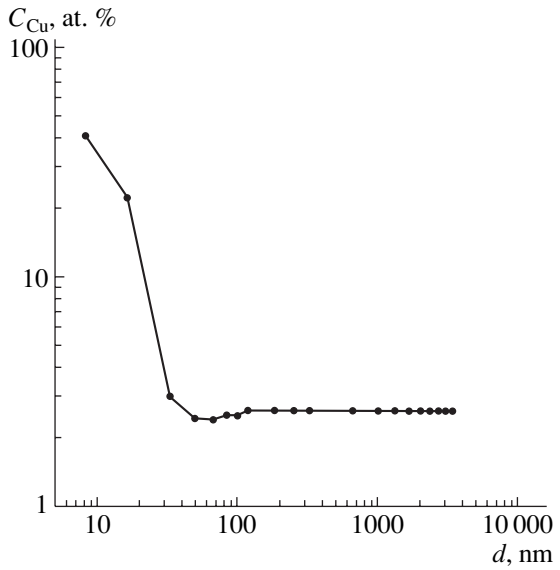

Fig. 7. Concentration profile of copper in aluminum after bombardment by N_2^+ ions with E = 30 keV and $D = 4 \times 10^{17}$ cm^{-2}.

ment with the results of simulation (Fig. 6). For this system, $d^{\text{theor}} = 2.01 \times 10^{16}$ atoms/cm^2 and $d^{\text{exp}} = 2.48 \times 10^{16}$ atoms/cm^2. As follows from Fig. 6, the surface concentration of gold reaches 10 at. %, while the fraction of nitrogen atoms is about 24 at. %. Our investigations suggest that such impurity concentrations are sufficient to significantly improve important surface properties of materials, such as wear resistance and lifetime. In particular, one can raise the temporal and temperature stability of contacting surfaces in industrial commutators [17, 18] (the reliability of contacting surfaces is a bottleneck of these devices). The application of the technology described to industrial switches can increase drastically the number of operating cycles to failure [17, 18].

CONCLUSIONS

An original setup for performing *in situ* ion implantation and deposition of metal films with the same ion beam is suggested. A program suite is developed with which IBAD in this setup is characterized and the radial and depth profiles of deposited and/or implanted ions are simulated. The suite can also be applied to material deposition on the inner surface of tubes with the use of a conical target. The experimental and analytical values of the deposition yield are in good agreement.

ACKNOWLEDGMENTS

The authors thank A.S. Kamyshan for taking Rutherford backscattering spectra.

This work was financially supported by the Foundation for Basic Research of Belarus (grant nos. F01-050 and F03-003) and the Mianowsky Foundation (Poland).

REFERENCES

1. W. Ensinger, Surf. Coat. Technol. **84**, 363 (1996).
2. F. F. Komarov, A. F. Komarov, and A. M. Mironov, Nucl. Instrum. Methods Phys. Res. B **115**, 505 (1996).
3. F. F. Komarov and A. F. Komarov, *Physics of Ion Implantation into Solids* (Tekhnoprint, Minsk, 2001).
4. F. F. Komarov, *Ion Implantation into Metals* (Metallurgiya, Moscow, 1990).
5. J. Sielanko and W. Szysko, Surf. Sci. **161**, 101 (1985).
6. J. Sielanko and W. Szysko, Nucl. Instrum. Methods Phys. Res. B **16**, 340 (1986).
7. F. F. Komarov, A. F. Komarov, V. V. Pilko, *et al.*, in *Proceedings of International Symposium "Ion Implantation in Science and Technology," Lublin, 1997*, pp. 38–41.
8. A. F. Komarov, A. A. Komarov, and P. Tarkovskiĭ, Zh. Tekh. Fiz. **65** (9), 201 (1995) [Tech. Phys. **40**, 976 (1995)].
9. F. F. Komarov, A. F. Komarov, and A. M. Mironov, Poverkhnost, No. 6, 68 (1997).
10. F. F. Komarov, A. F. Komarov, V. V. Pil'ko, *et al.*, in *Proceedings of the 2nd International Conference "Plasma Physics and Plasma Technology," Minsk, 1997*, pp. 570–573.
11. A. F. Komarov, F. F. Komarov, P. Zukowski, *et al.*, Nukleonika **44**, 363 (1999).
12. A. F. Komarov, F. F. Komarov, A. L. Shukan, *et al.*, Izv. Akad. Nauk Belarusi, Ser. Fiz.-Tekh. Nauk, No. 3, 19 (1999).
13. A. F. Komarov, F. F. Komarov, P. Zukowski, *et al.*, Vacuum **63**, 495 (2001).
14. F. F. Komarov, A. F. Komarov, P. Zukowski, *et al.*, in *Abstracts of the 4th International Conference on Modification of Properties of Surface Layers of Ionic Semiconductor Materials Using Particle Beams, Feodosia, Ukraine, 2001*, p. 48.
15. A. A. Komarov, A. F. Komarov, V. V. Pilko, *et al.*, in *Proceedings of the 4th International Conference on Interaction of Radiation with Solids, Minsk, 2001*, pp. 344–346.
16. L. H. van Vlack, *Elements of Materials Science and Engineering* (Addison-Wesley, Reading, 1975; Atomizdat, Moscow, 1975).
17. C. Karwat, Izv. Vyssh. Uchebn. Zaved. Énerg. Ob"edin. SNG, Énerg., No. 6, 33 (2001).
18. C. Karwat, P. Zukowski, and W. M. Mekonnen, Izv. Vyssh. Uchebn. Zaved. Énerg. Ob"edin. SNG, Énerg., No. 2, 43 (2001).

Translated by V. Isaakyan

Technical Physics, Vol. 48, No. 5, 2003, pp. 636–640. Translated from Zhurnal Tekhnicheskoĭ Fiziki, Vol. 73, No. 5, 2003, pp. 115–119.

EXPERIMENTAL INSTRUMENTS AND TECHNIQUES

Study of Components of Insulating Materials for Large-Sized Electric Machines

Yu. A. Panteleev and Yu. A. Polonskiĭ

St. Petersburg State Technical University, ul. Politekhnicheskaya 29, St. Petersburg, 195251 Russia

e-mail: pant@spb.cityline.ru

Received July 23, 2002; in final form, November 21, 2002

Abstract—Thermodepolarizing current spectra for components of mica-based insulating composites are presented. The variation of the thermograms with experimental conditions is revealed. The data reported are the initial results of elaborate measurements in this area and can be used in devising new insulating materials and new methods for the quality control of insulators. *© 2003 MAIK "Nauka/Interperiodica".*

INTRODUCTION

Mica-based insulating composites are widely used as insulation in high-voltage electric machines. In this work, we performed a careful investigation of these composites and their components by thermally activated current spectroscopy. The spectra of thermally stimulated depolarizing (TSD) current were taken under various charging and depolarization conditions over a wide temperature range (both above and below room temperature). From such experimental data, one can judge the nature of relaxation processes.

In addition, comparing the spectra taken from composites with and without a poly(ethylene terephthalate) (PETF) film, as well as from this film alone, one can trace the effect of PETF films on the charge distribution and charge-state decay in the composites. Specifically, by contrasting the TSD current spectra taken of composites and their components, charged regions were found at the PETF–glass fabric and PETF–mica paper interfaces [1]. This indicates that these interfaces are impermeable to charge carriers, which may be one reason for the dielectric durability of the composites. Such an effect was discovered during testing planar insulators and coils of high-voltage electric motors [2].

EXPERIMENTAL

As subjects of investigation, we used the components of composites produced by AO Élinar (Moscow oblast), the leading Russian maker of mica-based insulating materials for electric machine building. The components tested were a PETF film (State Standard 24234-80, Vladimir Chemical Factory) of thickness h = 30 μm, muskovite mica (20 μm), mica paper 2055 TP I02.013.0161.00007 (60 μm), alkali-free alumina borosilicate glass (specs. 6-19313-86; composition 55% SiO_2, 15% Al_2O_3, 10% B_2O_3, ≤0.5% $Na_2O + K_2O$, and ≤0.08% TiO_2; 2.81 ± 0.03 mm), glass fabric (State Standard 19907-83, specs. 6-48-578.6902-18-89; 40 μm), and epoxy–novolac varnish (specs. 16-504.046-81; 40 μm). Results obtained for the test glass were compared with those for KV pure quartz glass (99.98% SiO_2; 1.26 ± 0.05 mm) and KLR-1.1 TiO_2-doped quartz glass (7.3% TiO_2, 1.45 ± 0.04 mm). All the test samples were made in the form of 20 × 20-mm plates (the diameter of the upper electrode of the TSD current measuring device was 10 mm).

The experiments included four successive stages: the production of the spatially nonuniform charge distribution by applying an electric field, the freezing of the polarized state by fast liquid-nitrogen cooling to 293 or 93 K, and the neutralization of the excess charge in the glass via depolarization by linear heating.

The experimental data were processed by techniques described in [3–5]. The basic formula for the TSD current density has the form

$$j_{\mathrm{TSD}}(T) = j_{\mathrm{m}}\exp\left[\frac{W}{k}\left(\frac{1}{T_{\mathrm{m}}}-\frac{1}{T}\right)\right] \times \exp\left\{-\frac{W}{kT_{\mathrm{m}}^2}\int_{T_{\mathrm{m}}}^{T}\exp\left[\frac{W}{k}\left(\frac{1}{T_{\mathrm{m}}}-\frac{1}{T'}\right)\right]dT'\right\}, \quad (1)$$

where

$$j_{\mathrm{m}} = \frac{\varepsilon_0\varepsilon}{h\tau_{\mathrm{m}}}U_e(0) \times \exp\left\{-\frac{W}{kT_{\mathrm{m}}^2}\int_{T_0}^{T_{\mathrm{m}}}\exp\left[\frac{W}{k}\left(\frac{1}{T_{\mathrm{m}}}-\frac{1}{T'}\right)\right]dT'\right\}. \quad (2)$$

Here, U_e is the electret potential difference, W is the energy of activation, T_{m} is the temperature of the maximum, ε is the relative permittivity, and τ_{m} is the relaxation time in the maximum.

1063-7842/03/4805-0636$24.00

The frequency factor ω_0 is easily found from the expression

$$\frac{W\beta\exp\left(\frac{W}{kT_m}\right)}{kT_m^2\omega_0} = 1, \quad (3)$$

where β is the rate of heating.

RESULTS

The PETF film was found to be the least sensitive to the variation of the charging conditions (primarily to the temperature, T_p, and voltage, U_p, of polarization) (Fig. 1a). This is also supported by the data listed in Table 1, where the parameters of the curves depicted in Fig. 1a are compared with those of the curve obtained under standard experimental conditions (T_p = 373 K, U_p = 300 V, t_p = 3 min, and β = 4 K/min). Throughout the range of the charging parameters, the temperature T_m of the maximum changes by no more than 4 K and the activation energy, by no more than 0.2 eV. Such behavior of TSD current peaks in organic materials means that the dipole polarization or the uniform distribution of the space charge over the sample breaks down [6]. The peak of the TSD current in PETF films near 393 K is conventionally related to space charge relaxation [7]. It is also known [8] that the shape of dipole peaks is independent of the charging (polarization) time t_p. Therefore, the behavior of the basic TSD current peak in the high-temperature range may indicate that the space-charge mechanism of polarization prevails. One more piece of evidence in favor of this mechanism is that the energy of activation listed in Table 1 is close to that determined from the temperature dependence of the conductivity: W = 1.37 eV (another estimate is 1.44 eV [9]). It should also be noted that our TSD current spectra (Fig. 1a) are qualitatively similar to those taken in [9] for the same PETF films. Finally, the relatively high values of the frequency factor ω_0 (Table 1) are also typical of space-charge-related maxima.

An important finding also is the good stability of the values of W and ω_0 upon decreasing the rate of depolarization β. This decrease is accompanied by a sharp drop of the maximal current I_m and by a shift of the maximum toward lower temperatures. This suggests that

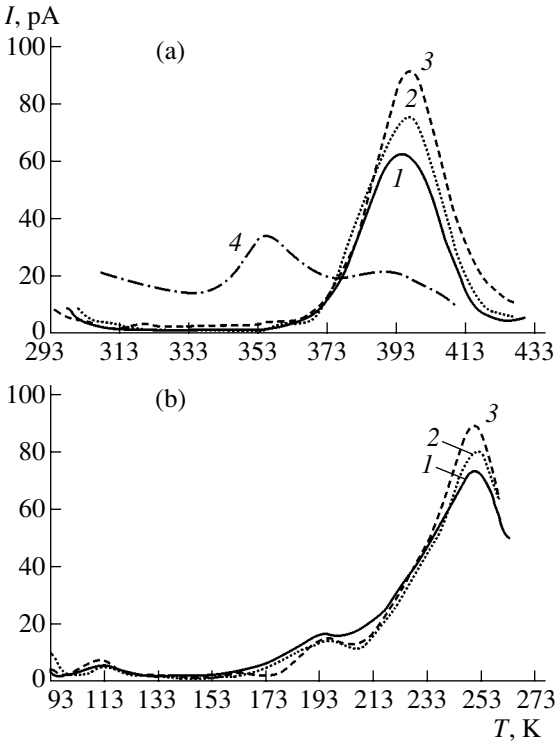

Fig. 1. TSD current spectra for the 30-μm-thick PETF film polarized under the condition U_p = 300 V, t_p = 3 min, β = 4 K/min, and T_p = (*1*) 373, (*2*) 403, and (*3*) 433 K. (*4*) Amorphous PETF (h = 200 μm, T_p = 373 K). (a) High- and (b) low-temperature range.

both the experimental and analytical data are fairly reliable. Qualitatively, all the other materials tested show the same behavior of the TSD current spectra.

As specific features of the PETF spectra in Fig. 1, we may also note the absence of a distinct peak at temperatures between 353 and 363 K, which is associated with dipole-segmentation processes, and the high values of T_m for all the peaks. This completely correlates with a high degree of crystallinity X_c of the film (X_c = 35% according to X-ray diffraction data), which was prepared by biaxial-orientation extrusion with an extrusion ratio of 3.3. An increase in the crystallinity decreases the fraction of the amorphous phase and increases the amount of the so-called hard amorphous phase, which, like the crystalline phase, cannot partici-

Table 1

	Standard conditions	T_p, K		U_p, V		p_p, min		β, K/min	
		403	433	200	100	10	30	2	1
T_m, K	397	397	399	395	397	395	395	386	381
I_m, pA	63	75.8	89.8	59	56.1	80.1	89.4	32.4	12.5
W, eV	1.29	1.29	1.32	1.39	1.32	1.44	1.48	1.34	1.31
ω_0, Hz	2×10^{14}	2×10^{14}	3×10^{14}	4×10^{15}	3×10^{14}	2×10^{16}	5×10^{16}	10^{15}	4×10^{14}

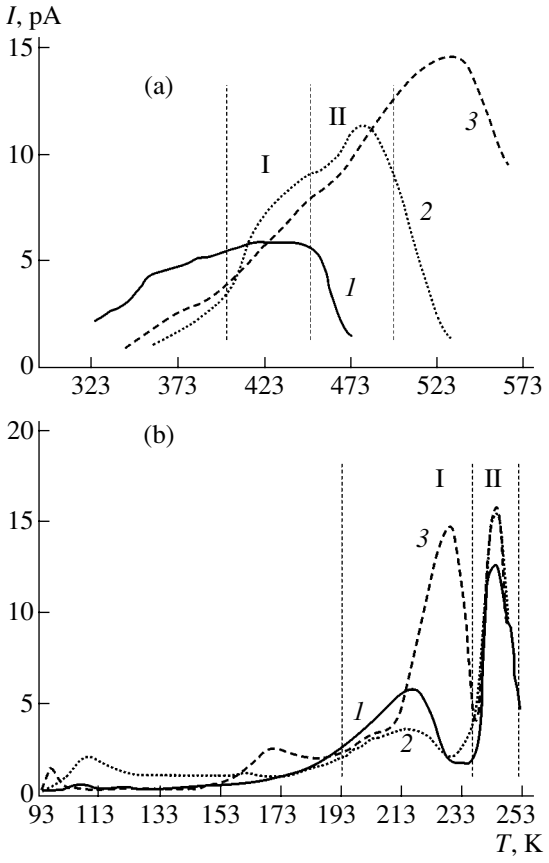

Fig. 2. The same as in Fig. 1 for muscovite mica (h = 20 μm).

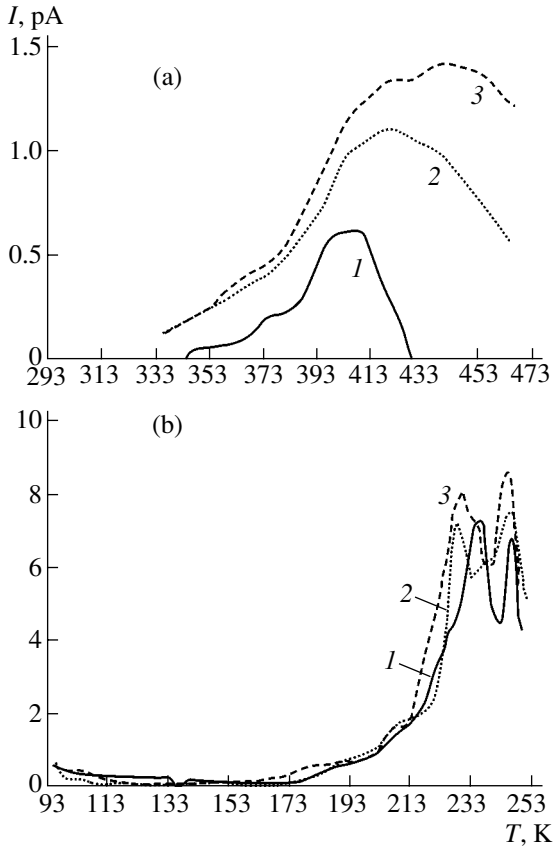

Fig. 3. The same as in Fig. 1 for Ca–Al–B–Mg–SiO_2 glass (h = 2.81 mm).

pate in dipole-segmentation motions. These statements are supported by the experimental data obtained for the amorphous (nonoriented) film (curve *4* in Fig. 1). The effect of X_c on the TSD current spectra of the PETF films is akin to that observed earlier [10].

The variation of the polarization conditions for the inorganic components within the same limits causes much more considerable changes in the thermograms, which is seen most vividly in the case of mica (Fig. 2a). As T_p rises, T_m and I_m increase and the shape of the curve changes. The increase in T_m even advances the growth of T_p. For the muskovite mica, the current peaks in this temperature range are due to the relaxation of the space charge captured by shallow (K^+) and deep (OH^-) traps [11]. The former are associated with minor maximum I in the current curves, while the latter are responsible for principal maximum II. The calculation based on the curve for T_p = 403 K underestimates the parameter values compared with [12]: for I, W is lower by 0.1 eV; for II, the values of T_m, W, and ω_0 are lower by 24 K, 0.022 eV, and a factor of 5, respectively (Table 2). Such discrepancies may arise because of different experimental conditions (various T_p in this case). Comparing the curves in Fig. 2b with the data in [11, 12] suggests (according to [11, 12]) that maxima I and II in this figure are due to the melting of a thick diffuse layer and to the middle part of the water film volume, respectively.

Table 2

	T_m, K	I_m, pA	W, eV	ω_0, Hz
Mica I	440	3.6	0.40	5×10^1
Mica II	476	8.6	0.58	3×10^3

In the low-temperature range (from 93 to 273 K), the rate of relaxation processes increases with temperature in all the samples, except for the varnish. Figure 3b shows the spectra for the alumina borosilicate glass, where current maxima lie at temperatures between 173 and 253 K. Comparing these curves with those obtained for TiO_2-doped quartz glass allows us to conclude that the glass composition influences TSD currents. Bearing in mind that strong covalent bonds prevail in quartz glasses [13] and also that KV glass is made by the gas-flame technique, we may assign these maxima (also observed in the temperature dependence of the dielectric loss [15]) to aluminum impurity [14], which is usually present in gas-flame quartz glasses in amounts of

Table 3

Glass	T_m, K	I_m, pA	W, eV	ω_0, Hz
KV	447	8.1	0.88	2×10^7
KLR-1.1	463	8.5	0.36	1×10^1
Ca–Al–B–Mg–SiO_2	414–444	0.48–0.51	0.71–0.74	3×10^5–3×10^6

$(10–50) \times 10^{-4}$%. The curves for the quartz glass doped by TiO_2 and especially those for Ca–Al–B–Mg–SiO_2 glass have maxima also at temperatures lower than 245 K. By comparing the TSD current spectra for pure KV quartz glass with those for other glasses, one can suggest that the peak at 245–255 K in Fig. 3b is associated with the migration of Al^{3+} ions and that at $T < 245$ K, with the migration of other ions: Ti^{4+} for the KLR-1.1 quartz glass and Na, K, Ca, Al, Mg, and Ti ions for the Ca–Al–B–Mg–SiO_2 glass.

The TSD current thermograms for the Ca–Al–B–Mg–SiO_2, KLR-1.1, and KV glasses in the high-temperature range are shown in Fig. 3a. From these curves (comparison is made for $T_p = 433$ K; Table 3), it follows that the KV glass has the highest W and ω_0, although the charge relaxation in it takes place at temperatures lower than in the KLR-1.1. This fact can be explained by dissimilar charge carriers (ions) responsible for conduction in these glasses. The TSD current curves for the Ca–Al–B–Mg–SiO_2 glass cannot be adequately analyzed in terms of a single appropriately selected current peak. Therefore, for this glass, the distribution of electroactive defects was found from I_m, T_m, and W (the ranges of these parameters are shown in Table 3). In spite of the great scatter in the values of T_m for electroactive defects, their W and ω_0 fall into a narrow interval. Such a situation is possible if similar defects are present in the material.

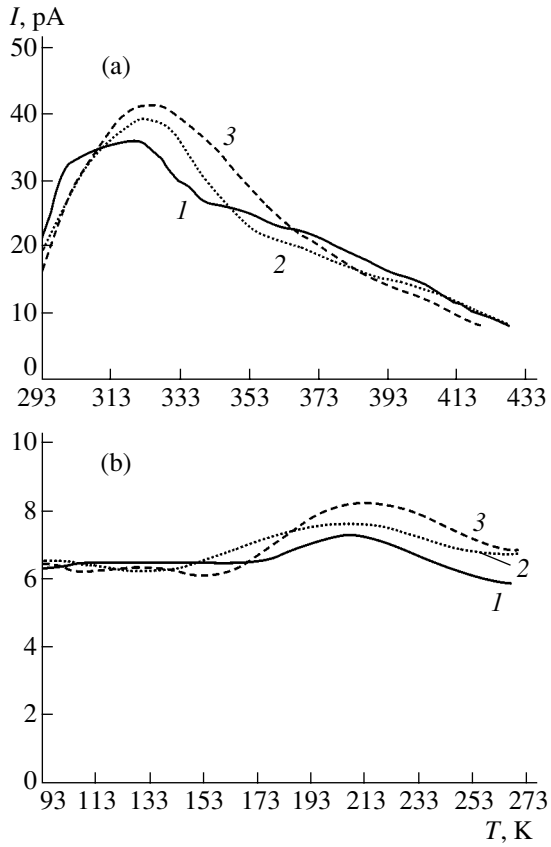

Fig. 4. The same as in Fig. 1 for epoxy–novolac varnish (resin) (h = 40 μm).

For the cured epoxy–novolac varnish, the TSD current curves have weak maxima in both the low- and high-temperature ranges (Fig. 4). The variation of U_p and t_p affect to an extent the space-charge relaxation [8]. The position of the high-temperature peak changes only slightly (not shown in Fig. 4). The small values of the electroactive defect parameters for this peak (taken under the standard conditions), namely, T_m = 316 K, W = 0.24 eV, and ω_0 = 10 Hz (I_m = 36.7 pA), indicate the presence of a large number of shallow traps in the material.

CONCLUSIONS

Among all the components of the composites, the energy of activation of space-charge relaxation is the highest for the PETF film and the lowest for the epoxy–novolac varnish. Also, small TSD currents for all the inorganic components in the high-temperature range (roughly one order of magnitude lower than for the organic constituents) are noteworthy. However, this does not mean that inorganic materials will not contribute to the spectra taken of the composites. When studying impregnated mica paper and especially varnished glass fabric, we found, in particular, that the current grows by about two orders of magnitude compared with that in as-prepared glass fabric. The interfaces between the components of the varnished glass fabric apparently act as traps for free ions, which may be present in both the resin and the glass. A high electrical conductivity of resins and the continuity of their structures make them an efficient medium for the transfer of charges being released from the traps.

REFERENCES

1. Yu. A. Panteleev and Yu. A. Polonskiĭ, Electrotehnica, No. 4, 13 (2002).
2. V. M. Pak, Élektrotekhnika, No. 6, 15 (2001).

3. S. N. Koykov, E. F. Rodionova, and Yu. A. Panteleev, Nondestr. Test. Comput. Simul. Sci. Eng. **4348**, 440 (2000).
4. S. N. Koĭkov and Yu. A. Panteleev, Izv. Vyssh. Uchebn. Zaved. Fiz., No. 5, 59 (2001).
5. Yu. A. Panteleev, Cand. Sci. Dissertation (St.-Petersburg, 2002).
6. R. Singh and S. C. Datt, J. Electrost. **8**, 279 (1980).
7. J. van Turnhout, *Thermally Stimulated Discharge of Polymer Electrets* (Amsterdam, 1975).
8. *Electrets*, Ed. by G. M. Sessler (Springer-Verlag, Berlin, 1980; Mir, Moscow, 1983).
9. A. I. Drachev, V. M. Pak, A. B. Gil'man, *et al*., Élektrotekhnika, No. 6, 46 (2001).
10. J. C. Canadas, J. A. Diego, J. Sellares, *et al.*, in *Proceedings of the 10th International Symposium on Electrets (ISE-10), Delphi, Greece, 1999*, pp. 103–106.
11. M. S. Metsik and G. K. Novikov, Élektrichestvo, No. 3, 43 (1997).
12. M. S. Metsik and L. A. Shcherbachenko, *Electrical Properties of Micas* (Irkutsk, 1990).
13. V. P. Pryanishnikov, *Silica System* (Leningrad, 1971).
14. V. K. Leko and O. V. Mazurin, *Properties of Quartz Glass* (Leningrad, 1985).
15. A. E. Owen and R. W. Douglas, J. Soc. Glass Technol. **43**, 159T (1959).

Translated by V. Isaakyan

Technical Physics, Vol. 48, No. 5, 2003, pp. 641–643. Translated from Zhurnal Tekhnicheskoĭ Fiziki, Vol. 73, No. 5, 2003, pp. 120–122.

BRIEF COMMUNICATIONS

Study of Rectifying and Photoelectric Properties of Barrier Structures Based on Vanadium-Doped Cadmium Telluride

S. Yu. Paranchych, L. D. Paranchych, V. N. Makogonenko, Yu. V. Tanasyuk, and R. N. Yurtsenyuk

Fed'kovich National University, ul. Kotsyubinskogo 2, Chernovtsy, 58012 Ukraine

e-mail: rektor@chnu.cv.ua

Received July 18, 2002

Abstract—Structures similar to Schottky diodes are prepared by the thermal evaporation of chromium on high-resistivity cadmium telluride substrates doped by vanadium (CdTe : V) to a concentration of 5×10^{18} cm^{-3}. The current–voltage and spectral characteristics of the Cr/CdTe : V barrier structures are studied, and their rectifying properties are evaluated. © *2003 MAIK "Nauka/Interperiodica".*

INTRODUCTION

Cadmium telluride, even though in wide use, is continuing to attract researchers' attention. Recent emphasis has been on applications where the semi-insulating properties of this material play a prominent part. X-ray and gamma radiation spectroscopy, electrooptical modulation, and photorefraction are just a few areas of scientific exploration where an intense search for new materials and their applications is being carried out. CdTe semiconductors doped by transition metals of the iron group are viewed as the most promising materials for the near-infrared (IR) spectral region. Doping by vanadium also makes it possible to use cadmium telluride as a photorefractive medium for recording optical information and its transmission via communication lines [1, 2]. Therefore, the number of studies on advanced CdTe technologies and on the electric and photoelectric properties of various structures based on undoped and doped cadmium telluride is growing [3–5].

In this work, Cr/CdTe : V barrier structures are prepared and their electrical and spectral characteristics are studied.

EXPERIMENTAL

Schottky-barrier metal/semiconductor junctions were prepared on single-crystalline *n*-CdTe : V wafers with a vanadium concentration $N_V = 5 \times 10^{18}$ cm^{-3}. The single crystals were grown by vertical directed crystallization at a cooling rate of 10 K/h with the free volume over the melt kept constant. Note that these two factors influence significantly the optical quality of the crystal and its electrical uniformity.

The wafers were cut from the middle part of the CdTe : V single-crystalline ingot normally to the growth direction. According to our electrical and galvanomagnetic studies, the ingot in this part had a free electron concentration $n_e \approx 5 \times 10^{11}$ cm^{-3} and a resistivity $\rho \approx 10^9$ Ω cm, i.e., was semi-insulating. The plane-parallel wafers were processed by conventional mechanical methods and rinsed carefully in ethanol.

Prior to chromium deposition, the substrates were cleaned by ion bombardment in argon for 7–8 min. Then, a chromium film was deposited onto one side of the wafer by thermal evaporation in a vacuum ($P = 6.7 \times 10^{-3}$ Pa). The substrate temperature was kept at 190–200°C. The metal film deposited had a thickness d of about 15 μm. The wafers thus produced were mechanically scribed into 2 × 3-mm chips to which copper wires were attached with contactol. Such Cr/CdTe : V structures were used to take steady-state *I–V* characteristics and spectral curves of photosensitivity.

RESULTS AND DISCUSSION

In Fig. 1, a typical *I–V* characteristic of the Cr/CdTe : V structures is shown. It is seen that the metal/semiconductor junctions (MSJs) offer good rectifying properties. For example, at a bias voltage of about 20 V, the forward current exceeds the reverse current by three orders of magnitude. The initial portion of the *I–V* characteristic is described by the diode equation, whereas at voltages >20 V the forward branch obeys the relationship [4, 6]

$$U = U_0 + R_0 I.$$

The bulk resistance R_0 derived from the slope of the linear portion is found to be about 10^7 Ω and the cutoff voltage is 14–15 V in different samples.

In Fig. 2, the *I–V* characteristic is plotted in the semi-logarithmic coordinates. The straight portion in this curve indicates that the current through the struc-

1063-7842/03/4805-0641$24.00

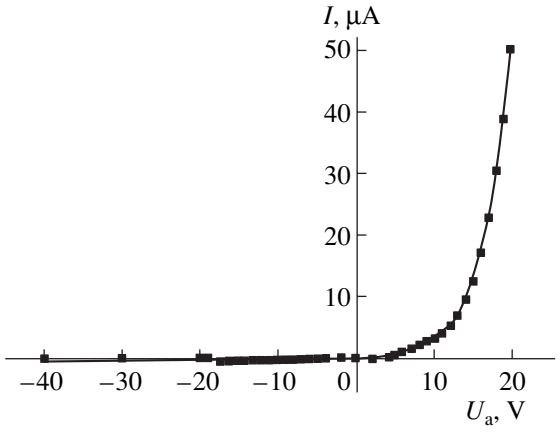

Fig. 1. *I–V* characteristics of the Cr/CdTe : V structures with $N_V = 5 \times 10^{18}$ cm^{-3}.

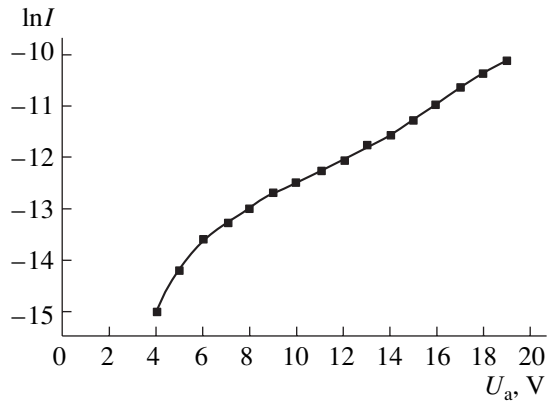

Fig. 2. Semi-logarithmic dependence of the forward current on the applied voltage for the Cr/CdTe : V contacts with $N_V = 5 \times 10^{18}$ cm^{-3}.

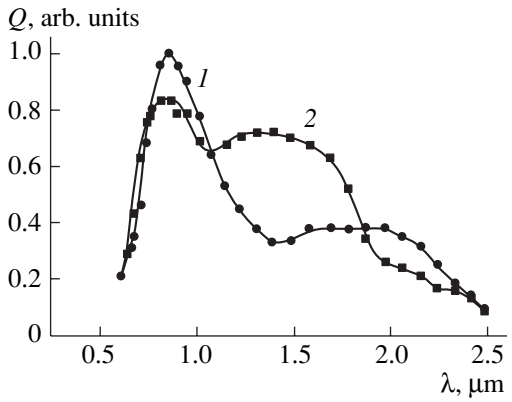

Fig. 3. Spectral dependence of the photosensitivity for the Cr/CdTe : V structures with $N_V = 5 \times 10^{18}$ cm^{-3} prepared from the (*1*) end and (*2*) central parts of the single-crystal substrate.

ture varies exponentially with voltage [7]:

$$I = I_s\left[\exp\left(\frac{qU_a}{nkT}\right) - 1\right], \quad (1)$$

where $I_s = AST^2\exp(-\phi_b/kT)$ is the saturation current, U_a is the applied voltage, n is the ideality factor, A is the Richardson constant, S is the junction area, and ϕ_b is the potential barrier height in the structure.

By extrapolating the linear portion of the curve to the zero bias voltage, one can find the saturation current by formula (1) and then, from the current value, the potential barrier height. If the Richardson constant is set equal to that of a free electron, 120 A/(cm^2 K^2), the value of ϕ_b for different samples varies between 0.7 and 0.75 eV. That is, ϕ_b roughly equals half the energy gap of cadmium telluride, which signifies the high quality of the rectifying contact. Note that similar data for Cr/CdTe in the literature are lacking (see, e.g. [7, 8]).

The photosensitivity studies of the Cr/CdTe : V junctions revealed the photovoltaic effect, which was observed under illumination of the structures on the crystal side (the metal film is opaque to light). In the best structures, the open-circuit voltage amounted to ~0.5 V. Figure 3 shows the spectral dependences of the photosensitivity for several structures. It is seen that the Cr/CdTe : V structures are photosensitive in the range 0.85–2.5 μm. The position of the short-wavelength edge of photosensitivity depends on the photosensitivity edge of the substrate material and corresponds to band-to-band electron transitions. The extension of the spectral dependence into the long-wave range is explained both by the presence of a deep vanadium-related level in the energy gap (E_V = 0.72–0.8 eV [9]) and by the photoemission of electrons from the metal into the semiconductor base. The different values of photosensitivity near 1.5 μm for samples 1 and 2 prepared from different parts of the wafer can be explained by the segregation of vanadium.

Thus, from our experimental studies, it can be concluded that Schottky diodes fabricated by thermally evaporating Cr films on semi-insulating CdTe : V crystals offer good rectifying properties and a high photosensitivity.

The use of a high-resistivity material (CdTe : V) in barrier structures allows one to extend the spectral range of sensitivity. Such structures are of interest for effectively separating charge carriers generated by ionizing particles of different energies.

ACKNOWLEDGMENTS

This work was supported by the Research Center of Ukraine (grant no. 2004).

REFERENCES

1. M. Zha, T. Gorog, A. Zappettini, *et al.*, J. Cryst. Growth **234**, 184 (2002).
2. Yu. P. Gnatenko, R. V. Gamernik, I. A. Farina, *et al.*, Fiz. Tverd. Tela (St. Petersburg) **40**, 1216 (1998) [Phys. Solid State **40**, 1107 (1998)].
3. N. V. Sochinskii, V. Munoz, J. M. Perez, *et al.*, Appl. Phys. Lett. **72**, 2023 (1998).
4. G. A. Il'chuk, V. I. Ivanov-Omskiĭ, V. Yu. Rud', *et al.*, Fiz. Tekh. Poluprovodn. (St. Petersburg) **34**, 1099 (2000) [Semiconductors **34**, 1058 (2000)].
5. L. A. Kosyachenko, V. M. Sklyarchuk, Ye. F. Sklyarchuk, *et al.*, Semicond. Sci. Technol. **14**, 373 (1999).
6. L. A. Kosyachenko, I. M. Rarenko, O. A. Bodnaruk, *et al.*, Fiz. Tekh. Poluprovodn. (St. Petersburg) **33**, 1438 (1999) [Semiconductors **33**, 1293 (1999)].
7. A. G. Milnes and D. L. Feucht, *Heterojunctions and Metal–Semiconductor Junctions* (Academic, New York, 1972; Mir, Moscow, 1975).
8. J. P. Ponpon, Solid-State Electron. **28**, 689 (1985).
9. H. R. Selber, P. Peka, H.-J. Schultz, *et al.*, Semicond. Sci. Technol. **14**, 521 (1999).

Translated by B. Kalinin

Technical Physics, Vol. 48, No. 5, 2003, pp. 644–646. Translated from Zhurnal Tekhnicheskoĭ Fiziki, Vol. 73, No. 5, 2003, pp. 123–125.

BRIEF COMMUNICATIONS

X–Y Photoelectric Sensors Based on Homogeneous Conducting Semiconductor Films

A. A. Klyukanov, É. A. Senokosov, V. V. Sorochan, and L. D. Tsirulik

Near-Dniester State University, Tiraspol, 3300 Moldova

e-mail: feshshenko@mail.ru

Received July 29, 2002

Abstract—The distributions of the dark voltage and photovoltage over the surface of a conducting semiconductor disk (film) with current is calculated analytically. For a photodetector with five ohmic contacts arranged in an appropriate pattern at the circumference of the disk, a relationship between the output signal, current, and local illumination position is found. Experimental data indicate the feasibility of using such photodetectors as *X–Y* optical sensors. *© 2003 MAIK "Nauka/Interperiodica".*

Among position-sensitive photodetectors, optical sensors based on *p–n* junctions were the first to be applied in practice [1]. The next one of this family of optoelectron devices was a sensing element that uses the position dependence of its internal resistance [2].

Position-sensitive optical sensors (photodetectors) that are made of homogeneous low-resistivity semiconductors and have unusual arrangement and connection of electrical contacts were first suggested in [3, 4]. In this work, we are looking for a functional relationship between the output signal of the photodetector with five ohmic contacts and the position of local illumination.

The coordinate dependence of the optical sensitivity of the photodetectors under study reflects the specific potential distribution over the semiconductor surface in the presence of current. We analyzed the distributions of the dark voltage φ_0 and photovoltage φ_1 in a photodetector made of a homogeneous conducting semiconductor disk (film) of thickness d and radius R with five ohmic contacts arranged along the circumference (Fig. 1). Voltage source *6* is connected to contacts *2* and *4*, and a current I is passed through the device. Load resistors *7* and *8* and voltage amplifiers *9* and *10* are inserted between contacts *1* and *5* and between contacts *1* and *3*.

To find the distributions of the dark voltage and photovoltage, we introduce the Cartesian (x, y, z) and spherical (r, Θ, ψ) coordinates, with their origin placed at the center O of the front surface of the disk. The axes X and Y are arranged so that the X axis runs through contacts *2* and *4* (Fig. 1).

The coordinate r of a point on the free surface of the disk is equal to the magnitude of its radius vector $\mathbf{r}$ ($r = |\mathbf{r}|$), and Θ is the angle between the vector $\mathbf{r}$ and positive direction of the Y axis. Since the disk is uniform in thickness, the voltages are independent of z (or ψ): $\varphi_0 = \varphi_0(x, y) = \varphi_0(\mathbf{r}) = \varphi_0(r, \Theta)$ and $\varphi_1 = \varphi_1(x, y) = \varphi_1(\mathbf{r}) = \varphi_1(r, \Theta)$.

When deriving an expression for the dark voltage $\varphi_0(r, \Theta)$, we used the Laplace equation

$$\Delta\varphi_0 = 0 \tag{1}$$

(Δ is Laplacian) and also equations relating the external electric field strength $\mathbf{E}$ to φ_0 and the current density $\mathbf{j}$ to the dark conductivity σ_0:

$$\mathbf{E} = -\nabla\varphi_0; \quad \mathbf{j} = \sigma_0\mathbf{E}. \tag{2}$$

The boundary conditions were as follows:

$$j_n = 0, \quad E_n = -[(\partial\varphi_0)/(\partial r)]_{r=R} = 0, \tag{3}$$

where n is the normal to the disk surface.

In view of the results obtained in [1], we expressed the dark voltage as an explicit function of the coordinates:

$$\varphi_0 = \frac{1}{\sigma_0\pi d}\ln\frac{|\mathbf{r} - \mathbf{R}_x|}{|\mathbf{r} + \mathbf{R}_x|}. \tag{4}$$

Here, $\mathbf{R}_x = R\mathbf{e}_\mathbf{x}$ and $\mathbf{e}_\mathbf{x}$ is the unit vector in the X direction. Now let a small area of disk surface be illuminated

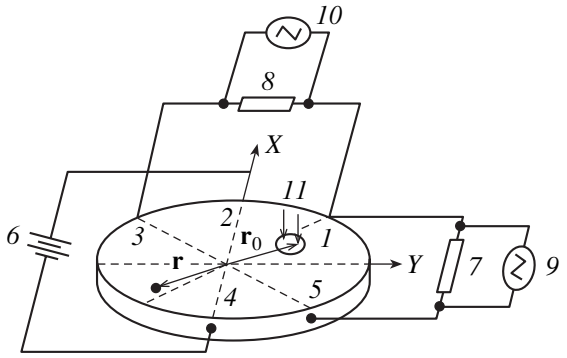

Fig. 1. Position-sensitive device based on a five-contact photodetector.

1063-7842/03/4805-0644$24.00 © 2003 MAIK "Nauka/Interperiodica"

by narrow beam *11* of optically active light (Fig. 1). In low-resistivity semiconductors, especially those subjected to weak electric fields, one can neglect the diffusion- and drift-related smearing of the boundary between the distributions of excess charge carriers in the dark and illuminated areas [5]. Therefore, we assume that the distribution of nonequilibrium excess carriers over the area of optical excitation and that of the light intensity L over the beam's cross section are the same.

Let $\delta\sigma$ be a change in the conductivity of the semiconductor at the center of the illumination spot with the coordinate $\mathbf{r}_0 = (r_0, \Theta_0)$. If it is assumed that the light intensity in the probing beam obeys the Gaussian distribution, the expression for the conductivity at any point $\mathbf{r} = (r, \Theta)$ on the disk's surface is given by

$$\sigma(\mathbf{r}) = \sigma_0 + \delta\sigma\exp\left[-\frac{(\mathbf{r}-\mathbf{r}_0)^2}{a^2}\right], \quad (5)$$

where a is the radius of the illumination spot.

Relationship (5) yields correct limiting values of $\sigma(\mathbf{r})$: $\sigma(\mathbf{r}_0) = \sigma_0 + \delta\sigma$ for $\mathbf{r} = \mathbf{r}_0$ and $\sigma(\mathbf{r}) = \sigma_0$ for $|\mathbf{r} - \mathbf{r}_0| > a$.

In a low-resistivity semiconductor, $(\delta\sigma)/\sigma \ll 1$; therefore, the voltage $\varphi(\mathbf{r})$ can be expressed as the series in powers of $(\delta\sigma)/\sigma$. In this case, φ_1 can be regarded as a first-order correction to φ_0:

$$\varphi(\mathbf{r}) = \varphi_0(\mathbf{r}) + \varphi_1(\mathbf{r}). \quad (6)$$

Under steady-state conditions, $\varphi(\mathbf{r})$ must satisfy the equations

$$\mathbf{j} = -\sigma\nabla\varphi, \quad \mathrm{div}\,\mathbf{j} = 0. \quad (7)$$

From (1) and (6) and also taking into account that the scalar product $\nabla\sigma\cdot\nabla\varphi_1 = \nabla\delta\sigma\cdot\nabla\varphi_1$ is proportional to $(\partial\sigma)/\sigma)^2$, which is a second-order infinitesimal, we arrived at a relationship that relates the dark voltage and photovoltage to each other:

$$\sigma\Delta\varphi_1 \approx -\nabla\sigma\nabla\varphi_0. \quad (8)$$

Substituting (4) into (8) and putting $\sigma \approx \sigma_0$, we find that

$$\Delta\varphi_1 \approx 2\frac{\delta\sigma}{\sigma}\frac{1}{a^2}\frac{I}{\pi\sigma d}\left[\frac{(\mathbf{r}-\mathbf{R}_x)\cdot(\mathbf{r}-\mathbf{r}_0)}{(\mathbf{r}-\mathbf{R}_x)^2} - \frac{(\mathbf{r}+\mathbf{R}_x)\cdot(\mathbf{r}-\mathbf{r}_0)}{(\mathbf{r}+\mathbf{R}_x)^2}\right]\exp\left[-\frac{(\mathbf{r}-\mathbf{r}_0)^2}{a^2}\right]. \quad (9)$$

A solution to Eq. (9) is the function φ_1, which depends not only on the coordinates $\mathbf{r} = (r, \Theta)$ of the point considered but also on the coordinates $\mathbf{r}_0 = (r_0, \Theta_0)$ of the illumination spot.

Of practical interest is the voltage drop across specific points on the photoconductor surface. Contacts *1*–*5* lie on the lateral surface of the photodetector at points specified by the angles $\Theta_1 = 45°$, $\Theta_2 = 90°$, $\Theta_3 = 135°$, $\Theta_4 = 270°$, and $\Theta_5 = 315°$. The angles are measured from the *Y* axis counterclockwise.

As follows from formula (4) and symmetry considerations, contacts *1* and *3* lie on an equipotential line; therefore, the dark voltage $V_{13}^{\mathrm{d}} = 0$. Contacts *1* and *5* do not lie on an equipotential line; hence, $V_{15}^{\mathrm{d}} \neq 0$.

Under local illumination, the conductivity of the photodetector changes ($\delta\sigma \ll \sigma_0$) and so does the potential (by a value of φ_1) [6]. If the radius of the light spot is small ($a \ll R$),

$$\varphi_1 = R^2\frac{\langle\delta\sigma\rangle}{\sigma}\frac{I}{\sigma\pi dc^2}\left[\frac{l_2 l}{l_2^2} - \frac{l_4 l}{l_4^2}\right], \quad (10)$$

where

$$\langle\delta\sigma\rangle = \frac{1}{\pi a^2}\iint\delta\sigma(x', y')dx'dy',$$

l is the distance from the point of observation to the illumination spot, and l_2 and l_4 are the distances from contacts *2* and *4* to the point of observation.

For all the five contacts, the voltage depends on the illumination spot coordinates. With formula (10), we obtain the following relationships for the voltage drop:

$$V_{13} = Ay'' \times\frac{1 + r^2 - 2\sqrt{2}y''}{[(1+r^2)^2 - 4y''^2][(1 + r^2 - 2\sqrt{2}x'')^2 - 2y''^2]}, \quad (11)$$

$$V_{15} = Ax'' \times\frac{1 + r^2 - 2\sqrt{2}y''}{[(1+r^2)^2 - 4y''^2][(1 + r^2 - 2\sqrt{2}y'')^2 - 2x''^2]}, \quad (12)$$

where

$$A = \frac{\langle\delta\sigma\rangle}{\sigma}\frac{I}{\sigma\pi d},$$

$x = r_0\sin\Theta_0$, $y = r_0\cos\Theta_0$, $r = \sqrt{x^2 + y^2}$, $x'' = x/a$, and $y'' = y/a$.

Relationships (11) and (12) define the potential drop under illumination. For small and moderate values of r_0, output characteristics (11) and (12) are seen to vary linearly with displacement; that is, $V_{13} \sim Ay$ and $V_{15} \sim Ax$. The signals V_{13} and V_{15} change sign when the sense of displacement is reversed. Thus, the output characteristics uniquely define the location of the light spot. The uniqueness is also retained if the characteristics are slightly nonlinear. This makes it possible to extend the applicability domain of the approach. The location characteristics involve design parameters that enter into the expression for A.

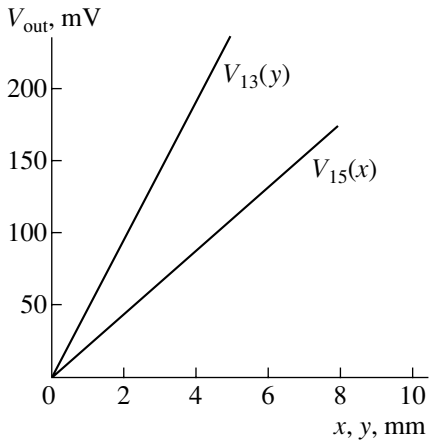

Fig. 2. Voltage differences V_{13} and V_{15} vs. light beam coordinates.

In experimental studies of CdS : Cu films [7], it was established that the dependences $V_{13}(y)$ and $V_{15}(x)$ are actually linear functions of the light source coordinates (Fig. 2). Therefore, CdS : Cu photodetectors of such a design can be used for uniquely locating a light source. For the CdS : Cu films, the components of the specific position sensitivity of the device,

$$\eta = \frac{\Delta V_{out}}{hIL}$$

(where L is the illuminance, ΔU_{out} is a change in the output voltage when the coordinate changes by h, and I is the current through the device), were equal to

$$\eta_y = 27\frac{\text{mV}}{\text{mm mA lx}}, \quad \eta_x = 15\frac{\text{mV}}{\text{mm mA lx}}.$$

REFERENCES

1. *Semiconductor Photodetectors and Converters of Radiation*, Ed. by A. I. Frimer and I. I. Gaubkin (Mir, Moscow, 1965).
2. A. N. Marchenko, S. V. Svechnikov, and A. K. Smovzh, *Semiconductor Potentiometric Sensors* (Radio i Svyaz', Moscow, 1988).
3. É. A. Senokosov, A. A. Klyukanov, A. N. Usatyĭ, *et al.*, USSR Inventor's Certificate No. 1436796 (1987).
4. A. A. Klyukanov, É. A. Senokosov, A. N. Usatyĭ, *et al.*, USSR Inventor's Certificate No. 1499119 (1989).
5. S. M. Ryvkin, *Photovoltaic Phenomena in Semiconductors* (Fizmatgiz, Moscow, 1963).
6. É. A. Senokosov, Doctoral Dissertation (Kishinev, 1989).
7. E. A. Senokosov, L. D. Tsirulik, I. I. Burdian, *et al.*, in *Abstracts of the 3rd International School–Conference on Physical Problems in Material Science of Semiconductors, Chernivtsi, 1999*, p. 263.

Translated by V. Isaakyan

Technical Physics, Vol. 48, No. 5, 2003, pp. 647–650. Translated from Zhurnal Tekhnicheskoĭ Fiziki, Vol. 73, No. 5, 2003, pp. 126–129.

BRIEF COMMUNICATIONS

Electrical Performance of HgInTe Surface-Barrier Photodiodes

L. A. Kosyachenko, Yu. S. Paranchich, V. N. Makogonenko, V. M. Sklyarchuk, E. F. Sklyarchuk, and I. I. German

Fed'kovich National University, ul. Kotsyubinskogo 2, Chernovtsy, 58012 Ukraine

e-mail: rektor@chnu.cv.ua

Received August 20, 2002

Abstract—Surface-barrier photodiodes prepared by the vacuum deposition of a semi-transparent gold layer on $Hg_3In_2Te_6$ single-crystal substrates are studied. *I–V* characteristics taken at temperatures between 278 and 323 K and the photosensitivity spectrum recorded in the range 0.6–1.8 μm, which is of great importance for fiber-optics communication, are given. Charge transfer mechanisms are treated in terms of generation–recombination processes in the space-charge region of the diode. *© 2003 MAIK "Nauka/Interperiodica".*

INTRODUCTION

The effective operation of fiber-optics communication lines implies the presence of fast efficient photodetectors. In quartz fibers, the least losses are observed at a wavelength of 1.55 μm (at 1.3 μm, the losses are somewhat higher). Silicon photodiodes, therefore, are not suitable for this purpose, and germanium diodes have large dark currents. In terms of spectral matching, $In_xGa_{1-x}As$ solid solution is best suited to fiber-optics communication. Epitaxial layers of this solid solution are usually grown on InP substrates, and the lattice mismatch is minimal for $x = 0.53$. In this case, the $In_xGa_{1-x}As$ energy gap is $E_g = 0.74$ eV and the absorption edge lies at 1.68 μm. To eliminate the undesired effect of the potential barrier at the $In_xGa_{1-x}As/InP$ interface, an extra interlayer of quaternary solid solution $Ga_xIn_{1-x}As_yP_{1-y}$ ($x = 0.6$–0.7, $y = 0.6$–0.9) may be introduced [1].

In [2, 3], a photodetector made of $Hg_3In_2Te_6$ was suggested for the range mentioned above. This device offers a nearly 100% internal photoelectric yield. A specific feature of this material is a high concentration of neutral cation vacancies, which makes it almost insensitive to many impurities and radiation-resistant [4]. Although the energy gap of $Hg_3In_2Te_6$ exceeds that of Ge insignificantly (only by ≈0.06 eV), the room-temperature minority carrier concentration (which is to a great extent responsible for the reverse current of a diode) in the former is less by roughly one order of magnitude. That is why $Hg_3In_2Te_6$ photodiodes seem to be promising for fiber-optics communication.

In this work, we experimentally study charge transfer in $Hg_3In_2Te_6$ photodiodes and analyze its physical mechanisms. These issues, which are not covered in previous publications, are intimately related to the efficiency of photoelectric conversion, as well as to the device's dark current and speed.

SINGLE CRYSTALS

The diodes were made of Bridgman-grown *n*-$Hg_3In_2Te_6$ single crystals. The electron concentration found by the Hall effect and conductivity measurements was 8×10^{14} cm^{-3}. The electron mobility was equal to 140–150 cm^2/(V s). Figure 1 shows the optical transmission (T) curve of $Hg_3In_2Te_6$ over a wide range of wavelengths λ (the break in the curve is due to the use of two spectral instruments). The value $T = 70$–71% for a plate 1 mm thick is noteworthy: it indicates the high quality of the single crystals. Assuming that, for such a high transparency, losses are due only to reflection and putting $T = (1 - r)/(1 + r)$ in view of the multi-

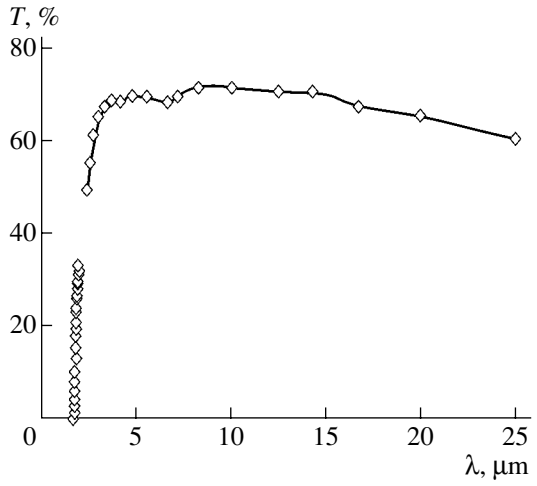

Fig. 1. Transmission spectrum of $Hg_3In_2Te_6$ single crystals at 300 K.

1063-7842/03/4805-0647$24.00 © 2003 MAIK "Nauka/Interperiodica"

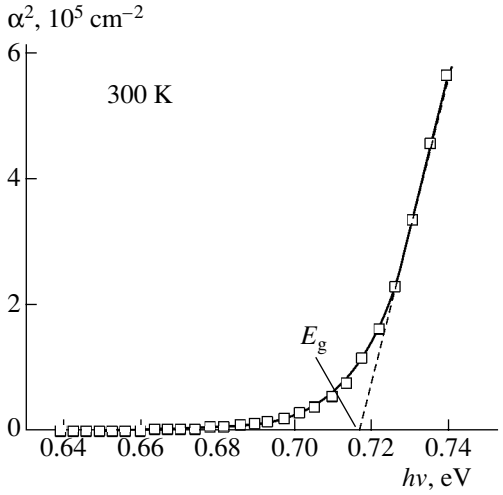

Fig. 2. Absorption curve near the absorption edge vs. dependence $\alpha \sim (h\nu - E_g)^{1/2}$.

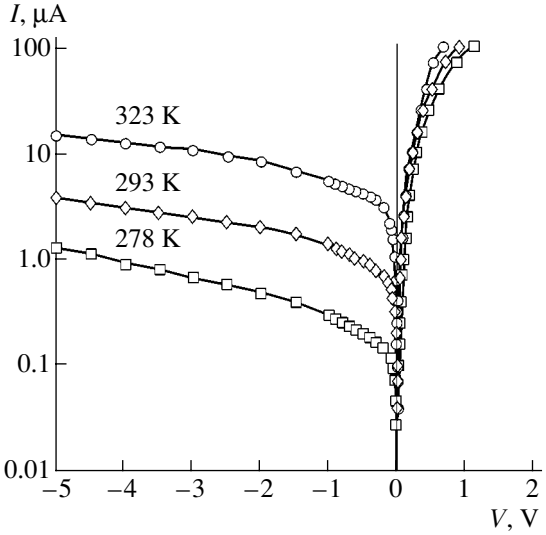

Fig. 3. *I–V* characteristics of the Au/HgInTe diode at three temperatures.

ple reflections [5], we find for the reflection coefficient $r = 0.17$. Although the reflection coefficient depends on wavelength, the value of r found can be used to construct the entire absorption curve without introducing a large error. In general, the absorption coefficient α, T, and the sample thickness d are related as [5]

$$\alpha = \frac{1}{d}\ln\left\{\frac{(1-r)^2}{2T} + \left[\frac{(1-r)^4}{4T^2} + r^2\right]^{1/2}\right\}. \qquad (1)$$

The α vs. $h\nu$ dependence ($h\nu$ is the photon energy) calculated from (1) is depicted in Fig. 2 in the coordinates α^2–$h\nu$. Here, it is taken into account that, for direct-gap semiconductors (which $Hg_3In_2Te_6$ is [4]), $\alpha \sim (h\nu - E_g)^{1/2}$. In these coordinates, the curve $\alpha(h\nu)$ then takes the form of a straight line intersecting the abscissa axis at the point $h\nu = E_g$. From Fig. 2 it follows that the energy gap E_g of $Hg_3In_2Te_6$ is close to 0.72 eV, which agrees with published data [4].

PROPERTIES OF THE DIODES

Photosensitive barrier structures were prepared by evaporating a semitransparent gold layer (≈200 Å thick) at a pressure of no more than 10^{-6} torr on $Hg_3In_2Te_6$ plates that were preliminary carefully polished and irradiated by Ar ions (ion-beam etching) with an energy of 500–700 eV and a current of 20 mA/cm² for 5 min.

The *I–V* characteristics of a 1-mm² Au/$Hg_3In_2Te_6$ diode taken at 278, 293, and 323 K are shown in Fig. 3, and its photosensitivity spectrum recorded in the range 0.6–1.8 μm at 300 K is displayed in Fig. 4.

The photosensitivity spectrum is seen to cover the whole interval of wavelengths used in optical fibers, i.e., 0.65, 0.84, 1.3, and 1.55 μm. The current sensitivity is quite acceptable for practical use but can be noticeably improved by thinning the semitransparent gold electrode to 80–100 Å. The dark currents of the diode are the same as in the best Ge photodiodes of the same area but are roughly one order of magnitude higher than those of $In_xGa_{1-x}As$ *p–n* junctions intended for operation at 1.55 μm (see, e.g., [6]).

Let us consider possible charge transfer mechanisms and ways of decreasing the dark current in Au/HgInTe diodes.

The fast, though sublinear, rise in the reverse current with voltage and its strong temperature dependence imply that the current is of a thermionic nature. At first glance, such a supposition seems doubtful, since the forward branch of the characteristic does not exhibit the dependence $I \sim \exp(eV/2kT)$, which is typical of recombination current [7]. It should be noted, however, that such a dependence was obtained for a conventional *p–n* junction [8]. For Schottky diodes, this dependence holds only if an inversion layer is present at the semiconductor surface (i.e., when the barrier height φ_0 exceeds $E_g/2 - \Delta\mu$, where $\Delta\mu$ is the spacing between the Fermi level and the conduction band bottom in the neutral part of the semiconductor) and the forward bias is not too large [9]. When these conditions are not met, the recombination current grows with voltage much weaker than the dependence $I \sim \exp(eV/2kT)$.

In general, the dependence $I(V)$ can be found by integrating the recombination rate $U(x)$ over the space-charge region of the diode:

$$I = Ae\int_0^W U(x)dx,$$

where A is the surface area of the diode; W is the width of the space-charge region that is equal to $(2\varepsilon\varepsilon_0(\varphi_0 -$

$eV)/e2N_d)^{1/2}$; ε and ε_0 is the permittivity of the semiconductor and the dielectric constant, respectively; and N_d is the concentration of uncompensated donors.

According to Shockley–Reed recombination statistics,

$$U(x, V) = \frac{n(x, V)p(x, V) - n_i^2}{\tau_{p0}[n(x, V) + n_1] + \tau_{n0}[p(x, V) + p_1]}, \quad (2)$$

where $n(x, V)$ and $p(x, V)$ are the nonequilibrium carrier concentrations in the conduction band and valence band, respectively; n_i is the intrinsic carrier concentration; and τ_{n0} and τ_{p0} are the effective lifetimes of electrons and holes, respectively, in the space-charge region.

The values of n_1 and p_1 are numerically equal to the equilibrium concentrations of electrons and holes when the Fermi level coincides with the recombination center (trap) level E_t; that is, $n_1 = N_c\exp(-E_t/kT)$ and $p_1 = N_v\exp(-(E_g - E_t)/kT)$.

If the energy is measured from the conduction band bottom in the neutral part of the crystal, the concentrations of electrons and holes in a section x at a voltage V are given by (see inset to Fig. 5)

$$n(x, V) = N_c\exp\left[-\frac{\Delta\mu + \varphi(x, V)}{kT}\right], \quad (3)$$

$$p(x, V) = N_v\exp\left[-\frac{E_g - \Delta\mu - \varphi(x, V) - eV}{kT}\right], \quad (4)$$

where

$$\varphi(x, V) = (\varphi_0 - eV)\left(1 - \frac{x}{W}\right)^2 \quad (5)$$

is the variation of the potential energy in the space-charge region.

The parameters necessary to calculate the current, the barrier height φ_0 and the energy position E_t of the generation–recombination center, are unknown. The situation is, however, simplified owing to the fact that, for $eV \gg kT$, the reverse generation current I_{gen} is given by [9]

$$|I_{gen}| = \frac{ep_1W}{\tau_{p0}}\frac{\sqrt{E_g - \Delta\mu - E_t - eV} - \sqrt{E_t - \Delta\mu}}{\sqrt{\varphi_0 - eV}}. \quad (6)$$

From this expression, it follows that I_{gen} does not depend on φ_0 ($W \sim (\varphi_0 - eV)^{1/2}$). Moreover, at elevated reverse biases, its V dependence does not change with E_t (but the current is a strong function of E_t). Formula (6) was derived for E_t lying in the upper part of the energy gap. For lower lying levels, the behavior of the current is similar [9].

Thus, to compare (1) with the experiment, one must preset a reasonable value of φ_0; calculate the currents for various E_t; and, by appropriately selecting coefficients, bring the experimental curve into coincidence with constructed curves in the range of elevated reverse biases. Then, by varying φ_0, the best fit between the experimental and constructed curves in the range of forward biases must be achieved. The results of such a procedure are illustrated in Fig. 5. The effective mass of an electron, m_e, is taken to be $0.47m_0$ (m_0 is the mass of a free electron); that of a hole, $m_h = 1.35m_0$ [4]; and $\Delta\mu = kT\ln(N_c/n) = 0.235$ eV at 296 K. It is seen that the behavior of the reverse current and the rectifying properties of the diode depend on E_t. Comparing the exper-

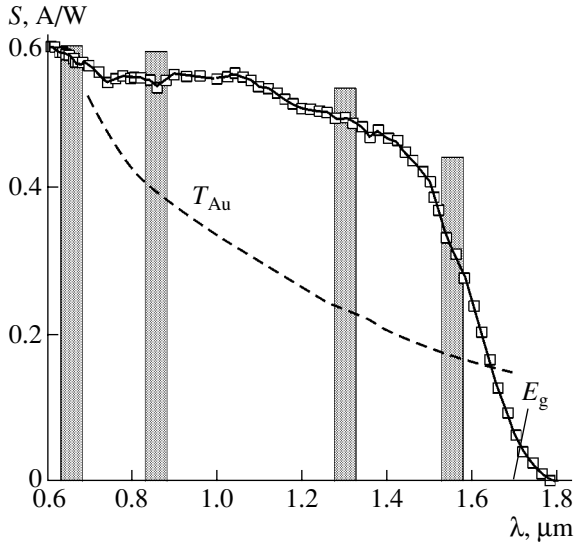

Fig. 4. Photosensitivity spectrum of the Au/HgInTe diode at 300 K. The dashed line shows the transmission of the 200-Å-thick gold film on the quartz plate. Four spectral ranges used in communication lines are shown.

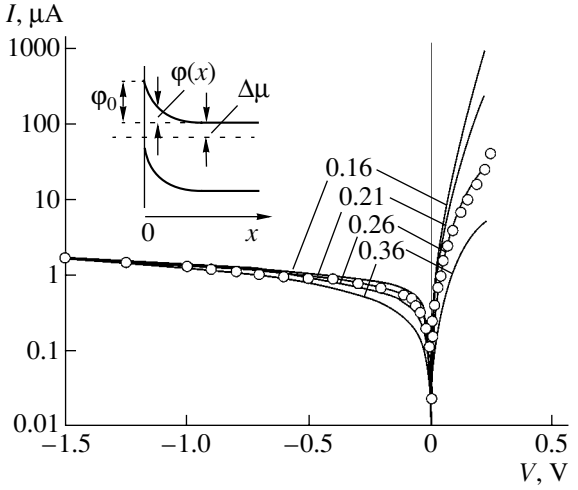

Fig. 5. Measured (circles) vs. calculated (continuous curves) I–V characteristics for different energy positions E_t of the generation–recombination level at 293 K. The figures by the curves are the values of E_t (eV). The inset shows the energy-level diagram of the junction used in the analysis.

imental and calculated results for reverse biases shows that the energy position of the generation–recombination center is 0.21–0.26 eV. The best fit between the calculated and measured forward branches is achieved when the barrier height φ_0 equals 0.37 eV. The calculation of the direct current can be made for voltages $V <$ 0.25 V, since the above-barrier thermionic current comes into play at higher voltages. For $\Delta\mu$ and φ_0 found, the saturation thermionic current $I_s = AA^*T^2\exp[-(\varphi_0 + \Delta\mu)/kT] = 3 \times 10^{-9}$ A at 296 K (A^* is the effective Richardson constant); that is, it is small compared with the generation current. However, the range of elevated forward biases is of minor importance for the operation of the device as a photodiode.

It is worth noting that formula (2) involves the carrier lifetimes τ_{n0} and τ_{p0}, which, however, influence only the current through the diode. This circumstance allows us to find their values by joining together the calculated and measured currents in that voltage range where the current is independent of other parameters (E_t and φ_0), i.e., at elevated reverse biases. In this voltage range, the best agreement between the simulation and experiment is reached at $\tau_{n0} = \tau_{p0} = 8 \times 10^{-8}$ s for $E_t = 0.21$ eV and $\tau_{n0} = \tau_{p0} = 1.5 \times 10^{-8}$ s for $E_t = 0.26$ eV.

Thus, the suggested procedure of processing experimental data allows for a fairly accurate determination of unknown parameters of the diode structure, namely, the barrier height φ_0, carrier lifetimes τ_{n0} and τ_{p0} in the space-charge region, and energy position E_t of recombination–generation levels. Of practical importance is the fact that the reverse current in an Au/HgInTe diode is governed by carrier generation in the depleted region of the barrier structure, i.e., by the parameters τ_{n0} and τ_{p0}. Hence, the reverse current of the diode can be decreased by using purer and more perfect crystals (since τ_{n0} and τ_{p0} are inversely proportional to the density of recombination–generation levels).

CONCLUSIONS

We fabricated efficient Au/HgInTe photodiodes whose sensitivity range covers the operating spectral range of fiber-optics communication lines. The electric performance of the diodes can be characterized by invoking the model of recombination and generation in the space-charge region with regard for specific processes occurring in surface-barrier structures. The energy position of generation–recombination levels is 0.21–0.26 eV, and the effective lifetime of charge carriers ranges from 10^{-8} to 10^{-7} s.

REFERENCES

1. B. G. Streetman and S. Banerjee, *Solid State Electronic Devices* (Prentice Hall, New Jersey, 2000, 5th ed.).
2. A. I. Malik, G. G. Grushka, and N. R. Tevs, Zh. Tekh. Fiz. **60** (6), 146 (1990) [Sov. Phys. Tech. Phys. **35**, 723 (1990)].
3. A. I. Malik and G. G. Grushka, Zh. Tekh. Fiz. **60** (10), 188 (1990) [Sov. Phys. Tech. Phys. **35**, 1227 (1990)].
4. G. G. Grushka, Z. M. Grushka, and N. P. Govaleshko, Ukr. Phys. J. **30**, 304 (1985).
5. Zh. Pankov, *Optical Processes in Semiconductors* (Mir, Moscow, 1973).
6. Products of GPD Optoelectronics Corp. http://www.gpd-ir.com.
7. S. Sze, *Physics of Semiconductor Devices* (Wiley, New York, 1981; Mir, Moscow, 1984).
8. C. Sah, R. Noyce, and W. Shockley, Proc. IRE **45**, 1228 (1957).
9. L. A. Kosyachenko, V. P. Makhniĭ, and I. V. Potykevich, Ukr. Phys. J. **23**, 279 (1978).

Translated by V. Isaakyan

Technical Physics, Vol. 48, No. 5, 2003, pp. 651–654. Translated from Zhurnal Tekhnicheskoĭ Fiziki, Vol. 73, No. 5, 2003, pp. 130–133.

BRIEF COMMUNICATIONS

Effect of Growth-Induced Internal Stresses on the Hematite Crystal Magnetization in the Basal Plane

A. T. Karaev and B. Yu. Sokolov

National University of Uzbekistan, Tashkent, 700174 Uzbekistan

e-mail: optic@nuuz.uzsci.net

Received September 19, 2002

Abstract—The behavior of the domain structure in thin hematite crystal platelets subjected to a magnetic field is studied. In a certain range of the magnetic field aligned with the hard magnetic axis in the basal plane, a magnetic superstructure with the ferromagnetic vector azimuth oscillating along the magnetic field is found to arise in the crystals with internal stresses. Experimental data are discussed in terms of the magnetization ripple theory. *© 2003 MAIK "Nauka/Interperiodica".*

INTRODUCTION

The domain structure (DS) of hematite, which is a weak ferromagnet, has been studied for more than 30 years by various investigation techniques, such as the method of power patterns [1], X-ray topography [2], and the magnetooptic method [3, 4]. The theoretical consideration of DSs in hematite was performed in [5]. One may thus be inclined to think that this issue has been well understood to date both theoretically and experimentally. However, an intriguing feature of the DS evolution in Ga-doped hematite magnetized along the hard magnetic axis has been recently found [6], namely, a quasi-periodic magnetic microstructure with the ferromagnetic vector azimuth oscillating along the magnetic field. This modulated magnetic structure (MMS) was attributed [6] to the transition of the crystal from the uniform to the nonuniform magnetic state and was treated in terms of the concept of random field appearing when diamagnetic Ga ions substitute for some of the Fe ions. Further investigations showed that the MMS is also observed in pure hematite crystals with internal stresses. Below, conditions for MMS excitation and existence in such crystals are discussed.

EXPERIMENTAL

α-Fe_2O_3 hematite single crystals (space group D_{3d}^6) were grown by oriented crystallization from solution in melt [7] and cut into plane-parallel 5×5-mm square platelets of thickness 200 to 300 μm. Their wide faces coincided with the (111) basal plane.

The DS was examined by the magnetooptic method. The domains were visualized by means of a crossed-analyzer transmission polarizing microscope (the transmission band of hematite is $0.9 < \lambda < 1.2$ μm) under normal incidence of light on the sample surface (i.e., light propagated along the C_3 axis). A video camera linked to a computer read out the DS image from the monitor of an electron–optical image converter. In addition, the intensity of the light transmitted through the polarizer–sample–analyzer system was measured as a function of the magnetic field and orientation (an FÉU-62 photoelectric multiplier was used as a photodetector).

A uniform magnetic field $H \le 100$ Oe was produced by two pairs of Helmholtz coils and could take any direction in the basal plane without changing its strength; i.e., $|H|$ remained the same. The samples were placed in an optical cryostat and were studied in the temperature range 80–290 K. Throughout the experiment, the sample surface was oriented normally to the terrestrial magnetic field.

It is known [8, 9] that the amount of magnetooptic effects in hematite depends substantially on the magnetization orientation in the basal plane. It is, therefore, of interest to trace the interplay between the azimuth angle of the ferromagnetic vector **m** and a magnetooptic-effect-induced change in the intensity of the light transmitted through the polarizer–sample–analyzer system. Using the Jones matrix formalism (the Jones matrix for weak rhombohedral ferromagnets was obtained in [10]) and taking into account that the Cotton–Mouton [8] and Faraday effects [9] are basic magnetooptic effects in the near-IR range, one can represent the light intensity at the exit of the polarizer–sample–analyzer system in the form

$$I(\varphi) \approx A\sin^2 2(\varphi + \varphi_1) + B\sin 3(\varphi + \varphi_1) + C\sin(\varphi + \varphi_2), \quad (1)$$

where A is the magnetooptic coefficient characterizing the Cotton–Mouton effect, B and C are the coefficients responsible for the Faraday effect, φ is the angle between the vector **m** and C_2 axis, and φ_1 and φ_2 are

1063-7842/03/4805-0651$24.00 © 2003 MAIK "Nauka/Interperiodica"

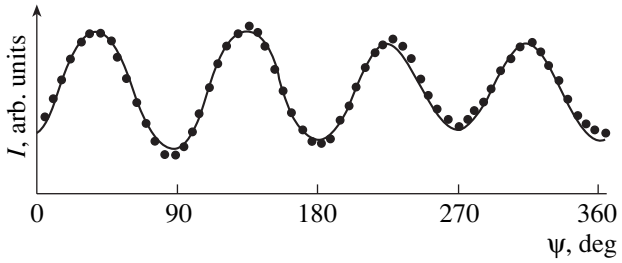

Fig. 1. Intensity of the light transmitted through the polarizer–sample–analyzer system vs. magnetic field (H = 100 Oe) orientation in the basal plane of α-Fe_2O_3. ψ is the angle between the vector **H** and an arbitrary direction in the basal plane of the crystal. Circles, data points; continuous curve, fitting with formula (1).

parameters depending on the orientation of the plane of polarization of incident light relative to the C_2 axis.

In (1), we take into account that the principal axis of symmetry may deviate somewhat from the direction of light propagation. Because of this, the Faraday effect from both the transverse (B harmonic) and longitudinal (C harmonic) components of the vector **m** contributes to $I(\varphi)$. To eliminate these effects, which are, generally speaking, a handicap to the determination of the vector **m**, we measured the photocurrent of the detector as a function of the applied magnetic field orientation in the basal plane. The field strength was taken such that the magnetic state of the sample was uniform (single-domain). Our experiments showed that such a situation occurs at $H > 30$ Oe.

Figure 1 demonstrates a typical orientation dependence of the intensity I for α-Fe_2O_3 at $T = 290$ K. From this curve, the amplitudes of the harmonics involved in (1) (the angle between the direction of light propagation and the C_3 axis is 1°–2°) were extracted by the least-squares method. The magnetooptic coefficients determined from Fig. 1 are related as $A : C : B \approx 10 : 1 : 0.1$. Consequently, the Cotton–Mouton effect is the main reason for the modulation of the intensity I. Then, decreasing the sample surface misorientation relative to the direction of incident light, one can diminish the fundamental harmonic amplitude so as to provide a correlation between the azimuth of the vector **m** and a change in the intensity I. Thus, from the integral characteristics of the light flux at the exit of the sample (expression (1)), one can find the orientation of the vector **m** in the basal plane (i.e., the direction of the C_2 axes), while the spatial variation of the magnetic order parameter of the crystal can be judged from the local characteristics of the light flux if the angle φ is considered as a function of the coordinates.

EXPERIMENTAL RESULTS

As follows from our experimental data for the DS evolution, when the field H in the basal plane is applied normally to the domain walls (DWs), which are observed in the demagnetized state of the sample, some of the hematite crystals exhibit MMSs similar to those obtained earlier in α-Fe_2O_3 : Ga [6]. Figure 2a shows the DS in one of the crystals that is visualized in the absence of the external magnetic field at room temperature. It turned out that the domain images become more contrasting if the C_3 axis is slightly deflected from the direction of light propagation; in other words, the Faraday effect is largely responsible for DS visualization in this case. This is possible if the domains are 90° or 180° domains. Since the insertion of a quarter-wavelength phase plate into the optical path of the microscope did not allow us to reliably observe the DS under normal incidence of light, we can infer that the domains are 180°. It is noteworthy that the wall to the right of Fig. 2a is diffuse; that is, it is inclined to the basal plane. Moreover, the orientation of the DWs coincides with none of the preferential directions in the basal plane (for most of the crystals studied, they were aligned with one of the C_2 axes, which are easy axes of in-plane crystallographic (hexagonal) anisotropy in hematite at room temperature [5]). One reason for the appearance of inclined DWs and the misalignment between the easy magnetic axis and C_2 axis in α-Fe_2O_3 is growth-induced internal stresses [5].

When the magnetic field in the basal plane is applied normally to the DWs in the demagnetized state, the sample first becomes single-domain. Then, at H = 6–15 Oe, the MMS in the form of diffuse-boundary fringes with different magnetooptic contrast appears in a certain area of the surface (Figs. 2b, 2c). With the vector **H** being deflected from this direction by an angle of less than 10°, the fringes shift, their width changes, but the direction and contrast of the image remain the same. As the angle of deflection increases, the MMS disappears.

As for the case of α-Fe_2O_3 : Ga, the spatial period λ of the MMS depends on the field: as H grows, the fringe spacing decreases (Figs. 2b, 2c). The period λ varies with the field stepwise: the number of fringes per length under observation changes. When the direction of **H** reverses, along with the pinning effect, the hysteresis of λ takes place: as the field declines (the backward run of magnetization), the mean period of the MMS is shorter than when the field rises.

It should be noted that the fringes in Figs. 2b and 2c are distinctly seen under normal incidence of light on the sample. In this case, the contrast of the MMS image can be inverted by appropriately selecting the azimuth of the polarizer. The contrast inversion was observed when the polarizer was rotated by an angle of ≈50° relative to the position in which the fringes in Figs. 2b and 2c appeared. This apparently means that the azimuths of the vector **m** at the centers of adjacent fringes differ approximately by 50°. The diffuse boundaries of the fringes lead us to conclude that **m** is not merely an alternating-sign vector, as in an ordinary DS, but has a smoothly varying direction. The MMS discovered can

be roughly represented by the one-dimensional oscillatory dependence of the azimuth angle β of the vector **m** on the spatial coordinate: $\beta \approx 25°\cos kx$, where $k = 2\pi/\lambda$ is the wavevector of the MMS and x is the running coordinate ($H \parallel X$).

A decrease in the temperature does not cause any noticeable change in the MMS period or contrast. However, at $T \approx 260$ K, both the DS and MMS in the crystal studied disappear almost stepwise. This could be expected, since, at the Morin temperature $T_M = 260$ K, α-Fe_2O_3 experiences a transition from the weak-ferromagnetic easy-plane state ($T > T_M$) to the easy-axis antiferromagnetic one ($T < T_M$). Comparing the field dependencies of the magnetooptic signal $I(H)$ that were taken from the area where the MMS was observed with those taken from areas where the MMS was absent shows that these areas differ by neither the coercive force nor the saturation field; however, the Morin temperature (determined from the disappearance of the signal I) turned out to be lower by approximately 3 K in the former case.

DISCUSSION

The MMS discovered in hematite crystals with internal stresses resembles the well-known magnetization ripple effect, which is common to polycrystalline Permalloy films [11]. Magnetization ripple arises in the films with in-plane magnetization and is associated with the transition of Permalloy to the magnetic phase where the local magnetization azimuth oscillates about the direction of the field H. In this case, the spatial period of modulation also decreases with increasing field (as for the MMS period in α-Fe_2O_3). It was shown [12] that the equilibrium magnetic structure, like magnetization ripple, arises owing to the combined effect of random anisotropy (crystallographic anisotropy in crystals arbitrarily oriented relative to each other), uniaxial anisotropy induced by the film texture, and an external magnetic field.

If the reason for the MMS is the same, one must assume that crystal areas where the MMS occurs possess uniaxial magnetic centers with randomly directed easy axes. These may be complexes formed by impurity ions (an uncontrollable amount of which is always present in real crystals) and surrounding ions of the Fe matrix. The difference in the ionic radii and/or charge states of the impurity and matrix ions inevitably causes lattice distortions. As a consequence, the orientation of the magnetic moments of the complexes will differ from the directions specified by the hexagonal anisotropy of the crystal. Such anisotropic magnetic centers are usually deemed to be the reason for additional uniaxial anisotropy in the basal plane of hematite [13, 14]. The occurrence of induced anisotropy is explained by impurity ion ordering, which takes place by ion diffusion. Growth-induced internal stresses specify the direction of this ordering and, thereby, the direction of the induced anisotropy axis. A lower Morin temperature in crystal areas with the MMS may be an indirect indication of the presence of impurities (it is well known [13] that impurities lower the Morin temperature T_M of hematite considerably: e.g., even if 1% of the Fe ions are substituted for by Sn ions, T_M tends toward subhelium temperatures [14]).

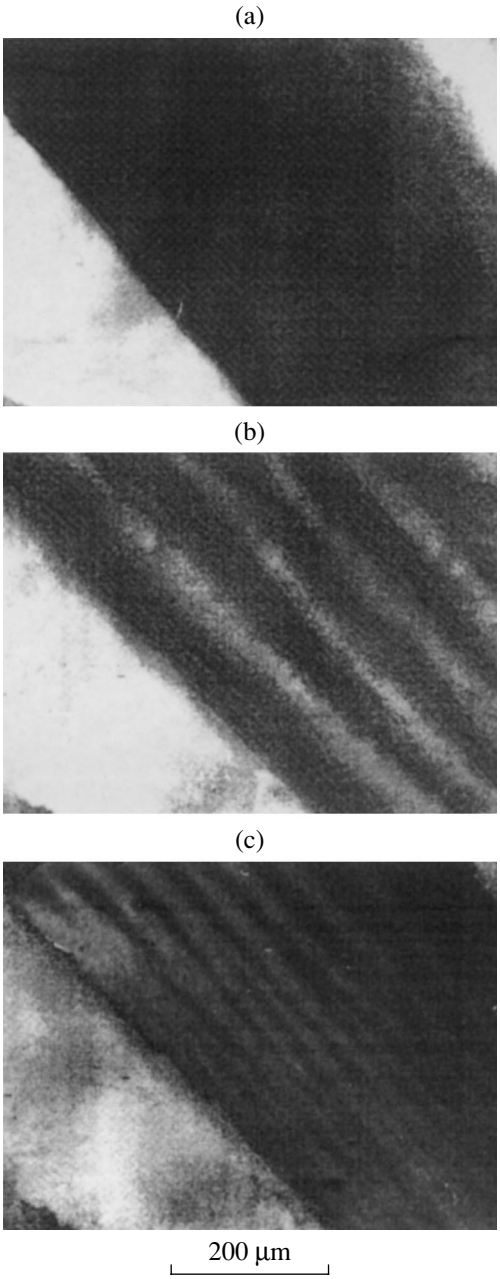

Fig. 2. α-Fe_2O_3 surface visualized in polarized light (sample thickness is 210 μm, $T = 290$ K). H = (a) 0, (b) 6, and (c) 14 Oe.

If the above assumptions are valid, then, based on the magnetization ripple theory and assuming (according to the theoretical model [12]) that $K_a > K \gg K_a N^{-1/2}$

(where K_a is the anisotropy constant, which defines the direction of the easy axis of a magnetic center; K is the constant of induced uniaxial anisotropy; and N is the number of uniaxial centers per unit volume), we can express the MMS period as

$$\lambda = 2\pi(J/K)^{1/2}(HM/2K - 1)^{-1/2}. \quad (2)$$

Here, J is the exchange constant and M is the spontaneous magnetization. Note that neither the impurity concentration nor the constant of in-plane hexagonal anisotropy (both parameters define the maximal angle of deflection of the local vector **m** from the magnetization direction) enter into (2) according to the model adopted.

From (2) it follows that the MMS appears if

$$H > H_0 = 2K/M. \quad (3)$$

This condition allows one to estimate the constant of induced uniaxial anisotropy. With H_0 = 6 Oe (the field of MMS occurrence) and M (T = 290 K) ≈ 2G [13], we find from (3) that $K \approx 6$ erg/cm^3 (cf. a constant of hexagonal anisotropy in hematite of 1–3 erg/cm^3 at room temperature [5]).

Unfortunately, the pinning and hysteresis effects, which are observed as the applied field varies, make it impossible to directly compare (2) with the experimental dependence $\lambda(H)$. However, the form of (2) implies that initially ($H \geq H_0$) the curve $\lambda(H)$ decreases sharply, but at higher H ($H \geq 2H_0$), one can set λ to be constant. Then, substituting $J = 2 \times 10^{-6}$ erg/cm [1], K = 6 erg/cm^3, and H = 12 Oe into (3), we find that $\lambda \approx$ 35 μm, which agrees well with the experimental data (Fig. 2c). This indicates that our model adequately fits the experiment. It is essential that (2) and (3) coincide with the relevant expressions [6] obtained by considering the thermodynamic potential of a weak rhombohedral ferromagnet if one puts $J = 2\gamma$, $K = -\alpha$, and $M = \mu l^2$, where γ, α, and μ are the coefficients of expansion of the thermodynamic potential in powers of the magnetic order and l is the magnitude of the antiferromagnetic vector.

As far as we know, an MMS like the one discovered in this work has not been observed before in hematite. A possible reason is the limitations of conventional experimental techniques applied to visualize hematite. For example, the method of powder patterns [1] or that based on the polar Kerr effect [3] require the magnetization to be out of plane, which is impossible when the basal plane of hematite is studied. X-ray topography [2] has a poor spatial resolution. Finally, [4], in which the DS was examined by a method similar to ours, seems to investigate perfect samples, as can be judged from the results reported.

REFERENCES

1. J. A. Eaton and A. H. Morrish, Can. J. Phys. **49**, 2768 (1971).
2. V. G. Labushkin, V. N. Seleznev, N. N. Faleev, *et al.*, Fiz. Tverd. Tela (Leningrad) **20**, 1544 (1978) [Sov. Phys. Solid State **20**, 891 (1978)].
3. A. A. Bogdanov and A. Ya. Vlasov, Fiz. Tverd. Tela (Leningrad) **12**, 164 (1970) [Sov. Phys. Solid State **12**, 130 (1970)].
4. V. L. Preobrazhenskiĭ, A. A. Shishkov, and N. A. Ékonomov, Fiz. Tverd. Tela (Leningrad) **29**, 3549 (1987) [Sov. Phys. Solid State **29**, 2034 (1987)].
5. M. M. Farzdinov and M. A. Shamsutdinov, Fiz. Tverd. Tela (Leningrad) **19**, 1422 (1977) [Sov. Phys. Solid State **19**, 1417 (1977)].
6. Z. T. Azamatov, A. T. Karaev, B. Yu. Sokolov, *et al.*, Zh. Tekh. Fiz. **71** (3), 84 (2001) [Tech. Phys. **46**, 354 (2001)].
7. R. A. Voskanyan and I. S. Zheludev, Kristallografiya **12**, 539 (1967) [Sov. Phys. Crystallogr. **12**, 473 (1967)].
8. V. S. Merkulov, E. G. Rudashevskiĭ, A. Le Gall', *et al.*, Zh. Éksp. Teor. Fiz. **80**, 141 (1981) [Sov. Phys. JETP **53**, 81 (1981)].
9. Yu. I. Shcherbakov, Fiz. Tverd. Tela (Leningrad) **26**, 866 (1984) [Sov. Phys. Solid State **26**, 524 (1984)].
10. Yu. M. Fedorov, A. A. Leksikov, and A. E. Aksenov, Fiz. Tverd. Tela (Leningrad) **26**, 220 (1984) [Sov. Phys. Solid State **26**, 128 (1984)].
11. A. Baltz and W. D. Doyie, J. Appl. Phys. **35**, 1814 (1964).
12. A. Hoffmann, J. Appl. Phys. **35**, 1790 (1964).
13. G. A. Petrakovskiĭ, A. I. Pankrats, V. M. Sosnin, *et al.*, Zh. Éksp. Teor. Fiz. **85**, 691 (1983) [Sov. Phys. JETP **58**, 403 (1983)].
14. B. Ya. Kostyuzhanskiĭ, M. Maryshko, and L. A. Prozorov, Zh. Éksp. Teor. Fiz. **77**, 764 (1979) [Sov. Phys. JETP **50**, 386 (1979)].

Translated by V. Isaakyan

Technical Physics, Vol. 48, No. 5, 2003, pp. 655–660. Translated from Zhurnal Tekhnicheskoĭ Fiziki, Vol. 73, No. 5, 2003, pp. 134–138.

BRIEF COMMUNICATIONS

On Nonlinear Effects in Condensation Models with Continuous and Discrete Descriptions of Nucleation

Yu. E. Gorbachev

Institute of High-Performance Computing and Information Systems, St. Petersburg, 191187 Russia
e-mail: gorbachev@hm.csa.ru

Received October 28, 2002

Abstract—A set of nonlinear equations for the evolution of the condensate fraction is suggested. The diffusion approximation to the Zel'dovich equation is shown to be fundamentally inapplicable for describing nonlinear effects. A diffusion equation with the applicability domain free of limitations due to supersaturation smallness is derived. © *2003 MAIK "Nauka/Interperiodica".*

INTRODUCTION

A great number of works (see, e.g., [1–3]) have been devoted to the derivation of equations for flows with in condensation. Although this procedure implies the reduction of the dimensionality of the problem [4, 5], this point has escaped researchers' attention. The basic reason is that slow and fast variables describing nucleation and condensation are difficult to separate. This is because condensation involves a set of characteristic times. It has been shown [6] that the evolution of the cluster size distribution toward its quasi-stationary value is defined by a set of times: kinetic time of relaxation τ_k [7, 8] and an infinite series of partial delay times $\tau_d(g)$, which depend on the cluster (g-mer) size. Such a situation makes the relaxation and condensation processes very specific. The times $\tau_d(g)$ were shown to be monotonically increasing functions [6]. For subcritical clusters ($g < g_*$), the delay time is less than the relaxation time; hence, the time it takes for the cluster size distribution to reach its quasi-stationary form depends only on the kinetic time. For supercritical clusters, the relationship between the relaxation and delay times is reverse and, starting with a certain size g_m, the value of $\tau_d(g)$ becomes comparable to the characteristic gasdynamic time τ_{gd}. In other words, sufficiently large clusters evolve only on a time scale on the order of τ_{gd}. It follows from the aforesaid that the term "critical size" separates clusters that have relaxed to their quasi-stationary size distribution by the time instant τ_k (subcritical clusters) from those that only begin to relax at the time instant τ_k [6] (supercritical clusters). Such a division is consistent with the definition of τ_k as the time within which a cluster of critical size forms [7, 8].

By a condensate, we mean clusters of supercritical size ($g > g_*$), considering them to be stable. Another argument in favor of this choice is the feature of cluster relaxation mentioned above. This feature allows one to assume that the flux of critical-size clusters during condensation is close to the quasi-stationary cluster flux [6]. An equation describing the behavior of a condensate can be obtained from kinetic equations for the cluster size distribution function.

Starting from [9], the condensation process was analyzed in terms of equations of the quasi-chemical condensation model. In this model, it is assumed that clusters grow via association reactions (a monomer is attached to a g-mer) and decay when a g-mer dissociates into a monomer and a $(g-1)$-mer:

$$A_{g-1} + A_1 \rightleftharpoons A_g; \quad g = 2, 3, \ldots. \tag{1}$$

The rate constants for association and decay reactions (1) will be designated as K^+_{g-1} and K^-_g, respectively. Then, the evolution of the cluster size distribution function n_g is defined by the set of equations

$$\frac{\partial n_1}{\partial t} + \nabla \cdot (\mathbf{u} n_1) = -I_2 - \sum_{j=2}^{\infty} I_j, \tag{2}$$

$$\frac{\partial n_g}{\partial t} + \nabla \cdot (\mathbf{u} n_g) = I_g - I_{g+1},$$
$$I_g = -K^-_g n_g + K^+_{g-1} n_1 n_{g-1}; \quad g = 2, \ldots, \infty. \tag{3}$$

The quantity I_g is the rate of formation of g-mers per unit volume as a result of the above reactions or a cluster flux in the dimensionality space. The validity of Eq. (2), as well as of all its modifications and consequences following from it, is based on the result [6] that the flux in the dimensionality space is absent if $g >$

1063-7842/03/4805-0655$24.00

$g_m(t)$. This means that $gj_m = 0$ for $g \longrightarrow \infty$ and also that the sum on the right of (2) converges in the limit.

The rate constants K_g^+ and K_g^- are related to each other as

$$K_g^- = K_g^0 K_g^+, \quad K_g^0 = n_{g-1}^e / n_g^e, \tag{4}$$

where K_g^0 is the equilibrium constant;

$$n_g^e = n_1 \exp\left(-\frac{\Phi(g)}{kT}\right), \quad n_1^e = n_1, \tag{5}$$

is the equilibrium distribution function, which turns the cluster flux in the dimensionality space to zero ($I_g(n_g^e) = 0$), $\Phi(g)$ is the minimal energy needed to form a g-mer, and T is the temperature of the monomer gas. Relationship (4) follows from the law of mass action.

Along with the equilibrium distribution, we will deal with the stationary distribution n_g^s. It is defined by the relationship $I(n_g^s) = \text{const} = I^s$. Here, for $g \geq 2$, $\dot{n}_g = 0$ but $\dot{n}_1 \neq 0$.

The set of equations (3) is the discrete description of nucleation. In [10, 11], its continuous analogue in the form of a diffusion equation in the dimensionality space was suggested. In terms of the law of mass action (see (4)), the expression for the nucleation flux I_g can be written (in view of (5)) as

$$I_g = K_{g-1}^+ n_1 n_{g-1}^e \left(\frac{n_{g-1}}{n_{g-1}^e} - \frac{n_g}{n_g^e}\right) \approx -K_{g-1}^+ n_1 n_g^e \frac{\partial}{\partial g}\frac{n_g}{n_g^e} \tag{6}$$

$$= -D_g\left(\frac{\partial n_g}{\partial g} - n_g \frac{\partial \ln n_g^e}{\partial g}\right) = -D_g\left(\frac{\partial n_g}{\partial g} + \frac{n_g}{kT}\frac{\partial}{\partial g}\Phi(g)\right) = j_g,$$

where $D_g = K_{g-1}^+ n_1$ is the diffusion coefficient.

Substituting the derivative for the finite difference on the right of (3), we arrive at a diffusion-like equation for the function n_g:

$$\frac{\partial n_g}{\partial t} + \nabla \cdot (\mathbf{u} n_g) = -\frac{\partial j_g}{\partial g}. \tag{7}$$

This equation with the flux j, which is given by (6), must be supplemented by the boundary conditions at $g = 1$ and $g = \infty$. It is natural to take Eq. (2) as the former; the latter is usually written in the form $n_g / n_g^e \longrightarrow 0$ with $g \longrightarrow \infty$. To make the description close, one should also take an equation for n_1. In view of (2), it can be represented as

$$\partial n_1 / \partial t + \nabla \cdot (\mathbf{u} n_1) = j_2 + \sum_{g=2} j_g \approx \int_1^\infty j_g dg \tag{8}$$

(as to divergence of the integral, see the comments following (3)).

Both functions n_g^e and n_g^s are defined by a set of thermodynamic parameters that describe the macroscopic state of the system. These are usually referred to as slow (gasdynamic) variables. If the rate of change of one of them, say, the monomer concentration, increases, the distribution function will deviate from its stationary value. It was found [6] that the associated quasi-stationary distribution is the time derivative of the stationary distribution, i.e., $\dot{n}_g^s$. In this respect, we go beyond the scope of the classical approach. The need for such an extension and the dependence of the condensation process not only on gasdynamic parameters but also on the rate of their change were discussed in [12, 13].

The deviation of the nucleation flux from its stationary value results in its dependence on the cluster size. However, as will be shown in further analysis, it is sufficient to know the nucleation flux value only for the critical size of a nucleus in order to characterize the behavior of the condensate fraction. It was noted above that the nucleus critical size can be set equal to its quasi-stationary value.

In this work, the evolution of the condensate fraction is described in two ways having a different accuracy. The accuracy of the continuous description is estimated by comparing with that of the discrete approach. It is demonstrated that the continuous approach yields incorrect values of the condensate fraction under a high supersaturation.

CONDENSATE FRACTION

The condensation process is usually described in terms of the condensate mass [1, 2], which is taken to be equal to the mass of supercritical nuclei:

$$\alpha = \left(\int_{g_*}^\infty m_1 g n_g dg\right) / \rho_\Sigma, \quad \rho_\Sigma = \int_1^\infty m_1 g n_g dg, \tag{9}$$

where m_1 is the mass of a monomer.

To derive an equation for the evolution of the condensate mass, we will take advantage of the same set of Eqs. (7) and (8) for the cluster size distribution function $n_g(g, t)$ as that used for solving the problem of nucleation (without invoking new kinetic equations involving a source term proportional to the delta function $\delta(g - g_*)$ [2]).

In view of definition (9) and Eq. (7) for the time derivative of the distribution function, differentiation

and integration by parts yield

$$\frac{d\alpha}{dt} = \frac{m_1}{\rho_\Sigma}\left(\int_{g_*}^{\infty} j\,dg + g_*\left(j_* - n_{g*}\frac{dg_*}{dt}\right)\right), \qquad \frac{d}{dt} = \frac{\partial}{\partial t} + \nabla\cdot\mathbf{u}. \tag{10}$$

Since the condensation process is *a fortiori* considered on a time scale much larger than the kinetic time τ_k, Eq. (10), according to [6], can be simplified if n_{g*} and j_* are replaced by their quasi-stationary values $n_{g_*}^{qs}$ and j_*^{qs}. Let us use expression (6) for the current and the expression

$$\frac{\Phi(g)}{kT} = a(g-1)^{2/3} - b(g-1), \qquad a = \frac{4\pi\sigma}{kT}\left(\frac{3v_l}{4\pi}\right)^{2/3}, \quad b = \ln s, \tag{11}$$

for the energy needed for the formation of a drop. Here, σ is the surface tension coefficient, v_l is the volume occupied by the monomer in the liquid phase, s is the supersaturation, and

$$D_g = K_g^+ n_1 \simeq K_1^+ n_1 g^{2/3} = D_*(g/g_*)^{2/3} \tag{12}$$

is the diffusion coefficient. Then, integrating (10) by parts yields

$$\int_{g_*}^{\infty} j\,dg = -\int_{g_*}^{\infty} D_g n_g^e \frac{\partial}{\partial g}\left(\frac{n_g}{n_g^e}\right)dg = D_*\left(n_{g_*} + g_*^{-2/3}\int_{g_*}^{\infty} n_g\left(\frac{2}{3}g^{-1/3} - \frac{2}{3}ag^{1/3} + g^{2/3}\ln s\right)dg\right).$$

Designating the moments of the distribution functions as

$$\Omega_\nu = \int_{g_*}^{\infty} g^{\nu/3} n_g\,dg \tag{13}$$

and bearing in mind that $2a/3 = g_*^{1/3}\ln s$, we obtain

$$\frac{d\alpha}{dt} = \frac{m_1}{\rho_\Sigma}\left(D_*\left(n_{g_*}^{qs} + g_*^{-2/3}(\Omega_2 - g_*^{1/3}\Omega_1)\ln s + \frac{2}{3}\Omega_{-1}\right) + g_*\left(j_*^{qs} - n_{g_*}^{qs}\frac{dg_*}{dt}\right)\right). \tag{14}$$

According to [6], the quasi-stationary cluster flux j_*^{qs} has the form

$$j_*^{qs} = j^s(1-\xi(1-\sqrt{1-\xi^{-2}\tilde{\mu}_*}))\exp[-\tilde{\mu}_*\tau_b/\tau_k + 2\xi(1-\sqrt{1+\xi^{-2}\tilde{\mu}_*})/\sqrt{\pi}] \simeq j^s\left(\frac{\varepsilon}{3}\right)^{2\tilde{\mu}_*/\pi}, \tag{15}$$

where

$$\xi = 1 + \frac{\sqrt{\pi}\dot{g}_*}{4}\tau_k, \quad \tau_k = \frac{\pi\Delta^2}{4D_*}, \qquad \dot{g}_* = \frac{d}{dt}g_*, \quad \tilde{\mu}_* = \tau_k\frac{d\ln n_*^s}{dt},$$

$$\frac{\tau_b}{\tau_k} = -\frac{1}{\tau_k}\int_1^{g_*-\Delta}\frac{dg'}{(\dot{g}(g') + g'\dot{g}_*/g_*)} \simeq \frac{2}{\pi}\ln\frac{3}{\varepsilon}, \qquad \varepsilon = \Delta/g_*, \quad \Delta = \left(-\frac{1}{2kT}\frac{\partial^2\Phi}{\partial g^2}\bigg|_*\right)^{-1/2}.$$

The drift velocity in the dimensionality space can be written as

$$\dot{g} = -\frac{j^s}{n_g^s} + D_g\frac{\partial\ln n_g^s}{\partial g} = -\left(\frac{2j^s}{n_g^s} + \frac{D_g}{kT}\frac{\partial\Phi}{\partial g}\right). \tag{16}$$

Differentiating relationship (13) with respect to time and using Eq. (7), we arrive at

$$\frac{d\Omega_\nu}{dt} + \Omega_\nu\nabla\cdot\mathbf{u} = \frac{\nu}{3}D_*\left(g_*^{\nu/3-1}n_{g_*}^{qs} + \frac{\nu-1}{3}\Omega_{\nu-4} + g_*^{-2/3}(\Omega_{\nu-1} - g_*^{1/3}\Omega_{\nu-2})\ln s\right) + g_*^{\nu/3}\left(j_*^{qs} - n_{g_*}^{qs}\frac{dg_*}{dt}\right); \quad \nu = 1, 2, \tag{17}$$

$$\frac{d\Omega_0}{dt} + \Omega_0\nabla\cdot\mathbf{u} = j_*^{qs} - n_{g_*}^{qs}\frac{dg_*}{dt}. \tag{18}$$

Neglecting Ω_{-2} in comparison with Ω_1 in the equation for Ω_2, we find for $\nu = 2$ and 1

$$\frac{d\Omega_2}{dt} + \Omega_2\nabla\cdot\mathbf{u} = \frac{2}{3}\frac{D_*}{g_*^{2/3}}(g_*^{1/3}n_{g_*}^{qs} + (\Omega_1 - g_*^{1/3}\Omega_0)\ln s) + g_*^{2/3}\left(j_*^{qs} - n_{g_*}^{qs}\frac{dg_*}{dt}\right), \tag{19}$$

$$\frac{d\Omega_1}{dt} + \Omega_1 \nabla \cdot \mathbf{u} = \frac{1}{3}\frac{D_*}{g_*^{2/3}}(n_{g_*}^{qs} + (\Omega_0 - g_*^{1/3}\Omega_{-1})\ln s) + g_*^{1/3}\left(j_*^{qs} - n_{g_*}^{qs}\frac{dg_*}{dt}\right). \quad (20)$$

We interrupt the series of equations for Ω_ν at $\nu = -1$ and use the closing relationship

$$\Omega_{-1}\Omega_1 = \Omega_0^2. \quad (21)$$

As a result, we have the closed set of five equations, (14) and (18)–(21), which describes the behavior of the condensate fraction. If Ω_{-2} is not rejected at $\nu = 2$ in (17), one more equation to close the set is necessary. This can be an equation similar to (21):

$$\Omega_{-2}\Omega_2 = \Omega_0^2. \quad (22)$$

In this case, the evolution of the condensate fraction is described by the set of six equations: (14), (17) with $\nu = 1$ and 2, (18), (21), and (22).

DISCRETE APPROACH

The Zel'dovich equation is widely used for studying the nucleation process; however, its applicability domain is difficult to estimate *a priori*. Frequently, such an estimate can be made only by comparing *a posteriori* the associated data with results obtained in terms of the discrete approach, which is based on the quasi-chemical model of condensation (see Eqs. (2) and (3)). In this case, analysis is conveniently performed in the new variables [6]

$$\tilde{n}_g = n_g/n_g^s. \quad (23)$$

Then, from Eq. (7) it follows that

$$\frac{d\tilde{n}_g}{dt} + \tilde{n}_g \nabla \cdot \mathbf{u} = \dot{g}\frac{\partial \tilde{n}_g}{\partial g} + \frac{\partial}{\partial g}D_g\frac{\partial \tilde{n}_g}{\partial g} - \tilde{n}_g\frac{d\ln n_g^s}{dt}, \quad (24)$$

where the drift velocity $\dot{g}$ in the dimensionality space is given by (16). From (3), we come to

$$\frac{d\tilde{n}_g}{dt} + \tilde{n}_g \nabla \cdot \mathbf{u} = n_1 K_g^+\left(1 - \frac{I^s}{n_1 K_g^+ n_g^s}\right)\Delta\tilde{n}_{g+1} - n_1 K_{g-1}^+\left(1 - \frac{I^s}{n_1 K_{g-1}^+ n_{g-1}^s}\right)\Delta\tilde{n}_g - \left(\frac{I^s}{n_{g-1}^s} + \frac{I^s}{n_g^s}\frac{K_g^+}{K_{g-1}^+}\right)\Delta\tilde{n}_g + n_1 K_g^+\left(1 - \frac{n_{g-1}^e}{n_g^e}\right)\Delta\tilde{n}_g - \tilde{n}_g\frac{d\ln n_g^s}{dt}, \quad (25)$$

where $\Delta\tilde{n}_g = \tilde{n}_g - \tilde{n}_{g-1}$.

Passing from the discrete form to the continuous, we obtain a diffusion equation with a modified (compared with Eq. (24), which was derived from the Zel'dovich equation) diffusion coefficient and drift velocity in the dimensionality space:

$$\frac{d\tilde{n}_g}{dt} + \tilde{n}_g \nabla \cdot \mathbf{u} = \dot{g}^*\frac{\partial \tilde{n}_g}{\partial g} + \frac{\partial}{\partial g}D_g^*\frac{\partial \tilde{n}_g}{\partial g} - \tilde{n}_g\frac{d\ln n_g^s}{dt},$$

$$D_g^* = D_g\left(1 - \frac{I^s}{n_1 K_{g-1}^+ n_{g-1}^s}\right), \quad (26)$$

$$\dot{g}^* = -\frac{I^s}{n_{g-1}^s} + n_1 K_g^+\left(1 - \frac{n_{g-1}^s}{n_g^s}\right),$$

with D_g defined by (12). Note that the use of diffusion equation (26) with variables (23) seems to be more adequate, since ratio (23), over a wide cluster size range, is a smoother function of g than n_g/n_g^e, which was used in deriving the Zel'dovich equation.

Estimating the expressions for the diffusion coefficient and drift velocity in (26) at $g = g_*$ in view of the approximate relationship for the stationary current $j^s = \left(\int_1^\infty (D_g n_g^e)^{-1} dg\right)^{-1} \simeq D_* n_*^e/(\Delta\sqrt{\pi})$, we find for the quantities calculated at $g = g_*$

$$\dot{g}_*^* = \dot{g}_*\left(1 - \frac{1}{\Delta\sqrt{\pi}}\right),$$
$$D_*^* = D_*\left(1 - \frac{2}{\Delta\sqrt{\pi}}\right), \quad \Delta \simeq \frac{3g_*^{2/3}}{\sqrt{a}} = \frac{4a^{3/2}}{3\ln^2 s}. \quad (27)$$

From (27) it follows that the difference between the expressions obtained by the continuous and discrete approaches is governed by the half-width Δ of the equilibrium cluster size distribution n_g^e near its minimum at $g = g_*$. Hence, at small Δ, the diffusion approach to describing the evolution of the distribution function $\tilde{n}_g$ (i.e., Eq. (7)) becomes invalid.

At the same time, Eq. (26), which describes the evolution of $\tilde{n}_g$ and was obtained directly from equations of the quasi-chemical model in view of the refined expressions for the flux in the dimensionality space and diffusion coefficient, adequately covers, within the diffusion approximation, situations with small Δ. In essence, this equation is a generalization of the Zel'dovich equation and its applicability domain is free

of restrictions due to the smallness of supersaturation (large Δ).

Now let us elucidate the difference in the condensate fractions estimated in terms of the continuous and discrete approaches.

Within the discrete approach, the condensate fraction is defined as

$$\alpha = \left(\sum_{g_*}^{\infty} m_1 g n_g\right)/\rho_\Sigma, \quad \rho_\Sigma = \sum_{1}^{\infty} m_1 g n_g. \tag{28}$$

From Eqs. (3), we find an equation for the condensate mass evolution:

$$\frac{d\alpha}{dt} = \frac{m_1}{\rho_\Sigma}\left(\sum_{g_*+1}^{\infty} I_g + g_*\left(I_* - n_{g_*}\frac{dg_*}{dt}\right)\right). \tag{29}$$

To close this equation, we use representation (6) of the flux. Rearranging the terms of the sum in (29), we come to

$$\sum_{g_*+1}^{\infty} I_g = n_1 K_{g_*}^+ + n_1 \sum_{g_*+1}^{\infty} K_g^+\left(1 - \frac{n_{g-1}^e}{n_g^e}\frac{K_{g-1}^+}{K_g^+}\right) n_g.$$

Assuming that $K_g^+ \simeq K_*^+ (g/g_*)^{2/3}$, $K_{g-1}^+/K_g^+ \simeq 1 - 2/(3g)$, and $n_{g-1}^e/n_g^e \simeq \exp(-(1-(g_*/g)^{1/3})\ln s)$, the sum can be rearranged into

$$n_1 K_{g_*}^+ + n_1 K_*^+ \sum_{g_*+1}^{\infty}\left(\frac{g}{g_*}\right)^{2/3} \times\left(1 - \left(1 - \frac{2}{3g}\right)\exp(((g_*/g)^{1/3} - 1)\ln s)\right) n_g.$$

Further, the exponential in this sum can be linearized at a small supersaturation. If $\ln s \ll 1$, $\exp(((g_*/g)^{1/3} - 1)\ln s) \sim 1 + ((g_*/g)^{1/3} - 1)\ln s$. Then, the sum takes the form

$$n_1 K_{g_*}^+ + n_1 K_*^+ \sum_{g_*+1}^{\infty}\left(\frac{g}{g_*}\right)^{2/3}\left((1 - (g_*/g)^{1/3})\ln s + \frac{2}{3g}\right) n_g.$$

The discrete analogues of expressions (13) for the moments of the distribution function are as follows:

$$\Omega_\nu = \sum_{g=g_*}^{\infty} g^{\nu/3} n_g \quad \text{or} \quad \tilde{\Omega}_\nu = \sum_{g=g_*}^{\infty} (g/g_*)^{\nu/3} n_g, \qquad \Omega_\nu = g_*^{\nu/3}\tilde{\Omega}_\nu. \tag{30}$$

For both the condensate fraction and the Ω moments, we arrive at equations that are exactly the same as those in the continuous approach. This means that the diffusion approximation describes adequately the variation of the condensate fraction only at small supersaturations and that the set of equations for the distribution function moments basically cannot be extended beyond the linear description. Linearity is inherent in all the available approaches considering the evolution of the condensate fraction except that suggested in [3]. To eliminate this restriction, we approximately sum the series, assuming $\alpha \simeq 1 - \exp(-\alpha)$. Neglecting quantities on the order of $\Omega_{\nu-3}/\Omega_\nu$ and using α defined by (28), we arrive at a closed set of equations for the condensate fraction evolution:

$$\frac{d\alpha}{dt} = \frac{m_1}{\rho_\Sigma}\Big[D_*(n_{g_*}^{qs} + \tilde{\Omega}_2(1 - s^{(\tilde{\Omega}_1/\tilde{\Omega}_2 - 1)})) + g_*\left(j_*^{qs} - n_{g_*}^{qs}\frac{dg_*}{dt}\right)\Big], \tag{31}$$

$$\frac{d\tilde{\Omega}_2}{dt} + \tilde{\Omega}_2\nabla\cdot\mathbf{u} = \frac{2}{3}\frac{D_*}{g_*}(n_{g_*}^{qs} + \tilde{\Omega}_1(1 - s^{(\tilde{\Omega}_0/\tilde{\Omega}_1 - 1)})) + j_*^{qs} - \left(n_{g_*}^{qs} + \frac{2}{3}g_*^{-1}\tilde{\Omega}_2\right)\frac{dg_*}{dt}, \tag{32}$$

$$\frac{d\tilde{\Omega}_1}{dt} + \tilde{\Omega}_1\nabla\cdot\mathbf{u} = \frac{1}{3}\frac{D_*}{g_*}(n_{g_*}^{qs} + \tilde{\Omega}_0(1 - s^{(\tilde{\Omega}_{-1}/\tilde{\Omega}_0 - 1)})) + j_*^{qs} - \left(n_{g_*}^{qs} + \frac{1}{3}g_*^{-1}\tilde{\Omega}_1\right)\frac{dg_*}{dt}, \tag{33}$$

$$\frac{d\tilde{\Omega}_0}{dt} + \tilde{\Omega}_0\nabla\cdot\mathbf{u} = j_*^{qs} - n_{g_*}^{qs}\frac{dg_*}{dt}, \tag{34}$$

$$\tilde{\Omega}_{-1}\tilde{\Omega}_1 = \tilde{\Omega}_0^2. \tag{35}$$

This set of equations completes the analysis aimed at deriving equations that describe the condensate fraction evolution in terms of the continuous and discrete approaches.

CONCLUSIONS

A set of equations for the condensate fraction evolution is derived, and several techniques to close the set are suggested. The consideration of condensation as the appearance of supercritical clusters is consistent with cluster stability analysis and also with the fact that they originate at larger-than-kinetic times. This is because the delay time of supercritical cluster formation exceeds the kinetic time (and not because of the presence of various relaxation times). The behavior of the condensate fraction is described in terms of the continuous and discrete approaches, which have different accuracies. The former involves the diffusion equation and corresponds to the linear approximation (small supersaturation). Data obtained with the continuous approach are compared with those of the discrete one to estimate the accuracy of the former. With the discrete approach, an equation of the diffusion type that is applicable over a wide supersaturation range is derived and

a closed set of equations for the condensate fraction evolution is suggested. This set extends beyond the scope of the linear approximation, which is typical of the continuous approach.

REFERENCES

1. P. G. J. Hill, J. Fluid Mech. **25**, 593 (1966).
2. L. E. Sternin, *Gas Dynamics of Two-Phase Flows in Nozzles* (Mashinostroenie, Moscow, 1974).
3. V. A. Shneĭdman and A. L. Shubenko, Izv. Akad. Nauk SSSR, Mekh. Zhidk. Gaza, No. 1, 108 (1990).
4. E. G. Kolesnichenko, Izv. Akad. Nauk SSSR, Mekh. Zhidk. Gaza, No. 3, 96 (1981).
5. N. G. van Kampen, Phys. Rep. **124** (2), 69 (1985).
6. Yu. E. Gorbachev and I. S. Nikitin, Zh. Tekh. Fiz. **70** (12), 28 (2000) [Tech. Phys. **45**, 1538 (2000)].
7. F. M. Kuni, in *Problems of Theoretical Physics*, Ed. by Yu. N. Demkov, Yu. V. Novozhilov, and P. P. Pavinskiĭ (Izd. Leningr. Gos. Univ., Leningrad, 1988), Vol. 3.
8. F. M. Kuni, Preprint ITP-84-178 E (Institute for Theoretical Physics, Kiev, 1984).
9. R. Becker and W. Döring, Ann. Phys. (Leipzig) **24**, 719 (1935).
10. Ya. B. Zel'dovich, Zh. Éksp. Teor. Fiz. 525 (1942).
11. Ya. I. Frenkel', *Collection of Selected Works* (Akad. Nauk SSSR, Moscow, 1959), Vol. 3, pp. 358–407.
12. Yu. E. Gorbachev and V. Yu. Kruglov, Pis'ma Zh. Tekh. Fiz. **16** (8), 1 (1990) [Sov. Tech. Phys. Lett. **16**, 283 (1990)].
13. Yu. E. Gorbachev, in *Proceedings of the 20th International Symposium on Rarefied Gas Dynamics, Beijing, China, 1996*, Ed. by Ching Shen (Peking Univ. Press, Beijing, 1997), pp. 853–858.

Translated by V. Isaakyan